

Geomechanical Controls on Multiphase Fluid Flow in Naturally Fractured Carbonate Reservoirs

by

Amir Hossein Haghi

A thesis submitted in partial fulfillment of the requirements for the degree of

Doctor of Philosophy

in

Geotechnical Engineering

Department of Civil and Environmental Engineering
University of Alberta

© Amir Hossein Haghi, 2020

Abstract

Carbonate formations host 50% of the world's oil and gas reserves and a major portion of the world's groundwater resources. Additionally, 85% of carbonate reservoirs are naturally fractured. Porous rock matrix and fractures in carbonate formations can be greatly influenced by the effective stress-induced deformation. Fluid production or injection in subsurface porous media will locally change pore pressures and in-situ stresses. These stress changes will, in turn, lead to pore and fracture deformation in naturally fractured carbonate reservoirs (NFCR) in response to the pore pressure/stress coupling effect. Similarly, pore volume has been shown experimentally in the literature to directly impact on absolute permeability and relative permeability of porous media. Relative permeability and capillary pressure are the governing parameters that characterize multiphase fluid flow mechanism (e.g. forced drainage and spontaneous imbibition) in porous media for diverse natural and industrial applications, including surface water infiltration into the ground, CO₂ sequestration, and hydrocarbon enhanced recovery. Although the drastic effects of deformation of porous media on single-phase fluid flow have been well established, the stress dependency of flow in multiphase systems is not yet fully explored.

This research has started with geomechanical investigation of an NFCR case study, Bangestan Reservoir, in SW of Iran. A wide ranges of field data including image logs, XLOT, acid fracturing, density logs, hydraulic fracturing tests, sonic wave velocity, and transient flow test were collected, analyzed, and used to quantify and model the state of in-situ stress, pore pressure and mechanical properties of the reservoir. The study

suggested that the contemporary state of stress in the reservoir was characterized by normal faulting (NF) stress regime.

A novel semi-analytical model was then developed to study the influence of stress-dependent effects on porosity, absolute permeability, relative permeability, and capillary pressure on the imbibition and oil recovery mechanisms of both intact rock and fracture in a cubic block model. To capture the geomechanical interactions involved, pure compliance poroelastic definitions and nonlinear joint normal stiffness equations were used to assess the deformation of intact rock and fracture, respectively. To evaluate the accuracy of the model, database from the Bangestan reservoir and some stress-dependent multiphase flow properties from the literature were used. It was shown how shifts in multiphase flow properties in response to an increase in effective stress from 0MPa to 30MPa decreased the oil recovery by 50%. For confirmation, multiphase flow simulation and coupled geomechanical and dual permeability flow simulation techniques were used to study the stress-dependent spontaneous imbibition and cumulative oil production in a block-scale and reservoir-scale models, respectively.

Finally, changes in the hydrodynamic properties of Berea sandstone, Indiana limestone, and an artificially fractured carbonate specimen from the middle Devonian Calumet member of the Waterways formation (Foster Creek North project, Alberta) at a constant temperature of 40⁰C were reported as isotropic effective confining stress was increased from 10MPa to 30MPa. Through a novel consecutive approach, porosity, absolute permeability, drainage relative permeability, and drainage capillary pressure were shown to change, systematically, with increases in effective stress. The relative permeability measurements were taken using a steady-state method for the N₂/water fluid

pair. A second method, in which a saturated core/fracture with the wetting phase was flushed with the non-wetting phase at an increasing flow rate, was used to determine the drainage dynamic capillary pressure. Gas separation units and mass balance were used to determine core saturation. Additionally, we used X-ray computed micro-tomography and micro-scale proxy model to quantify the stress-dependent structure and shape of the pores, together with the pore size distribution and two metrics (fractal dimension and degree of anisotropy). Using micro-scale investigation techniques, we recognized a leftward shift in pore size distribution and closure of micro-channels to be responsible for the systematic core-scale changes in multiphase flow properties with effective stress.

Preface

A majority of this thesis has been published in peer-reviewed journals and presented in conferences, which are foot-noted at the beginning of each chapter. For all papers, I designed the research, conducted the experiments, analyzed the data, and wrote the manuscript. Stephen Talman from the University of Alberta contributed to the experimental design and data analysis. Sebastian Geiger from Heriot-Watt University (co-supervisor) helped in the development of the analytical model. Hossein Ghobadi from NIOC provided us access to the required field data. A list of all papers are given below:

1- Published journal papers:

Haghi, A.H., Talman, S., Chalaturnyk, R. (2020). Consecutive Experimental Determination of Stress-dependent Fluid Flow Properties of Berea Sandstone and Implications for Two-phase Flow Modelling. *Water Resources Research*, 56(1), <https://doi.org/10.1029/2018WR024245>

Haghi, A.H., Chalaturnyk, R., Talman, S. (2019) Stress-Dependent Pore Deformation Effects on Multiphase Flow Properties of Porous Media. *Scientific Reports*, 9(1), 1-10.

Haghi, A. H., Chalaturnyk, R., Geiger, S. (2018). New Semi-Analytical Insights into Stress-Dependent Spontaneous Imbibition and Oil Recovery in Naturally Fractured Carbonate Reservoirs. *Water Resources Research*, 54(11), 9605-9622.

Haghi, A. H., Chalaturnyk, R., Ghobadi, H. (2018). The state of stress in SW Iran and implications for hydraulic fracturing of a naturally fractured carbonate reservoir. *International Journal of Rock Mechanics and Mining Sciences*, 105, 28-43.

2- Conference Papers:

Haghi, A.H., Talman, S., Chalaturnyk, R., Geiger, S., (2018). New Experimental Approach for Stress-Dependent Capillary Pressure and Relative Permeability Curves in Porous Media. 4th UK InterPore Conference, Aberdeen, UK

Haghi, A.H., Chalaturnyk, R., Geiger, S., Abbasi, Y., (2018). Coupled Simulation of Stress-Dependent Spontaneous Imbibition in Dual-Perm Models. Third EAGE Workshop on Naturally Fractured Reservoirs, Muscat, Oman

Haghi, A.H., Chalaturnyk, R., Geiger, S., (2016). Reservoir Geomechanical Characterization of the Naturally Fractured Carbonates. Foundation CMG Summit, Calgary, Canada

Dedicated to my father who is no longer between us but I am sure he is happy today.

Acknowledgments

This major step could not be taken without the support of some special persons in my life. I am deeply grateful to my wife Ghazal for all her love, encouragement, inspiration, and supports during these years. Her presence beside me from the first day we arrived in Canada has been extremely hearth-warming. Additionally, the unconditional support and love of my mom, sisters, and brother during this period is appreciated so much.

I would like to express my sincere gratitude to my supervisor Dr. Rick Chalaturnyk for his immense knowledge, continuous supports, valuable advices, and mostly for his patience. Being a student in RG² under his supervision has been a great honor and privilege for me not only because of his internationally well-established name and first-class research facilities but especially because of the wonderful person he is. Talking to him has always been enlightening, pleasant, and full of energy and new ideas.

Besides my supervisor, I also wish to thank Dr. Stephen Talman for his technical supports and being a wonderful friend. He had definitely a great role in my Ph.D. research and life which I am grateful for it. I would like to thank my co-supervisor Dr. Sebastian Geiger from Heriot-Watt University for his valuable guidance and helps of other people at the University of Alberta during the last four years: Hope Walls, Keivan Khaleghi, Kevin Hodder, Alireza RS, Nathan Deisman, and Gilbert Wang... Thanks a million...

Table of Contents

1. Introduction.....	1
1.1 Carbonate Rocks	1
1.2 Naturally Fractured Reservoirs	5
1.2.1 Spontaneous imbibition	6
1.2.2 Gravity Drainage.....	7
1.3 Problem Statement	8
1.4 Research Objectives and Methodology.....	9
1.5 Thesis Organization.....	10
2. Geomechanical Investigation of a NFCR Case Study in SW of Iran.....	12
Abstract.....	12
2.1 Introduction	13
2.2 Geological Summary.....	14
2.3 The In-Situ Stress Tensor of Bangestan Reservoir	17
2.3.1 Maximum Horizontal Stress Orientation	17
2.3.2 Vertical Stress Magnitude.....	21
2.3.3 Minimum Horizontal Stress Magnitude.....	21
2.3.4 Maximum Horizontal Stress Magnitude.....	23
2.4 Construction 1D MEM for Bangestan Reservoir.....	32
2.5 Discussion	34
2.6 Conclusions	37
3. New Semi-Analytical Insights into Stress-Dependent Spontaneous Imbibition and Oil Recovery in Naturally Fractured Carbonate Reservoirs	40
Abstract.....	40
3.1 Introduction	41
3.2 Experimental Results.....	43
3.3 Derivation of Semi-Analytical Model.....	46
3.3.1 Stress-Dependent Counter-Current Fractional Flow Formulation.....	47
3.3.2 Matrix Stress-Dependent Properties Specification	51

3.3.3	Fracture Stress-Dependent Properties Specification.....	54
3.3.4	Dual Continuum Stress-Dependent Properties Specification	58
3.4	Results	63
3.5	Discussion	67
3.5.1	Comparison between Stress-Dependent and Independent Spontaneous Imbibition.....	68
3.6	Conclusions	71
4.	Numerical Simulation of Stress-Dependent Spontaneous Imbibition in Fractured Porous media.....	72
	Abstract.....	72
4.1	Introduction	73
4.2	Block-Scale Modeling:.....	74
4.2.1	Results:.....	76
4.3	Reservoir-scale Modeling:	81
4.3.1	Results:.....	82
4.4	Conclusions	87
5.	Consecutive Experimental Determination of Stress-dependent Fluid Flow Properties of Intact Berea Sandstone and Fractured Calumet Carbonate.....	88
	Abstract.....	88
5.1	Introduction	89
5.2	Theoretical Concepts and Prior Work.....	91
5.2.1	Stress, Strain, and Porosity Relations	91
5.2.2	Porosity and Permeability Relations.....	95
5.2.3	Two-phase Flow.....	97
5.3	Materials and Equipment	99
5.3.1	Rock Samples.....	99
5.3.2	Fluids.....	104
5.3.3	Core Flooding Set-up.....	104
5.4	Methodology	106
5.4.1	Stress-Dependent Porosity and Absolute Permeability Measurement.....	107

5.4.2	Stress-dependent Drainage Relative Permeability and Capillary Pressure Measurement.....	109
5.5	Results	111
5.5.1	Stress-dependent Porosity and Absolute Permeability	111
5.5.2	Stress-Dependent Drainage Relative Permeability and Capillary Pressure 113	
5.6	Discussion	119
5.6.1	Reproducibility of Sandstone Experimental Data.....	119
5.6.2	Stress-Dependent Porosity and Absolute Permeability of Berea Sandstone 122	
5.6.3	Stress-Dependent Relative Permeability of Berea Sandstone and Two-phase Flow Modelling.....	123
5.6.4	Stress-Dependent Capillary Pressures of Berea Sandstone	128
5.7	Conclusions	130
6.	Stress-Dependent Pore Deformation Effects on Multiphase Flow Properties of Porous Media.....	132
	Abstract.....	132
6.1	Introduction	133
6.2	Stress-Dependent Flow Properties from Core-Scale Experiments	135
6.3	Pore-Scale Observations and Conceptual Proxy Modelling	136
6.4	Analytical Modelling of Stress-Dependent Multiphase Flow Properties	136
6.5	Results and Discussions	138
6.5.1	Core-Scale Approaches.....	138
6.5.2	Pore-Scale Approaches.	143
6.5.3	Implicational Insights.....	147
6.6	Summary and Conclusions.....	148
6.7	Materials and Methods.....	149
6.7.1	Core-Scale Experiments.....	149
6.7.2	Imaging and Proxy Modelling	151
6.7.3	Pore Size Distribution and Pore Metrics.....	151
7.	Summary and Conclusions	153

7.1	NFCR Case Study in SW of Iran	153
7.2	Semi-Analytical and Numerical Approaches.....	153
7.3	Pore-Scale to Core-Scale Experimental Approaches.....	154
7.4	Future Research.....	154
	Bibliography	156
	Appendix A: Derivation of Similarity Variable	177
	Appendix B: Berea Sandstone Experimental Database	179
	Appendix C: Analytical Model Derivation	182
	Analytical Model Results.....	184

List of Tables

Table 2.1 Well data that are considered for stress induced features from image logs in Bangestan Reservoir.....	16
Table 2.2 Maximum horizontal stress orientation and the given quality ranking scheme	18
Table 2.3 Well and field specification	29
Table 3.1 Modified Brooks and Corey equation to fit curves on the Lian et al.'s (2012) Experimental Data.....	46
Table 3.2 Modified Brooks and Corey equations to fit curves on the McDonald et al.'s (1991) Experiment Data.....	46
Table 3.3 Initial and boundary conditions for the semi-analytical model shown in Fig. 3.4	49
Table 3.4 Parameter set for semi-analytical model.....	63
Table 4.1 Parameters used for numerical model as initial condition.....	74
Table 5.1 Calculated fitting constants in Eq.(5.4)-(5.5) for Zhu and Wong's (1997) experiment.....	95
Table 5.2 Calculated fitting constants in Eq.(5.11) for Zhu and Wong's (1997) experiment.....	96
Table 5.3 Calculated fitting constants in Eq.s (5.12)-(5.14) using the least square technique	99
Table 5.4 Calculated fitting constants in Eqs.(5.12)-(5.14) for the Berea sandstone experiment.....	119
Table 5.5 Calculated fitting constants in Eq.(5.28) for the Berea sandstone experiment	129
Table 5.6. Stress-dependent porosity and absolute permeability database.....	179
Table 5.7. Stress-dependent relative permeability database	180
Table 5.8. Stress-dependent capillary pressure database	181
Table 6.1 Calculated fitting constants for the power-law correlation functions using least square regression technique.	184

List of Figures

Fig. 1.1 Global spatial distribution patterns of liquid petroleum for the carbonates (Ehrenberg and Nadeau, 2005).....	1
Fig. 1.2 Porosity classification in carbonate rocks, image from Choquette and Pray, 1970	2
Fig. 1.3 Interparticle porosity classification of carbonate rocks, image from Lucia (1995).	3
Fig. 1.4 Vuggy porosity classification of carbonate rocks, image from Lucia (1995).	4
Fig. 1.5 Nelson classification of fractured reservoirs (Nelson, 2001). The indices f and m refer to fracture and matrix properties, respectively.	6
Fig. 1.6 Schematic curve of the imbibition and drainage mechanisms in capillary pressure plot. Here P_e , S_{wir} , and S_{or} refer to entry capillary pressure, irreducible wetting phase saturation, and residual non-wetting phase saturation, respectively.	7
Fig. 1.7 Schematic of water imbibition and gas drainage process in rock blocks. Here blue, green, and red colors indicate water, oil, and gas phases, respectively.....	7
Fig. 2.1 Geology and tectonics of Zagros Belt and the study area of Bangestan Reservoir, SW of Iran (Modified after http://www.world-stress-map.org/casmo/) and location of studied wells inside the Bangestan reservoir. Heavy arrows show motion of the Arabian plate relative to the Eurasian. Abbreviations: DE- Dezful Embayment, LS- Lorestan Salient, ZDF-Zagros deformation front, ZFTB-Zagros Fold and Thrust Belt.....	15
Fig. 2.2 Cretaceous stratigraphy of the Bangestan Reservoir, SW of Iran.	16
Fig. 2.3 Maximum horizontal stress variation with depth for seven wells across Bangestan Reservoir. This graph shows the sharp deviation of SH orientation for well B-3 within the interval 3600-3800 from the general NE-SW trend due to heterogeneity	19
Fig. 2.4 UBI log, natural fracture azimuth and porosity profile of a well in the eastern part of Bangestan Reservoir. This chart shows the sharp deviation of stress orientation with depth in well B3.	20

Fig. 2.5 Surface pressure and injection rate curves versus time of an XLOT test in Bangestan Reservoir for well B8.....	22
Fig. 2.6 Analysis of a) Instantaneous Shut-In Pressure (ISIP), b) Fracture Closure Pressure (FCP) using square root of time and c) Fracture Closure Pressure (FCP) using pressure derivative curve versus G function on the curve of XLOT test for Sh measurement in Bangestan Reservoir.	24
Fig. 2.7 a) Simulated ΔP_{frac} curve versus time on the basis of bilinear flow theory for different acid injection rates. The curve of injection rate 30 bbl/min best simulates the measured value of Sh based on field data. b) Simulated F function with time for well B9 in Bangestan Reservoir	27
Fig. 2.8 Bottom hole pressure versus fracture conductivity in acid injection test. As it is shown, increasing the fracture conductivity, bottom hole pressure decrease due to fluid deflation from the fracture	28
Fig. 2.9 Comparison between the magnitude of SV (Density log), reservoir pressure (from Repeat Formation Test), and Sh and SH based on XLOT, DDT and sonic wave velocity analysis. Vertical stress is calculated as the maximum principal stress ($S1=SV$) while the minimum horizontal stress is estimated as the least principal stress ($S3=Sh$).....	31
Fig. 2.10 Sonic wave velocity analysis for well B10 in Bangestan reservoir.....	33
Fig. 2.11 Maximum horizontal stress orientations in SW Iran from the WSM database (modified after Heidbach et al., 2016) and for the studied area, subdivisions of Zagros Belt (Alavi, 2007). Symbols and different colors indicate the method of measurement and the stress regime. The NE-SW SH orientations observed in wells B-1 to B-7 (the location of the stress indicators for this study in red are not exact) are consistent with the motion of the Arabian plate relative to the Eurasian (heavy arrows) and focal mechanism solutions observed in the Zagros Mountain belt. Abbreviations: UDMA-Urumieh Dokhtar magmatic assemblage, ZIZ -Zagros imbricate zone. This study reveals that normal stress regime exists in ZFTB outer lowland while focal mechanism solution records thrust faulting regime in the ZFTB inner highlands.	35

Fig. 2.12 Comparison between <i>kave</i> ratio versus depth for the Bangestan reservoir with stress data of other fields in Iran and worldwide data (Haghi et al., 2013a; Elyasi et al., 2014; Karimnezhad et al., 2014; Yaghoubi and Zeinali., 2009; Saeidi and Ahmadi, 2012; Heidbach et al., 2016).....	38
Fig. 3.1 Schematic description of stress-dependent spontaneous imbibition curve in a bundle of capillary tubes	43
Fig. 3.2 Relative permeability curves based on Lian et al.'s [2012] experiment. The dots define the experimental data and the solid lines indicate the curve fitting lines.	44
Fig. 3.3 Relative permeability curves based on McDonald et al.'s [1991] experiment. The dots define the experimental data and the solid lines indicate the curve fitting lines.....	44
Fig. 3.4 Block model consisting of X*Y*Z of orthogonal plane fractures.....	47
Fig. 3.5 Deformation of matrix block due to effective confining stress	53
Fig. 3.6 Arbitrary fracture geometry inside the block model	55
Fig. 3.7 Fracture closure versus normal stress in a) linear and b) nonlinear methods.....	56
Fig. 3.8 Investigation of the accuracy of Eqs.(3.59)-(3.62) for relative permeability curves in the case of 20 MPa effective confining stress	62
Fig. 3.9 Work flow of the semi-analytical solution for stress-dependent capillary imbibition	62
Fig. 3.10 Variation in stress-dependent spontaneous imbibition parameters a) imbibition <i>Pct</i> , b) ϕt c) <i>kt</i> , and d) Imbibition <i>krt</i> end-points.....	64
Fig. 3.11 Capillary pressure versus wetting phase saturation and the fitted line representing the linearity of data in a Log-Log scale	64
Fig. 3.12 Comparison between the a) geo-dynamic Buckley-Leveret and b) capillary-driven fractional flow in NFCRs	65
Fig. 3.13 Oil recovery profile for NFCRs as a function of changes to effective confining stress in 2D and 3D scales	66
Fig. 3.14 Saturation profiles for 10, 20 and 30 MPa effective confining stress	67
Fig. 3.15 Comparison of a) porosity and b) permeability changes with time and stress to a block of rock. Scenario 1: Geo-dynamic spontaneous imbibition. Scenario 2: stress-independent spontaneous imbibition.....	69

Fig. 3.16 Changes in a) relative permeability and b) capillary pressure curves over time in scenario 1 (geo-dynamic spontaneous imbibition).....	70
Fig. 3.17 Comparison of oil recovery from a block of rock between geo-dynamic spontaneous imbibition (Scenario 1) and stress-independent spontaneous imbibition (Scenario 2).....	70
Fig. 4.1 3D Fine-grid model employed to simulate stress-dependent spontaneous imbibition in the NFCR (right). 2D cross-sectional model presenting the phase distribution (green=oil, blue=water) in the fractures and the matrix (top left) and the distribution of the phases after the water imbibes into the matrix from the fracture (bottom left)	75
Fig. 4.2 Comparison of matrix block oil recovery for 10, 15, 20, 25 and 30 MPa effective confining stress considering only porosity and absolute permeability as stress-dependent parameters in (a) 2D plot and (b) 3D plot in the NFCRs.....	77
Fig. 4.3 Comparison of matrix block oil recovery for 10-30 MPa effective confining stress considering only relative permeability and capillary pressure as stress-dependent parameters in 2D plot (top), 3D plot for water-wet (bottom left), and 3D plot for mixed-wet (bottom right) in the NFCR.	78
Fig. 4.4 Comparison of matrix block oil recovery for 10 and 30 MPa effective confining stress considering porosity, absolute permeability, relative permeability, and capillary pressure as stress-dependent parameters in a) 2D plot and b) 3D plot in the NFCR.....	80
Fig. 4.5 Comparison of fine-grid matrix block oil recovery for 10 and 30 MPa effective confining stress conditions.	80
Fig. 4.6 a) 3D view of the fine-grid 5-spot model used to investigate the geomechanical controls on imbibition in NFCR. b) reservoir pressure history	82
Fig. 4.7 A comparison between 3D plots of porosity for conventional and coupled models.....	83
Fig. 4.8 A comparison between 3D plots of absolute permeability for conventional and coupled models.....	83
Fig. 4.9 Stress-dependent imbibition capillary pressure curves for fractured carbonate rock based on derived equation in section 3.3.4.4.....	84

Fig. 4.10 Stress-dependent imbibition relative permeability curves for fractured carbonate rock based on derived equation in section 3.3.4.4.....	85
Fig. 4.11 Comparing the cumulative oil production results from conventional and coupled simulation models in (a) 2D and (b) 3D plots.	86
Fig. 5.1 Plots (a) and (b) present stress-dependent porosity and absolute permeability, respectively, for five different sandstone rocks, based on data from Zhu and Wong's (1997) experiment, combined with the fitted curves (dotted lines). Plots (c) and (d) provide relative permeability and capillary pressure curves derived from the literature using an N ₂ /water (brine) fluid pair on Berea sandstone under less than 10Mpa effective stress condition, combined with the fitted Brooks and Corey correlation.	94
Fig. 5.2 (a) Measured cumulative pore size distribution and specific pore surface area of the Berea sandstone specimen using BJH and BET techniques, respectively, and (b) the contact angle of water droplet at its surface.....	100
Fig. 5.3 (a)-(b) Intact Calumet carbonate and (c)-(d) artificially fractured specimens...	101
Fig. 5.4 (a) Measured cumulative pore size distribution and specific pore surface area using BJH and BET techniques, respectively and (b) the uniaxial compressive strength test results of the intact Calumet carbonate specimen.....	102
Fig. 5.5 Measured contact angle of water droplet at the dry surface of (a) dark gray and (b) light crystal part of the rock. (c) Sessile drop test result showing an initial wettability of the carbonate rock to the oil phase.....	103
Fig. 5.6 Schematic of the core flooding apparatus.....	105
Fig. 5.7 This figure provides 3D plots of stress-dependent single-phase pressure drop versus (a) time (min), and (b) water flow rate (mL/min) and stress-dependent multiphase pressure drop versus (c) time (min), and (d) gas flow rate (mL/min) across the Berea sandstone specimen.	113
Fig. 5.8 This figure presents our experimental stress-dependent plots of: (a) porosity and absolute permeability, (b) gas injection flow rate versus corrected gas pressure drop, (c) relative permeability curves, and (d) capillary pressure curves of the intact Berea sandstone specimen.	116

Fig. 5.9 This figure presents our experimental stress-dependent plots of: (a) porosity and absolute permeability, (b) fracture closure, (c) relative permeability curves, and (d) capillary pressure curves of the fractured Calumet carbonate specimen. All data are provided in Appendix B.....	118
Fig. 5.10 Plot (a) illustrates a small downward shift in stress-dependent porosity-absolute permeability curve of Berea sandstone after 5 months and plot (b) indicates the percentage of decline of each property at different effective stress condition .	122
Fig. 5.11 This figure provides: (a) 3D plot of stress-dependent gas fractional flow curves versus gas saturation and (b) stress-dependent gas front location and saturation profile for Berea Sandstone	126
Fig. 5.12 Pressure drop versus dimensionless time at three different effective confining stress conditions during mixed N ₂ /water core flooding experiment of Berea core at gas fractional flow of: (a) 0.4 and (b) 0.6.....	127
Fig. 5.13 Modified J-function data at three different effective stress conditions for Berea Sandstone.....	129
Fig. 6.1 Proxy modelling work flow in 7 steps: (a) Choosing a new effective stress and find experimental pore strain ϵ_{PEXP} (b) Uploading original X-ray μ CT Image (c) Filtering (d) Binarization (e) Thresholding (f) Bitwise operation (g) Proxy modelling and analysis based on model pore strain ϵ_{pM}	137
Fig. 6.2 Core-scale experimental results representing the stress dependency of structural, single-phase flow, and multiphase flow properties of the carbonate rock: (a) stress-dependent permeability versus porosity plot, (b) normalized tortuosity versus porosity ratio, (c) stress-dependent relative permeability, and (d) stress-dependent capillary pressure.	140
Fig. 6.3 The plots provide stress-dependent (a) irreducible water saturation (S_{wir}) and water saturation at the intersection point of water and gas relative permeability curves (S_{wm}), (b) maximum gas relative permeability ($k_{rg} - max$), and (c) entry and maximum capillary pressure (P_e and P_{cmax} , respectively).	142
Fig. 6.4 This figure presents: (a) a 3D image of a single pore in the carbonate core (gray) and its proxy model at 30MPa effective stress condition; a single pore channel at (b) 0MPa, (c) 10MPa, (d) 20MPa, and (e) 30MPa effective confining stress	

condition; and (f) a 3D plot of the channel radius versus the critical capillary number at a range of effective stress conditions from zero to 30MPa. 144

Fig. 6.5 This figure provides insights into stress-dependent (A) 3D pore size distribution in a semi-log plot, (B) 3D fractal dimension (Df), and (C) 3D degree of anisotropy (DA) at a range of effective stress conditions from zero to 30MPa for the carbonate sample. 146

Fig. 6.6 Uniaxial compressive strength test results on an Indiana limestone specimen (3.81cm in diameter and 7.62cm in length) measured based on ISRM suggested standard methods for determining the uniaxial compressive strength and deformability of rock materials (ASTM D7012)..... 150

Fig. 6.7 Measured air-water contact angle (α) equal to 18.8 degrees using a drop shape analyzer (DSA) at equilibrium condition. Based on the measured contact angle smaller than 90^0 , the carbonate is categorized as a strong water-wet rock. 150

1. Introduction

Carbonate rocks host 50% of the world's hydrocarbon reserves (Burchette, 2012), including many of the reservoirs in Western Canada and the Middle East, and carbonate aquifers supply a quarter of global request to freshwater (Hartmann et al., 2014). Almost 85% of carbonate formations are affected in some way by natural fractures. Natural fractures help create secondary porosity and promote communication between formation compartments. Fig. 1.1 provides the spatial distribution patterns of the Earth's known hydrocarbon resources for the carbonates (Ehrenberg and Nadeau, 2005).

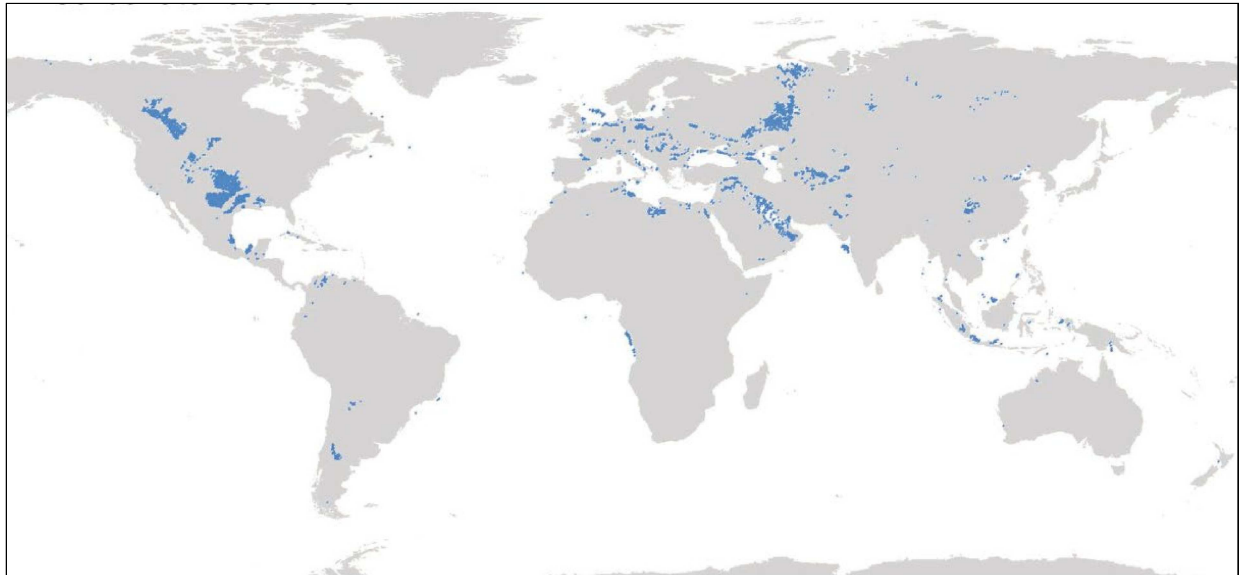


Fig. 1.1 Global spatial distribution patterns of liquid petroleum for the carbonates (Ehrenberg and Nadeau, 2005)

1.1 Carbonate Rocks

Most carbonate rocks are composed of particles of clay to gravel size that were generally deposited in a marine environment (Gluyas and Swarbrick, 2013). They differ from sandstones in that they are deposited as locally produced lime particles while sandstones are composed of particles moved by water currents from an outside source. The more important difference between carbonates and sandstones is the post-depositional diagenesis in carbonates which is

ranging from simple cementation of the original particles to complete recrystallization or replacement by dolomite or chert (Gluyas and Richard, 2004). Components of carbonate rocks are usually (1) grains of various kinds, (2) lime mud, and (3) carbonate cement precipitated later (Robert, 1980). Carbonate rocks mainly consist of three minerals including Calcite, aragonite, and dolomite, which the first two are rhombohedral and orthorhombic systems of CaCO_3 , respectively, and the third one is a rhombohedral system of $\text{CaMg}(\text{CO}_3)_2$.

Because of the complex nature of carbonate ingredients and diagenesis, carbonates have a wide range of pore structures. The first classification of the carbonate rocks based on the porosity information was presented by Archie (1952). He classified the porosity of carbonates into visible porosity and matrix porosity and described the visible porosity based on the pore size, with a range of classes from pinpoint (class A) to centimeter size (class D). Perhaps, Choquette and Pray (1970) classification is the most popular method used widely for geological modeling, which categorized porosity in carbonates into the fabric and non-fabric selective types (Fig. 1.2).

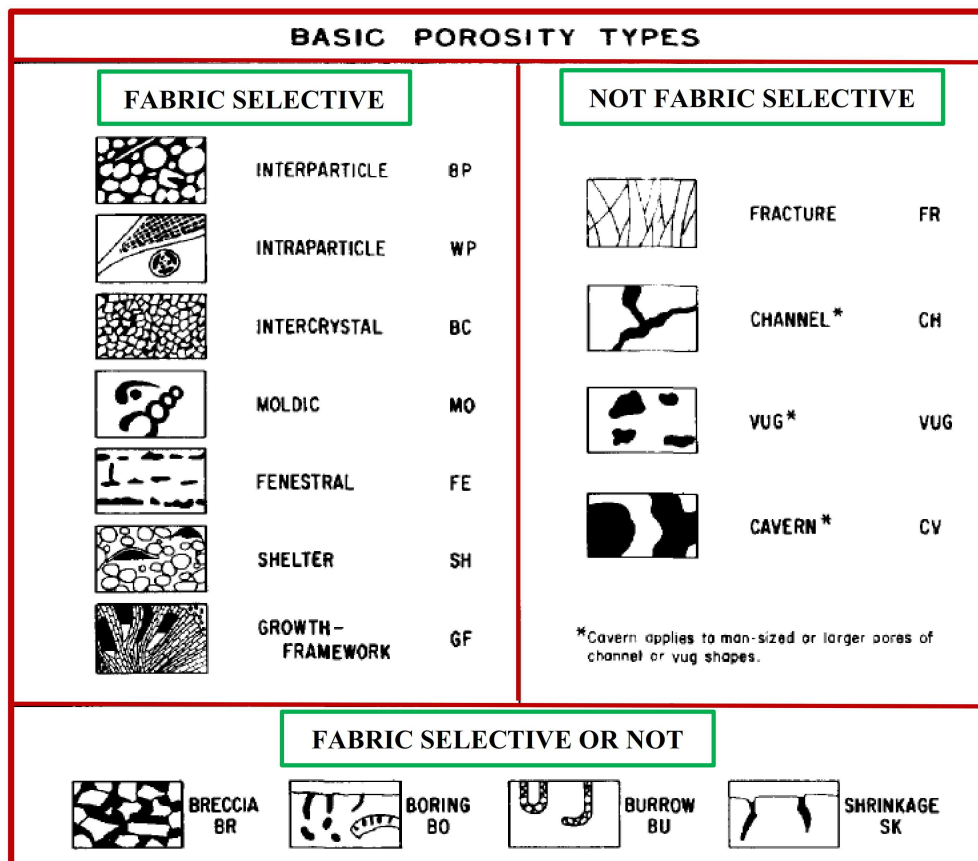


Fig. 1.2 Porosity classification in carbonate rocks, image from Choquette and Pray, 1970

Later, Lucia (1995) classified carbonates porosity into interparticle (intergrain and intercrystal) and vuggy pores (Fig. 1.3 and Fig. 1.4, respectively) to allow more valid petrophysical quantification of carbonate geological models. He found a relationship between particle size, sorting, interparticle porosity with permeability, and capillary properties of non-vuggy carbonate rocks.

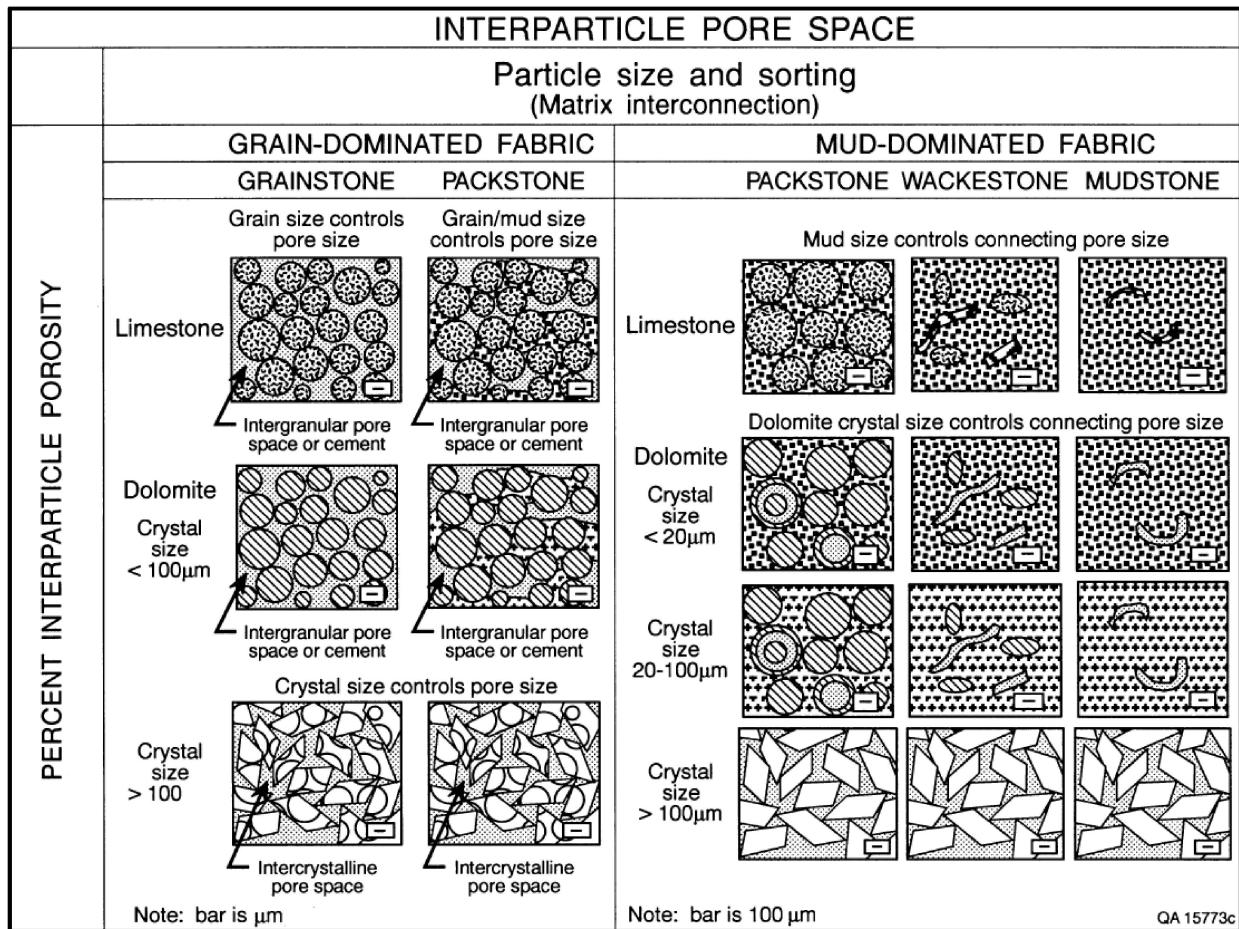


Fig. 1.3 Interparticle porosity classification of carbonate rocks, image from Lucia (1995).

As it is illustrated in Fig. 1.2, Choquette and Pray (1970) introduced 15 physically and genetically distinctive porosity types based on characteristics such as pore size, genesis, shape, etc. In Fig. 1.2, interparticle (in grainstones), intraparticle (in fossils), fenestral, shelter (cavities under fossils or intraclasts), and growth-framework (cavities in reefs or coralline algae beds) porosity are different types of primary porosity. Fenestral porosity refers to primary pores which are bigger than the surrounding grain-supported fabric and are commonly developed in beach sands or carbonate muds due to gas or air bubbling in the sediments (Moore and Wade, 2013).

Although the primary porosity of the carbonate rocks progressively decreases due to the overburden pressure induced-compaction, some secondary porosity-generating processes (e.g. diagenetic) act to increase pore volume and permeability of the evolving limestone over the time. Some of the most significant processes associated with the formation of secondary porosity in carbonate rocks are (1) dissolution (due to a dramatic change in the chemistry of pore fluid), (2) dolomitization, and (3) fracturing (in NFCR) (Moore and Wade, 2013). Although natural fractures may significantly increase permeability in carbonate reservoirs, their impact on the pore volume could be intangible (Moore and Wade, 2013).

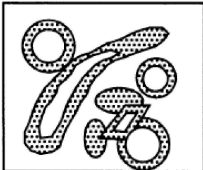


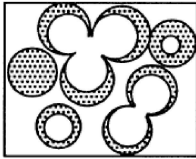

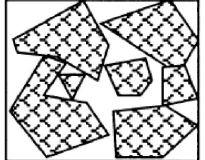
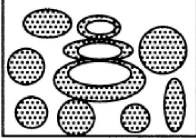

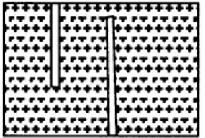
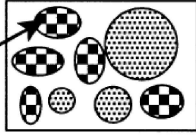
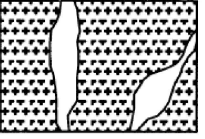
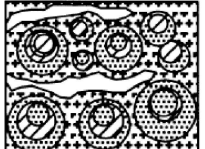
VUGGY PORE SPACE			
SEPARATE-VUG PORES (VUG-TO-MATRIX-TO-VUG CONNECTION)			TOUCHING-VUG PORES (VUG-TO-VUG CONNECTION)
PERCENT SEPARATE-VUG POROSITY	GRAIN-DOMINATED FABRIC	MUD-DOMINATED FABRIC	GRAIN- AND MUD-DOMINATED FABRICS
	EXAMPLE TYPES	EXAMPLE TYPES	EXAMPLE TYPES
	<p>Moldic pores</p> 	<p>Moldic pores</p> 	<p>Cavernous</p> 
	<p>Composite moldic pores</p> 	<p>Intrafossil pores</p> 	<p>Breccia</p> 
	<p>Intrafossil pores</p> 	<p>Shelter pores</p> 	<p>Fractures</p> 
	<p>Intragranular microporosity</p> 		<p>Solution-enlarged fractures</p> 
			<p>Fenestral</p> 

Fig. 1.4 Vuggy porosity classification of carbonate rocks, image from Lucia (1995).

1.2 Naturally Fractured Reservoirs

Natural fractures are a common feature in nearly all hydrocarbon reservoirs. Brittle failure is mainly responsible for natural fractures in subsurface reservoirs, usually due to factors such as (a) folding, (b) faulting, (c) fluid pressure, (d) release of lithostatic pressure, (e) pressure solution, (f) dehydration, (g) weathering, (h) cooling, and (i) impact craters. Conceptually, the NFCR refer to reservoirs where oil recovery and reservoir performance are significantly influenced by the natural fractures. Hence, their properties as the secondary porosity media with essential permeability should be evaluated carefully to characterize the fluid flow in the reservoir (Ahmed and McKinney, 2011). Different classifications have been presented for the NFCR with perhaps the most recognized one being Nelson's (2001) classification where fractured reservoirs are classified into four types (Fig. 1.5):

- Type I: Fractures have high porosity and permeability while the matrix has low porosity and permeability;
- Type II: Fractures still provide the main reservoir permeability but have less storage capacity. Rock matrix has the essential storage capacity but low permeability;
- Type III: Fractures has a moderate permeability and low porosity in a reservoir with good matrix porosity and permeability; and
- Type IV: Fractures have intangible porosity and permeability in an already producible reservoir, but act as flow barriers.

Type II is a prevailing scenario for the NFCR. In this case, the flow properties of the tortuous and high permeable natural fractures govern the overall fluid flow in the reservoir, with the isolated matrix block porosity acting as the main petroleum storage.

For this class of reservoirs, the success of recovery techniques such as water flooding or alkaline surfactant polymer flooding (ASP) is negatively impacted by the limited pressure difference that arises in the reservoir as a result of highly permeable fractures dominating fluid flow. In these cases, capillary imbibition, as opposed to viscous displacement, becomes the dominant recovery mechanism enabling hydrocarbon to flow from the matrix into the fracture system. Spontaneous imbibition and gravity drainage are essential recovery mechanism in NFCR, and their performance is determined by the drainage/imbibition capillary pressure curves, which is a function of pore structure and wettability (Ferno, 2012). Increasingly, there has been a

recognition that the geomechanical behavior of NFCR can influence hydrocarbon recovery (Settari et al., 1999).

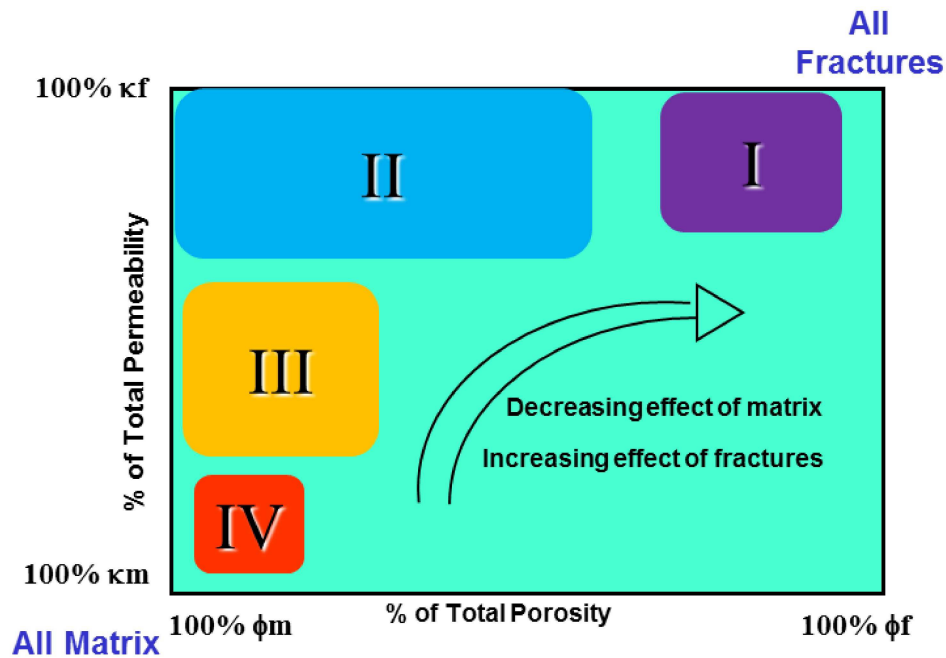


Fig. 1.5 Nelson classification of fractured reservoirs (Nelson, 2001). The indices f and m refer to fracture and matrix properties, respectively.

1.2.1 Spontaneous imbibition

Generally, imbibition is the process that the wetting phase absorbed into a porous rock while the saturation of the non-wetting phase decreases (red curve at Fig. 1.6). As it is illustrated in Fig. 1.6, the wetting phase saturation increases with decreasing the capillary pressure. Imbibition is important in a water-drive reservoir because it improves water movement and controls areal sweep efficiency. Spontaneous imbibition refers to the process of absorption due to capillary suction with no external viscous pressure driving the phase into the rock. The same rock can imbibe both water and oil, with water imbibing at low in-situ water saturation, displacing excess oil from the surface of the rock grains, and oil imbibing at low in-situ oil saturation, displacing excess water. In terms of strong hydrophilic rocks, water imbibes spontaneously at any saturation of water. Strong hydrophobic rocks reversely tend to absorb oil spontaneously at any saturation of water. An imbibition test is a comparison of the imbibition potential of water and oil into a rock. Spontaneous imbibition of water is a direct function of the capillary and gravity forces, and depends on the pore system, the wettability (Zhou et al., 2000),

matrix-block sizes and shape (Mattax and KYTE, 1962; Zhang et al., 1996; Torsaeter and Silseth, 1985), the interfacial tensions (Karimaie and Torseter, 2007), boundary conditions (Bourbiaux and Kalaydijan, 1990) and initial water saturation (Viksund et al., 1998).

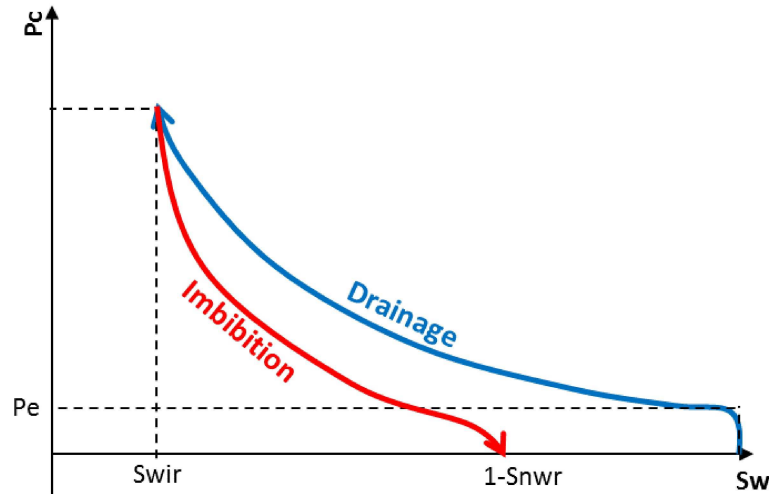


Fig. 1.6 Schematic curve of the imbibition and drainage mechanisms in capillary pressure plot. Here P_e , S_{wir} , and S_{or} refer to entry capillary pressure, irreducible wetting phase saturation, and residual non-wetting phase saturation, respectively.

1.2.2 Gravity Drainage

Gravity drainage was first introduced by Cardwell and Parsons (1949). In contrast with imbibition, gravity drainage is the process in which the saturation of the non-wetting phase increases with the increase of the capillary pressure (blue curve in Fig. 1.6). Gravity drainage is generally a gas-oil displacement process where gravity forces dominate over viscous and capillary forces and may result in high oil recovery (Hagoort, 1980).

Schematics of water imbibition and gas drainage process in a block of rock are illustrated in Fig. 1.7.

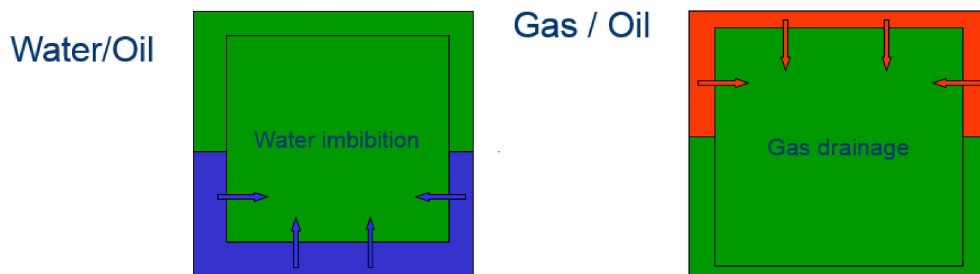


Fig. 1.7 Schematic of water imbibition and gas drainage process in rock blocks. Here blue, green, and red colors indicate water, oil, and gas phases, respectively.

1.3 Problem Statement

Porous rocks buried kilometers beneath the earth surface are exposed to a state of in-situ stress. Many authors have estimated the present-day in-situ stress state around the world (Heidbach et al., 2018; Haghi et al., 2013a). The state of stress in porous rocks varies over geological time depending on external (e.g. massive material movement due to erosion) and internal (e.g. depositionally induced compaction and tectonic forces) geological processes (Heidbach et al., 2010). Much more rapid human induced-changes arise due to injection and production operations in almost all petroleum/geothermal reservoirs and CO₂ storage formations (Haghi et al., 2013b). Changes in effective stress leads to shape and size alterations among pores within porous media, directly impacting both intrinsic rock properties such as porosity and absolute permeability (Geertsma, 1957; Zimmerman et al., 1986; Zhu and Wong 1997; Morris et al., 2003; Schutjens et al. 2004; Iglauer et al., 2014) and multiphase flow properties including capillary pressure and relative permeability curves (Li et al., 2004). These flow properties are fundamental for describing simultaneous flow of multiple phases in natural porous media, and slight changes in them induces a significant effect on the reserve and recovery of oil and gas fields and geothermal reservoirs (Ahmed and McKinney, 2011), transport of contaminating nonaqueous liquid phase in aquifers (Pak et al., 2015), performance of CO₂ subsurface sequestration (Szulczewski et al., 2012), and rainwater infiltration into ground (Cueto-Felgueroso and Juanes, 2008).

Despite an abundance of experimental studies of relative permeability and capillary pressure from both pore-scale and core-scale studies, the impact of pore deformation induced by effective stress changes on multiphase flow properties remains poorly explored (Huo and Benson, 2016). For conditions of increasing effective stress, existing experimental evidence (McDonald et al., 1991; Lian et al., 2012) reveal contradictory shifts in the relative permeability curves. Recognition of this contradiction has resulted in several authors conducting experiments to tackle the challenges in core-scale experiments (Huo and Benson, 2016) and pore-scale physical models (Li et al., 2019), independently. However, a comprehensive study of multiphase flow properties (e.g. relative permeability and capillary pressure) in both core-scale and pore-scale under a wide range of effective stress conditions has yet to be undertaken.

1.4 Research Objectives and Methodology

The main objective of this research was to develop an integrated approach to characterize geomechanical controls on flow properties (e.g. porosity, absolute permeability, relative permeability, and capillary pressure) and analyze how they influence multiphase fluid flow and recovery in naturally fractured carbonate reservoirs. We have investigated the problem using novel analytical, numerical, and experimental (both core-scale and pore-scale) approach. This thesis suggested an alternative understanding of the concept of multiphase flow for applications associated with geoscience and geo-energy industry.

For this purpose, we initially defined geomechanical process and parameters in an NFCR. We developed the first full in-situ stress tensor and a 1D mechanical earth model (MEM) of the Bangestan reservoir in SW of Iran using variety of data and methods including an acid re-fracturing test, an XLOT, a step-rate well test, seven full-bore images, 13 hydraulic fracturing test, a sonic wave velocity log, and 200 density and porosity logs. A Deformation/Diffusion/Thermal (DDT) approach was introduced to calculate S_H combining poroelastic theories for the circular underground cavities, bilinear theory for fluid flow through the preexisting induced fracture and thermal stress. These geomechanical properties have been employed in our analytical and numerical models.

Next, we presented a semi-analytical solution for stress-dependent capillary-driven fractional flow equation in NFCR. To do so, we derived analytical equations to specify the unknown stress-dependent parameters including porosity, absolute permeability, relative permeability, and capillary pressure in our semi-analytical solution. We characterized the stress-dependent properties of intact rock and fracture independently based on pure compliance poroelastic and nonlinear fracture stiffness equations, respectively, and then combined them with equivalent continuum concepts. Using the developed semi-analytical equation, fluid flow properties and oil recovery of a cubic block of carbonate rock with three orthogonal fractures were calculated under an increasing effective stress condition from 10MPa to 30MPa.

In order to validate the results of semi-analytical approach, the same block of rock with three orthogonal fractures was then modeled numerically using CMG (Computer Modelling Group) reservoir simulator and implementing same rock properties at each effective stress condition. CMG uses finite difference numerical approach for solving flow equation in reservoir

models. Three fine-grid models were constructed to simulate the spontaneous imbibition mechanism in a classical sugar-cube array of Warren and Root's [1963] original dual-porosity model at 10, 20, and 30 MPa effective stress condition (Elfeel et al., 2016) and their stress-dependent oil recoveries were compared. In a different approach, coupled geomechanical and dual permeability flow simulation technique is used to study the stress-dependent spontaneous imbibition and cumulative oil production in a 5-spot (a producing and 5 injecting wells) reservoir-scale model.

Our analytical and numerical results were promising enough to motivate us upgrading an apparatus in GeoREF lab to track and explain the changes in rock porosity, absolute permeability, drainage capillary pressure, and drainage relative permeability by raising triaxial isotropic effective confining pressure to 30 MPa in an isothermal condition (40°C). The apparatus gave us the opportunity to conduct the full test in a continuous manner on a Berea sandstone, Indiana limestone, and an artificially fractured Calumet carbonate specimen from the Waterways formation, Alberta. Additionally, we used X-ray computed micro-tomography and micro-scale proxy model to quantify the stress-dependent structure and shape of the pores, together with the pore size distribution, fractal dimension, and degree of anisotropy. This provides us with some comprehensive understanding of the significant changes induced by effective stress changes on multiphase flow properties and fluid transport (e.g. drainage/imbibition cycle) in natural porous media, which has been much less explored in the literature.

1.5 Thesis Organization

This dissertation is structured in paper-based format and the papers have been mainly peer-reviewed for journal publication (IJRMMS, WRR, SR). A glance on the content of the chapters is given below:

Chapter 2: Geomechanical Investigation of a NFCR Case Study in SW of Iran

This chapter offers insights into the state of present-day stress and 1D geomechanical model of the Bangestan Reservoir, SW of Iran.

Chapter 3: New Semi-Analytical Insights into Stress-Dependent Spontaneous Imbibition and Oil Recovery in Naturally Fractured Carbonate Reservoirs

A comprehensive study of stress-dependent spontaneous imbibition in NFCRs by defining the capillary-driven fractional flow and geo-dynamic rock properties is presented in this chapter.

Chapter 4: Numerical Simulation of Stress-Dependent Spontaneous Imbibition in Fractured Porous media

This chapter provides fundamental approaches in the simulation of spontaneous imbibition in block-scale and reservoir-scale by promoting conventional simulation into coupled geomechanical/dual-permeability flow simulation techniques considering stress-dependent porosity, permeability, relative permeability and capillary pressure for both fracture and matrix media in NFCR.

Chapter 5: Consecutive Experimental Determination of Stress-dependent Fluid Flow Properties of Intact Berea Sandstone and Fractured Calumet Carbonate

An experimental technique is presented in this chapter to measure porosity, absolute permeability, relative permeability, and capillary pressure in a consistent and consecutive procedure under variable triaxial isotropic isothermal effective confining stress condition (zero up to 30 MPa, 40⁰C) using N₂/water as the immiscible fluid pair for an intact Berea sandstone and a fractured Calumet carbonate specimens.

Chapter 6: Stress-Dependent Pore Deformation Effects on Multiphase Flow Properties of Porous Media

In this chapter, the systematic impact of pore deformation as a result of effective stress changes on the single-phase and multiphase fluid flow properties of an Indiana limestone specimen is shown experimentally via a series of core-flooding experiments and X-ray computed micro-tomography observations.

Chapter 7: Summary and Conclusion

2. Geomechanical Investigation of a NFCR Case Study in SW of Iran *

Abstract

The Formation of Bangestan, SW of Iran, is a large northwest-southeast-trending anticline with a subsurface area of 70 km by 8 km. This study provides an interpretation of the present-day stress state and mechanical parameters for the giant Bangestan reservoir. Herein, a total of 28 drilling induced tensile fractures (DITF) and 172 breakouts are mapped in seven wells in the Bangestan reservoir using image logs. The average maximum principal horizontal stress (S_H) direction for each well is given a quality ranking according to the World Stress Map (WSM) criteria. The mean orientation of S_H estimates to be $N44^\circ(\pm 9.95^\circ)$. A correlation is seen between this data and stress orientations from earthquake focal mechanism solution. This suggests that stresses are related to tectonic forces generated by Arabia–Eurasia collision. Estimates of vertical principal stress (S_v) gradients vary between 23.3 and 24.7 kPa/m (1.03 to 1.09 psi/ft), based on empirical methods and density log data, respectively. Minimum horizontal stress (S_h) gradient estimates vary from 15.2 to 17.4 kPa/m (0.67 to 0.77psi/ft) using extended leak-off test (XLOT) and step-rate test results, respectively. Uncertainties remain in estimating S_H from acid fracturing in the deep naturally fractured carbonate reservoirs. Herein, an approach called Deformation/Diffusion/Thermal (DDT) is suggested to estimate S_H in the Bangestan Reservoir. The method combines poroelastic theories for the circular underground cavities, bilinear theory for fluid flow through a pre-existing induced fracture and thermal stress. Using this method, S_H gradient is calculated to be 18.9 kPa/m (0.83psi/ft). For comparison, horizontal stress magnitudes and mechanical parameters are computed from sonic wave velocity using poroelastic-tectonic stress equations over the full reservoir layer thickness. All data are calibrated with field tests and lab results. The measured S_H is in good agreement with the previous analytical results. The study

* This chapter was published in the international Journal of Rock Mechanics and Mining Science: Haghi, A. H., Chalaturnyk, R., & Ghobadi, H. (2018). The state of stress in SW Iran and implications for hydraulic fracturing of a naturally fractured carbonate reservoir. International Journal of Rock Mechanics and Mining Sciences, 105, 28-43.

suggests that the contemporary state of stress in the reservoir is characterized by a normal faulting (NF) stress regime.

2.1 Introduction

Giant oil fields along the northern border of Persian Gulf, SW of Iran, cover approximately 80% of the total oil production of Iran. Even though, understanding the present-day state of stress in regions with extensive E&P industries is important, little is known about the state of stress in Iran. The 2016 WSM database contains a few numbers of high-quality stress data and presents mainly low-quality (mainly C) data based on deep focal mechanism solutions in Iran (Heidbach et al., 2016). Furthermore, the majority of the earthquake focal mechanism solution data for south of Iran are located along the boundary between the Arabian and Eurasian plates, and there are concerns surrounding the reliability of stress information derived from earthquakes near the plate boundaries as to their relevance to oil field operations (Heidbach et al., 2010). Recently, some researchers have studied the contemporary state of stress in some parts of Iran (Yaghoubi and Zeinali, 2009; Rajabi et al., 2010; Elyasi et al., 2014; Karimnezhad et al., 2014; Saeidi and Ahmadi, 2012). Haghi et al. (2013b) presented the first stress tensor for the central part of Persian Gulf. They concluded that the region was characterized by a strike-slip stress. All the research indicates that the stresses in south and SW of Iran are linked to the tectonic forces generated by the Arabia–Eurasian collision.

This study examines the present-day stress in the Bangestan Reservoir in SW of Iran using a variety of resources and methods including an acid re-fracturing test, an XLOT, a step-rate well test, seven full-bore images, 13 hydraulic fracturing test, a sonic wave velocity log, and 200 density and porosity logs. Two reasons that hydraulic fracturing is not routinely used to determine S_H in cased wellbores include: 1) it is very difficult to detect fracture initiation at the wall of the wellbore during pressurization, and 2) the Kirsch equation may not describe the near-wellbore stress field. Depending on the stress state, the breakdown pressure may not be the fracture initiation pressure (Zoback, 2010). To eliminate errors in estimating S_H from the breakdown pressure in prevailing fracturing methods, the reopening pressure in the second pressurization curve is used. A log-log plot of pressure derivative versus time is analyzed to extract fracture conductivity and half-length of the pre-existing fracture before reopening. Then, using the measured S_h , S_H is estimated. The estimated S_H from the DDT method is then

compared with measured S_H from the poroelastic-tectonic equations assuming the reservoir responds elastically to the contemporary tectonic stresses. The orientation of S_H is determined from borehole breakout and tensile fracture data. All combined, the vertical, maximum and minimum horizontal stress magnitudes and stress direction provide a first estimate of the full stress tensor and the tectonic stress regime of the Bangestan Reservoir.

2.2 Geological Summary

The field in this study is a giant northwest-southeast-trending anticline with a subsurface area of 70 by 8 km. it is located in the northern Dezful Embayment DE (SW of Iran, Fig. 2.1), which is one of the main structural subdivisions of the Zagros fold-and-thrust belt (ZFTB) (McQuarrie, 2004; Alavi, 2004, 2007). The Zagros mountain range resulted from the collision between the Eurasian and the Arabian plates, whose convergence started at the beginning of the Late Cretaceous (Haghi 2013b; Rajabi et al, 2010; Ricou, 1974; Berberian and King, 1981).

Bangestan is a middle to the upper Cretaceous group of formations, where in this chapter we refer the producing part of the group as Bangestan reservoir. The reservoir is named after Kuh-e-Bangestan in Khuzestan Province. Bangestan reservoir is a carbonate reservoir of $\approx 1000\text{m}$ thickness which is entirely composed of limestone. Based on lithological and petrophysical studies, the Bangestan reservoir is divided into 10 zones from A to J. Zones A, B and C pertain to the Ilam formation; and zones D, E, F, G, H, I and J constitute the Sarvak formation.

The Sarvak formation conformably overlies the Kazhdumi Formation with a transitional contact. The upper contact with the marl and shale of the Gurpi Formation is sharp (Fig. 2.2). These units are widely distributed in Khuzestan and Fars provinces. In northwestern Lurestan and toward Iraq, they interfinger with the Garau Formation. In the coastal Fars Province, the Bangestan reservoir has affinities with the equivalent units of the mid-Cretaceous Wasia Group in Arabia and is divided into two members. The lower, the Mauddud Member consists of 61-122m (200-400ft) of thick-bedded, grey to brown, Orbitolina-rich limestone. The upper, the Ahmadi Member, consists of 30.5-61m (100-200ft) of gray-to-green shale and thin-bedded limestone. Its contact with the overlaying Ilam Formation is disconformable (Alavi, 2004, 2007).

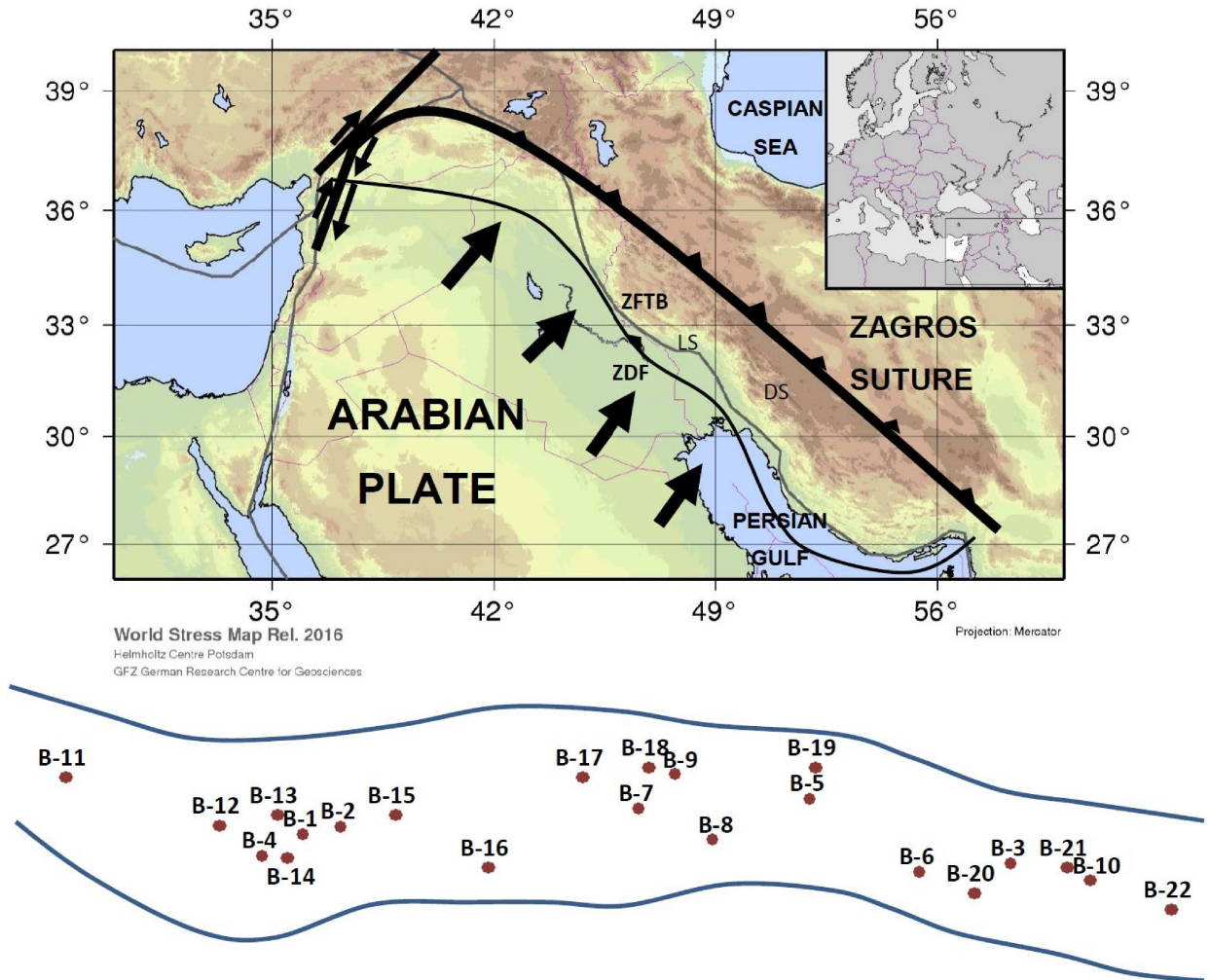


Fig. 2.1 Geology and tectonics of Zagros Belt and the study area of Bangestan Reservoir, SW of Iran (Modified after <http://www.world-stress-map.org/casmo/>) and location of studied wells inside the Bangestan reservoir. Heavy arrows show motion of the Arabian plate relative to the Eurasian. Abbreviations: DE- Dezful Embayment, LS- Lorestan Salient, ZDF-Zagros deformation front, ZFTB-Zagros Fold and Thrust Belt

The first well in the studied area was drilled in 1959 and the field has been developed up to the present. In this study, Image logs of seven different vertical wells are analyzed to characterize stress induced features observed across the whole field (Table 2.1). Furthermore, XLOT, acid fracturing, density logs, hydraulic fracturing tests, sonic wave velocity and transient flow analysis data are investigated across the field. All wells are completed in the Bangestan Formation and they are selected based on the availability of data (Fig. 2.1).

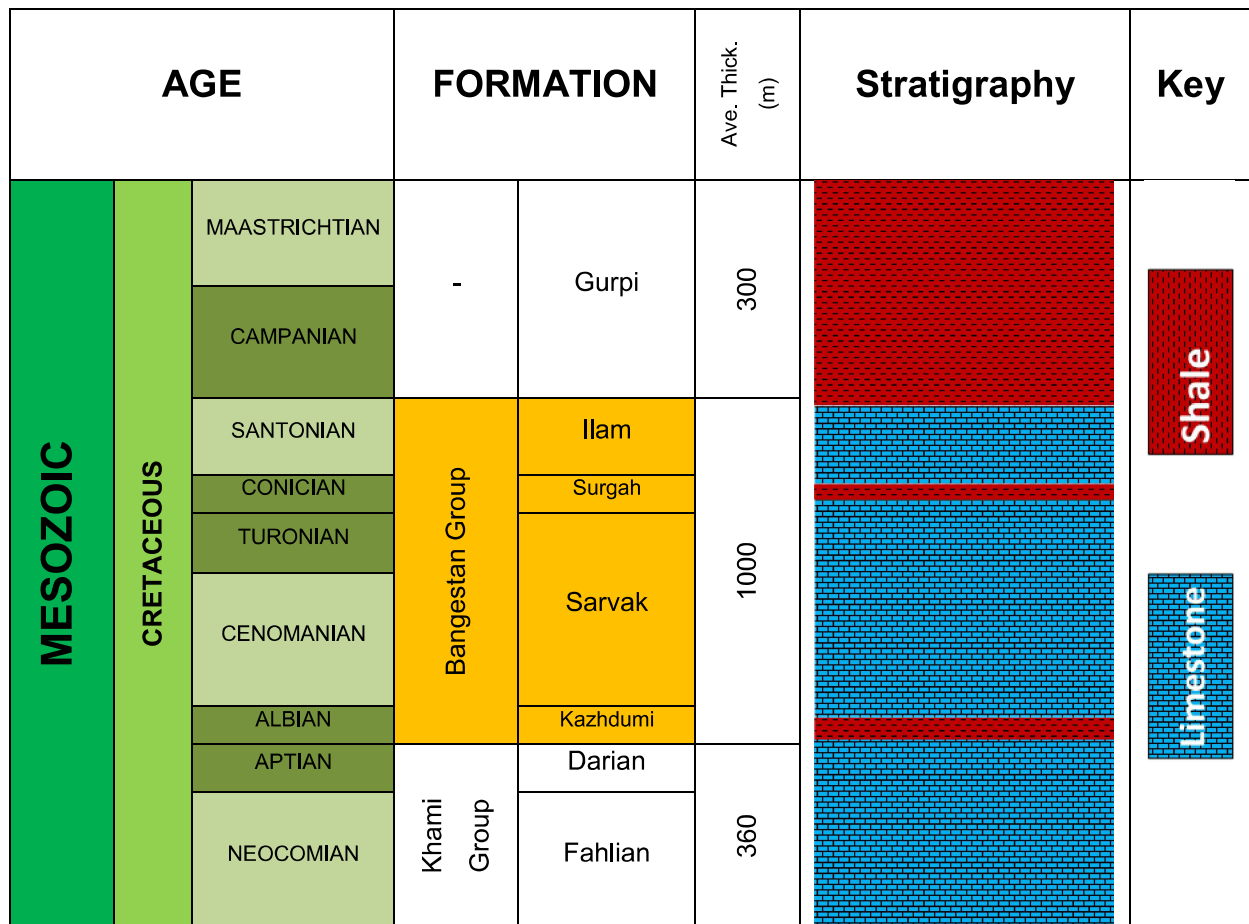


Fig. 2.2 Cretaceous stratigraphy of the Bangestan Reservoir, SW of Iran.

Table 2.1 Well data that are considered for stress induced features from image logs in Bangestan Reservoir

Well Name	Image log type	Logging Interval (m)
B-1	UBI	3525-3710
B-2	UBI	3664-3960
B-3	UBI	3364.7-3863.5
B-4	FMI	3552-3835
B-5	OBMI-UBI	3160-3332
B-6	OBMI-UBI	3597-3130
B-7	UBI	3148-3364 and 3400-4067

2.3 The In-Situ Stress Tensor of Bangestan Reservoir

Mathematically, the stress tensor is a second order Cartesian tensor with nine stress components. The earth's surface is a free surface on which no shear stress acts and hence, is a principal plane of stress. In areas of low topographic variation such as sedimentary basins of SW of Iran, particularly at depths greater than one kilometer, the vertical direction can be assumed to be a principal stress direction (Bell, 1996). Consequently, the two remaining principal stress directions are in the horizontal plane. Accordingly, the stress tensor can be completely constrained by the orientation of one of the horizontal stresses and the magnitudes of the three principal stresses (Haghi, 2013b; Tingay, 2009a; Bell, 1996b; Engelder, 2014; Zoback, 2010).

Two important types of stress-induced fractures in wellbores are recognized as borehole breakouts and drilling induced tensile fractures (DITF). The compressive failure as breakouts can form by axial splitting (aka spalling) as well as shearing and/or tensile failure of the wellbore wall that we will refer to as DITF (Plumb and Hickman, 1985; Bell, 1996b; Pierdominicietal, 2011).

Increasing the drilling fluid pressure at the bottom-hole, borehole circumferential stress decreases and the wellbore wall can locally go into tension in the direction of S_H ; and this leads to the creation of DITF (Bell, 1996a; Plumb and Hickman, 1985). By contrast, slightly decreasing the drilling fluid pressure, the circumferential stress concentration around the wellbore exceeds the rock strength and the rock will compressively fail (breakout). The elongation of the cross-sectional shape of the wellbore is the result of this compressive shear failure on intersecting conjugate planes. As failure progresses, borehole elongation develops parallel to S_h and perpendicular to S_H . The conjugate failure planes associated with the shear failure of breakouts would appear as vertical fractures at the azimuth of S_h (Haghi et al., 2013, Plumb, 1989).

2.3.1 Maximum Horizontal Stress Orientation

Herein, borehole breakouts and DITF are used to determine horizontal stress orientation. For this purpose, different types of image logs have been interpreted across the Bangestan reservoir. A total of 28 DITF's and 172 breakouts were detected in seven vertical wells in the Bangestan reservoir within the given intervals in Table 2.1. As indicated in Table 2.2, the

direction of S_H is mainly NE-SW within the whole field except the eastern section. The average S_H direction is given a quality-ranking according to the WSM criteria (Heidbach et al., 2010). The WSM standard quality-ranking scheme 2008 assigns stress indicators a ranking from A-quality (highest reliability, S_H accurate to $\pm 12^\circ$ and observed in a significant volume of rock) through to D-quality (S_H accurate to $\pm 40^\circ$) and E-quality. As presented in Table 2.2, the quality of stress data assigned for each well is ranked based on the WSM quality-ranking scheme. Ignoring well B-3, the mean orientation of S_H is approximated $N44^\circ$ with the standard deviation of 9.95° for the whole field. Several researchers have investigated the impact of local factors such as faults, folds, salt diaper, and material properties on the stress orientation with depth (Martin and Chandler, 1993; Barton and Zoback, 1994). Later, Yaghoubi and Zeinali (2009) and Haghi et al. (2013b) found the stress orientation not to be constant with depth in Cheshmeh Khush and Kangan/Dalan reservoirs in Iran due to fault slippage.

Table 2.2 Maximum horizontal stress orientation and the given quality ranking scheme

Well Name	Stress indicator	Zone number	Standard deviation	Quality ranking	S_H orientation
B-1	Breakout	6	$\pm 2.165^\circ$	B	37°
B-2	DITF	4	$\pm 1.08^\circ$	C	41°
B-3	Breakout	16	$\pm 28^\circ$	D	14°
B-4	Breakout	2	$\pm 0^\circ$	E	51°
B-5	Breakout	12	$\pm 2.46^\circ$	A	39°
B-6	Breakout	24	$\pm 7.33^\circ$	A	40°
B-7	DITF	24	$\pm 18.68^\circ$	B	66°
B-7	Breakout	112	$\pm 20^\circ$	B	42°

In the eastern part of the Bangestan reservoir, no fault was detected through image loges. However, plotting S_H orientation versus depth in all wells (Fig. 2.3), well B-3 at the eastern part shows a sharp deviation within the interval of 3600-3700 m. This sector contains two layers of highly fractured stiff carbonate with matrix porosity close to zero (Fig. 2.4). This specifically localized heterogeneity has been intensively seen at the eastern part of the field at the same depth. Well production history, transient flow test and facies analysis confirms the drastic drop in reservoir quality and validates the hypothesis of localized heterogeneity at the eastern part of the field. These observations suggest the effect of heterogeneity or perhaps the variation of elastic rock properties on stress perturbation with depth for the eastern part of the Bangestan reservoir.

The effect of the elastic rock parameter variation with depth is subsequently re-investigated in Fig. 2.10.

The extensively NE–SW S_H orientation observed in this study is broadly consistent with both S_H orientation, derived from nearby earthquake focal mechanism solutions in 2016 WSM database (Heidbach et al., 2016), and the direction of absolute plate motion of the Arabian plate. Hence, the largely NE–SW S_H orientation observed herein is likely to be associated with tectonic forces generated at the Arabia–Eurasian continental collision zone.

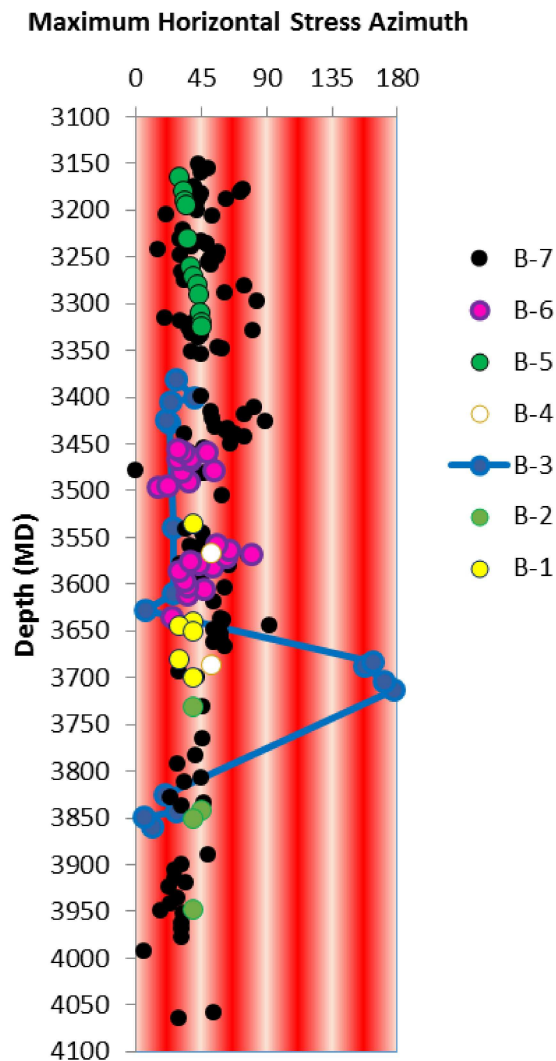


Fig. 2.3 Maximum horizontal stress variation with depth for seven wells across Bangestan Reservoir. This graph shows the sharp deviation of S_H orientation for well B-3 within the interval 3600-3800 from the general NE-SW trend due to heterogeneity

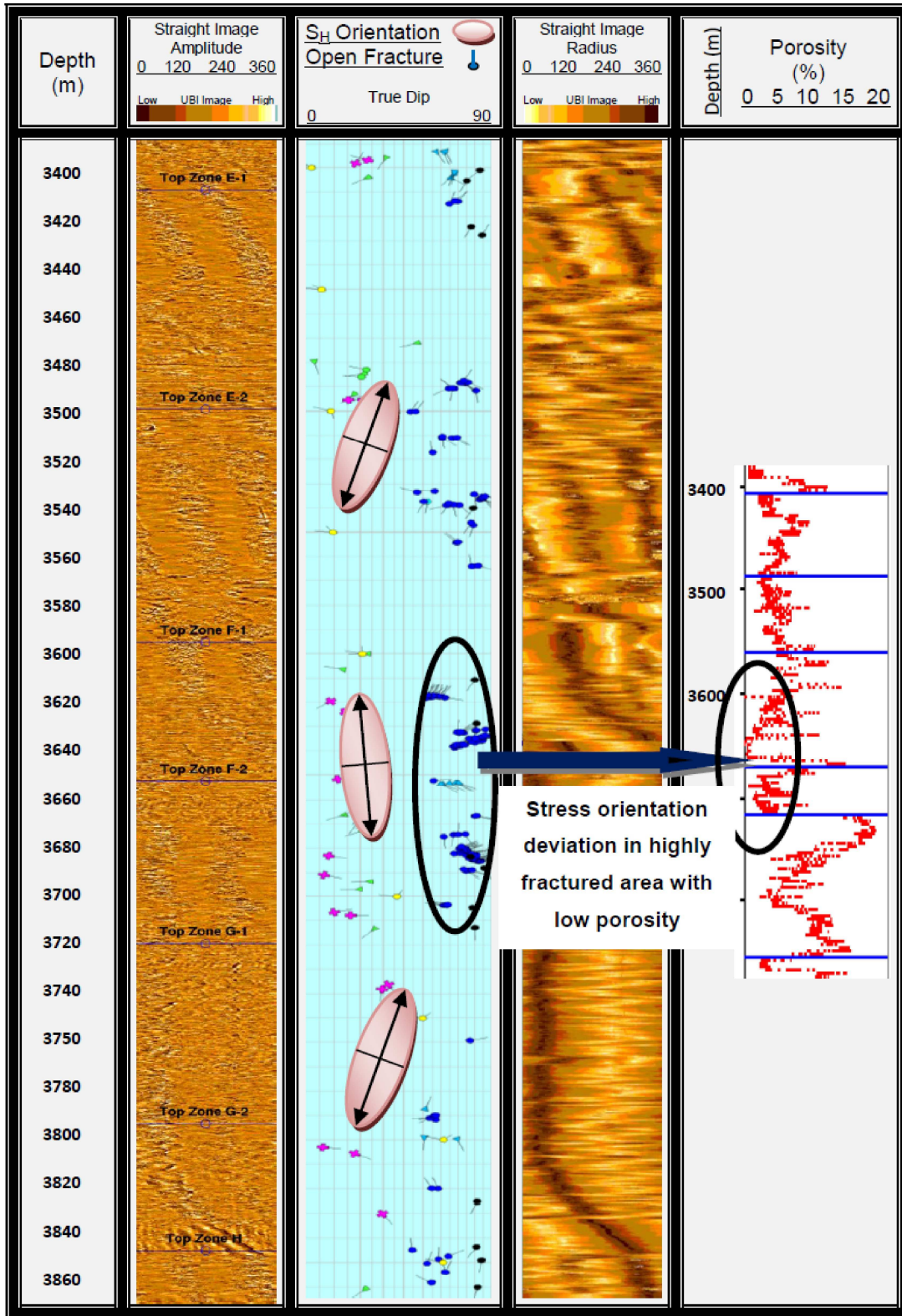


Fig. 2.4 UBI log, natural fracture azimuth and porosity profile of a well in the eastern part of Bangestan Reservoir. This chart shows the sharp deviation of stress orientation with depth in well B3.

2.3.2 Vertical Stress Magnitude

The vertical stress (S_v) magnitude has been found to be the weight of the overburden rock layers and can be easily calculated by integrating the density log from the surface to the depth of interest (Engelder, 2014).

Gardner et al. (1974) found an experimental equation for density based on P-wave velocity by using controlled field and laboratory measurements of saturated sedimentary rocks. Similarly, Zare et al., (2010) presented a relationship between bulk density and P-wave velocity for the Bangestan Reservoir using log data of six wells. They found that S_v gradient in the Bangestan reservoir is equal to 23.3kPa/m (1.03 psi/ft).

However, S_v gradient approximates 24.7 kPa/m (1.09 psi/ft) directly from the average density of the density logs data for the wells across the Bangestan reservoir. A comparison of the mean total bulk density below the surface exhibits an increase from 2.475 g/cm³ in the first few hundred meters to 2.7g/cm³ at a higher depth in the Bangestan reservoir. For shallow depths, an average of the density of either drilling cuttings/cores from the wells or outcrops has been used to roughly estimate the density.

2.3.3 Minimum Horizontal Stress Magnitude

In sedimentary basins, the minimum horizontal stress (S_h) magnitude is typically the least principal stress and the primary control on the fracture gradient (Breckels and vanEekelen, 1982). Two field tests that are commonly used in oil and gas industries, which can be used for S_h measurement, are called leak-off test (LOTs) and XLOT (extended LOT) (Zoback et al., 2003). Herein, S_h magnitude is determined from typical XLOT test in the Bangestan formation.

In an XLOT, the mud is pumped with a constant rate into the well. As the volume of the wellbore is fixed and assuming the drilling fluid is incompressible, the pressure should primarily increase linearly with time. The peak pressure during an XLOT is termed the formation breakdown pressure (FBP) and represents the pressure at which unstable fracture propagation away from a wellbore occurs. It should be emphasized that observation of a distinct FBP is not an indication of a reliable XLOT (Zoback, 2010). At this point, the pressure will drop dramatically to a relatively constant value called the fracture propagation pressure (FPP). As soon as the pumps are off, a sudden drop will happen in the pressure curve and pressure will fall

to a value called Instantaneous Shut-in Pressure (ISIP). This drop happens because the pressure caused by flow turbulence and friction during injection instantly disappears after pumping is stopped. In XLOT, FPP will increase due to large mud friction losses. In such cases, the fracture closure pressure (FCP) is the better measure of the least principal stress rather than the ISIP. Many different methods have been introduced for FCP measurement. For this study, FCP was determined by: 1) plotting pressure versus \sqrt{time} and detecting a change in linearity of the pressure decay (Nolte and Economides, 1989) and 2) the G-function plot ($G = 16/3\pi ((1 + \Delta t)^{1.5} - \Delta t^{1.5} - 2)$).

Fig. 2.5 shows the result of a highly reliable XLOT showing distinct ISIP and FCP for the S_h magnitude measurement in the central part of Bangestan reservoir at the depth of 3513 m (well B-8). As illustrated in Fig. 2.6a), The ISIP is determined 54.47 MPa (7900 psi) from the shift in the rate of rapid pressure decrease to a more gradual decay on the linear plots of pressure versus time. The FCP is approximated as 53.4 MPa (7747 psi) from the pressure versus \sqrt{time} and G-function plots that are shown in Fig. 2.6b) and c), respectively. Accordingly based on FCP, which presents the most reliable estimation of S_h value, S_h gradient approximates 15.2 kPa/m (0.67psi/ft).

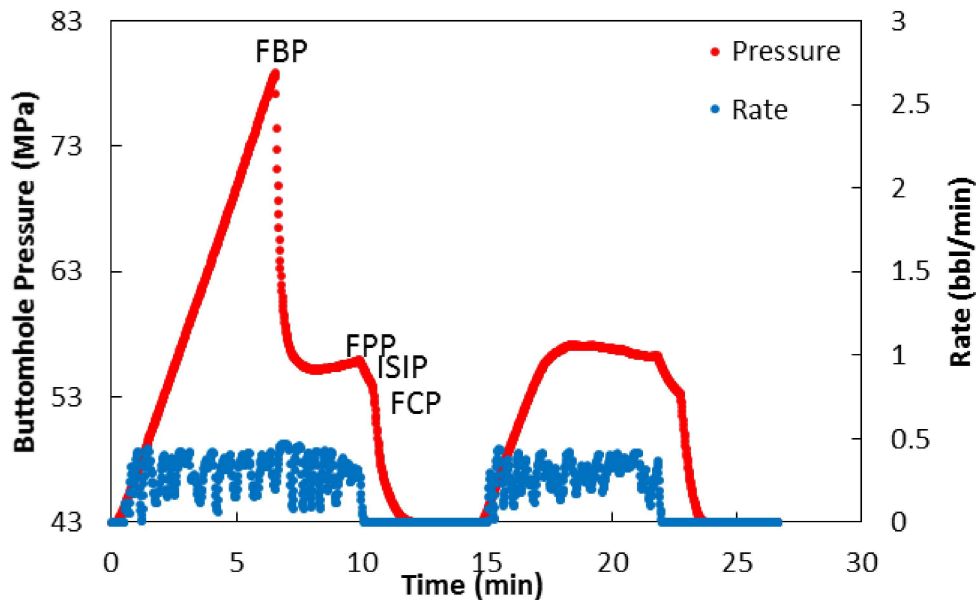


Fig. 2.5 Surface pressure and injection rate curves versus time of an XLOT test in Bangestan Reservoir for well B8.

Another method to measure the least principal stress is to conduct step-rate test which involves injection into the well at a number of fixed flow rates. It is easy to detect the pressure at which a fracture opens; injection can take place at increasingly higher flow rates with only minimal increases in wellbore pressure. Prior to the fracture opening, there is a strong increase in pressure with flow rate, as expected for a system dominated by diffusion, into the formation and/or a closed hydraulic fracture. S_h is recognized by the distinct change in slope in the pressure at which the fracture opens (Zoback, 2010). Accordingly, this method overestimates the minimum horizontal stress.

The gradient of S_h from the step-rate test for the well B-9 in the central part of Bangestan Reservoir is estimated as 17.4 kPa/m (0.77 psi/ft) (Shadizadeh et al., 2009). This presents an upper bound for the S_h gradient in the Bangestan reservoir.

2.3.4 Maximum Horizontal Stress Magnitude

The challenge in estimating a reliable magnitude for S_H remains despite research on multiple methods (Hubbert and Willis, 1972; Bredehoeft, et. al., 1976; Desroches, 1995; Daemen & Schultz (eds), 1995) and no widely accepted petroleum industry techniques are available for directly and reliably estimating the S_H magnitude (Bell, 1996b).

As a contribution to the ongoing efforts to improve estimates for S_H , Haghi et al. (2013a) recently introduced a triple Deformation/Diffusion/Thermal (DDT) analytical solution that utilizes data from the second injection cycle of HCL-based fracturing. Herein, the presented method is modified for an acid re-fracturing test in the Bangestan Reservoir, SW of Iran.

Similar to other fracturing operations (e.g. hydraulic fracturing and XLOT), acid fracturing is a process in which an acid, typically hydrochloric acid for carbonates, is pumped into a sealed section of the borehole (sealed by packers) at a specific depth. As the pressure increases, the critical circumferential stress at the borehole is reduced and at the same point becomes tensile. When this stress reaches the tensile strength, a crack is formed and then propagates into the formation before the injection shut-in. Acid will partially dissolve the rock and by creating some edges, keeps the induced fracture open. Furthermore, it may connect the induced fracture with the natural fracture sets by dissolving channels which provide interconnectivity pathways.

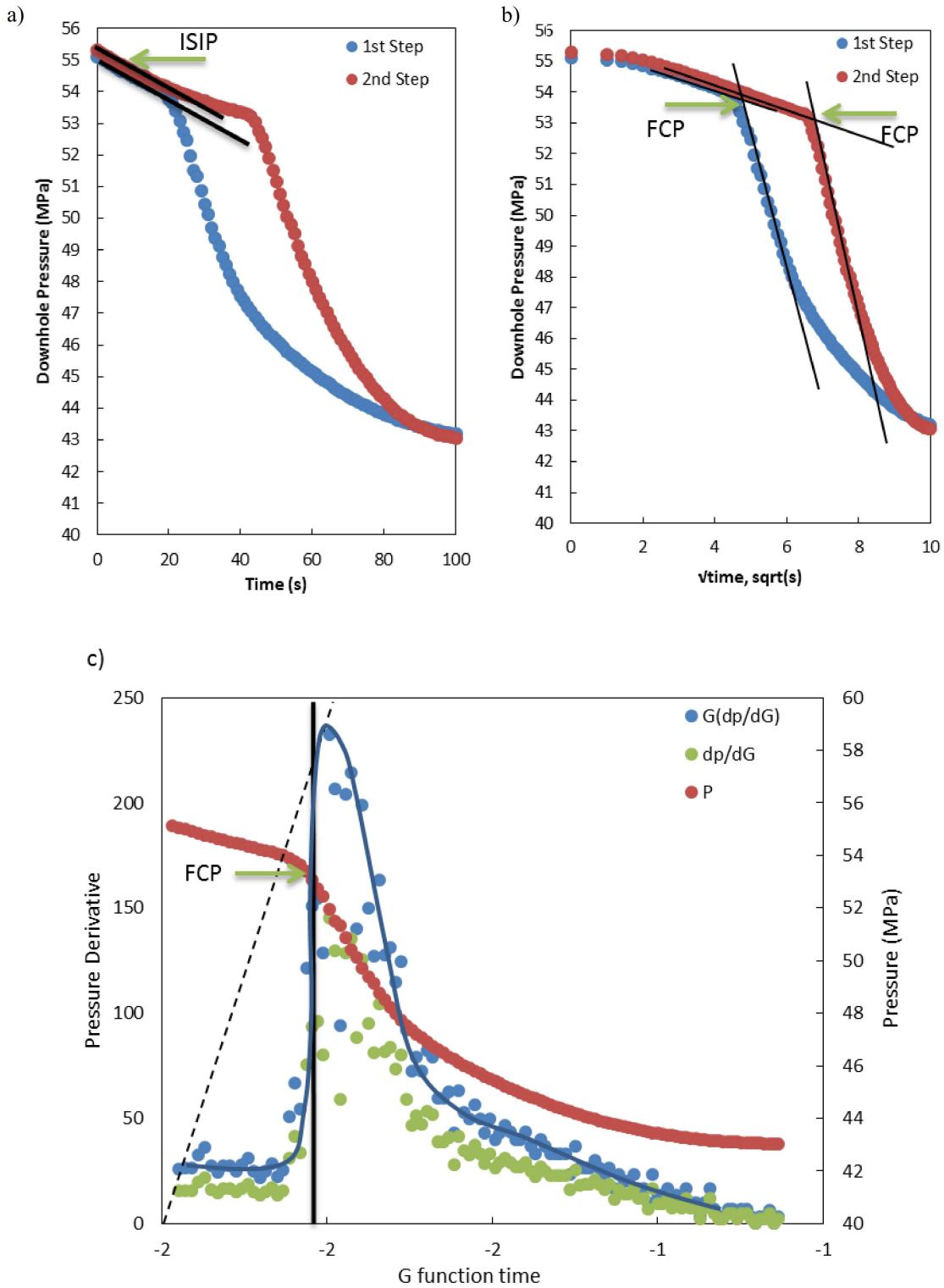


Fig. 2.6 Analysis of a) Instantaneous Shut-In Pressure (ISIP), b) Fracture Closure Pressure (FCP) using square root of time and c) Fracture Closure Pressure (FCP) using pressure derivative curve versus G function on the curve of XLOT test for S_h measurement in Bangestan Reservoir.

This process repeats for acid re-fracturing in the presence of a primary induced fracture. Accordingly, for the Hydrochloric acid-based re-fracturing operation the circular fluid flow (for the first injection step) is replaced by bi-linear flow of acid through the fracture and from the fracture into the formation. Based on the bi-linear flow assumption, the difference between injection pressure inside the well (P_w) and formation pore pressure (P_o) during acid re-fracturing (ΔP_{frac}) can be defined as (Cinco and Samaniego, 1981; Ahmed and McKinney, 2011):

$$\Delta P_{frac} = P_w - P_o = \frac{44.1q\mu}{h(K_f b_f)^{1/2}(\phi\mu c_t K)^{1/4}} \sqrt[4]{t} \quad (2.1)$$

where, $q, \mu, h, K_f b_f, \phi, c_t,$ and K are defined as injection flow rate, acid viscosity, reservoir thickness, fracture conductivity, porosity, total compressibility, and reservoir permeability, respectively, all in petroleum field units. Given an estimate of the pre-existing induced fracture length and conductivity, the re-fracturing pressure curve is simulated using the Kirsch equation (Kirsch, 1898) for tangential stress $S_{\theta\theta}$ distribution at the borehole wall and in the direction of maximum horizontal stress (Zoback, 2010; Fjaer et al., 2008; Hudson and Harrison, 2000). This could be done simply by replacing pressure difference ΔP in Eq.(2.2) with ΔP_{frac} from Eq.(2.1) (based on bilinear theory for fluid flow through pre-existing induced fracture) and using Eq.(2.3) for the thermal stress term ($\sigma^{\Delta T}$) (Fjaer et al., 2008; Haghi et al 2013a).

$$S_{\theta\theta} = \sigma_{\theta\theta} + P_o = 3S_h - S_H - P_o - \sigma^{\Delta T} - \Delta P \quad (2.2)$$

$$\sigma^{\Delta T} = \frac{\alpha_t E \Delta T}{1 - \nu} \quad (2.3)$$

where $\alpha_t, E, T,$ and ν represent rock thermal coefficient, Young's Modulus, formation temperature, and Poisson's ratio, respectively. Due to the existence of the induced fracture from the first fracturing step, the tensile strength is assumed to be negligible ($\sigma_r = \sigma_{\theta\theta} = 0$) in the analysis of the re-fracturing step. It is also expected that the permeability of the existing fracture will be higher than the original formation permeability and consequently the fluid will preferentially flow within the fracture and follow bilinear flow behavior. Accordingly, based on the given information on the fluid diffusivity and thermal equations (Eq.'s (2.1) and (2.3), respectively), Eq.(2.2) can be rewritten as,

$$S_H - 3S_h = -2P_o - \frac{\alpha_t E \Delta T}{1 - \nu} - \left(\frac{44.1q\mu}{h(K_f b_f)^{1/2}(\phi\mu c_t K)^{1/4}} \sqrt[4]{t_{crit}} \right). \quad (2.4)$$

Eq.(2.4) defines the DDT solution as a linear function of S_h and S_H based on acid re-fracturing data. Eq.(2.4) models the fracture reopening pressure at the wellbore wall as a function of time and can be rewritten in terms of effective stresses ($\sigma = S - P = S - P_p$):

$$3\sigma_h - \sigma_H = \frac{\alpha_t E \Delta T}{1 - \vartheta} + \left(\frac{44.1 q \mu}{h(K_f b_f)^{1/2} (\Phi \mu c K)^{1/4}} \sqrt[4]{t_{crit}} \right) = \mathcal{F}_{reopening}(DDT)$$

$$\mathcal{F} = \frac{\alpha_t E \Delta T}{1 - \vartheta} + \left(\frac{44.1 q \mu}{h(K_f b_f)^{1/2} (\Phi \mu c K)^{1/4}} \sqrt[4]{t} \right) \quad (2.5)$$

where the “ \mathcal{F} ” function is a time-dependent DDT function used for stress estimation at $\mathcal{F}(t = t_{crit}) = \mathcal{F}_{reopening}(DDT)$ (peak point of \mathcal{F}) based on the results from an acid re-fracturing test. Defining a parameter, k , as the ratio of minimum effective horizontal stress (σ_h) to the maximum effective horizontal stress (σ_H), Eq.(2.5) can be expressed as:

$$\sigma_H = \left(\frac{1}{3k - 1} \right) \mathcal{F}_{reopening}(DDT) = \mathbb{H} \mathcal{F}_{reopening}(DDT) \quad (2.6)$$

$$\sigma_h = \left(\frac{k}{3k - 1} \right) \mathcal{F}_{reopening}(DDT) = \mathbb{L} \mathcal{F}_{reopening}(DDT) \quad (2.7)$$

where \mathbb{H} and \mathbb{L} coefficients are functions of $k = \sigma_h/\sigma_H$ parameter. Additional details on the application of this approach to acid re-fracturing data obtained within the Kangan/Dalan reservoir, Persian Gulf, can be found in Haghi et al. (2013a). Results from an acid fracturing operation conducted in Well B-9 in the Bangestan reservoir are used to apply the DDT approach for estimating S_H . Well B-9 was drilled at the eastern flank of the reservoir and perforated from 3450 to 3480 m depth. To help define the characteristics of the induced fracture created from a successful acid fracturing treatment, a pressure build-up test was conducted in the well. Using a log-log plot of pressure derivative versus time, the fracture half-length and conductivity are estimated equal to 40 m (130 ft) and 6363 mD.m (20876 mD.ft), respectively. Unfortunately, no acid re-fracturing stimulation was conducted in this well and to apply the DDT technique, synthetic re-fracturing data was generated by simulating the re-fracturing process based on the initial acid fracturing data. Fig. 2.7a) illustrates the simulated process of the acid re-fracturing behavior with time using the bilinear flow assumption defined in Eq.(2.1) at different injection rates of 10, 20, 30, 40 and 50 bbl/min. Utilizing the field and well data summarized in Table 2.3, the simulated curves show an increase of ΔP_{frac} to the maximum value of $\Delta P_{reopening}$. At this

moment, as the fracture conductivity rises up, Fig. 2.8, ΔP_{frac} declines sharply and then becomes almost steady. As soon as the injection stops, a sudden drop happens and the pressure falls to a value called ΔP_{ISIP} . The pressure drop takes effect by subtracting the effect of friction after pump shut-in. Again, the bilinear flow equation is used to model pressure fall-off and flow-back from the formation to the fracture and from the fracture to the well (right side of the curves).

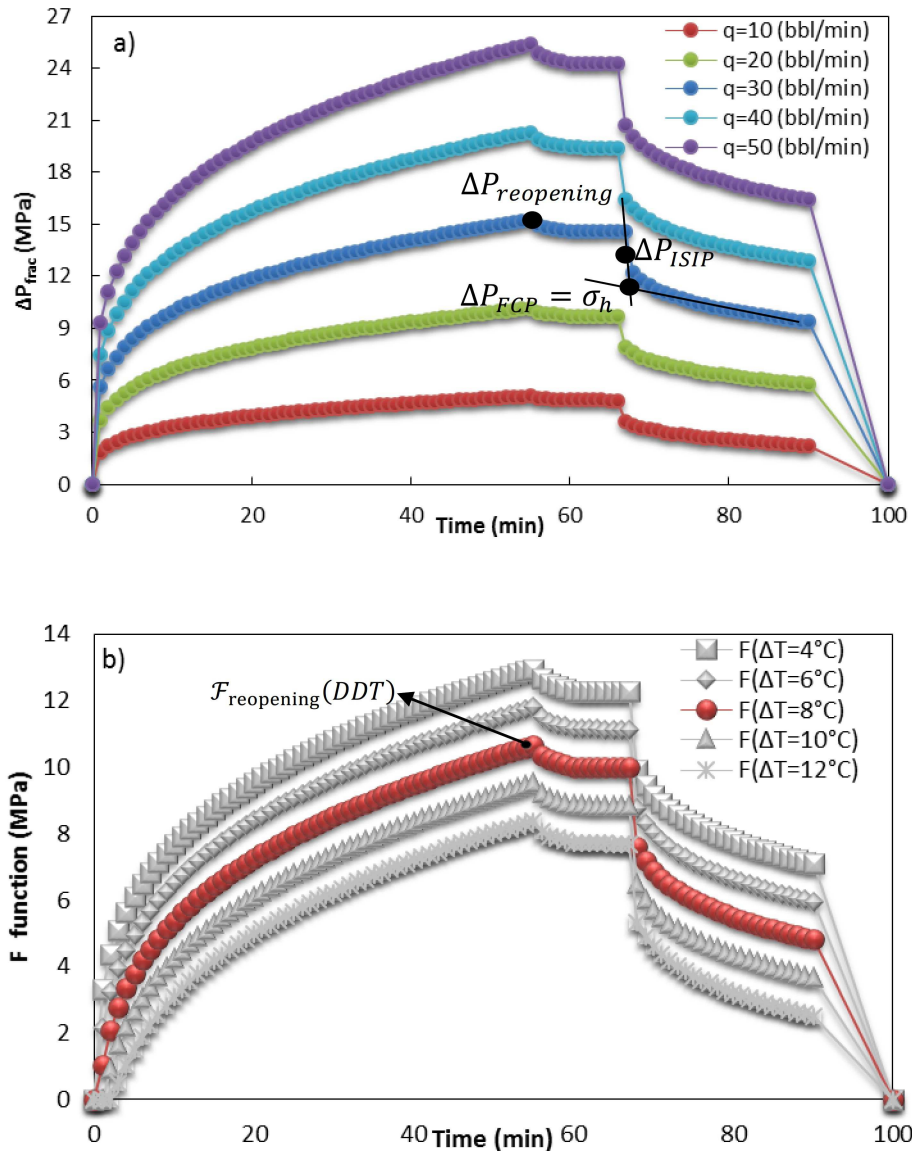


Fig. 2.7 a) Simulated ΔP_{frac} curve versus time on the basis of bilinear flow theory for different acid injection rates. The curve of injection rate 30 bbl/min best simulates the measured value of S_h based on field data. b) Simulated F function with time for well B9 in Bangestan Reservoir

As discussed in the previous section, the S_h at depth 3450 m is best measured 52.44 MPa (7608 psi), or 11.6 MPa for σ_h , in the Bangestan Reservoir. Among the curves shown in Fig. 2.7a), the curve of $q=30\text{ bbl/min}$ (4.7 m^3/min) gives the best match for σ_h based on the simulated fracture closure pressure ΔP_{FCP} .

The red circle symbol on Fig. 2.7b) shows the variations of "F" function (Eq.(2.5)) with time for the well based on the flow diffusivity and thermal parameters (Table 2.3). Fig. 2.7b) clearly demonstrates the sensitivity of "F" function with ΔT . Based on Fig. 2.7, $\mathcal{F}_{\text{reopening}}(DDT)$ calculates 10.65 MPa (1545psi) at the depth of 3450 m. Knowing the values of $\sigma_h = S_h - P_o = 11.6 \text{ MPa}$ (1683 psi) and $\mathcal{F}_{\text{reopening}}(DDT)=10.65\text{MPa}$, the "ln" function and "k" value could be easily calculated as 1.09 and 0.48, respectively (from Eq.(2.7)). Accordingly, "III" function is calculated 2.27 from Eq.(2.6). Finally, S_H at the depth of 3450 m is calculated as follows:

$$S_H = \sigma_H + P_o = \text{III}\mathcal{F}_{\text{reopening}}(DDT) + 41 = 65 \text{ MPa} (9428 \text{ psi})$$

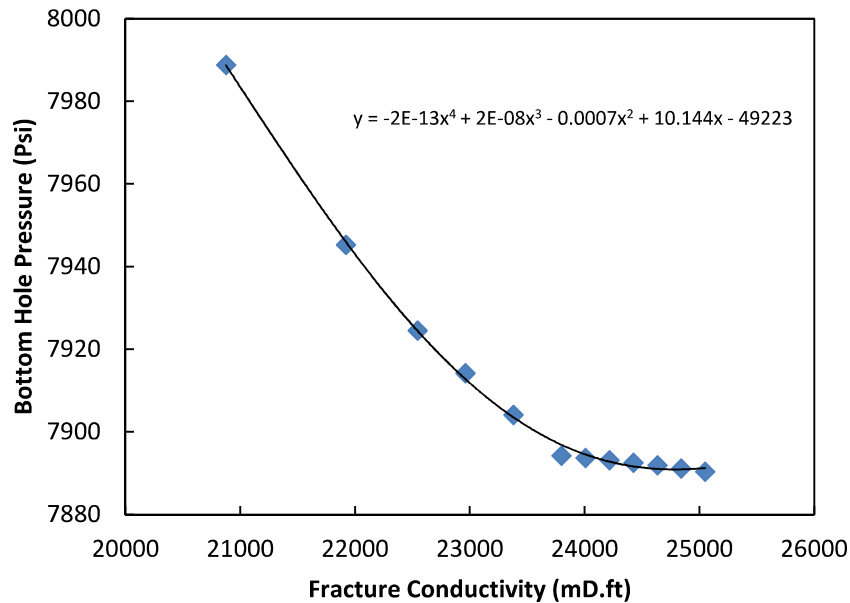


Fig. 2.8 Bottom hole pressure versus fracture conductivity in acid injection test. As it is shown, increasing the fracture conductivity, bottom hole pressure decrease due to fluid deflation from the fracture

Table 2.3 Well and field specification

Parameter	Unit	Value	Parameter	Unit	Value
Porosity	(%)	12.7	Well radius	(ft)	0.354
Permeability	mD	3.07	Pore Pressure at datum	(psi)	5780
Thermal Expansion Coeff.	1/°C	1E-5	Temperature change	(°C)	8
Poison Ratio	-	0.30	Compressibility	(1/psi)	1.1E-5
Producing layer Thickness	(ft)	326	Static Young Modulus	(GPa)	40

Accordingly, S_H gradient at 3450 m depth is calculated 18.84 kPa/m (0.83 psi/ft). The magnitude of three principal stresses in the Bangestan reservoir is plotted in Fig. 2.9. As it is illustrated, S_V has the greatest gradient (24.68 kPa/m) while S_h has the least value of 15.2 kPa/m. Note that some S_h data from hydraulic fracturing tests are given in Fig. 2.9, as well.

2.3.4.1 Sensitivity analysis of the calculated S_H from DDT solution:

The DDT technique, as applied in this case study, has some drawbacks for calculation of S_H in well B-9 in the Bangestan reservoir. Ideally, Eq.(2.2) would be applied to uncased-unperforated vertical boreholes, although it has been widely used for stress estimation in cased-hole wells in oil and gas industry for decades (Zoback, 2010; Fjaer et al.,2008). Well B-9 had been cased and perforated at the time of acid fracturing in Bangestan Formation. In cased-hole wells, the fracturing fluid flows into the formation through the perforation tunnels to pass the casing and cement. Consequently, Eq.(2.2) is no longer relevant because the stress concentration around the well does not govern fracture initiation (Zoback, 2010).

It is well known that hydraulic fracturing tests in perforated wells yield accurate estimates of the least principal stress. This is because once a fracture propagates away from the wellbore, it propagates perpendicular to the least principal stress (Zoback, 2010). Knowing S_h and fracture specifications from the primary pressurization cycle in the well B-9, we have applied the DDT approach to examine a range of bilinear ΔP models that provide the best match of S_h . Many researchers have found Eq.(2.2) to be applicable for the second pressurization cycle considering a zero tensile strength (Zoback, 2010; Hubbert and Willis, 1972). We have adopted the same assumption in this study. Many researchers believe that the most important reason that hydraulic fracturing cannot be used to determine S_H is that it is essentially impossible to detect

fracture initiation (or opening) during pressurization (re-pressurization) in field tests (Lee and Haimson, 1989; Zoback and Haimson, 1983).

As an attempt to overcome this limitation, we have assumed that a small fracture conductivity in the bilinear ΔP models will remain constant up to the critical time when the fracture starts to open. History matching with the DDT approach to identify the optimum bilinear ΔP model is then used to simulate the fracture opening pressure, which for the case of Well B-9, is postulated to provide a more suitable estimate of 15.225 MPa in Eq.(2.2) than the field recorded value of 19 MPa ($\Delta P_{reopening} = \Delta P_{fracturing} - \sigma_T$). Finally, ΔP at the critical time is then inserted into the Eq.(2.2) to find S_H .

It is noteworthy that the shot density and orientation, which can lead to changes in fracture initiation pressure, may also complicate the application of Eq.(2.2). Some researchers have proposed perforations design to obtain successful fracturing treatment (El Rabaa, 1989; Abass et al., 1996), where perforations have been treated as perpendicular holes relative to the well axis. The general form of tangential stress distribution at the base of the perforation is given as (Hossain et al., 2000):

$$\begin{aligned} \sigma_{\theta\theta} = & (\sigma_x + \sigma_y + \sigma_{z\theta}) + 2(\sigma_x + \sigma_y - \sigma_{z\theta})\cos 2\theta' \\ & - 2(\sigma_x - \sigma_y)(\cos 2\theta + 2\cos 2\theta\cos 2\theta') - 4\tau_{xy}(1 + 2\cos 2\theta)\sin 2\theta \\ & - 4\tau_{z\theta}\sin 2\theta' - P_w(2\cos 2\theta' + 2). \end{aligned} \quad (2.8)$$

The variables θ and θ' in Eq.(2.8) are the perforation direction with respect to σ_x and $\sigma_{z\theta}$, respectively. The fracture re-opening pressure for a vertical well with the perforation channel directed along S_H can be calculated using the simplified shape of Eq.(2.8):

$$P_w = \frac{1}{4}(9S_h - 3S_H - S_v + 2\vartheta(S_H - S_h)) \quad (2.9)$$

Using Eq.(2.9) and stress/pressure data from previous section, S_H is computed to be 62 MPa, which is close to the calculated value from the DDT approach and sonic wave analysis result described below. It is likely that the similarity in computed values is due to same orientation of initial induced acid fracture and oriented perforation in Well B-9.

In addition to the impact that perforation geometry had on the solution, the sensitivity of the DDT approach to the thermal effect was analyzed. Fig. 2.7b) shows the sensitivity of “F”

function with temperature for Well B-9. Using five simulated $\mathcal{F}_{\text{reopening}}(DDT)$ curves at five different ΔT (from 4°C to 12°C) yields a range S_H values of 63 to 67 MPa. Completely discounting thermal effects in the DDT approach yields an estimated S_H equal to 61 MPa. These analyses indicate that for the Bangestan reservoir, the DDT approach is relatively insensitive to the thermal impact due to acid and carbonate chemical reactions. Accordingly, we have concluded that the uncertainty in our estimate of S_H using the DDT approach is ± 4 MPa.

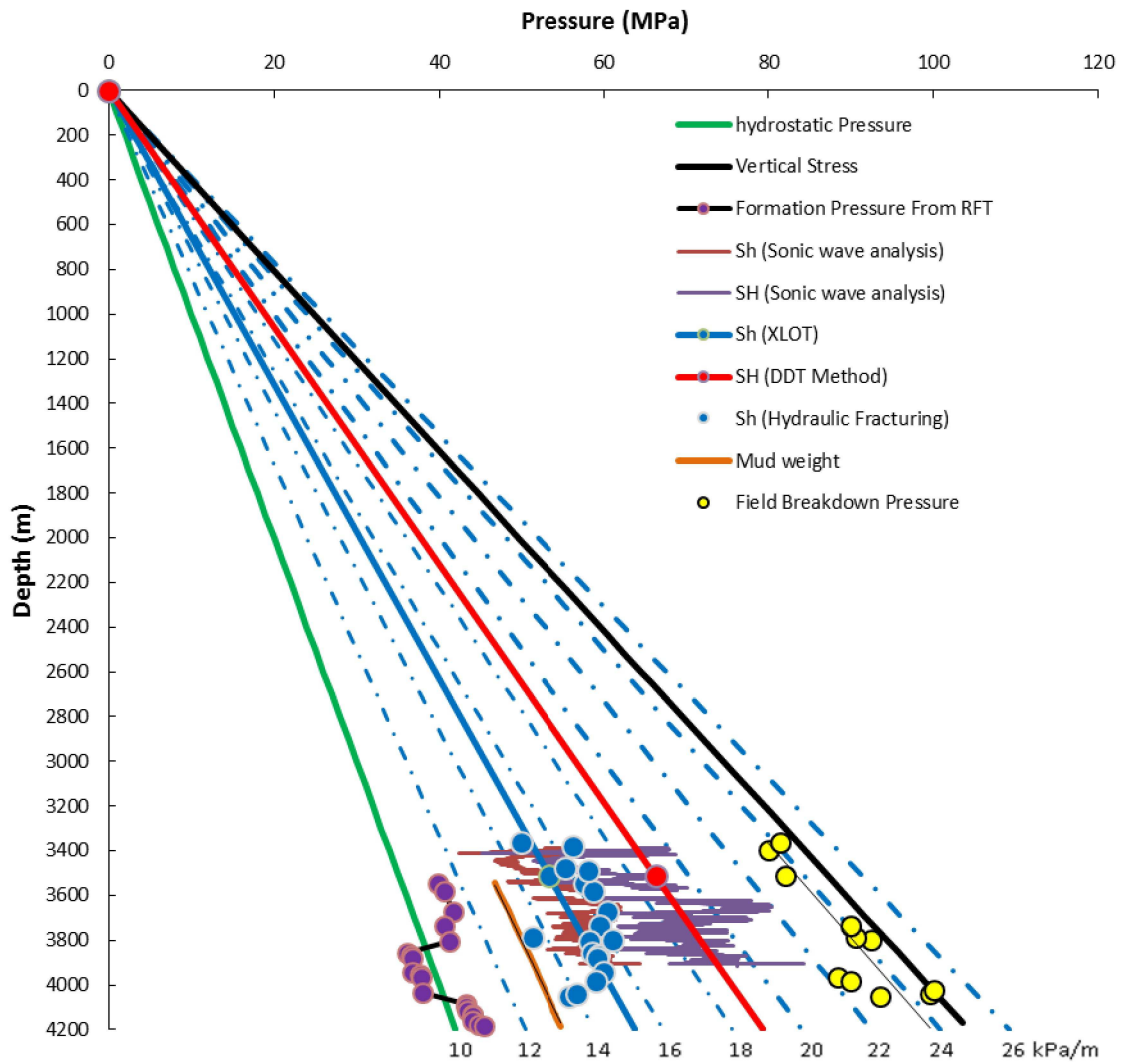


Fig. 2.9 Comparison between the magnitude of S_V (Density log), reservoir pressure (from Repeat Formation Test), and S_h and S_H based on XLOT, DDT and sonic wave velocity analysis. Vertical stress is calculated as the maximum principal stress ($S_1=S_V$) while the minimum horizontal stress is estimated as the least principal stress ($S_3=S_h$).

2.4 Construction 1D MEM for Bangestan Reservoir

A Mechanical Earth Model (MEM) contains different data required for geomechanical modeling including: geo-model, pore pressure distribution, in-situ stress distribution, and rock mechanical properties including elastoplastic properties and strength parameters. One dimensional MEM corresponds to MEM in well scales. For this purpose, sonic wave velocity data along the wells are transferred into stress and mechanical properties and the resulted curves then are calibrated with the field and lab data.

In an elastic, isotropic, homogeneous solid, the dynamic elastic moduli can be determined from the velocity of compressional waves (V_p) and shear waves (V_s) extracted from DSI tool using the following relationships (Goodman, 1989),

$$\vartheta_d = \frac{[2V_s^2 - V_p^2]}{2[V_s^2 + V_p^2]} \quad (2.10)$$

$$G = \rho_b V_s^2 \quad (2.11)$$

$$E_d = 2G(1 + \vartheta_d) \quad (2.12)$$

where ϑ_d , E_d , G and ρ_b are dynamic Poisson's ratio, Young's modulus, shear modulus, and bulk density, respectively. However, several researchers criticized the accuracy of the dynamic elastic moduli for geomechanical modeling due to several issues, such as rock's pore and cracks, pore pressure, type of cement, and stress-strain etc, in comparison to the static elastic modulus from the rock labs which are considered more realistic (Fjear 2008). Many worldwide empirical equations in the literature are presented by different researcher to shift dynamic elastic modulus to static ones (Brotons et al, 2015). Several equations are also presented to predict the rock mass strength parameters (Asef and Farrokhrouz 2010; Ameen et al 2009). Some experimental equations have been recommended for the same formation in the local area by Najibi et al, (2015). These correlations have been used to estimate the static Young's Modulus and uniaxial compressive strength (UCS) in this study as well. The results are given in Fig. 2.10.

$$E_s = 0.169V_p^{3.324} \quad (2.13)$$

$$UCS = 12.8 \left(\frac{E_d}{10} \right)^{1.32} \quad (2.14)$$

Knowing the elastic modulus (E_s) and Poisson's ratio, the magnitude of horizontal stress could be estimated using poroelastic-tectonic equation (Zoback, 2010). Assuming the earth responds to a tectonic strain in the direction of S_H as an isotropic poroelastic material and the

vertical stress is a principal stress, then the horizontal stresses can be calculated using the following equations (Blanton and Olson, 1997; Thiercelin and Plumb, 1994):

$$\sigma_h = \frac{\nu}{1-\nu} \sigma_v + \frac{1-2\nu}{1-\nu} \alpha p_p + \frac{\nu E}{1-\nu^2} \epsilon_H \quad (2.15)$$

$$\sigma_H = \frac{\nu}{1-\nu} \sigma_v + \frac{1-2\nu}{1-\nu} \alpha p_p + \frac{E}{1-\nu^2} \epsilon_H \quad (2.16)$$

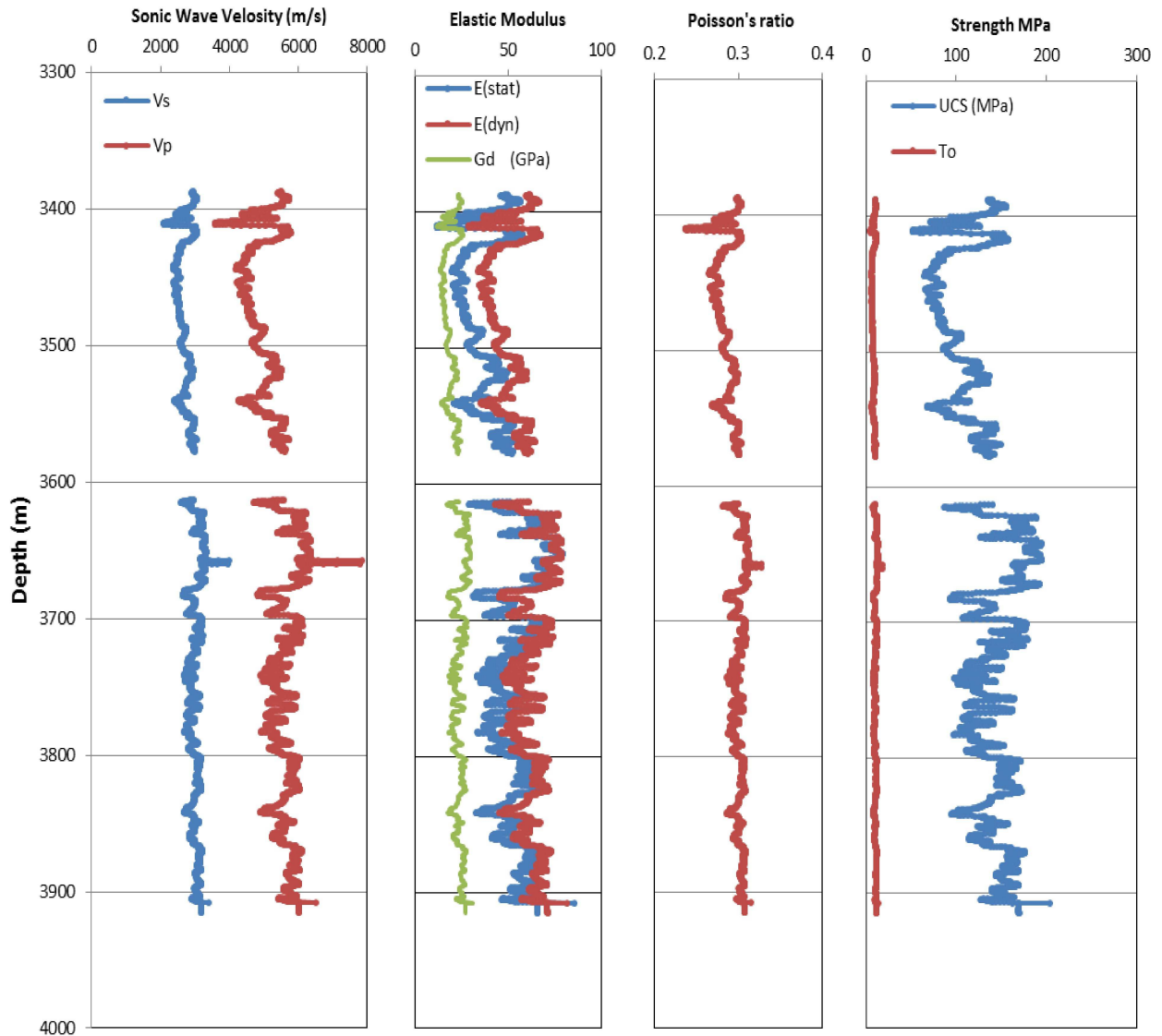


Fig. 2.10 Sonic wave velocity analysis for well B10 in Bangestan reservoir

In Eqs.(2.15) and (2.16), α and ε_H are Biot's coefficient and horizontal tectonic strain in σ_H direction, respectively. There will always be uncertainty in converting vertical stress into horizontal stress in tectonically active area. However, the given poroelastic-tectonic equation, which considered the horizontal tectonic strains instead of tectonic stress, has been widely used to construct 1D mechanical model based on sonic data in the tectonically active areas like western Canada, US, and SW of Iran (Song and Hareland, 2012; Sone and Zoback, 2014; Molaghab et al., 2017; Hayavi and Abdideh, 2016; Tingay et al., 2009). Using Eqs.(2.15) and (2.16), the horizontal stresses versus depth are computed for Well B-10 in the Bangestan reservoir and are illustrated in Fig. 2.9. As illustrated, the computed value of S_h based on poroelasticity equations are calibrated with the measured S_h using the fracture closure pressure data. Given ε_H , S_H can then be computed. The two estimates of S_H are in good agreement, as shown in Fig. 2.9.

2.5 Discussion

Based on many researchers, the convergence of the Arabian and Eurasian Plates at Zagros Orogen is the main geodynamic setting that should be considered for the studied area in SW of Iran (Fig. 2.11; McClusky et al., 2003, Haghi et al 2013). The Zagros orogen as a part of the Alpine-Himalaya mountain chain is a well-defined active asymmetric orogenic belt (Alavi, 1994). It consists of three distinctive parallel tectonic zones (Fig. 2.11). To the northeast, the Uremiah–Dokhtar magmatic assemblage (UDMA) is a relatively narrow (50–80 km), linear belt of intrusive and extrusive rocks (Schroeder, 1944; Stocklin, 1968, 1974; Falcon, 1974; Alavi, 1994; Berberian et al., 1982) (Fig. 2.11). Southwest of the UDMA, the Zagros imbricate zone (ZIZ) forms the core of the orogen and consists of thrust systems ranging in age from Late Cretaceous to recent (Alavi, 1994). The Zagros fold-thrust belt (ZFTB), with an average width of 300 km, extends parallel and to the southwest of the ZIZ (Fig. 2.11). The ZFTB forms the upper part of the northeastern present-day Arabian continental margin. The Arabian and Eurasian (including Turan and Iranian) plates are converging in a NNE–SSW direction (DeMets et al, 1990, 1994; McCluskey, 2000; Sella et al, 2002).

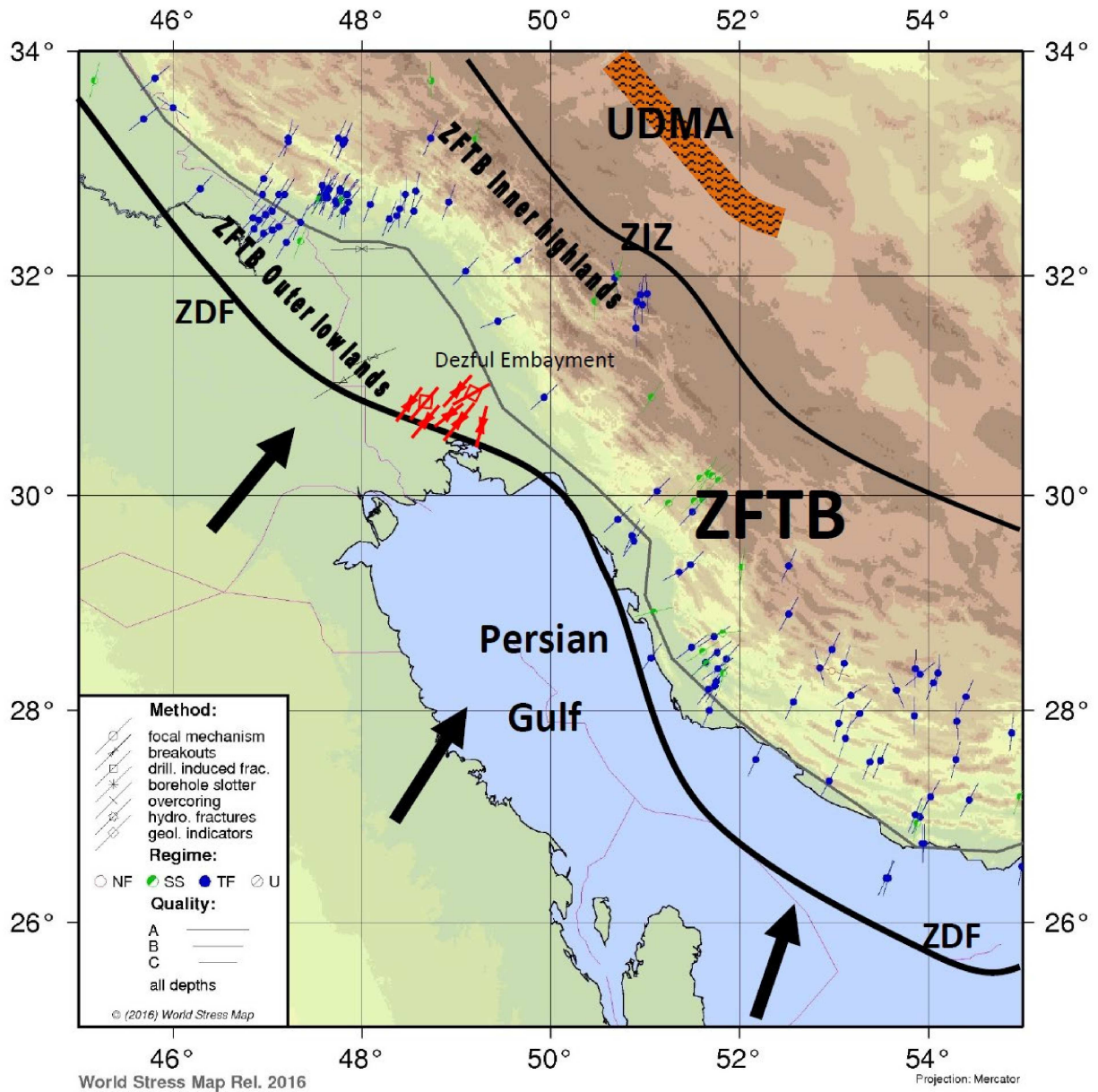


Fig. 2.11 Maximum horizontal stress orientations in SW Iran from the WSM database (modified after Heidbach et al., 2016) and for the studied area, subdivisions of Zagros Belt (Alavi, 2007). Symbols and different colors indicate the method of measurement and the stress regime. The NE-SW S_H orientations observed in wells B-1 to B-7 (the location of the stress indicators for this study in red are not exact) are consistent with the motion of the Arabian plate relative to the Eurasian (heavy arrows) and focal mechanism solutions observed in the Zagros Mountain belt. Abbreviations: UDMA-Urumieh Dokhtar magmatic assemblage, ZIZ -Zagros imbricate zone. This study reveals that normal stress regime exists in ZFTB outer lowland while focal mechanism solution records thrust faulting regime in the ZFTB inner highlands.

The Arabian and Iranian plates converge at an angle of 60° to the collisional plate boundary. So, convergence resolves into two components: one is parallel to the NW–SE Zagros trend at 0.3 cm/yr (Vernant and others, 2004). The other component is at right angles to the Zagros trend at 0.65 cm/yr (Berberian et al., 1982), producing the dominant Zagros constructional folds and thrusts. Bangestan Reservoir is located in the Dezful embayment (Dezful Recess) which is one of the main segments of ZFTB (Fig. 2.11). In fact, as inferred from deep and intermediate earthquake focal mechanism method (Heidbach et al., 2010), the convergence and compressive regime is the dominant regime in the Zagros thrust and fold belt.

Along the Bangestan Reservoir, breakout and DITF results confirm that S_H is oriented toward NE-SW, with minor localized stress rotations with depth, presumably related to the effects of material property heterogeneity. Herein, the analysis on wave velocity, Fig. 2.11, at the eastern part of formation confirms that Young's modulus rises up at the interval of 3600 to 3700 m, which confirms the S_H direction perturbation at the same depth. Density log, XLOT/step-rate test and DDT approach for acid re-fracturing data are used to calculate the magnitude of S_V , S_h , and S_H , respectively. Vertical stress is calculated as the maximum principal stress ($S_1=S_V$) while the minimum horizontal stress is estimated as the least principal stress ($S_3=S_h$). Accordingly, present-day stress data reveals a normal stress regime ($S_V>S_H>S_h$) in the Bangestan reservoir with NE-SW orientation of S_H .

The present-day stress in the Bangestan Reservoir is consistent with the Arabian-Eurasian convergence direction. However, the interpreted state of stress indicates a normal faulting tectonic stress regime and so is inconsistent with the compressive regime (indicated by several deep focal mechanism solutions), in the ZFTB. Note that the depth of focal mechanics data is mainly more than 10 km.

As illustrated in Fig. 2.11, the Bangestan Reservoir is located in the outer lowland of Zagros thrust and fold belt. From the inner highland to the outer lowland of ZFTB the intensity of tectonic activity reduces (Alavi, 2007). The lack of active thrust faults, the existence of numerous extensional fractures, and vertical DITF inside the wells of the Bangestan Reservoir is consistent with this reduced tectonic activity. Furthermore, the high density of overburden rock leads to overtaking of vertical stress rather than the maximum horizontal stress. Accordingly, although basement tectonic in response to geodynamic events is considered the main cause of the

deformations associated with the basement-cored structures in the ZFTB, it is not surprising to see a normal tectonic regime in the deeply buried fields like the Bangestan reservoirs in the outer lowland of ZFTB.

Finally in this research, k_{ave} ratio (Eq.2.17) versus depth for the Bangestan reservoir is compared with previously published stress data of other fields in Iran (Haghi et al., 2013a; Elyasi et al., 2014; Karimnezhad et al., 2014; Yaghoubi and Zeinali, 2009; Saeidi and Ahmadi, 2012) and 306 published data through the WSM 2016 project (Heidbach et al., 2016).

$$k_{ave} = \frac{(S_h + S_H)}{2S_v} \quad (2.17)$$

Brown and Hoek (1978) showed that k_{ave} ratio generally lies within the limits defined by,

$$\frac{100}{Z} + 0.3 \leq k_{ave} \leq \frac{1500}{Z} + 0.5 \quad (2.18)$$

As illustrated in Fig. 2.12, the data of the current research lies greatly between above limits. k_{ave} for the Bangestan reservoir varies between 0.65 to 0.71. Similarly, the previous studies of the stress state in deep reservoirs of Iran presented k_{ave} values which placed within the above limits, but, closer to the upper bound. The reason could be investigated into the normal tectonic regime in the Bangestan Reservoir. The global stress data shows good agreement with the presented upper and lower limits, Eq.(2.18), and the presented data for the Bangestan reservoir in Dezful embayment basin.

2.6 Conclusions

The results of this study offer insights into the state of present-day stress in the Bangestan Reservoir, SW of Iran. The direction of S_H is mainly NE-SW in the whole field except the eastern section. Ignoring anomalous data from well B-3, the mean orientation of S_H is approximated at $N44^\circ$ with the standard deviation of 9.95° for the whole filed. Vertical stress gradient approximates between 3.38 to 3.58 psi/m (1.03 to 1.09 psi/ft), based on some empirical methods and density log data, respectively. The average horizontal stress magnitude estimates 65-71% of the vertical stress magnitude. In this research, merging the definitions of bilinear flow, fracture conductivity changes, pressure change due to friction loss, it is attempted to model the acid re-fracturing process and match the models with field data. Then, this model goes into

the poroelastic equation with thermal terms to estimate the S_H in the Bangestan reservoir. Log-log plot of pressure derivative versus time is analyzed to extract fracture conductivity of 20880 mD.ft and half-length of the pre-existing fracture of 130 ft. Employing this method, S_H is calculated as 18.88kPa/m (0.83psi/ft).

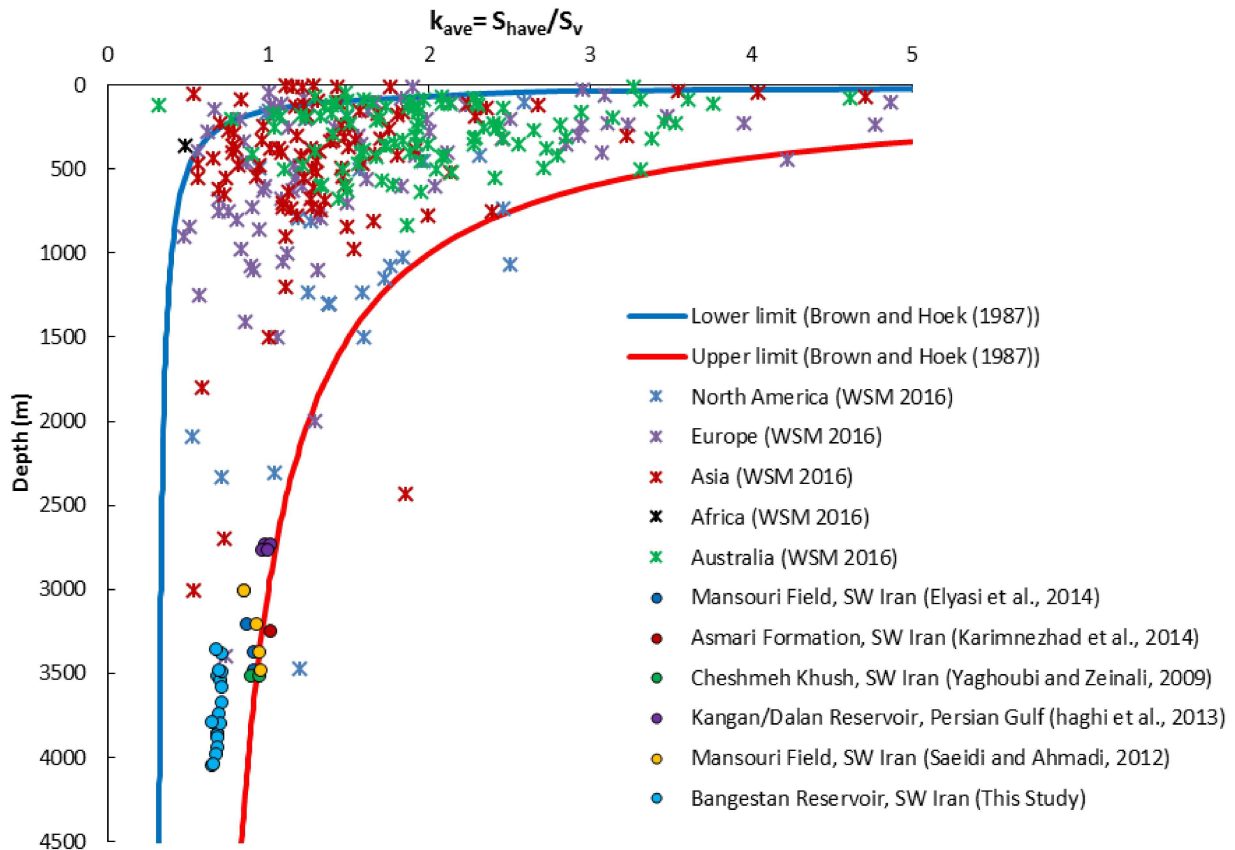


Fig. 2.12 Comparison between k_{ave} ratio versus depth for the Bangestan reservoir with stress data of other fields in Iran and worldwide data (Haghi et al., 2013a; Elyasi et al., 2014; Karimnezhad et al., 2014; Yaghoubi and Zeinali., 2009; Saeidi and Ahmadi, 2012; Heidbach et al., 2016).

Stress directions measured from images are much more relevant for asset development than are earthquake fault plane solutions coming from crustal depths well below the reservoirs. However, this study shows a good correlation between S_H orientation derived from Image logs and focal mechanism solution in this region. Compression (reverse and strike-slip stress regimes) is the dominant tectonism in the Arabian-Eurasian continental collision zone and ZFTB. This study indicates that in the deep outer lowland of ZFTB, due to tectonic activity's attenuation,

vertical stress is founded as the maximum principal stress ($S_1=S_V$), while the minimum horizontal stress is estimated as the least principal stress ($S_3=S_h$) based on the XLOT data. Accordingly, this study reveals that a normal faulting stress regime ($S_V>S_H>S_h$) occurs in the Bangestan reservoir. Base on the given tectonic regime, the typical strike direction of the induced hydraulic fracture plane must be NE-SW. However, some local present-day stress perturbation at the eastern part of the reservoir could deviate the fracture plane direction toward SSE-NNW.

3. New Semi-Analytical Insights into Stress-Dependent Spontaneous Imbibition and Oil Recovery in Naturally Fractured Carbonate Reservoirs*

Abstract

Fluid injection and withdrawal in a porous medium create changes in pore pressure that alter effective stresses within the medium. This leads to pore volume changes, which can be described by the poroelastic theory. These changes in pore volume can influence fluid flow processes, such as capillary diffusion and imbibition, potentially altering multiphase flow characteristics in subsurface reservoirs with a focus on oil recovery in the naturally fractured carbonate reservoirs (NFCRs). In this study, a semi-analytical model is developed to analyze the impact of stress-dependent spontaneous imbibition. The model allows us to study the influence of stress-dependent effects on porosity, absolute permeability, relative permeability, and capillary pressure on the imbibition and oil recovery mechanisms of both intact rock and fracture in NFCRs. In order to capture the geomechanical interactions involved, pure compliance poroelastic definitions and nonlinear joint normal stiffness equations are used to assess the deformation of intact rock and fracture, respectively. The model shows that increasing effective confining stress shifts the imbibition capillary pressure curve upward, resulting in improved absorption of the wetting phase into the smaller pores and enhanced extraction of the non-wetting phase. Model calculations provide a rationale for how and why irreducible water saturation increases during compression of mixed-wet carbonates and decreases in the case of initially strong water-wet carbonates. It is also shown how higher relative permeability of the wetting phase leads to a greater diffusion of the wetting phase and improved oil recovery for the less deformed mixed-wet rock.

* This chapter was published in *Water Resources Research*: Haghi, A. H., Chalaturnyk, R., & Geiger, S. (2018). New Semi-Analytical Insights into Stress-Dependent Spontaneous Imbibition and Oil Recovery in Naturally Fractured Carbonate Reservoirs. *Water Resources Research*, 54(11), 9605-9622.

3.1 Introduction

The objective of this study is to develop relationships for stress-dependent static/dynamic flow properties and analyze how they influence spontaneous imbibition and oil recovery. Counter-current spontaneous imbibition is the dominant production mechanism in fractured reservoirs in cases in which matrix blocks are not fully surrounded by water (Pooladi-Darvish and Firoozabadi, 2000). For this application, a new definition of capillary-driven fractional flow is presented taking into account the effect of porosity changes over time. Dynamic porosity, dynamic permeability, and geo-dynamic flow properties are then specified for a dual continuum model (e.g. carbonate matrix and fracture). We have chosen the term geo-dynamic to refer to initially dynamic properties such as relative permeability and capillary pressure that vary due to geomechanical processes.

Natural fractures are a common feature in nearly all hydrocarbon reservoirs that can significantly influence oil recovery and reservoir performance (Ahmed and McKinney, 2011). This study focuses on naturally fractured carbonate reservoirs (NFCRs) classified as Type II (Nelson, 2001), in which fractures provide most of the reservoir's permeability, while the rock matrix provides its main hydrocarbon storage capacity.

For this class of reservoirs, the success of recovery techniques such as water flooding or alkaline surfactant polymer flooding (ASP) is negatively impacted by the limited pressure difference that arises in the reservoir as a result of highly permeable fractures dominating fluid flow. In these cases, capillary imbibition, as opposed to viscous displacement, becomes the dominant recovery mechanism enabling hydrocarbon to flow from the matrix into the fracture system. Counter-current spontaneous imbibition is an essential recovery mechanism in NFCRs, and its performance is determined by the capillary pressure curve, which is a function of pore structure and wettability (Ferno, 2012). Increasingly, there has been a recognition that the geomechanical behavior of NFCRs can influence hydrocarbon recovery (Settari et al., 1999).

Surprisingly little has been published regarding the stress-dependent relative permeability of the matrix or intact rock within NFCRs. Li and Horn (2006) presented the commonly used modified Brooks and Corey relation (Corey, 1954; Brooks and Corey, 1966) to

describe capillary pressure (P_c) and relative permeability of the wetting (k_{rw}) and non-wetting (k_{rnw}) phases:

$$P_c = P_e (S_w^*)^\beta \quad (3.1)$$

$$k_{rw} = k_{rw-max} (S_w^*)^{n_w} \quad (3.2)$$

$$k_{rnw} = k_{rnw-max} (1 - S_w^*)^{n_{nw}} \quad (3.3)$$

$$S_w^* = \frac{S_w - S_{wir}}{1 - S_{wir} - S_{nwr}} \quad (3.4)$$

where S_{wir} and S_{nwr} refer to the irreducible wetting and residual non-wetting phase saturation. Additionally, P_e , k_{rw-max} , and $k_{rnw-max}$ denote entry capillary pressure (threshold pressure), and the maximum relative permeability of the wetting and non-wetting phases, respectively.

The power law coefficients β , n_w , and n_{nw} can be related to the pore size distribution index λ^* ($\lambda^* > 0$) (Brooks and Corey, 1966), with the following equations:

$$\beta = -\frac{1}{\lambda^*} \quad (3.5)$$

$$n_w = \frac{A + B\lambda^*}{\lambda^*} \quad (3.6)$$

$$n_{nw} = \frac{A' + B'\lambda^*}{\lambda^*} \quad (3.7)$$

where A , A' , B , and B' are curve-fitting constants. These can be estimated using the least square regression method on the experimental data.

The bundle of capillary tubes illustrated in Fig. 3.1 serves as an analogue to pore size distribution and the index λ^* . For a given, original pore size distribution, the black curve shown in Fig. 3.1 illustrates the process of spontaneous imbibition, as the wetting phase saturation increases with decreasing capillary pressure over a range of pore sizes (i.e. capillary tube diameter). For cases in which increasing effective stress leads to a reduction in pore sizes (i.e. a reduction in capillary tube diameters), the change in the red curve in Fig. 3.1 illustrates how the capillary curve shifts upwards, altering the spontaneous imbibition characteristics of the matrix.

In the case illustrated in Fig. 3.1, effective stress induced-deformation enhances the imbibition process. Alternatively, if effective stress changes lead to increases in pore sizes, the spontaneous imbibition process is attenuated. Additional capillary pressure for the deformed rock spontaneous imbibition line decreases permeability due to decrease in the tubes' cross sectional area and porosity. Given the importance of quantifying the imbibition process under these conditions, understanding and quantifying the stress-dependent dynamic properties in NFCRs is critical for improving field recovery and optimizing reservoir management.

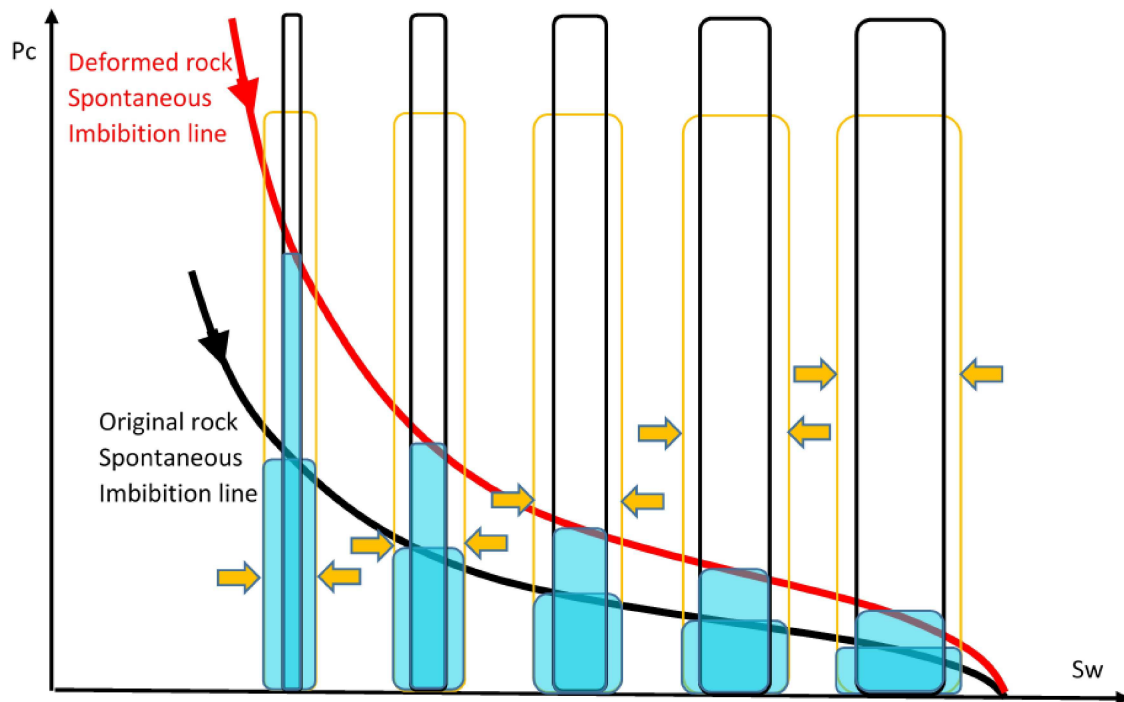


Fig. 3.1 Schematic description of stress-dependent spontaneous imbibition curve in a bundle of capillary tubes

3.2 Experimental Results

In terms of laboratory experiments, there is little data showing effective stress effects on relative permeability in NFCRs. For this study, the results from experiments conducted by McDonald et al. (1991) and Lian et al. (2012) are analyzed to establish the key parameters required for the semi-analytical model. Both experimental programs demonstrated the stress dependency of oil-water relative permeability in fractured carbonates (fracture dominated). The imbibition relative permeability experimental results from Lian et al. (2012), shown in Fig. 3.2,

indicated that the irreducible wetting phase (water) saturation, S_{wir} , increases with effective confining stress, σ' , while the water relative permeability, k_{rw} , shifts to the right. This behavior suggests the rock becomes increasingly water-wet as effective stress increases. In contrast, the experimental results from McDonald et al. (1991), shown in Fig. 3.3, indicate that increasing stress results in a reduction of irreducible water saturation and causes the relative permeability curves to shift to the left.

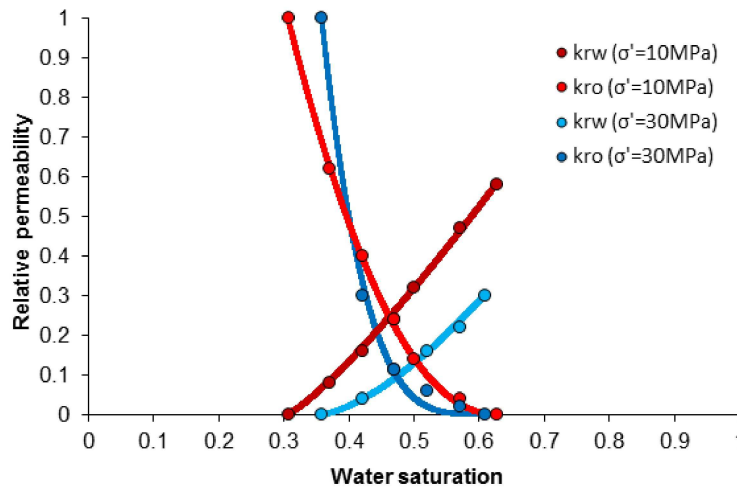


Fig. 3.2 Relative permeability curves based on Lian et al.'s [2012] experiment. The dots define the experimental data and the solid lines indicate the curve fitting lines.

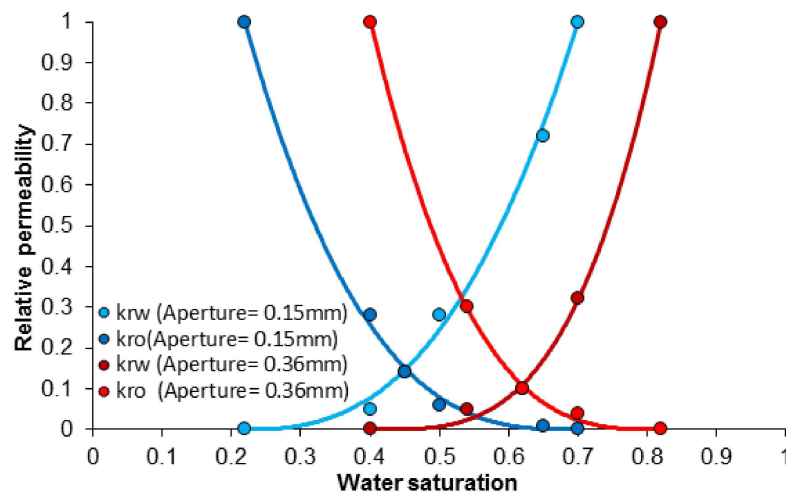


Fig. 3.3 Relative permeability curves based on McDonald et al.'s [1991] experiment. The dots define the experimental data and the solid lines indicate the curve fitting lines.

Hue and Benson (2016) concluded that this apparent contradiction in behavior can be explained by the relative weight of viscous and capillary forces, termed the *capillary number*. The capillary number is defined as (Peters, 2012):

$$N_c = \frac{\mu V}{\sigma_{st} \cos \theta} \quad (3.8)$$

where μ is the dynamic viscosity of the liquid, V is a characteristic velocity and $\sigma_{st} \cos \theta$ is the surface or interfacial tension between the two fluid phases. The authors concluded that under constant capillary number conditions (constant V), the irreducible water saturation increases with increasing effective confining stress (as in the case of Lian et al., (2012)). However, in experiments with a constant flow rate, higher effective confining stress decreases the irreducible water saturation (case of McDonald et al., 1991).

The relative permeability curves from Lian et al. (2012), Fig. 3.2, and McDonald et al. (1991), Fig. 3.3, are based on lab experiments on mainly mixed-wet and strongly water-wet carbonates, respectively. Hence, the wetting phases differ between the tests. Accordingly, the results from the two experimental programs are consistent and show an increase in the irreducible saturation of the wetting phase as the confining stress and capillary pressure increase. Consequently, the results from both experimental programs are utilized in this study.

Implementing the least square technique, Eqs.(3.2)-(3.4) have been utilized to find the best match for the stress-dependent relative permeability data from both McDonald et al. (1991) and Lian et al. (2012). Fig. 3.2 illustrates the relative permeability curve correlation for 10 MPa and 30 MPa effective confining stress based on modified Brooks-Corey relations combined with data presented by Lian et al. (2012).

Table 3.1 provides the equations for the given fitting curves illustrated in Fig. 3.2. Similarly, Fig. 3.3 shows the relative permeability curve for 6.9 MPa (0.36 mm fracture aperture) and 26.5 MPa (0.15 mm fracture aperture) effective confining stress based on the modified Brooks-Corey relations (see Table 3.2) and data presented by McDonald et al. (1991).

Table 3.1 Modified Brooks and Corey equation to fit curves on the Lian et al.'s (2012) Experimental Data

Relative Permeability	$\sigma' = 10MPa$	$\sigma' = 30MPa$
k_{rw}	$0.58 \times \left(\frac{S_w - 0.307}{0.32} \right)^{1.2}$	$0.3 \times \left(\frac{S_w - 0.359}{0.25} \right)^{1.5}$
k_{rnw}	$1 \times \left(\frac{0.627 - S_w}{0.32} \right)^{2.1}$	$1 \times \left(\frac{0.609 - S_w}{0.25} \right)^{3.8}$

Table 3.2 Modified Brooks and Corey equations to fit curves on the McDonald et al.'s (1991) Experiment Data

Relative Permeability	Aperture = 0.36 mm ($\sigma' = 6.9MPa$)	Aperture = 0.15 mm ($\sigma' = 26.5MPa$)
k_{rw}	$1 \times \left(\frac{S_w - 0.4}{0.42} \right)^{3.4}$	$1 \times \left(\frac{S_w - 0.22}{0.48} \right)^{2.6}$
k_{rnw}	$1 \times \left(\frac{0.82 - S_w}{0.42} \right)^3$	$1 \times \left(\frac{0.7 - S_w}{0.48} \right)^{2.9}$

3.3 Derivation of Semi-Analytical Model

In this section, a semi-analytical solution is derived to model the stress-dependent spontaneous imbibition in a cubic block of rock. Analogues with *Warren and Root's* [1963] sugar cube model, orthogonal fracture sets inside the block are assumed to be perpendicular to the plane surface of the cubic matrix block (Fig. 3.4), and three principal stresses are applied normal to the sides of the block. Section 3.3.1 describes the solution of the capillary diffusivity equation considering a time- (or effective stress-) dependent porosity for the counter-current imbibition of the wetting phase on each side of the block. Sections 3.3.2.1 and 3.3.1 describe the stress-dependent porosity of the block using poroelastic theory and non-linear joint normal stiffness equations for intact rock and fracture deformations, respectively. Sections 3.3.2 to 3.3.4 provide the solutions for absolute permeability, relative permeability, and capillary pressure, which are updated in each effective stress condition, using appropriate theories for the dual medium. We have assumed that the matrix-fracture's effects can be added as an averaged two-medium property to the block model in Fig. 3.4 and that the medium properties are distributed uniformly.

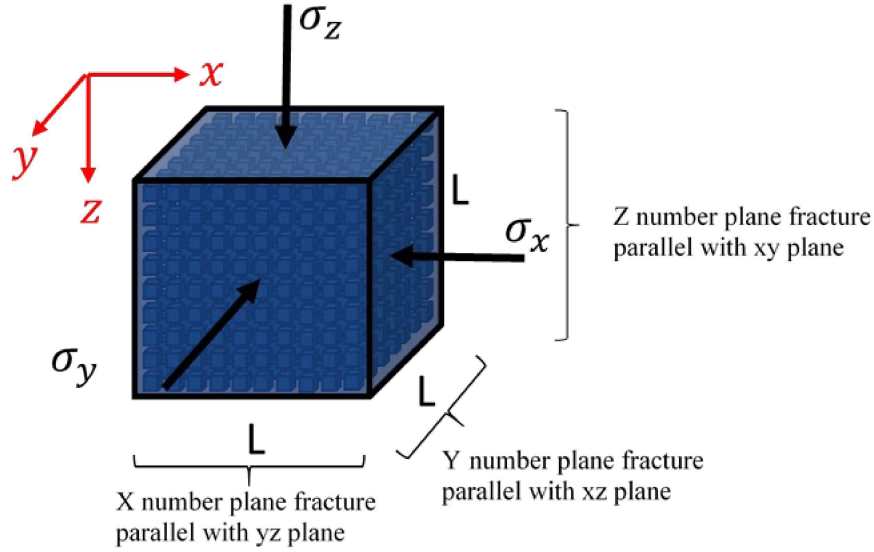


Fig. 3.4 Block model consisting of X*Y*Z of orthogonal plane fractures

3.3.1 Stress-Dependent Counter-Current Fractional Flow Formulation

Rewriting the mass-balance equation for two phase flow in 1D (each side of the block) for incompressible phase ($\rho_w = cte$, Eq.(3.9)) at constant temperature through homogeneous porous media with porosity (ϕ), we obtain the continuity equation (Bear, 2013)

$$\frac{\partial}{\partial t} (S_w \phi) = - \frac{\partial q_w}{\partial x} \quad (3.10)$$

We assume that the flow rate of the wetting and non-wetting phase, q_w and q_{nw} , respectively, can be specified by the Darcy equation (Peters, 2012)

$$q_w = - \frac{k k_{rw}}{\mu_w} \left(\frac{\partial P_w}{\partial x} + \rho_w g \sin \alpha \right) \text{ and} \quad (3.11)$$

$$q_{nw} = - \frac{k k_{rnw}}{\mu_{nw}} \left(\frac{\partial P_{nw}}{\partial x} + \rho_{nw} g \sin \alpha \right) \quad (3.12)$$

where k is the absolute permeability, μ_w is the viscosity of the wetting phase, μ_{nw} is the viscosity of the non-wetting phase, and k_{rnw} and k_{rw} are the relative permeability of the non-wetting phase and the wetting phase, respectively. Combining Eqs.(3.11)-(3.12) results in the following equation:

$$\frac{q_w \mu_w}{k k_{rw}} - \frac{q_{nw} \mu_{nw}}{k k_{rnw}} = \frac{\partial P_{nw}}{\partial x} - \frac{\partial P_w}{\partial x} - \Delta \rho g \sin \alpha. \quad (3.13)$$

Using the definitions for capillary pressure (P_c), fractional flow (f), total flow (q_t), and the mobility ratio (λ), Eq.(3.13) can be rewritten as (Peters, 2012):

$$q_w = \frac{\lambda_w}{\lambda_t} q_t + k \frac{\lambda_w \lambda_{nw}}{\lambda_t} \frac{\partial P_c}{\partial x} - k \frac{\lambda_w \lambda_{nw}}{\lambda_t} \Delta \rho g \sin \alpha. \quad (3.14)$$

Eq.(3.14) shows that water velocity is a result of the total viscous velocity, a gradient in capillary pressure and gravity, as represented by the first, second and third terms on the right hand side of equation, respectively. Ignoring capillary and gravity forces (by setting the second and third terms in Eq.(3.14) to zero), the Buckley-Leverett solution can be derived (Buckley and Leverett, 1942). Considering counter-current spontaneous imbibition ($q_t = 0$) but ignoring the gravitational forces (third terms), Eq.(3.14) becomes

$$q_w = -D \frac{\partial S_w}{\partial x}. \quad (3.15)$$

Herein, we used the chain rule for the capillary gradient ($\frac{\partial P_c}{\partial x} = \frac{\partial P_c}{\partial S_w} \times \frac{\partial S_w}{\partial x}$) and the nonlinear capillary diffusion coefficient with the unit of length squared over time (Eq.(3.16)) (McWhorter and Sunada, 1990). In this study we considered D to be not only a function of wetting phase saturation, but also, since the rock properties are stress-dependent, a function of effective stress in the reservoir:

$$D(S_w, \sigma') = -\frac{k \lambda_w \lambda_{nw}}{\lambda_t} \frac{\partial P_c}{\partial S_w}. \quad (3.16)$$

Replacing q_w in Eq.(3.10) with the derived q_w in Eq.(3.15) leads to Eq.(3.17) for capillary imbibition. As rock porosity is effective stress-dependent, and effective stress changes with time, in this study we consider it to be a dynamic rock property. Accordingly, the general partial differential equation for counter-current spontaneous imbibition flow with deforming rock assumption is specified as follows:

$$S_w \frac{\partial \varphi}{\partial t} + \varphi \frac{\partial S_w}{\partial t} = \frac{\partial}{\partial x} \left(D(S_w, \sigma') \frac{\partial S_w}{\partial x} \right). \quad (3.17)$$

Note that $D(S_w, \sigma')$ is zero if $S_w = S_{wir}$. Table 3.3 provides the initial and boundary conditions for Eq.(3.17). *Schmid et al.* [2016] used the similarity variable $\omega = x/\sqrt{t}$ and presented a general solution in terms of the derivative of a capillary-driven fractional flow function (F) as follows:

$$\omega(S_w) = \frac{2C}{\varphi} \frac{\partial F}{\partial S_w}, \quad (3.18)$$

where C is deemed to be proportionality constant with the unit of m/ \sqrt{s} (C^2 has the units of a diffusion coefficient) and is specified as follows:

$$q_w(x = 0, t) = \frac{C}{\sqrt{t}} \quad (3.19)$$

In this study, the parameter ω is used to describe capillary-driven spontaneous imbibition.

Table 3.3 Initial and boundary conditions for the semi-analytical model shown in Fig. 3.4

Initial Conditions	Boundary Conditions
$\varphi(x, 0) = \varphi_0$	$S_w(L/2, t) = 1 - S_{or}$
$S_w(x, 0) = S_{wir}$	$q_w(0, t) = Ct^{-1/2}$

Appendix A provides a proof that the similarity variable ω , given in Eq.(3.18), is valid for the class of problem presented in this research. The proportionality constant, C, controls the imbibition of the wetting phase at the inlet ($x=0$) of rock, and it is a function of flow parameters such as relative permeability, capillary pressure, and viscosity. In this study, C is not a constant but an effective stress-dependent parameter (C') since static and dynamic flow properties change with rock deformation.

Similarly, ω is also a stress-dependent variable. Given the similarity between the capillary-driven flow Eq.(3.18) and the Buckley-Leverett viscous-driven flow equation (Buckley and Leverett, 1942), Schmid and Geiger (2012) concluded that F is the fractional flow function for the case of capillary-driven flow. Hence, F is given by the ratio of water flow as a function of saturation to its maximum value at the inlet. Eq.(3.17) now becomes

$$S_w \omega \frac{d\varphi}{d\omega} + \varphi \omega \frac{dS_w}{d\omega} = -2 \frac{d}{d\omega} \left(D(S_w, \sigma') \frac{dS_w}{d\omega} \right), \quad (3.20)$$

using the following relations:

$$\frac{\partial S_w}{\partial t} = \frac{\partial S_w}{\partial \omega} \frac{\partial \omega}{\partial t} = -\frac{\omega}{2t} \frac{dS_w}{d\omega} \quad (3.21)$$

$$\frac{\partial S_w}{\partial x} = \frac{\partial S_w}{\partial \omega} \frac{\partial \omega}{\partial x} = \frac{1}{\sqrt{t}} \frac{dS_w}{d\omega} \quad (3.22)$$

$$\frac{\partial \varphi}{\partial t} = \frac{\partial \varphi}{\partial \omega} \frac{\partial \omega}{\partial t} = -\frac{\omega}{2t} \frac{\partial \varphi}{\partial \omega}. \quad (3.23)$$

Integrating both sides of Eq.(3.20) leads to the following equation,

$$\int_{\varphi_i}^{\varphi_t} S_w \omega d\varphi + \int_{S_{wir}}^{1-S_{or}} \varphi \omega dS_w = -2D(S_w, \sigma') \frac{dS_w}{d\omega}, \quad (3.24)$$

where φ_t is the dynamic porosity. The term *dynamic* is used to emphasize the fact that porosity is not a static rock property in the model, but a dynamic property that changes with stress based on poroelastic theory. Meanwhile, φ_t is uniform in space. Note that the integral limits in Eq.(3.24) for the similarity variable ω are zero to $(L/2)/\sqrt{t^*}$ (or $x = 0$ to $L/2$) for the finite block of rock with a dimension of L (Fig. 3.4). Here, the early time imbibition, t^* , is defined as follows:

$$t^* = \left(\frac{L}{2\omega(S_{wir})} \right)^2. \quad (3.25)$$

Assuming S_w and φ are independent parameters, and replacing ω with the terms given in Eq.(3.18), Eq.(3.24) can be written as follows:

$$\left(S_w \ln(\varphi_t/\varphi_i) \frac{dF}{dS_w} + F \right) \frac{d^2 F}{dS_w^2} = -\frac{\varphi_t}{2C'^2} D(S_w, \sigma'). \quad (3.26)$$

Eq.(3.26) can be solved both analytically and numerically using the finite difference approximation method. Herein, we propose a numerically backward-differencing approximation to solve Eq.(3.26).

$$\begin{aligned}
F_1 &= -BF_2 - 0.5F_3 \\
&+ \sqrt{B^2F_2^2 + 0.25F_3^2 + BF_2F_3 - \frac{1}{(1-A)}(AF_2F_3 - 2AF_2^2 + \frac{\varphi_t}{2C'^2} D(S_w, \sigma')\Delta S_w^2)}, \tag{3.27}
\end{aligned}$$

where $A = \frac{S_w \ln(\varphi_t/\varphi_i)}{\Delta S_w}$ and $B = \frac{(3A-2)}{2(1-A)}$ are simplifying parameters. Classical approaches, which neglect porosity change ($\varphi_t = \varphi_i$), employ $A = 0$ and $B = -1$; this reduces Eq.(3.27) to the definition of capillary-driven fractional flow term presented by Schmid et al. (2016). In Eq.(3.27), F_1 , F_2 , and F_3 refer to $F(S_w)$, $F(S_w + \Delta S_w)$, and $F(S_w + 2\Delta S_w)$, respectively. From Eq.(3.27), we can determine F at each saturation, which allows $\frac{\partial F}{\partial S_w}$ to be inserted into Eq.(3.18) to obtain the saturation distribution with ω . However, Eq.(3.27) still requires that we know C' and the stress-dependent rock properties at each stress condition (e.g. φ_t , $D(S_w, \sigma')$). The parameter C' can be computed by choosing a starting value and iterating it until some convergence criteria for F (e.g. $F(S_w = S_{wir}) = 0$ and $F(S_w = 1) = 1$) at each effective stress state is met (Schmid et al. 2016). To specify the stress-dependent rock properties for such a dual continuum model, we need to determine the property for each medium separately and mix them together to find the equilibrium continuum properties (Bagheri and Settari, 2008). Hence, to define φ_t and $D(S_w, \sigma')$ in Eq.(3.27), we need to derive representative equations for stress-dependent porosity, absolute permeability, relative permeability, and capillary pressure for a block of rock which contains both fracture and intact rock. In the following sections (3.3.2 to 3.3.4), additional expressions are developed for these stress-dependent rock properties.

3.3.2 Matrix Stress-Dependent Properties Specification

3.3.2.1 Matrix Dynamic Porosity (φ_{mt})

The effective constitutive relation (stress-strain) for intact rock is assumed to follow Hook's law and mathematically takes the following form in index notation (Bagheri and Settari, 2008):

$$\varepsilon_{ij} = C_{ijkl} \sigma'_{kl} \tag{3.28}$$

where ε_{ij} is the strain tensor, σ'_{kl} is the effective stress tensor for porous media, and C_{ijkl} is a 6×6 stiffness matrix. The constitutive equation in which strain and increment of fluid content

are paired as dependent variables, and stress and pore pressure are considered independent variables, is called the pure compliance model (Wang, 2017). The poroelastic constitutive equation for the pure compliance model is given as follows (Segal, 1989):

$$\varepsilon_{ij} = \frac{1}{2G} \left(\sigma_{ij} - \left(\frac{\vartheta}{1 + \vartheta} \right) \sigma_{kk} \delta_{ij} + \left(\frac{1 - 2\vartheta}{1 + \vartheta} \right) \alpha P \delta_{ij} \right) \quad (3.29)$$

where ϑ , α and G are drained Poisson's ratio, Biot coefficient, and shear modulus, respectively. The strain and stress tensors each contain six components for an arbitrary orientation of the coordinates system. However, for deep oil and gas reservoirs, it is common to use principal coordinates in which shear stress and shear strains are zero. This is the case here, as we assumed the principal effective stresses were perpendicular to the plane surface of the cubic matrix block (Fig. 3.5). The three principal strains corresponding to three principal stresses based on Eq.(3.29) are specified as follows:

$$\varepsilon_x = \frac{1}{2G} \left(\sigma_x - \left(\frac{\vartheta}{1 + \vartheta} \right) (\sigma_x + \sigma_y + \sigma_z) + \left(\frac{1 - 2\vartheta}{1 + \vartheta} \right) \alpha P \right) \quad (3.30)$$

$$\varepsilon_y = \frac{1}{2G} \left(\sigma_y - \left(\frac{\vartheta}{1 + \vartheta} \right) (\sigma_x + \sigma_y + \sigma_z) + \left(\frac{1 - 2\vartheta}{1 + \vartheta} \right) \alpha P \right) \quad (3.31)$$

$$\varepsilon_z = \frac{1}{2G} \left(\sigma_z - \left(\frac{\vartheta}{1 + \vartheta} \right) (\sigma_x + \sigma_y + \sigma_z) + \left(\frac{1 - 2\vartheta}{1 + \vartheta} \right) \alpha P \right). \quad (3.32)$$

Accordingly, the volumetric strain can be computed as (Wang, 2000)

$$\varepsilon_v(t) = \varepsilon_x + \varepsilon_y + \varepsilon_z = \frac{(1 - 2\vartheta)}{E} (\sigma_x(t) + \sigma_y(t) + \sigma_z(t)) + \frac{\alpha}{K} P(t) \quad (3.33)$$

where $E = 2G(1 + \vartheta)$ is drained Young's modulus, and $K = \frac{E}{3(1-2\vartheta)}$ is bulk modulus. Assuming equal horizontal stress, $\sigma_x = \sigma_y = \sigma_3$, and $\sigma_z = \sigma_1$, we have

$$\varepsilon_v(t) = \varepsilon_x + \varepsilon_y + \varepsilon_z = \frac{2(1 - 2\vartheta)}{E} \sigma_3(t) + \frac{(1 - 2\vartheta)}{E} \sigma_1(t) + \frac{\alpha}{k} P(t). \quad (3.34)$$

In Eq.(3.34), the signs of σ_i and ε_i for compression are negative. Knowing the volumetric strain, the dynamic porosity of the intact rock can be computed as follows (Tortike and Ali, 1993; Li and Chalaturnyk, 2003):

$$\varphi_{mt} = \frac{V_{pi} + \Delta V_p}{V_{bi} + \Delta V_b} = \frac{V_{pi} + (\Delta V_b - \Delta V_s)}{V_{bi} + \Delta V_b} \times \frac{V_{bi}}{V_{bi}} = \frac{\varphi_{mi} + \varepsilon_v - \Delta V_s/V_{bi}}{1 + \varepsilon_v} = \frac{\varphi_{mi} + \varepsilon_v(t)}{1 + \varepsilon_v(t)} \quad (3.35)$$

where V_α , $\alpha = b, p, s$ indicates bulk, pore and grain volume, respectively. Given the relative incompressibility of the grains, the term $\Delta V_s/V_{bi}$ has been neglected in the formulation. Eq.(3.35) allows the matrix porosity component of the total porosity in the capillary diffusion solution given in Eq.(3.27) to be updated at each effective stress condition. The fracture porosity component of the total porosity is described in Section 3.3.3.1.

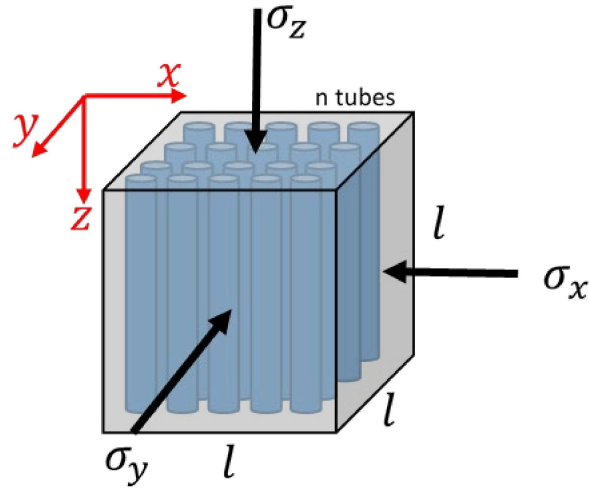


Fig. 3.5 Deformation of matrix block due to effective confining stress

3.3.2.2 Matrix Dynamic Absolute Permeability (k_{mt})

For the initial stage of model development, we have adopted the bundle of tubes model to express absolute permeability as a function of porosity (Washburn, 1921). Assuming n number of parallel and equal capillary tubes inside the block of matrix in Fig. 3.5, we investigate the effect of deformation on the absolute permeability of the intact rock. Based on Hagen-Poiseuille's law for the steady, laminar flow of Newtonian fluid through a bundle of n number capillary tubes of radius r , the flow rate can be determined as follows (Dake, 1983):

$$q = - \left(\frac{n\pi r^4}{8\mu} \right) \frac{\Delta P}{l}. \quad (3.36)$$

In Eq.(3.36) the tortuosity term has been disregarded. Comparing this equation with the linear Darcy flow equation through a cube of dimension l ($q = -\left(\frac{l^2 k}{\mu}\right) \frac{\Delta P}{l}$, Fig. 3.5), the absolute permeability equation in terms of porosity is

$$k = \left(\frac{n\pi r^4}{8l^2}\right) = \frac{\varphi r^2}{8}. \quad (3.37)$$

Application of effective confining stresses on the block of intact rock in Fig. 3.5 will result in deformation based on the poroelastic equation presented in Section 3.3.2.1. Hence, the ratio between the dynamic (k_{mt}) and initial (k_{mi}) absolute permeability is defined based on the following equation:

$$\frac{k_{mt}}{k_{mi}} = \frac{\varphi_{mt} r_t^2}{\varphi_{mi} r_i^2} = \frac{\varphi_{mt} n\pi r_t^2 l^2}{\varphi_{mi} n\pi r_i^2 l^2} = \left(\frac{\varphi_{mt}}{\varphi_{mi}}\right)^2. \quad (3.38)$$

Eq.(3.38) allows the dynamic absolute permeability to be computed. This equation is subsequently combined with an equation derived for the absolute permeability of the fracture (Section 3.3.3.2) to describe average absolute permeability of the whole block.

3.3.3 Fracture Stress-Dependent Properties Specification

Given the nonlinear deformation of fractures in response to effective stress changes, fracture properties should be treated as dynamic properties due to changing effective stresses during production and injection operations. The following sections describe the procedure to derive fracture dynamic porosity and absolute permeability.

3.3.3.1 Fracture Dynamic Porosity (φ_{ft})

Fracture deformation modes will vary under the application of normal and shear stresses. In many cases, the effect of shear stresses on fracture deformation in naturally fractured reservoirs is neglected in reservoir simulations (Bagheri and Settari, 2008) due to the extensive lab work required to define this behavior. In addition, major difficulties exist in upscaling lab work to full field simulation models, and the effect of shear stress is less well understood than that of normal stress. Consequently, for the current semi-analytical formulation, shear stress effects have also been disregarded. Considering the fracture aperture as a narrow layer of different material than the matrix rock, we apply Hooke's law to describe the fracture stress–

strain relations. As in the case of intact rock deformation, the constitutive equation to investigate deformation in fractures would be

$$d\varepsilon_{ij} = D_{ijkl}\Delta\sigma'_{kl}n_k, \quad (3.39)$$

where n_k represents the components of the normal vector to the joint surface (Bagheri and Settari, 2008). Considering single plane fractures perpendicular to one of the principal stresses (shear displacement being disregarded) with an aperture J_o (see Fig. 3.6), the joint stress-strain relations become (Pariseau, 2011)

$$d\sigma_n = k_n dJ_n, \quad (3.40)$$

where k_n is the fracture normal stiffness that relates stress to the relative displacement between opposing points on the two surfaces of fracture. Here, the fracture closure is considered to be positive.

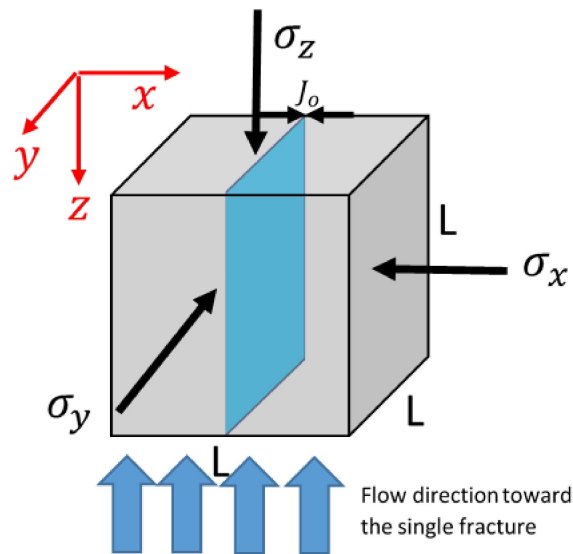


Fig. 3.6 Arbitrary fracture geometry inside the block model

There are different models of fracture deformation (Hudson and Harrison, 2000; Pariseau, 2011; Cundall and Lemos, 1990) including 1) the Coulomb friction, 2) the continuously-yielding joint model, and 3) the Barton-Bandis joint model.

The Coulomb friction is a linear deformation model in which the fracture aperture closes elastically up to a limit of ΔJ_{\max} under normal compressive stress (Fig. 3.7a). As illustrated in Fig. 3.7b, the Barton-Bandis joint model is a nonlinear fracture deformation model. Bandis et al. (1983) and Barton et al. (1985) described the impacts of surface roughness on fracture deformation by developing empirical relations between stress, fracture closure, and two parameters: the joint roughness coefficient, JRC, and joint wall compressive strength, JCS.

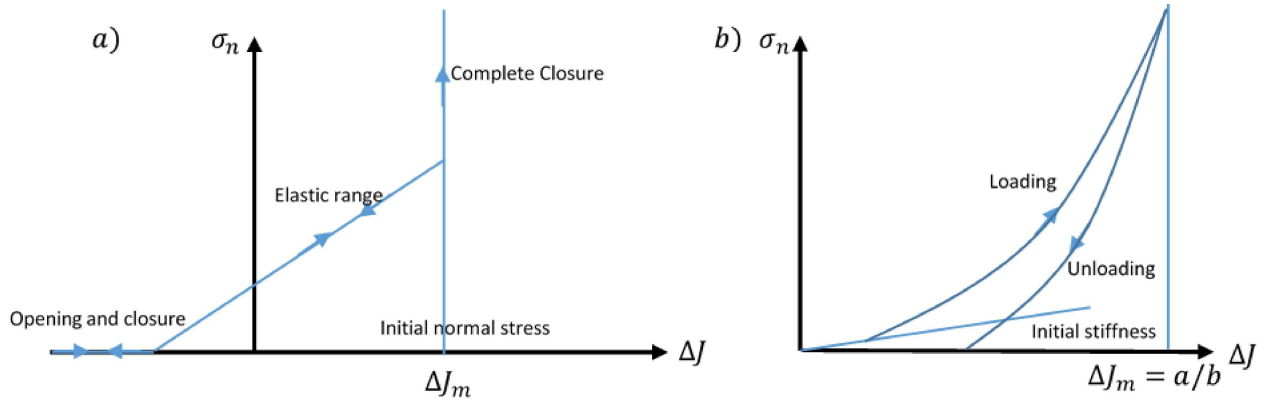


Fig. 3.7 Fracture closure versus normal stress in a) linear and b) nonlinear methods

The Barton–Bandis fracture model includes hyperbolic loading and unloading curves (Fig. 3.7b) in which normal stress and fracture closure, ΔJ , are related by the following equation,

$$\sigma_n = \frac{\Delta J}{(a - b\Delta J)}, \quad (3.41)$$

where a and b are constants. Rewriting Eq.(3.41) with effective normal stress terms, the equation describing fracture closure becomes

$$\Delta J = \frac{\sigma'_n}{\left(k_{ni} + \frac{\sigma'_n}{\Delta J_{max}}\right)}, \quad (3.42)$$

where the initial fracture normal stiffness, k_{ni} , is equal to $1/a$ and the maximum fracture closure, ΔJ_{max} , is defined as a/b . Accordingly, the expression for normal stiffness becomes

$$k_n = k_{ni} \left[1 - \frac{\sigma'_n}{(\Delta J_{max} k_{ni} + \sigma'_n)} \right]^{-2}, \quad (3.43)$$

which reflects the dependency of fracture normal stiffness on effective stress [*Barton et al.* 1985].

In this study, we have utilized the Barton-Bandis nonlinear deformation model, which has been acknowledged universally in the literature on NFCRs (Bagheri and Settari, 2008). Considering the fracture closure model geometry shown in Fig. 3.6, the initial single fracture porosity will be defined as:

$$\varphi_{fi} = \frac{V_{ft}}{V_b} = \frac{J_o \times L^2}{L^3} = \frac{J_o}{L}. \quad (3.44)$$

The dynamic fracture porosity can now be estimated using Eq.(3.44) for fracture closure using the following equation:

$$\varphi_{ft} = \frac{V_{ft}}{V_{bt}} = \frac{(J_o + \Delta J) \times L^2}{(L + \Delta J)L^2} = \frac{(J_o + \Delta J)}{(L + \Delta J)}. \quad (3.45)$$

Application of the Barton-Bandis non-linear fracture closure model allows the fracture porosity in the capillary diffusion solution given in Eq.(3.27) to be updated at each effective stress condition.

3.3.3.2 Fracture Dynamic Absolute Permeability (K_{ft})

Adopting Hagen-Poiseuille's law for steady, laminar flow of a Newtonian fluid (but this time through a slit of aperture J_o with same width and length of L) yields the following equation (Peters, 2012):

$$q = -\left(\frac{LJ_o^3}{12\mu}\right)\frac{\Delta P}{L}. \quad (3.46)$$

Comparing this equation with the linear Darcy equation for flow through a fracture of the same dimension, $q = -\left(\frac{LJ_o^k}{\mu}\right)\frac{\Delta P}{L}$ (also see Fig. 3.6), the fracture absolute permeability can be computed as (Peters, 2012)

$$k = \frac{J_o^2}{12}. \quad (3.47)$$

For effective normal confining stresses on the fracture, the fracture will close or open based on the nonlinear fracture closure equation presented in Eq.(3.42). Hence, the ratio between

the dynamic and initial fracture absolute permeability (k_{ft} and k_{fi} , respectively) is defined based on the following equation:

$$\frac{k_{ft}}{k_{fi}} = \frac{(J_o + \Delta J)^2}{J_o^2} \quad (3.48)$$

3.3.4 Dual Continuum Stress-Dependent Properties Specification

3.3.4.1 Total Dynamic Porosity (φ_t)

For our semi-analytical model, the dual continuum dynamic porosity is computed as follows:

$$\varphi_t = \frac{V_{ft} + V_{pt}}{V_{bt}} = \varphi_{ft} + \frac{V_{pt}}{V_{bt}} = \varphi_{ft} + \varphi_{mt} \frac{V_{bmt}}{V_{bt}} \quad (3.49)$$

where V_{bmt} is the dynamic matrix bulk volume. Then,

$$\varphi_t = \varphi_{ft} + \varphi_{mt} \frac{V_{bt} - V_{ft}}{V_{bt}}. \quad (3.50)$$

Total dynamic porosity can be estimated as follows:

$$\varphi_t = \varphi_{ft} + \varphi_{mt}(1 - \varphi_{ft}). \quad (3.51)$$

In Eq.(3.51), φ_{mt} and φ_{ft} indicate the matrix and fracture dynamic porosity, which are defined by Eq.s(3.35) and (3.45), respectively. Eq.(3.51) specifies the dynamic porosity of the whole block of rock (φ_t), and it is inserted as a measure of stress-dependent porosity into the solution of the capillary imbibition in Eq.(3.27).

3.3.4.2 Total Dynamic Absolute Permeability (k_t)

Given $X \times Y \times Z$ number of plane fractures oriented parallel with $yz \times xz \times xy$ planes, respectively, for the cube shown in Fig. 3.4, the block contains $(X - 1) \times (Y - 1) \times (Z - 1)$ matrix blocks. The total dynamic permeability in δ direction ($\delta = x, y, z$) can be computed using a combination of weighted (arithmetic) and harmonic averaging for parallel and series layers, respectively, as follows:

$$k_{\delta t} = \frac{\sum_{i=1}^n [A_i \left(\frac{\sum_{j=1}^m l_j}{\sum_{j=1}^m \frac{l_j}{k_{\delta j}}} \right)]}{\sum_{i=1}^n A_i}. \quad (3.52)$$

In Eq.(3.52), A_i and l_j refer to the media (fracture or matrix) area and length, respectively. Additionally, n represents the number of media in a plane normal to the flow direction (for k_{z_t} case the plane would be yz plane) and m represents the number of planes (fracture and matrix) that the flow intersects in any direction. For instance, in the z direction n contains $(X+Y)$ number of fractures and $(X-1)(Y-1)$ number of matrix blocks. Extending Eq.(3.52), the cube's total dynamic absolute permeability in x, y and z directions is defined as follows:

$$k_{z_t} = \frac{\left(\frac{k_{ft}k_{mt}(L - X(J_o + \Delta J))(L - Y(J_o + \Delta J))}{k_{ft}(L - Z(J_o + \Delta J)) + k_{mt}Z(J_o + \Delta J)} \right) + (X + Y)k_{ft}(J_o + \Delta J)}{L}; \quad (3.53)$$

$$k_{y_t} = \frac{\left(\frac{k_{ft}k_{mt}(L - X(J_o + \Delta J))(L - Z(J_o + \Delta J))}{k_{ft}(L - Y(J_o + \Delta J)) + k_{mt}Y(J_o + \Delta J)} \right) + (X + Z)k_{ft}(J_o + \Delta J)}{L}; \text{ and} \quad (3.54)$$

$$k_{x_t} = \frac{\left(\frac{k_{ft}k_{mt}(L - Z(J_o + \Delta J))(L - Y(J_o + \Delta J))}{k_{ft}(L - X(J_o + \Delta J)) + k_{mt}X(J_o + \Delta J)} \right) + (Z + Y)k_{ft}(J_o + \Delta J)}{L}. \quad (3.55)$$

k_{mt} and k_{ft} in Eqs.(3.53)-(3.55) refer to the dynamic absolute permeability of the matrix and fracture, respectively. The dynamic absolute permeability of the matrix, k_{mt} , and the dynamic absolute permeability of the fracture, k_{ft} , are defined by Eqs.(3.38) and (3.48), respectively. The averaged dynamic absolute permeability computed from Eqs.(3.53)-(3.55) is assigned to the whole block of rock and inserted as a stress-dependent parameter into the solution of capillary imbibition in Eq.(3.27).

3.3.4.3 Total Geo-Dynamic Capillary Pressure ($P_c(t)$)

Capillary pressure refers to the pressure difference which exists at the interface of two immiscible fluids (Ahmed and McKinney, 2011). In general, the capillary pressure curve versus saturation for a porous medium is a function of the (1) pore size, (2) pore size distribution, (3) pore structure, (4) fluid saturation, (5) fluid saturation history, (6) wettability of the rock and (7) interfacial tension of the fluids involved (Peters, 2012).

Capillary pressure is the most effective flow-dynamic and geo-dynamic parameter in this research for capillary-driven spontaneous imbibition. We describe it as *flow-dynamic* because it

changes with saturation and *geo-dynamic* because it is a function of stress-dependent pore size. However, it is often necessary to convert the capillary pressure data for cores in the lab to the reservoir condition. This conversion can be done using the Leverett J-function, which is a dimensionless capillary pressure function (Leverett, 1941).

$$J(S_w) = \frac{P_c}{\sigma \cos\theta} \sqrt{\frac{k}{\phi}} \quad (3.56)$$

Eq.(3.56) suggests that at the same saturation, rocks with the same fabric, Γ , but different static properties (e.g. porosity and permeability) will have a similar Leverett J-function. In this study, we assume that rock fabric does not change with stress, but that voids (porosity) will vary with stress. This allows the Leverett J-function to be used for cases before and after applying effective stress:

$$\frac{P_c(t)}{\sigma \cos\theta} \sqrt{\frac{k_t}{\phi_t}} = \frac{P_c}{\sigma \cos\theta} \sqrt{\frac{k_i}{\phi_i}}, \text{ or} \quad (3.57)$$

$$P_c(t) = P_c \sqrt{\frac{k_i}{k_t}} \sqrt{\frac{\phi_t}{\phi_i}} \quad (3.58)$$

Consequently, having previously determined the dynamic total porosity (Eq.(3.51)) and permeability (Eqs.(3.53)-(3.55)), Eq.(3.58) yields the geo-dynamic capillary pressure for the whole block in the solution for capillary diffusion given in Eq.(3.27).

3.3.4.4 Total Geo-Dynamic Relative Permeability (k_{rt})

Relative permeability curves are flow-dynamic properties of rock and fluid. As summarized previously, several researchers provided different correlations to model the so-called flow-dynamic relative permeability curves based on wetting phase saturation. However, relative permeability curves are stress-dependent and hence are identified as geo-dynamic parameters as well.

While Khan (2009), Hamoud et al. (2012) and Ojagbohunmi et al. (2012) have presented empirical functions relating porosity change fraction and relative permeability end-points for Canadian oil sands, similar relationships are required for carbonates. As discussed previously, two lab experimental programs on naturally fractured carbonate undertaken by McDonald et al. (1991) and Lian et al. (2012) provided opposite results in terms of the changes to irreducible

water saturation with compaction. Both experimental programs showed that wettability, in addition to pore size, must be considered to explain stress-dependent relative permeability end-points. This suggests that the water-wet rock for the experiment of McDonald et al. (1991) does not behave in the same manner as the mixed-wet rock used in the Lian et al. (2012) experiment. Given the more common condition of mixed wettability for NFCRs, the results from Lian et al. (2012) are used in this study.

Since capillary pressure allows us to capture the pore size and wettability effect, as well as to identify phase trapping and the end-points of relative permeability, we have modified the linear empirical functions developed by Khan (2009), Hamoud et al. (2012), and Ojagbohunmi et al. (2012) to derive the following equations to describe the relationship between the end-points of geo-dynamic relative permeability and geo-dynamic capillary pressure:

$$S_{wir}(t) = S_{wir} \left(-12.15 + 13.15 \left(\frac{P_c(t)}{P_c} \right) \right); \quad (3.59)$$

$$S_{nwr}(t) = S_{nwr} \left(-2.75 + 3.75 \left(\frac{P_c(t)}{P_c} \right) \right); \quad (3.60)$$

$$K_{rw-max}(t) = K_{rw-max} \left(38.52 - 37.52 \left(\frac{P_c}{P_c(t)} \right) \right); \text{ and} \quad (3.61)$$

$$K_{rnw-max}(t) = K_{rnw-max} \left(1.001 - 0.001 \left(\frac{P_c}{P_c(t)} \right) \right). \quad (3.62)$$

All of the constants in Eqs.(3.59)-(3.62) have been estimated using the least square technique, based on the data on stress-dependent relative permeability at 10 MPa and 30 MPa effective stress reported in Lian et al.'s (2012) experiment. Eq.(3.62) indicated negligible stress-sensitivity of $K_{rnw-max}(t)$; this is due to the dominant flow of the non-wetting phase at S_{wir} during imbibition relative permeability test in Lian et al.'s (2012) experiment and wetting phase is immobile ($k_{nw} = k$, hence $K_{rnw-max}(t) = 1$). Same end-points' saturation are applied for geo-dynamic capillary pressure curves. For validation, we compute the end-points of relative permeability curves for the case of effective confining stress of 20 MPa using Eqs.(3.59)-(3.62), derive appropriate k_r equations (similar with Table 3.1), and then compare k_r curves with experimental data (circle symbols in Fig. 3.8). As illustrated in Fig. 3.8, Eqs.(3.59)-(3.62) provide an excellent match with the experimental results for 20 MPa effective confining stress.

All of the equations required for the stress-dependent counter-current spontaneous imbibition semi-analytical method have now been described. Fig. 3.9 provides a flow chart summarizing the analysis workflow, which has been coded in MS Excel.

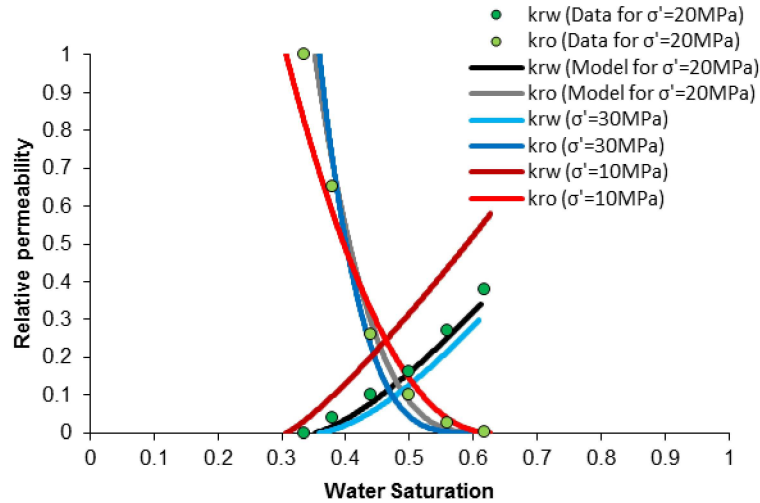


Fig. 3.8 Investigation of the accuracy of Eqs.(3.59)-(3.62) for relative permeability curves in the case of 20 MPa effective confining stress

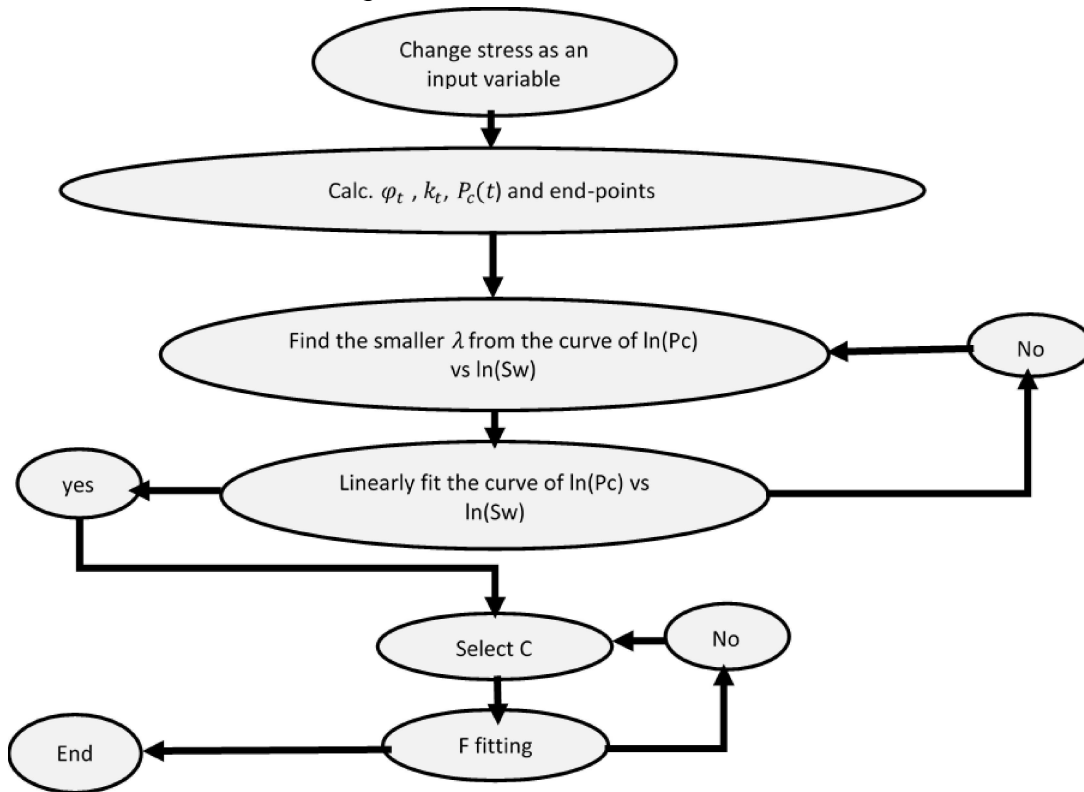


Fig. 3.9 Work flow of the semi-analytical solution for stress-dependent capillary imbibition

3.4 Results

In this section, we utilize the semi-analytical model to investigate the geomechanical impacts on spontaneous imbibition and oil recovery in a cubic block of fractured carbonate rock with three orthogonal fractures parallel with the block sides. Capillary pressure table for the case of mixed-wet fractured carbonate (Lian et al., 2012) is used as input in the model. Additional rock and fluid properties based on a real carbonate reservoir case are summarized in Table 3.4 (chapter 2). In the simulations, the effective confining stress is considered an input variable at the beginning of the procedure (Fig. 3.9). The stress-dependent porosity, absolute permeability, capillary pressure and end-points of the relative permeability curve are calculated based on Eqs.(3.51), (3.52), (3.58), and (3.59)-(3.62), respectively, and illustrated in Fig. 3.10. Note that great upward shift in the geo-dynamic P_c curves (Fig. 3.10a) is a mixed result of a small decrease in the total porosity (Fig. 3.10b) and great drop in the fracture absolute permeability (Fig. 3.10c) with stress based on Eq.(3.58), and the curvature of the plots. We use modified Brooks and Corey (1966) type curves to numerically fit the experimental imbibition capillary pressure data and define the curvature of geo-dynamic capillary pressure curves (Eq.(3.1)). The process of finding the pore size distribution index ($\lambda = -1/\beta$) requires the creation of a log-log plot of S_w^* (Eq.(3.4)) versus P_c , as shown in the workflow in Fig. 3.9. Based on the Brooks-Corey (1966) model, i.e. Eq.(3.63), the graph must be linear. If the graph is nonlinear, λ is adjusted iteratively until the graph becomes linear (Fig. 3.11).

$$\ln S_w^* = -\lambda \ln P_c + \lambda \ln P_e \quad (3.63)$$

Table 3.4 Parameter set for semi-analytical model

Parameter	Units	Value	Parameter	Units	Value
L	m	0.1	k_{fi}	m^2	9.1E-11
k_{mi}	m^2	3.0E-16	ϑ	-	0.3
φ_{mi}	-	0.3	E	MPa	20000
k_{nn}	MPa/m	20014	α	-	0.7
V_o	m	0.000033	μ_w	Pa.s	0.001
φ_{fi}	-	0.00033	μ_o	Pa.s	0.003

As Fig. 3.10a) clearly shows, the difference between the imbibition capillary pressure curves in the effective confining stress range of 20 MPa to 30 MPa is much less than the difference in the range between 10 MPa and 20 MPa. This is due to the effect of non-linear fracture closure at high stresses. Note that Fig. 3.10a) presents only spontaneous imbibition part ($P_c \geq 0$) of the P_c curves and the forced imbibition part with $P_c < 0$ for mixed-wet rocks is not

provided. Great initial drop in the total absolute permeability in Fig. 3.10c) is due to the great initial fracture closure in Eq.(3.52).

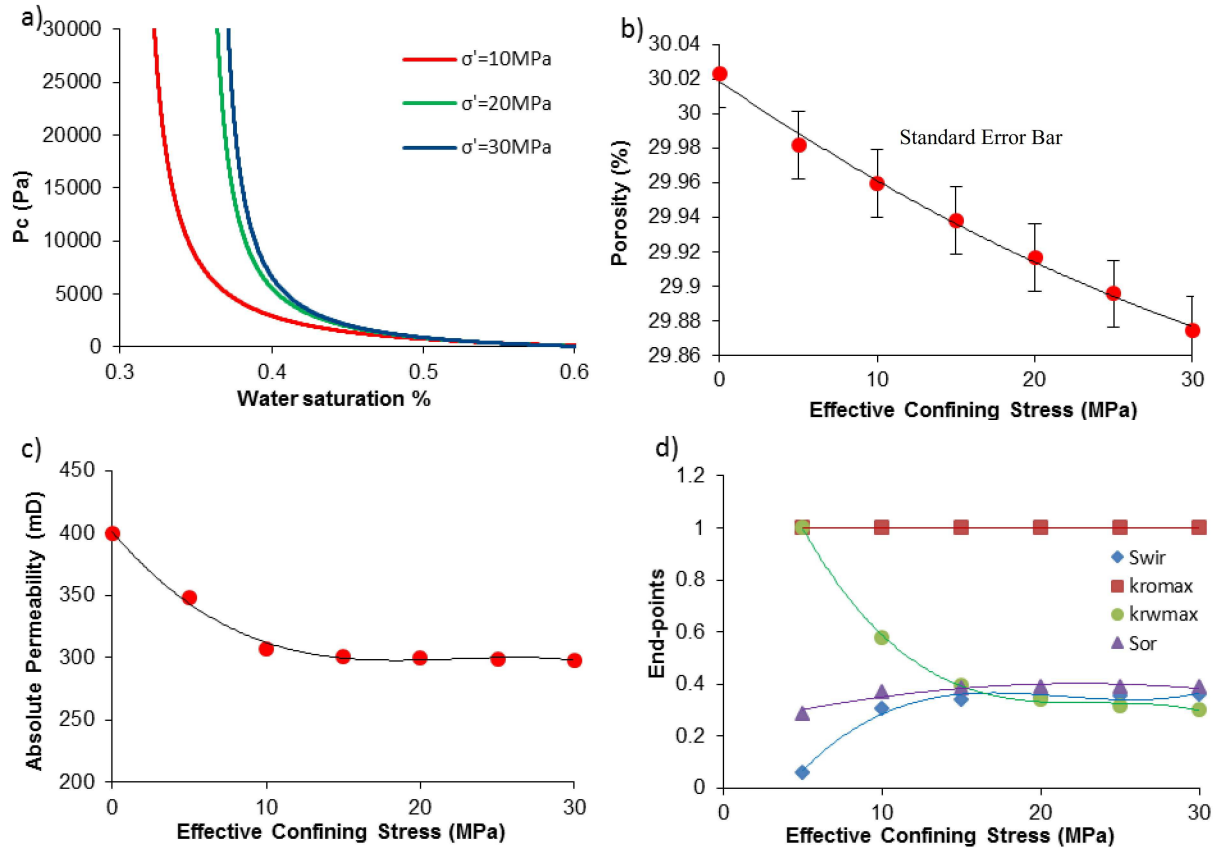


Fig. 3.10 Variation in stress-dependent spontaneous imbibition parameters a) imbibition $P_c(t)$, b) φ_t c) k_t , and d) Imbibition $k_{r,t}$ end-points

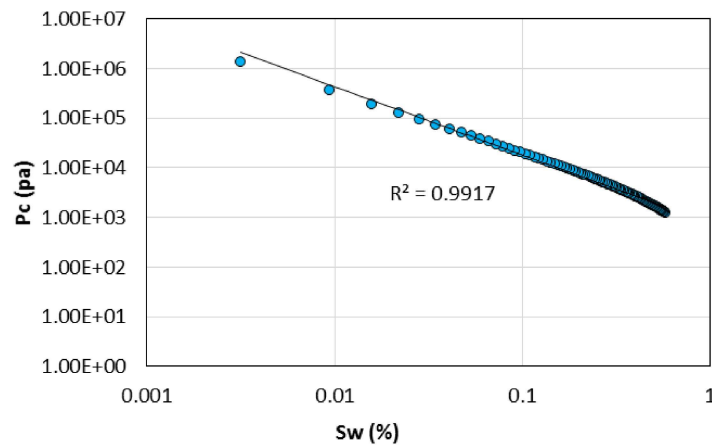


Fig. 3.11 Capillary pressure versus wetting phase saturation and the fitted line representing the linearity of data in a Log-Log scale

The fitting constants in Eqs.(3.6)-(3.7) are estimated next using the least square method as $A = -1.5$, $A' = -8.5$, $B = 2.955$, and $B' = 12.045$. Using the semi-analytical framework described above, all of the stress-dependent properties are inserted into Eq.(3.27), which allows the geo-dynamic capillary-driven fractional flow (F) to be determined. As mentioned previously, C' in Eq.(3.20) is no longer a constant but a stress-dependent parameter. Thus, at each stress state, it should be recalculated iteratively to fit the F function into the limits of 0 to 1 for S_{wir} to $(1-S_{or})$, respectively. Fig. 3.12 compares the geo-dynamic Buckley-Leverett and capillary-driven fractional flow curves. Both methods present distinct curves for 10, 20, and 30 MPa effective confining stress; these shift from left to right from the 10 MPa curve to the the 30 MPa curve.

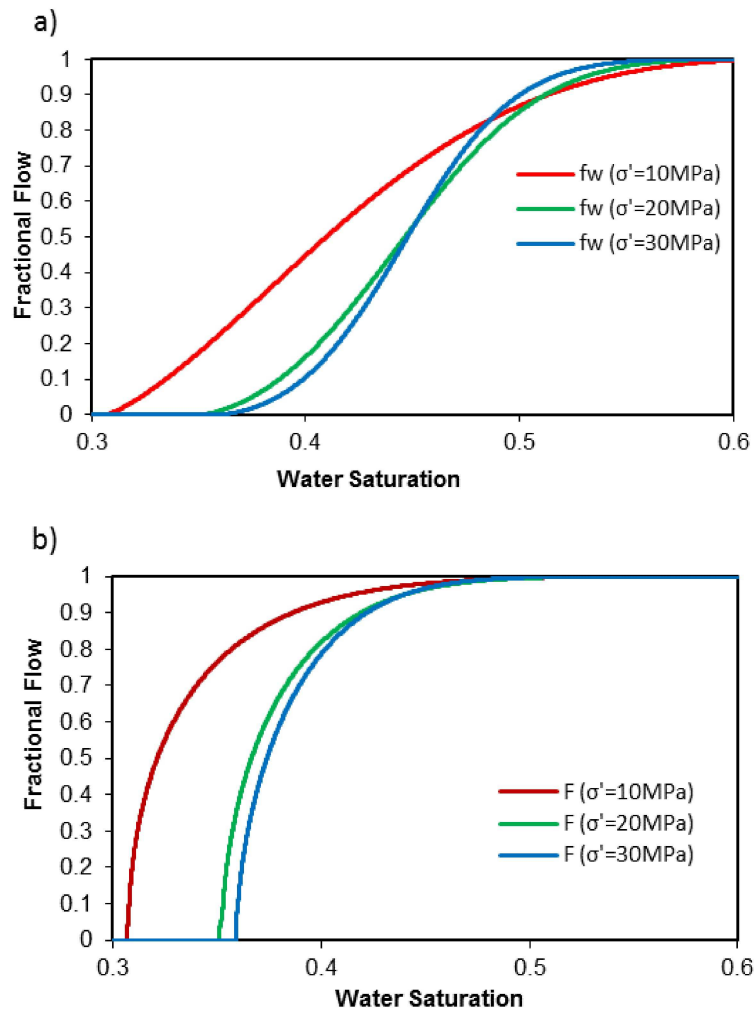


Fig. 3.12 Comparison between the a) geo-dynamic Buckley-Leverett and b) capillary-driven fractional flow in NFCRs

As illustrated in Fig. 3.13, for the given carbonate block dimensions and properties in Table 3.4, increasing the effective stress from 10 MPa to 30 MPa, the model developed in this study predicts that the recovery factor of the block will decrease by approximately 50% after 20 hr. First integration of Eq.(3.19) is used to calculate cumulative counter-current imbibition of water into the block of rock ($Q_w(t) = 2C'\sqrt{t}$) and determine the oil recovery in Fig. 3.13. This highlights the significant impact geomechanical processes may have on oil recovery in NFCRs.

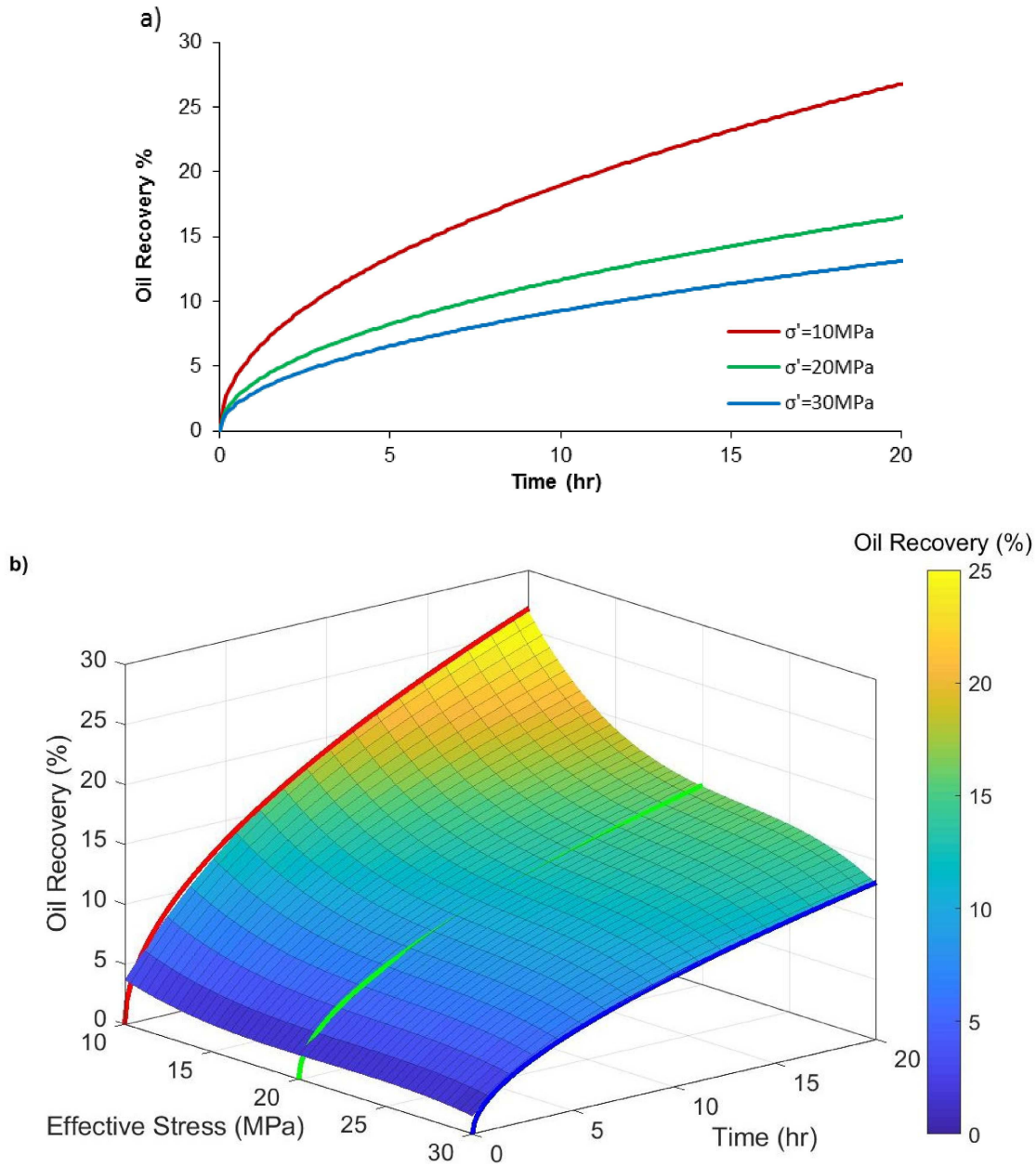


Fig. 3.13 Oil recovery profile for NFCRs as a function of changes to effective confining stress in 2D and 3D scales

Finally, the saturation curve versus similarity variable ω , shown in Fig. 3.14, also illustrates the stress dependency of ω in spontaneous imbibition. As noted in Fig. 3.14, $\omega(S_w = S_{wir})$ increases as the effective confining stress decreases from 30 MPa to 10 MPa. Using Eq.(3.25), early time imbibition (t^*) is computed equal to 0.86, 4.64, and 11.69 hours for the cases of 10 MPa, 20 MPa, and 30 MPa effective confining stress, respectively. The reduced imbibition times at lower effective confining stresses are primarily the result of higher transmissibility in the less deformed rock. Fig. 3.14 also indicates a better sweep efficiency at 30 MPa effective stress condition compared with the case of 10 MPa effective stress. This leads to an increasing rate of late-time recovery for the case of 30MPa stress in Fig. 3.13.

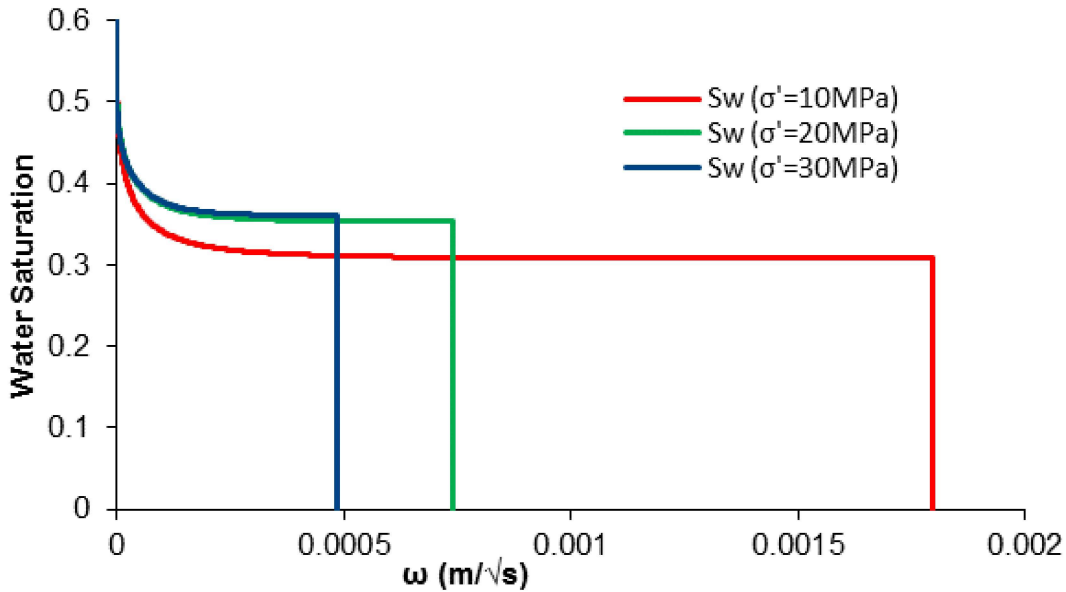


Fig. 3.14 Saturation profiles for 10, 20 and 30 MPa effective confining stress

3.5 Discussion

Water-wet NFCRs are among the best examples of spontaneous capillary imbibition in nature (Peters, 2012). Many authors have assumed that fractures have small or negligible capillary pressure (Peters, 2012; Elfeel et al., 2016). At equilibrium condition, the capillary pressures in the fracture and matrix must be equal at their boundary (Eq.(3.64)).

$$P_{cf} = P_{cm} \quad (3.64)$$

When the 100% saturated fractures make contact with the oil saturated matrix blocks, the capillary equilibrium is disturbed. Hence, fluid exchanges between the fracture and matrix block occur to recover the capillary equilibrium condition. Water and oil are exchanged between two media until the water saturation in the matrix is increased to the maximum possible value over time ($S_w = 1 - S_{or}$).

Injection and production operations change the pore pressure within the pore spaces. Based on poroelasticity theory (Detournay and Cheng, 1993), effective stress change leads to pore size changes (bigger or smaller depending on the process). It is well known that capillary pressure is a function of the pore size of the porous media. Accordingly, effective stress should directly affect capillary diffusion in the reservoir. Furthermore, some experimental results on NFCRs have proven the stress-dependency of the end-points and wettability of the relative permeability curves. This is again a result of changing the pore size due to stress. Experiments have shown that the irreducible water saturation increased significantly as confining stress increased in the case of mixed-wet carbonate rock. Accordingly, when applying higher effective stress, the rock tends to be stronger water-wet. However, in cases where higher effective stress was applied to strong water-wet rock, the irreducible water saturation decreased.

These findings will be developed and further validated in our next chapters. Both our consecutive experimental program and our advanced coupled flow-geomechanical approach will be used to apply the concept of geo-dynamic spontaneous imbibition in naturally fractured carbonates within models ranging from the block-scale to the reservoir-scale.

3.5.1 Comparison between Stress-Dependent and Independent Spontaneous Imbibition

In the current semi-analytical model of geo-dynamic spontaneous imbibition, the derived equations for porosity, absolute permeability, capillary pressure, and relative permeability are all based on effective stress. Thus, the effective stress is the input of the solution (see the workflow presented in Fig. 3.9). Generally, spontaneous imbibition by itself does not change effective stress; it only controls saturation distribution and fluid exchanges. To obtain a model of effective stress change over time, we need a reservoir model that includes injecting and producing wells in which the pore pressure changes with time. In that case, spontaneous imbibition is not the only production mechanism, as viscous forces, which change pore pressure, are also involved in

production. Hence, the semi-analytical workflow given in Fig. 3.9 is part of a larger code that calculates effective stress as a function of time.

This study focuses only on modelling the capillary imbibition from fracture to a block of rock in different stress conditions. However, to compare the spontaneous imbibition oil recovery predicted by a semi-analytical geo-dynamic solution (scenario 1, given in section 3.3) with that predicted by a stress-independent solution (scenario 2), we assume that, uniformly over a 50-hour period, the whole block (matrix and fracture) undergoes polynomial build-up in effective stress from 10 MPa to 30MPa in scenario 1 and no effective stress control in scenario 2 (see horizontal projection in Fig. 3.17). The scenario 1 solution given in section 3.3 can easily be converted to that of scenario 2 by positing that $A=0$ in Eq.(3.27) and implementing stress-independent porosity, absolute permeability, capillary pressure, and relative permeability curves. Fig. 3.15 compares changes in porosity and absolute permeability of the block over time between scenario 1 and scenario 2. Additionally, Fig. 3.16 illustrates the geo-dynamic relative permeability and capillary pressure curves for the block in which the colors indicate time lapse.

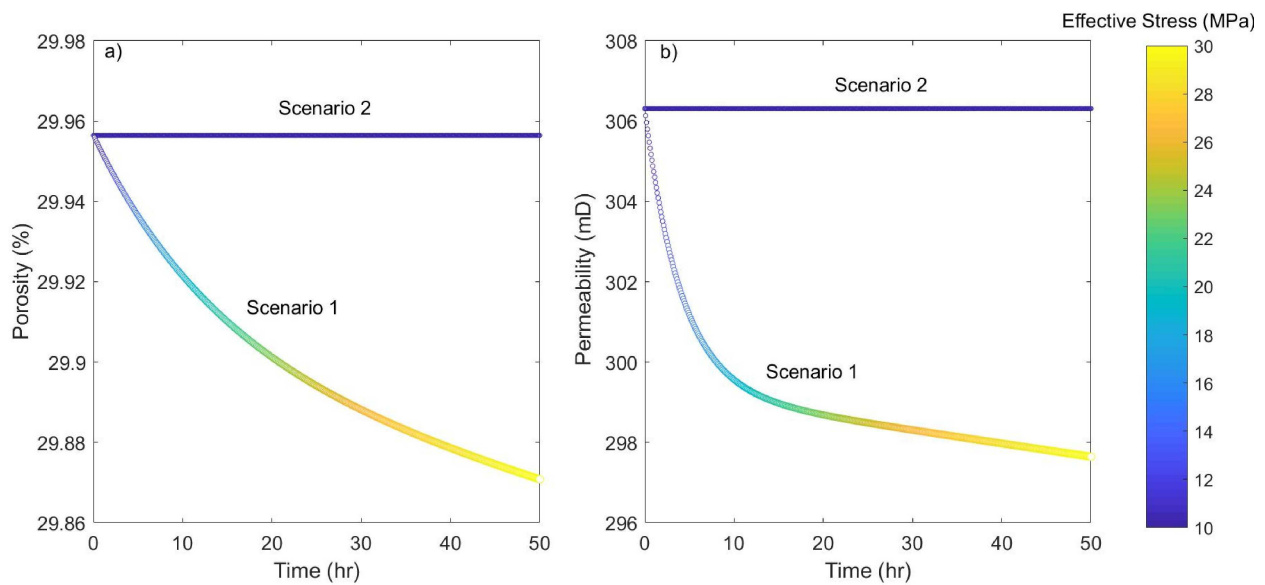


Fig. 3.15 Comparison of a) porosity and b) permeability changes with time and stress to a block of rock. Scenario 1: Geo-dynamic spontaneous imbibition. Scenario 2: stress-independent spontaneous imbibition.

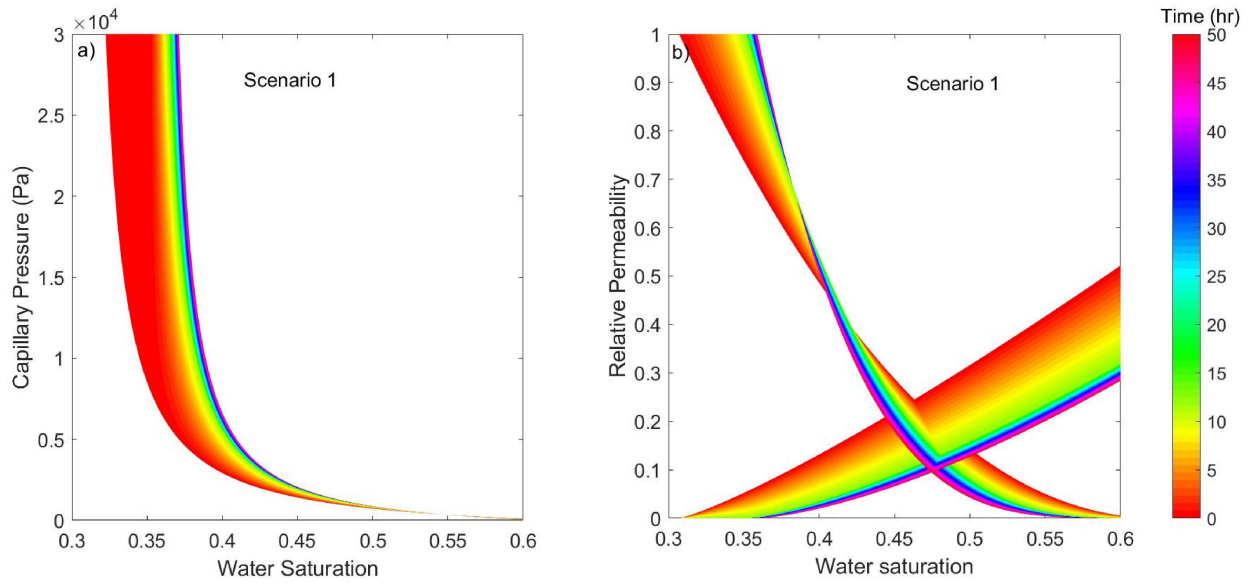


Fig. 3.16 Changes in a) relative permeability and b) capillary pressure curves over time in scenario 1 (geo-dynamic spontaneous imbibition)

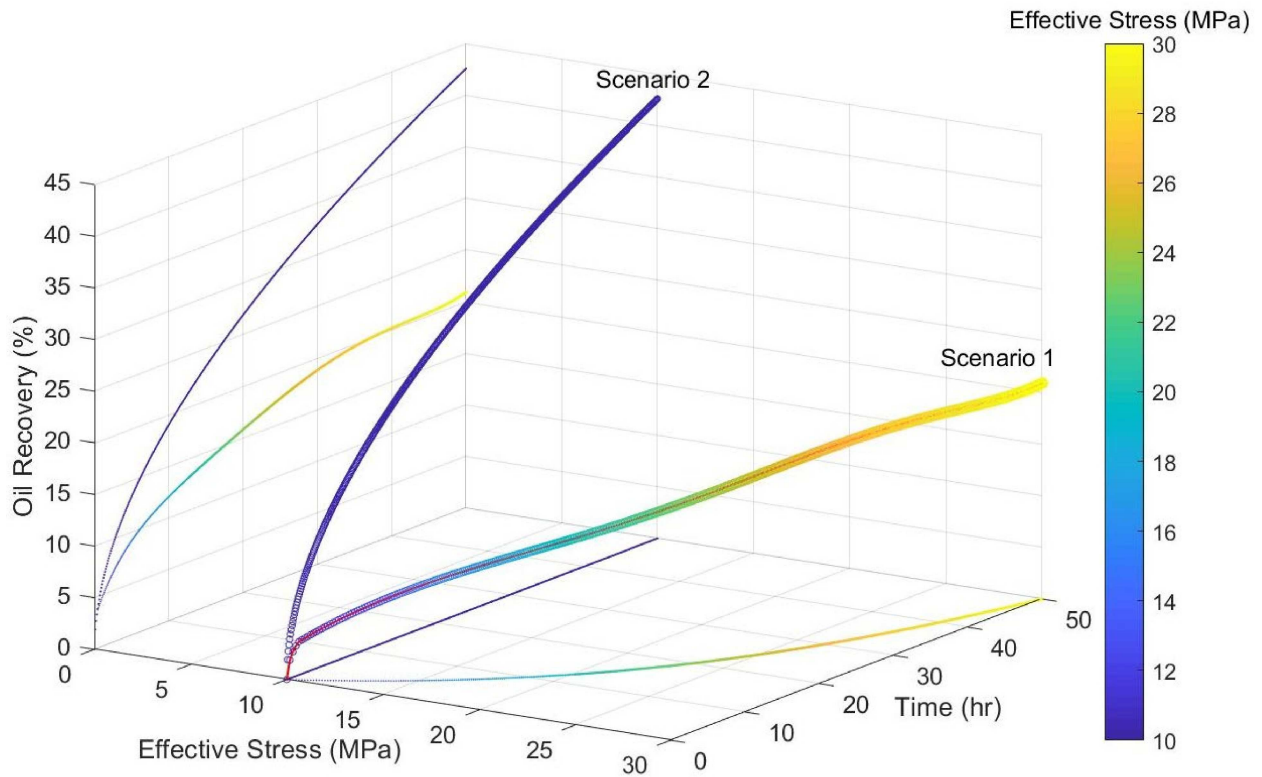


Fig. 3.17 Comparison of oil recovery from a block of rock between geo-dynamic spontaneous imbibition (Scenario 1) and stress-independent spontaneous imbibition (Scenario 2)

Note that in this analysis, both cases start from the same initial condition. However, as Fig. 3.17 reveals, their oil recovery lines increase in different ways. In Fig. 3.17, the colors indicate the effective stress value; comparing the oil recovery from both scenarios (illustrated in the vertical projection), it is evident that the negligible difference present at early times turns into a significant drop in spontaneous imbibition oil recovery at later times. This is due to the impact of rock and fracture deformation in response to increase in effective stress. In the case of scenario 1, the oil recovery initially increases sharply, but by the time, its rate of increase attenuates. Additionally, Fig. 3.17 illustrates the 3D nature of oil recovery curve in reservoir management.

3.6 Conclusions

The current study presents comprehensive insights into stress-dependent spontaneous imbibition in NFCRs by defining capillary-driven fractional flow and geo-dynamic rock properties. We presented a semi-analytical solution for geo-dynamic capillary-driven fractional flow equation in NFCRs. To do so, we derived analytical equations to specify the unknown stress-dependent parameters in our semi-analytical solution. We characterized the geo-dynamic behavior of intact rock and fracture independently based on poroelastic and nonlinear fracture stiffness equations and combined them with equivalent continuum concepts. The results from the semi-analytical solution for the case of mixed-wet NFCRs reveals a 50 percent reduction in the oil recovery factor as effective confining stress increases from 10 MPa up to 30 MPa. This proves the significant impact of effective stress on spontaneous imbibition in NFCRs.

4. Numerical Simulation of Stress-Dependent Spontaneous Imbibition in Fractured Porous media*

Abstract

Spontaneous Imbibition is an important flow mechanism in naturally fractured reservoirs. Conventional simulation techniques generally ignore the significant geomechanical impacts on intrinsic, e.g. porosity and permeability, and multiphase flow, e.g. relative permeability and capillary pressure, properties of rock. Due to the presence of fracture, the role of geomechanics is even more crucial in NFCR. In this chapter, the impact of stress-dependent porosity, absolute permeability, relative permeability, and capillary pressure on spontaneous imbibition mechanism and oil recovery is investigated at three fixed effective stress condition (10, 20 and 30MPa) using single-porosity simulation method in a fine-grid cubic block model of rock with three orthogonal fractures. Then a coupled geomechanical and dual-permeability flow simulation code is employed to quantify the effects of pore and fracture deformation on the media's fluid flow properties and cumulative production in a fine-grid five-spot (4 injecting wells and one production well) reservoir-scale model. The code is designed to sequentially update coupled flow-geomechanical model using stress-dependent multiphase flow property (e.g. relative permeability and capillary pressure curves) of each medium. The simulation results represent a significant drop in cumulative oil production as a result of geomechanical effects. Due to geomechanical controls on both single-phase and multiphase flow properties of each medium, conventional simulation approaches for NFCR are needed to be promoted to a more reasonable scheme capturing advanced physics of flow in deformable porous media.

* Some parts of this chapter related to the reservoir-scale modeling were presented at: Haghi, A.H., Chalaturnyk, R., Geiger, S., Abbasi, Y. (2018). Coupled Simulation of Stress-Dependent Spontaneous Imbibition in Dual-Perm Models. Third EAGE Workshop on Naturally Fractured Reservoirs, Muscat, Oman

4.1 Introduction

The geomechanical behavior of dual continuum rocks (fracture and matrix) has become increasingly important to hydrocarbon operations (Settari et al., 1999). As reservoirs experience depletion or changes in recovery mechanism, pore pressures and in-situ stresses are affected correspondingly. The induced volumetric response depends on the rock geomechanical properties and the pore pressure/stress coupling effect. As the reservoir responds to the pore pressure/stress coupling effect, the bulk volume will adjust based on the poroelasticity theory (Geertsma, 1957). Zimmerman et al. (1986) studied the effect of effective stress variation on the volume of void space contained in the rock. They had experimentally/theoretically demonstrated the dependency of the pore size and pore compressibility on the effective stress variation. Changing the pore size and geometry leads to the variation of the stress-dependent parameters like porosity, absolute permeability, effective permeability, capillary pressure, transmissibility, and phase saturations (Li & Chalaturnyk, 2004). Fractures are generally more sensitive to effective stress changes than intact rocks, which results in strongly stress-dependent fluid flow in fractures.

In the previous chapter, the significant effect of geomechanics on spontaneous imbibition was investigated semi-analytically for a block of fractured carbonate. Otherwise, flow diffusivity equation for counter-current spontaneous imbibition was solved semi-analytically considering effective confining stress effect on single-phase and multiphase rock flow properties. To validate the results of semi-analytical approach, in this chapter, the same block of rock with three orthogonal fractures is initially modeled numerically using CMG (Computer Modelling Group) reservoir simulator and implementing same stress-dependent rock properties.

Then, coupled geomechanical and dual permeability flow simulation technique is used to study the stress-dependent multiphase fluid flow and cumulative oil production in a naturally fractured carbonate reservoir-scale model. Pure compliance poroelastic model (Detournay and Cheng, 1993) and Carman-Kozeny correlation (Carman, 1956) are used to specify the intact rock's stress-dependent intrinsic properties (e.g. porosity and absolute permeability). In terms of fracture's stress-dependent intrinsic properties, non-linear joint normal stiffness equations are used (Barton et al. 1985). Knowing porosity and absolute permeability changes, the stress-dependent capillary pressure is calculated using Leverett J-function (Leverett, 1941). Similarly,

stress-dependent relative permeability end-points are calibrated with capillary pressure variation. Here, the tables of all single-phase and multiphase rock flow properties from previous chapter are inserted into the simulation code as a function of effective stress. Stress-dependent multiphase flow property (e.g. relative permeability and capillary pressure curves) of each medium is sequentially updated into the coupled flow-geomechanical model.

4.2 Block-Scale Modeling:

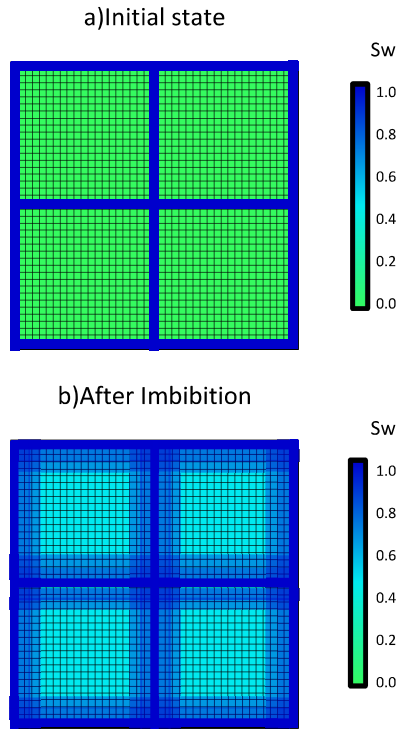
A fine-grid cubic simulation model comprising $41 \times 41 \times 41$ cells was constructed (each cell is $1 \times 1 \times 1$ m). The block consists of 8 ($2 \times 2 \times 2$) matrix blocks of $19 \times 19 \times 19$ cells each (Table 4.1). This simulates the classical, sugar cube array of Warren and Root's (1963) original dual-porosity model (Elfeel et al., 2016; Fig. 4.1). However, in this section, we use single-porosity flow modeling technique in the simulating software. Accordingly, only one property is assigned to each grid block in the simulation model. In our single-porosity model, some blocks get matrix properties and some others representing fractures get fracture properties.

Table 4.1 Parameters used for numerical model as initial condition

σ' <i>MPa</i>	Cube Dimension <i>m</i>	number of cells	ϕ_{mt} %	ϕ_{ft} %	k_{mt} <i>mD</i>	k_{ft} <i>mD</i>
10	41	68921	0.300	2.0e-005	0.299	352.969
20	41	68921	0.299	1.1e-005	0.298	93.974
30	41	68921	0.298	7.0e-006	0.297	42.67

As illustrated in Fig. 4.1, an extra layer of single-cell dimensions (specified with blue color) was added on all sides of the matrix blocks to model the fractures. Generally, high permeable fractures in the NFCR limit the buildup of large differential pressures across the reservoirs (Ferno, 2012). Accordingly, limited viscous forces due to high fracture transmissibility weaken the effect of viscous displacement on oil recovery. Capillary imbibition in the absence of viscous displacement is the key recovery mechanism in the water-wet NFCR. To simulate the capillary imbibition process, all the fracture plains in our model was attached to an infinite steady-state aquifer boundary condition to provide a constant pressure source of water inside the fracture plains. The aquifer kept the fracture pressure constant equal to initial matrix block pressure in order to eliminate the viscose displacement (in Eq.(3.14), $(\lambda_w/\lambda_t)q_t = 0$) and fixed the whole block at constant effective confining stress. Furthermore, we considered equal density for all fluid phases (in Eq.(3.14), $\Delta\rho = 0$) to weaken the gravity drainage effect on oil recovery.

2D Cross-Sectional View



3D View

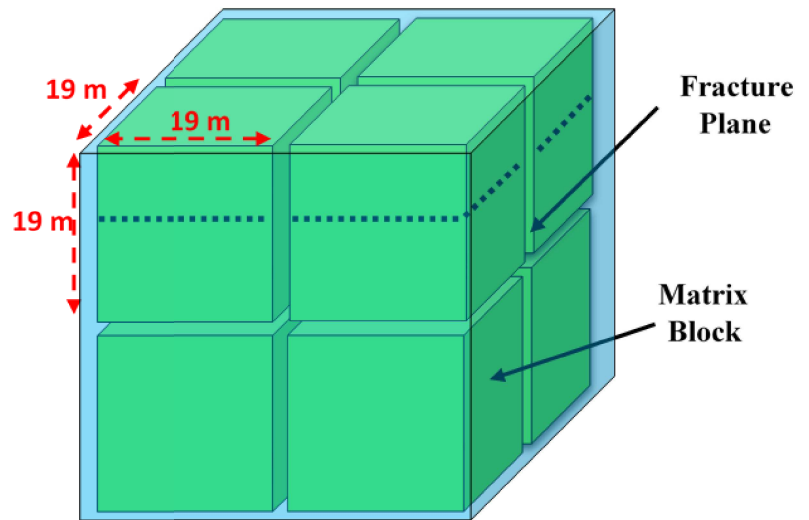


Fig. 4.1 3D Fine-grid model employed to simulate stress-dependent spontaneous imbibition in the NFCR (right). 2D cross-sectional model presenting the phase distribution (green=oil, blue=water) in the fractures and the matrix (top left) and the distribution of the phases after the water imbibe into the matrix from the fracture (bottom left)

To simulate spontaneous imbibition of water from the fracture into the matrix, the fractures are initially filled with water (Fig. 4.1a). Accordingly, all 8 matrix blocks in the model were surrounded by water. However, due to the capillary discontinuity between the fracture and matrix, water imbibe into the matrix blocks spontaneously and oil transfers into the fracture and produces from the fractures. Fig. 4.1b shows the spontaneous imbibition of water from the fracture into the matrix block. Accordingly, our single-porosity model simulates the behavior of Warren and Root's (1963) original dual-porosity model. All the stress-dependent rock properties from the previous semi-analytical model at each effective confining stress (10-30 MPa) are initially assigned to the discretized block. The imbibition time in all simulations is four years to allow water-fronts to advance deeply into the matrix blocks. This model aims to analyze the sensitivity of spontaneous imbibition and oil recovery with stress-dependent porosity, absolute

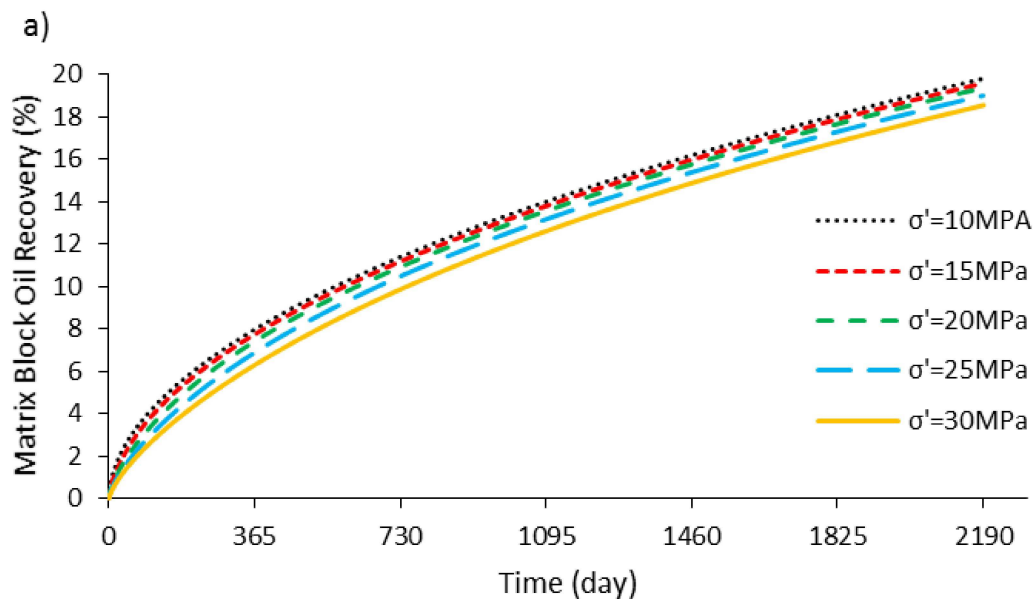
permeability, relative permeability, and capillary pressure, at the continuum scale where fractures and matrix are presented.

4.2.1 Results:

In this section, the results from the single-porosity numerical method are presented to study the sensitivity of spontaneous imbibition and oil recovery with stress-dependent porosity, absolute permeability, relative permeability, and capillary pressure.

4.2.1.1 Stress-Dependent Porosity and Absolute Permeability

Poroelastic and nonlinear fracture closure equations described for the semi-analytical model in chapter 3 are used to specify stress-dependent porosity for matrix block and fracture, respectively. The stress-dependent absolute permeability is calculated using Hagen-Poiseuille's law for both media. These data are implemented in GEM model to investigate numerically the stress-dependent spontaneous imbibition. The sensitivity of spontaneous imbibition and oil recovery from the matrix considering stress-dependent porosity and absolute permeability during production is shown in Fig. 4.2. Oil recovery drops by 6% when the effective confining stress increases from 10 MPa to 30 MPa. Similarly, water imbibition into the matrix from fracture continues to increase with decreasing the stress.



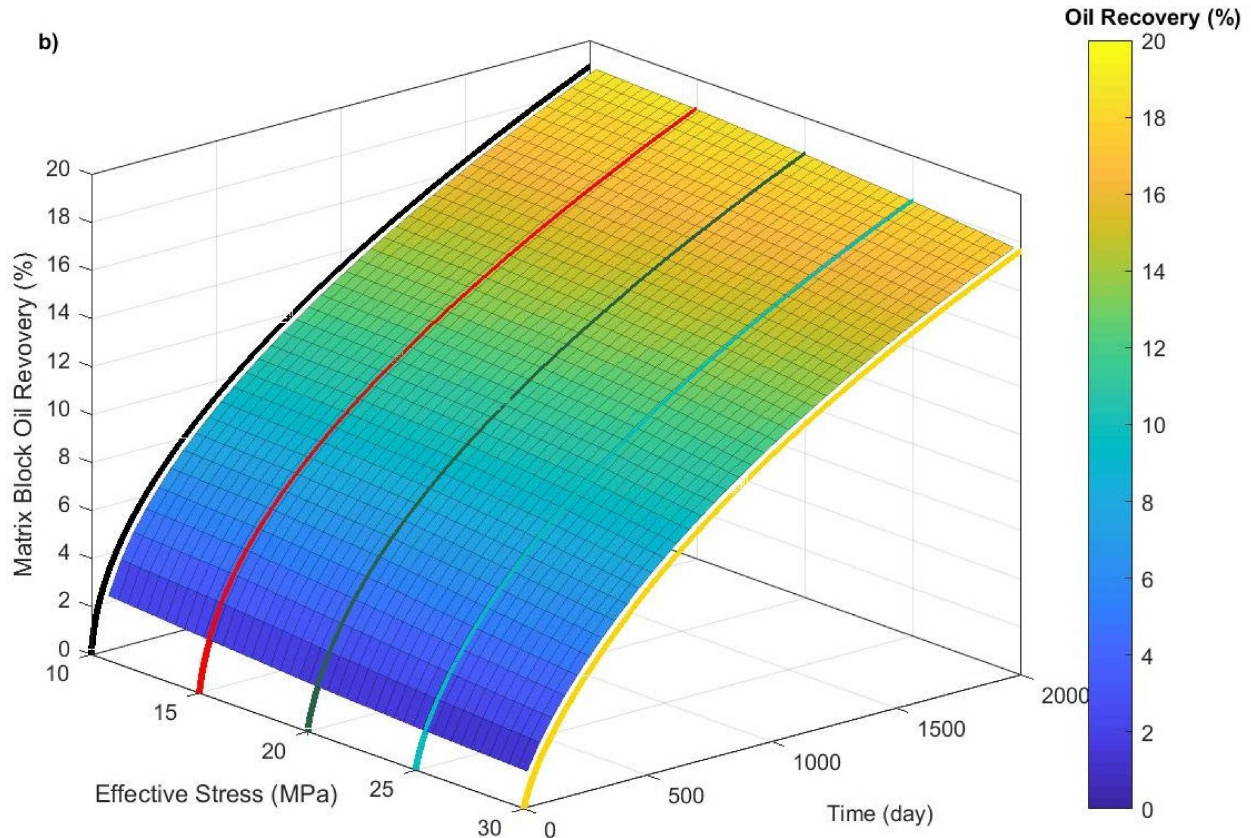


Fig. 4.2 Comparison of matrix block oil recovery for 10, 15, 20, 25 and 30 MPa effective confining stress considering only porosity and absolute permeability as stress-dependent parameters in (a) 2D plot and (b) 3D plot in the NFCRs

Fig. 4.2 proves the small impact of stress-dependent porosity and absolute permeability terms on oil recovery and spontaneous imbibition, independently. Stress-dependent porosity and permeability is the only option that current commercial reservoir simulation software offer for coupled geomechanical and dual-porosity flow simulation of the stiff NFCR.

4.2.1.2 Stress-Dependent Relative Permeability and Capillary Pressure Curves

Fig. 4.3 shows the resulting recovery profiles for the cases considering only relative permeability and capillary pressure curves as stress-dependent flow properties. As it is discussed in previous sections, the manifestation of fluid's wettability in relative permeability and capillary pressure curves varies when the medium changes its deformation state. Furthermore, the relative permeability and capillary pressure curves in deformed rocks depend on the fluids wettability at the initial state. The experimental results show a stress-dependent rightward shift in relative

permeability curves intersection for the case of mixed-wet naturally fractured carbonate (Fig. 3.2) and a leftward shift for the case of water-wet naturally fractured carbonates (Fig. 3.3).

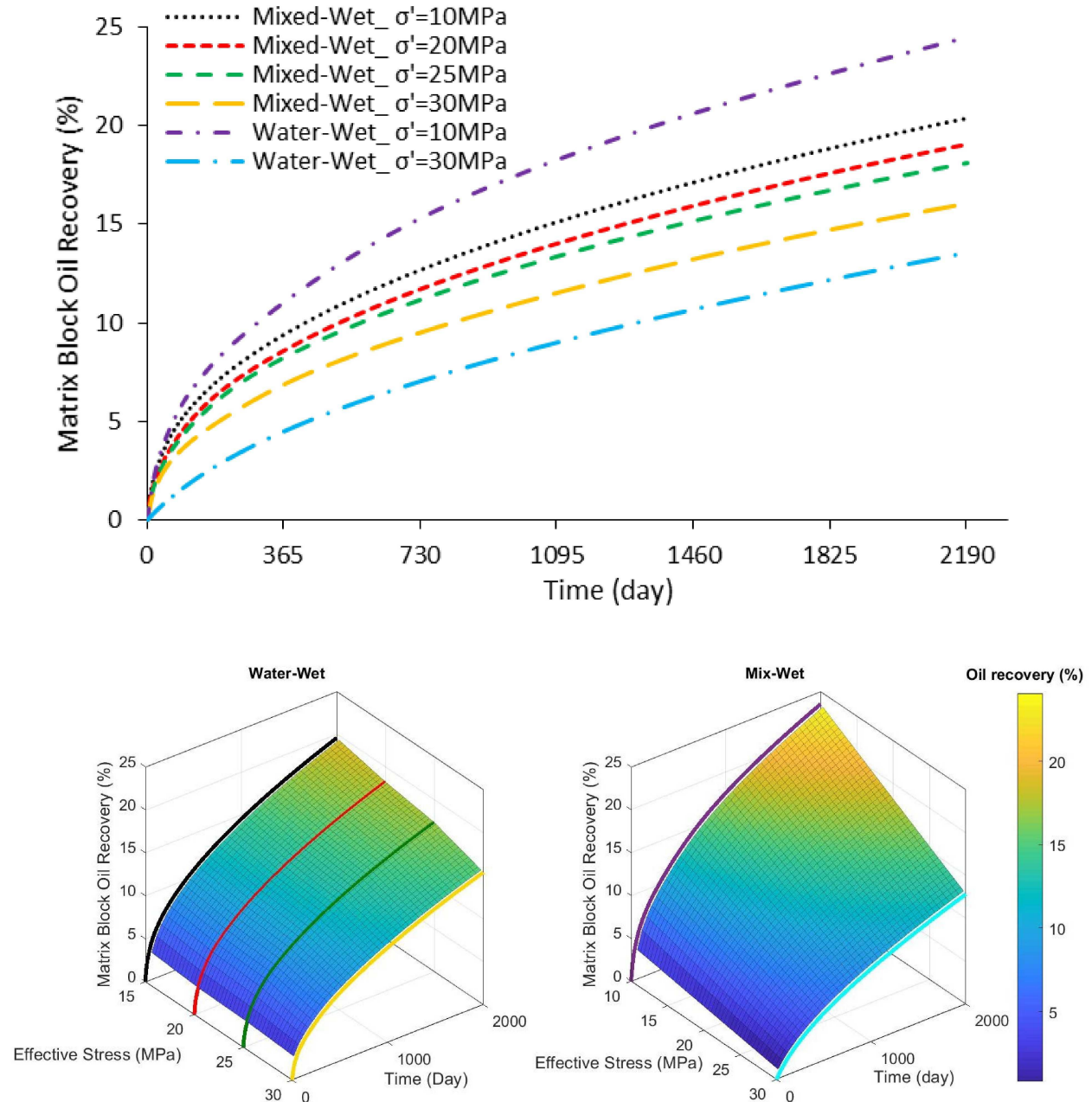
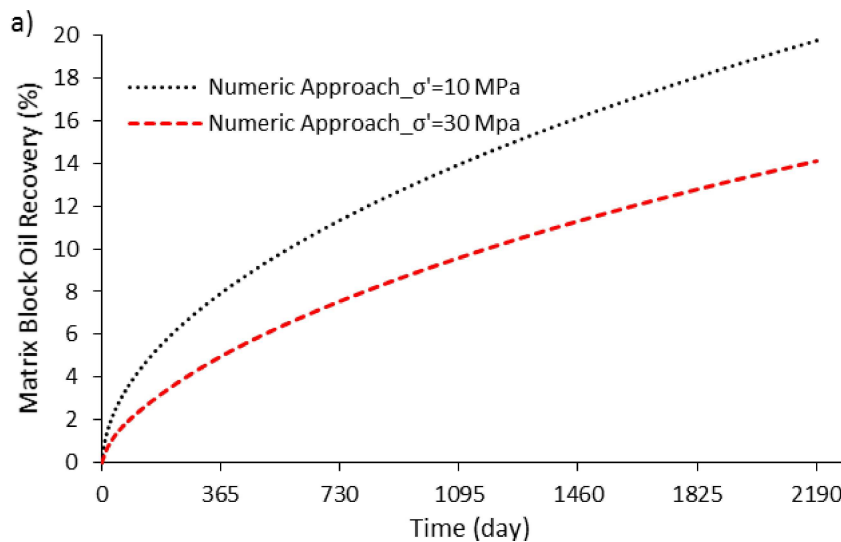


Fig. 4.3 Comparison of matrix block oil recovery for 10-30 MPa effective confining stress considering only relative permeability and capillary pressure as stress-dependent parameters in 2D plot (top), 3D plot for water-wet (bottom left), and 3D plot for mixed-wet (bottom right) in the NFCR.

Generally, for capillary-dominated recovery, there is a direct relationship between the water wettability and the recovery factor (Behbahani and Blunt, 2005; Haugen et al., 2008). This is because in water-wet rocks water-oil capillary is a positive driving force which helps the water imbibing into the smaller pores and extract the oil from them. Our simulation shows a 21% and 44% drop in oil recovery by incrementing the stress for 20 MPa for the cases of initially mixed-wet and water-wet fractured carbonate block, respectively. The reason for the higher sensitivity of oil recovery for the water-wet carbonate with stress could be investigated through the higher deformability of its pore spaces. A comparison between Fig. 3.2 and Fig. 3.3 demonstrates the higher sensitivity of water-wet carbonate's relative permeability curves with stress. This section proves the tremendous impact of stress-dependent parameters on imbibition and oil recovery of the NFCR.

4.2.1.3 Stress-Dependent Spontaneous Imbibition and Oil Recovery

Fig. 4.4 shows the recovery profile considering stress-dependent porosity, permeability, relative permeability, and capillary pressure for the case of the mixed-wet fractured carbonate block. This plot presents a drop of matrix block oil recovery for the case of 10MPa effective confining stress by increasing the stress for another 20 MPa which is almost 50% drop at the early time and it decreases to 30% at the late time. Otherwise, the oil recovery of the block of naturally fractured carbonate, which is under capillary-driven imbibition, is significantly affected by rock and fracture deformation.



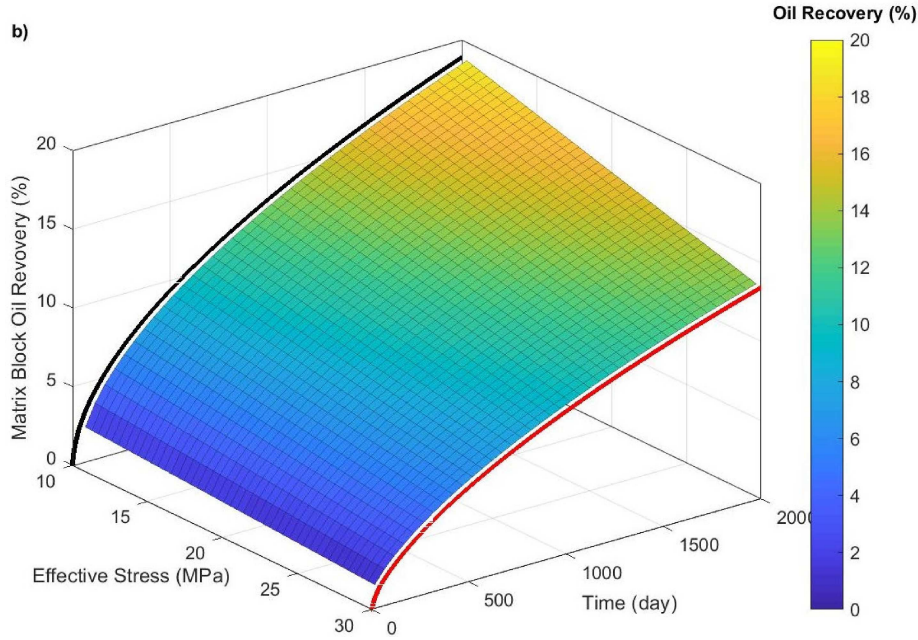


Fig. 4.4 Comparison of matrix block oil recovery for 10 and 30 MPa effective confining stress considering porosity, absolute permeability, relative permeability, and capillary pressure as stress-dependent parameters in a) 2D plot and b) 3D plot in the NFCR.

To investigate the impact of grid-size on the results, we repeat above simulation processes using a finer block-scale model, under similar stress-dependent properties, by decreasing the matrix block size by 40% (11*11*11m). As it is illustrated in Fig. 4.5, although ultimate oil recovery of the fine-grid matrix block at both 10 and 30 MPa effective stress conditions is increased, a similar 30% drop of matrix block ultimate oil recovery is observed in response to an increase in effective stress from 10 MPa to 30 MPa.

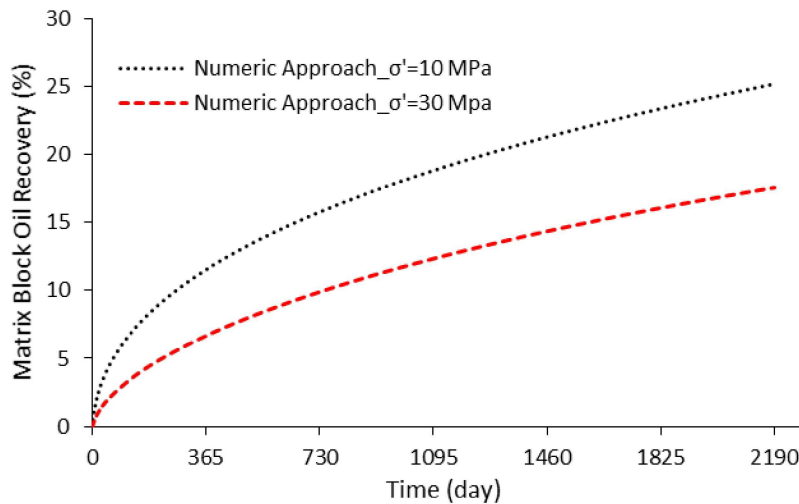
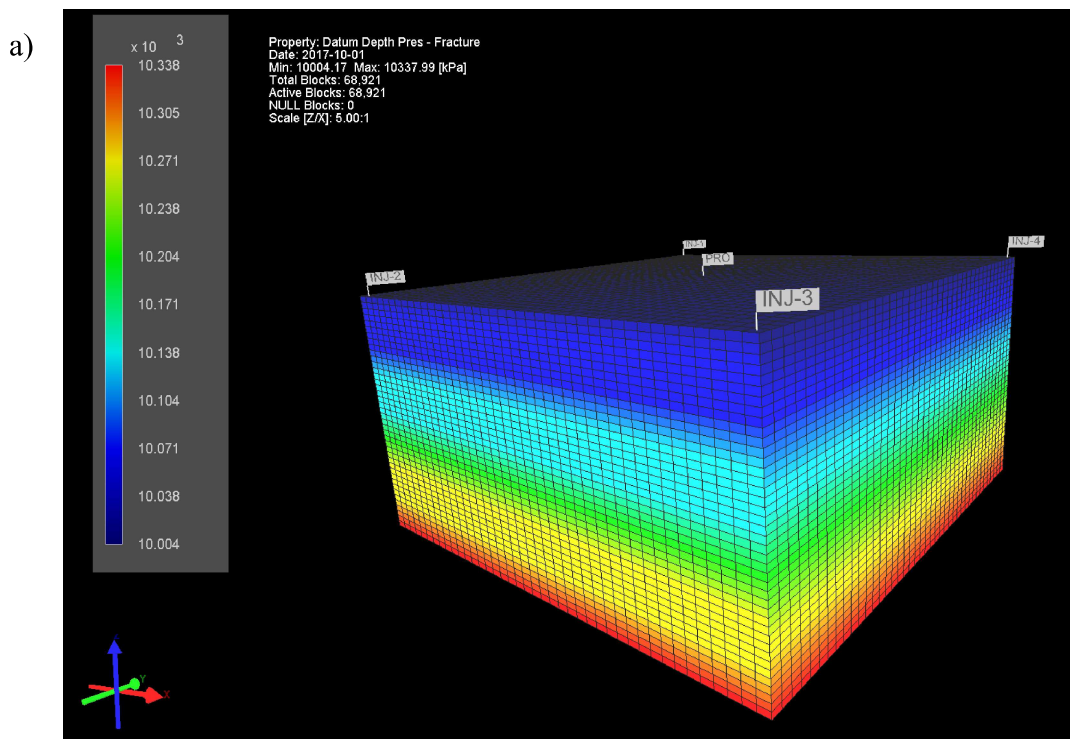


Fig. 4.5 Comparison of fine-grid matrix block oil recovery for 10 and 30 MPa effective confining stress conditions.

4.3 Reservoir-scale Modeling:

In order to investigate the geomechanical controls on multiphase fluid flow in NCFR, a cubic 5-spot reservoir (four injectors at the corners and one producer at the center) is modeled numerically using CMG-GEM simulator. A fine-grid simulation model comprising $41 \times 41 \times 41$ cells was constructed (each cell is $10 \times 10 \times 1$ m; Fig. 4.5a).

To contribute the significant role of natural fractures in fluid flow, the dual-permeability technique is used and intact rock/fracture single-phase and multiphase flow properties are assigned separately in the code. Stress-dependent multiphase flow property (e.g. relative permeability and capillary pressure curves) of each medium is sequentially updated into the coupled model. Water flooding operation starts after one year from production to activate the spontaneous imbibition mechanism between the fractures and matrix. The main objective of this study is to compare the results of a conventional simulation with coupled simulation methods considering the significant impact of stress-dependent porosity, permeability, relative permeability and capillary pressure in spontaneous imbibition in a stiff NCFR.



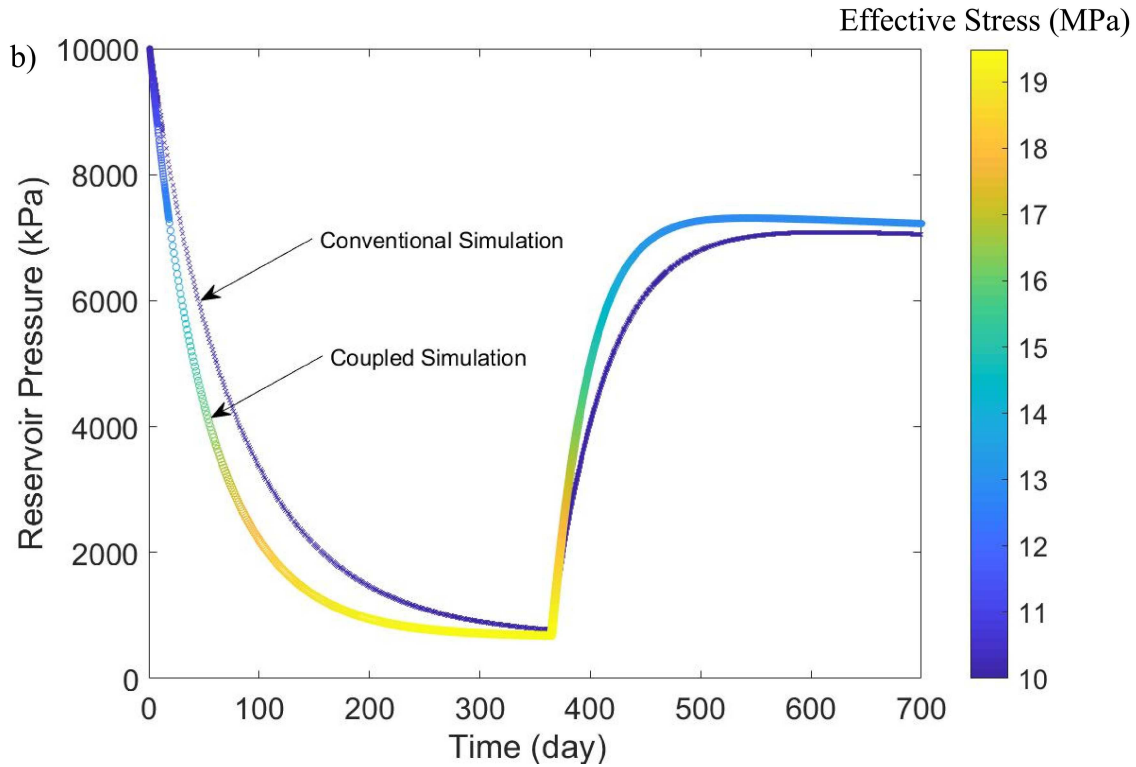


Fig. 4.6 a) 3D view of the fine-grid 5-spot model used to investigate the geomechanical controls on imbibition in NFCR. b) reservoir pressure history

4.3.1 Results:

In this section, the results from the conventional and coupled numerical methods are presented to study the impact of geomechanics on porosity, absolute permeability, relative permeability, capillary pressure, and oil production. Fig. 4.5b compares the simulated pressure history using the conventional method with the presented advanced coupled simulations techniques.

4.3.1.1 Stress-Dependent Porosity

As discussed early, poroelastic and Barton-Bandis models are used as the reference to calculate stress-dependent porosity tables in the model for intact rock and fracture, respectively. Due to the change in effective stress, the advanced coupled model shows the intact rock deformation and fracture closeness. Although the impact is negligible ($\varphi = 0.3$) for the current model of the stiff carbonate, still it shouldn't be neglected in the NFCR simulation (Fig. 4.6).

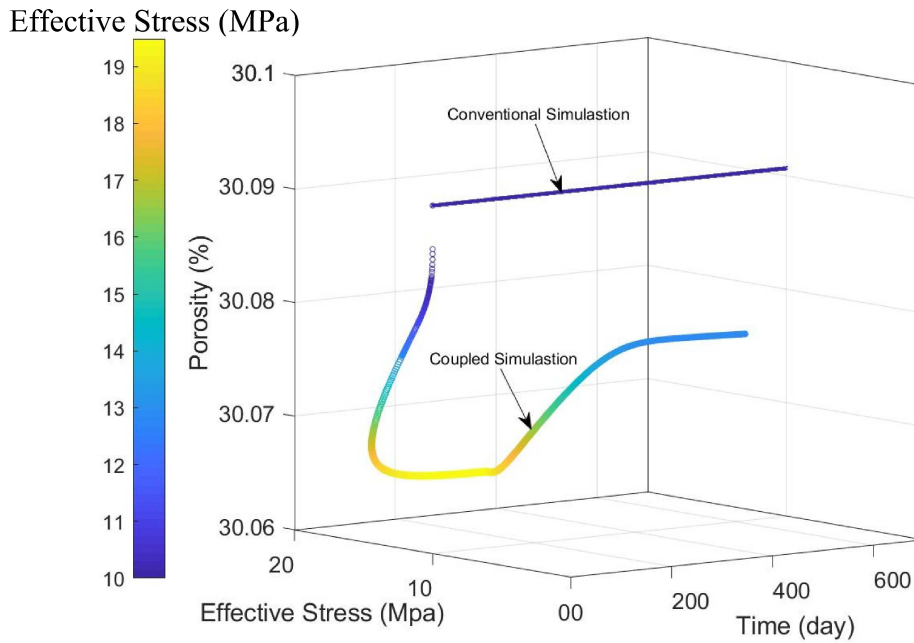


Fig. 4.7 A comparison between 3D plots of porosity for conventional and coupled models

4.3.1.2 Stress-Dependent Absolute Permeability

Stress-dependent absolute permeability is calculated using Hagen-Poiseuille's law for both intact rock and fracture. Due to change in effective stress, the coupled model presents changes in absolute permeability with time while the conventional model keeps it constant (Fig. 4.8).

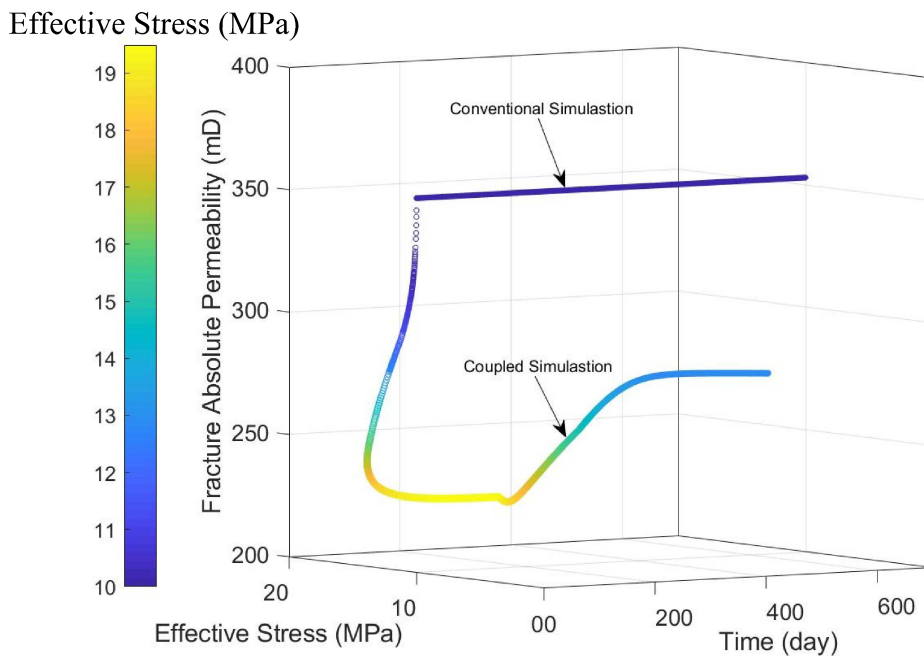


Fig. 4.8 A comparison between 3D plots of absolute permeability for conventional and coupled models

4.3.1.3 Stress-Dependent Imbibition Capillary Pressure

Considering the Leverett J-function similarity variable and stress-dependent porosity and absolute permeability from the previous section, the stress-dependent capillary pressure is calculated (Section 3.3.4.3). As illustrated in Fig. 4.8, the 3D plot of capillary pressure/water saturation/effective stress changes due to geomechanical impacts. Intuitively, high permeability of fractures leads to a limited pressure difference and viscous forces in the NFCR. Accordingly, spontaneous imbibition is the dominant production mechanism in NFCR and the performance of this process is mainly governed by the capillary pressure curve. This important effect has been neglected in conventional simulation models of NFCR.

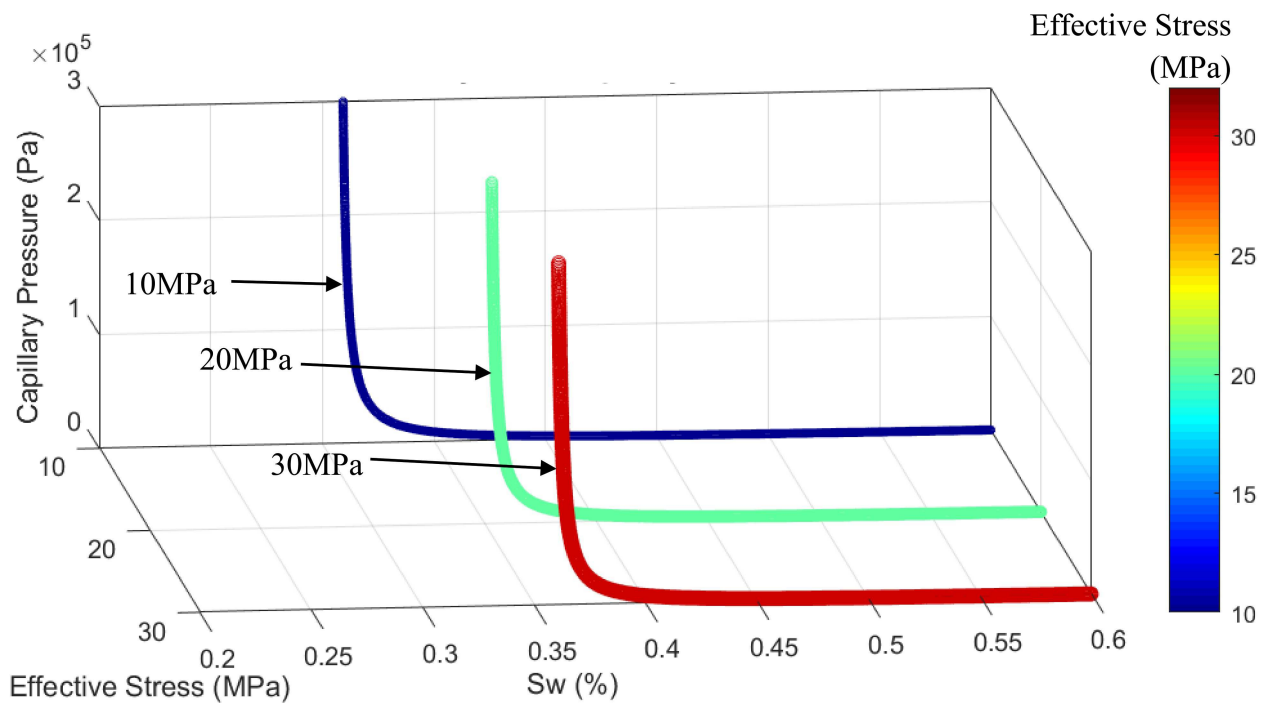


Fig. 4.9 Stress-dependent imbibition capillary pressure curves for fractured carbonate rock based on derived equation in section 3.3.4.4

4.3.1.4 Stress-Dependent Imbibition Relative Permeability

Some experimental (Lian et al. 2012) and analytical results (chapter 3) on the NFCR confirmed the dependency of relative permeability curve's end-points and wettability with stress. Experiments showed that the irreducible water saturation increased significantly as confining stress increased for the case of mixed-wet carbonate rock. Analytical approaches also confirm the experiments. Relative permeability has a direct impact on multiphase flow and counter-

current spontaneous imbibition in NFCR. Fig. 4.9 shows the stress-dependent relative permeability plot based on the equations driven for an NFCR in section 3.3.4.4.

4.3.1.5 Oil Production

Fig. 4.10 proves the great impact of geomechanics on the field production profile considering stress-dependent porosity, permeability, relative permeability, and capillary pressure effect. The 3D plot indicates a 40% difference in cumulative oil production between coupled and conventional simulation methods after one year production. Otherwise, the oil recovery of the block of naturally fractured carbonate, which is under capillary-driven imbibition, is significantly affected by rock and fracture deformation. However, after water flooding, as effective stress decreases, the difference between the two simulation techniques decreases.

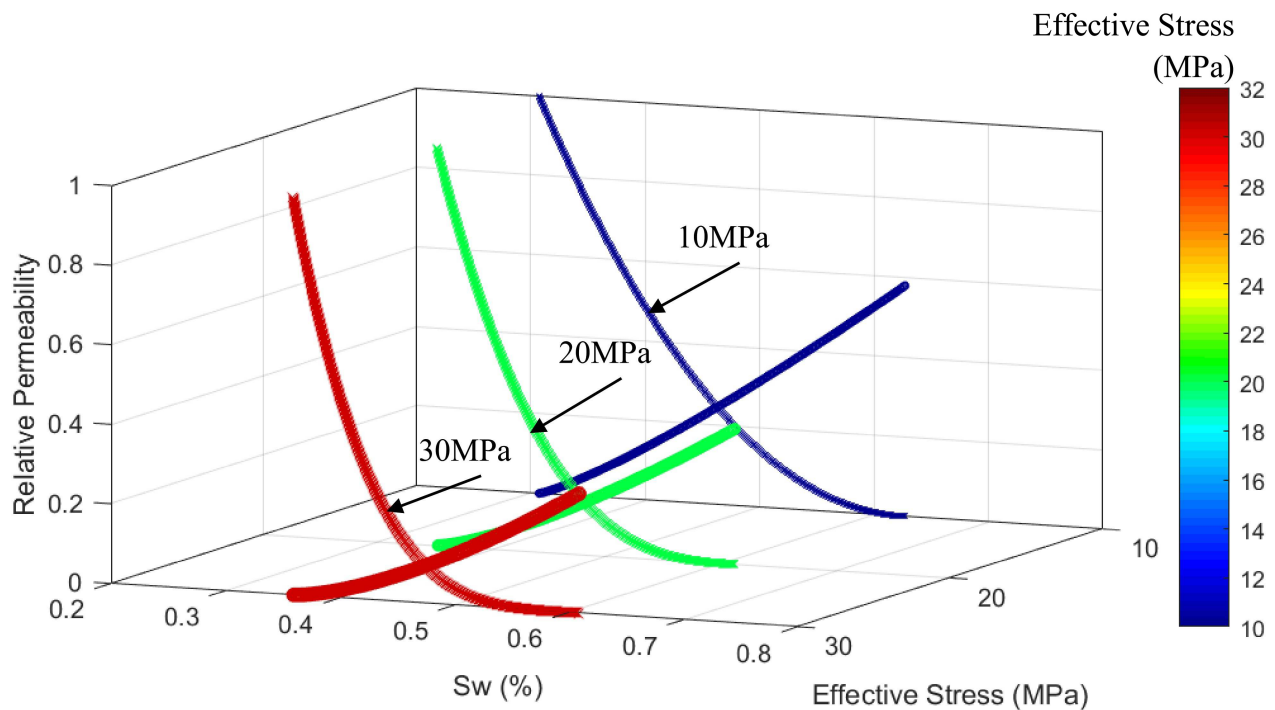


Fig. 4.10 Stress-dependent imbibition relative permeability curves for fractured carbonate rock based on derived equation in section 3.3.4.4

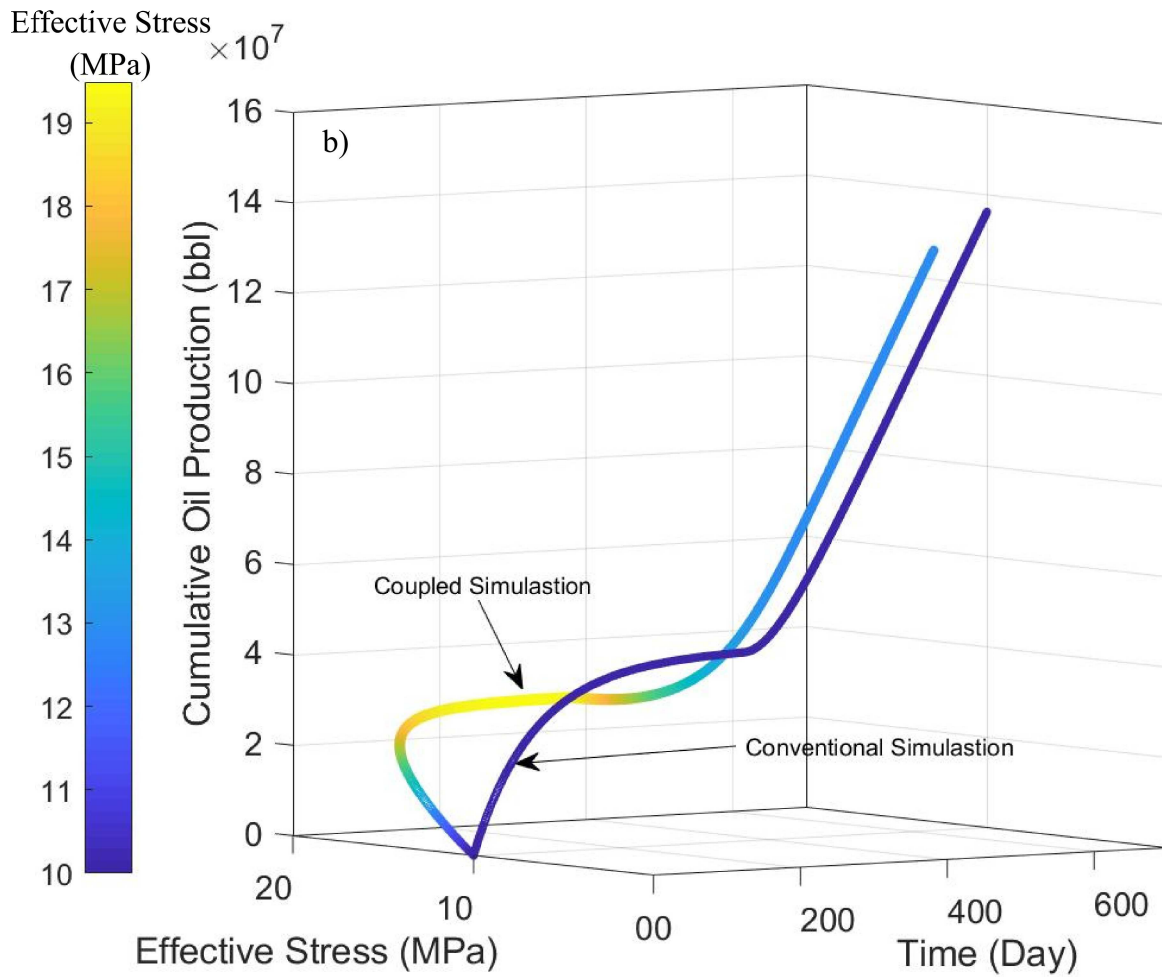
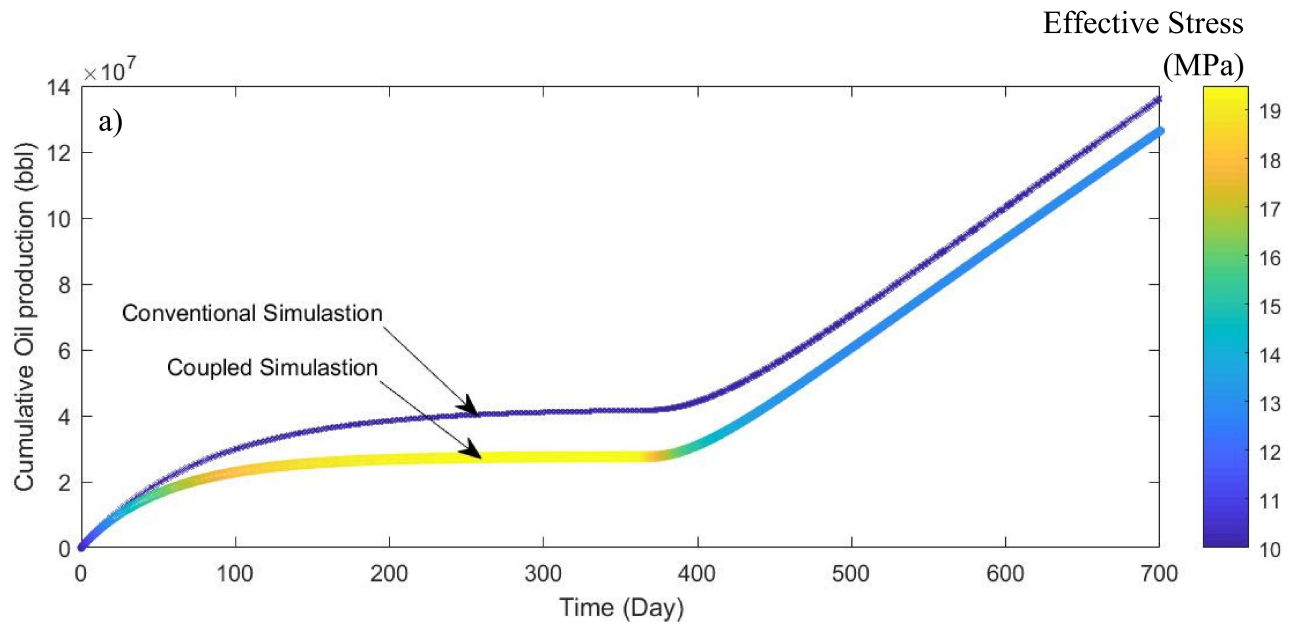


Fig. 4.11 Comparing the cumulative oil production results from conventional and coupled simulation models in (a) 2D and (b) 3D plots.

4.4 Conclusions

To validate the stress-dependent recovery from the derived semi-analytical solution in chapter 3, we developed a sugar-cube model based on Warren and Root's [1963] original dual-porosity model. The sensitivity analysis found the effect of stress-dependent relative permeability and capillary pressure curves much greater than the effect of stress-dependent porosity and permeability on capillary-driven oil recovery. This stress-dependent effect has been neglected in commercial reservoir simulators in the oil and gas industry. Comparing the results from the semi-analytical solution from chapter 3 with the numerical solution for the case of mixed-wet NFCR, both methods calculated almost the same drop in early time oil recovery factor ($\approx 50\%$) with incrementing the effective confining stress from 10 MPa to 30 MPa.

Additionally, The reservoir-scale study provides fundamental approaches in the simulation of spontaneous imbibition by promoting conventional simulation into coupled geomechanical/dual-permeability flow simulation techniques considering stress-dependent porosity, permeability, relative permeability and capillary pressure for both fracture and matrix media in NFCRs.

5. Consecutive Experimental Determination of Stress-dependent Fluid Flow Properties of Intact Berea Sandstone and Fractured Calumet Carbonate*

Abstract

In this study, changes in the hydrodynamic properties of intact Berea sandstone and fractured Calumet carbonate at a constant temperature of 40°C are reported as effective confining stress is increased to 30 MPa. Through a novel consecutive approach, porosity, absolute permeability, drainage relative permeability, and drainage capillary pressure were shown to systematically change with effective stress. The relative permeability measurements were taken using a steady-state method for the N₂/water fluid pair. A second method, in which a saturated core with the wetting phase was flushed with the non-wetting phase at an increasing flow rate, was used to determine the drainage capillary pressure. Core saturation was determined using a gas separation unit and mass-balance consideration. This study revealed a decrease in porosity and absolute permeability of intact Berea sandstone, from 13.16% and 58 mD to 12.24% and 36 mD, respectively with the increase in effective confining stress. In a similar way, fracture porosity and absolute permeability of the Calumet carbonate decreased, from 1.5% and 19.79 D to 1.18% and 219 mD, respectively, with an increase in effective confining stress from zero up to 10MPa. In terms of relative permeability curves, this study showed a systematic decrease in irreducible wetting phase saturation from 0.44 to 0.24 as effective stress increased; this could be interpreted in core-scale as a progressive tendency of the initially water-wet Berea sandstone to the gas phase. In contrary, irreducible wetting phase saturation increased from 0.28 to 0.49 as effective stress for the initially mixed-wet Calumet carbonate increased. The capillary pressure curve also

*Some parts of this chapter related to the Berea sandstone experiments were published in Water Resources Research (AGU): Haghi, A.H., Talman, S., Chalaturnyk, R. (2020). Consecutive Experimental Determination of Stress-dependent Fluid Flow Properties of Berea Sandstone and Implications for Two-phase Flow Modelling. Water Resources Research, 56(1), <https://doi.org/10.1029/2018WR024245>

presented an upward shift in response to increased effective stress for both specimens. These changes in the hydrodynamic rock properties with stress suggest that scaling flow parameters of porous media under effective stress conditions may be required to accurately predict flow behavior under conditions of changing stress.

5.1 Introduction

Porous rocks buried kilometers beneath the earth surface are exposed to a state of in-situ stress. Many authors have estimated the present-day in-situ stress state around the world (Heidbach et al., 2018; Haghi et al., 2013a; Haghi et al., 2018a). The state of stress in porous rocks have varied over geological time depending on external (e.g. massive material movement due to erosion) and internal (e.g. depositionally induced compaction and tectonic forces) geological processes (Heidbach et al., 2010). Much more rapid human induced-changes arise due to injection and production operations in almost all petroleum/geothermal reservoirs and CO₂ storage formations (Haghi et al., 2013b). Changes in effective stress leads to shape and size alterations among pores and changes in fracture opening within porous media, directly impacting both intrinsic rock properties such as porosity and absolute permeability (Geertsma, 1957; Zimmerman et al.1986; Zhu and Wong 1997; Morris et al., 2003; Schutjens et al. 2004; Iglauer et al., 2014) and multiphase flow properties including capillary pressure and relative permeability curves (Li et al., 2004). These flow properties are essential for describing multiphase fluid flow in porous media, and slight changes in them can induce a significant effect on the reserve and recovery of oil and gas fields and geothermal reservoirs (Ahmed and McKinney, 2011), transport of contaminating nonaqueous liquid phase in aquifers (Pak et al., 2015), performance of CO₂ subsurface sequestration (Szulczewski et al., 2012), and rain water infiltration into ground (Cueto-Felgueroso and Juanes, 2008).

The theory of multiphase flow in porous media is generally treated with empirical correlations of the capillary pressure curves as a function of wetting phase saturation (Hassanizadeh and Gray, 1993). In physical essence, capillary pressure is defined as the pressure difference or excess pressure at the interface of two immiscible phases, which particularly depends on the curvature of their separating interface (Peters, 2012). The interaction between different fluid phases and solid surfaces significantly impacts flow properties and reduces the intrinsic absolute permeability of rock to its fluid effective permeability (Muskat, 1937). Relative

permeability is a dimensionless fluid effective permeability calculated by dividing each phase effective permeability at a certain saturation by the absolute permeability of a fully saturated porous media with the wetting phase (Peters, 2012). Experimental determination of the variation of capillary pressure and relative permeability with phase saturation for different materials have been routinely performed for decades. These curves, together with flow diffusivity equations, have been used to describe multiphase flow in porous media for a variety of applications such as geological storage of carbon dioxide, water aquifer remediation, and oil and gas production (Pini and Benson, 2013).

Although researchers have investigated the impact of stress on relative permeability curves in different materials (Abbas et al., 2009; Khan, 2009; Hamoud et al., 2012; Jones et al., 2001), no one has specifically studied and quantified the impacts of effective confining stress on the relative permeability and capillary pressure curves together. As noted above, reservoir pore pressure is affected by both fluid production and injection. These changes in pore pressure can lead to dramatic changes in effective stress. Some experimental studies have shown that the impact of effective confining stress on the fracture relative permeability curves can be significant (McDonald et al. 1991; Lian et al. 2012). Similarly, Hue and Benson (2016) experimentally investigated the stress dependency of relative permeability in fractures and concluded that there is a direct relationship between an increase in stress and decreasing irreducible water saturation. Irreducible water saturation defined as the minimum saturation in which water can no longer produce under normal flow operation (Peters, 2012). Building on these findings, we discussed in Chapter 3, both conceptually and analytically on the basis of a bundle of capillary tubes and pore throat model, the stress-dependent flow properties of rock and their impacts on spontaneous imbibition in naturally fractured carbonate reservoirs.

The main objective of this study is to track and explain the changes in intact rock and fractures porosity, absolute permeability, drainage capillary pressure, and drainage relative permeability associated with a 30MPa increase in effective confining pressure under isotropic loading and isothermal conditions (40°C). The apparatus we have designed gave us the opportunity to conduct the full test in a continuous manner on the same specimen. This provides us with some comprehensive understanding of the significant changes induced by effective stress

changes on multiphase flow properties in porous media, which has been much less explored in the literature.

5.2 Theoretical Concepts and Prior Work

In this section, appropriate theoretical models and correlation are derived to fit curves on experimental data for different sandstone samples from literature. These same equations will be applied to our experimental data in the next sections; fitting parameters and curves from this section will be used as a benchmark for the measured experimental data in this study. All related case-studies and models associated with fracture's deformation, porosity, and flow properties are already discussed in chapter 3.

5.2.1 Stress, Strain, and Porosity Relations

Reservoir rocks respond to internal and external effective stresses by showing strain or deformation. The poroelastic constitutive equations for a fluid saturated porous media are derived based on assumptions regarding the stress (σ_{ij}) and strain (ε_{ij}) linearity, and the reversibility of the media deformation (Biot, 1941). The general poroelastic constitutive equation for an isotropic linear elastic material is given in Eq.(5.1) (Detournay and Cheng, 1993).

$$\varepsilon_{ij} = \frac{\sigma_{ij}}{2G} - \left(\frac{1}{6G} - \frac{1}{9K} \right) \delta_{ij} \sigma_{ij} + \frac{1}{3H'} \delta_{ij} P \quad (5.1)$$

The parameters G and K are the drained elastic shear and bulk modulus, respectively. The constitutive constant H' specifies the grain and fluid stress/strain coupling. Eq.(5.2) defines the bulk volumetric strain (ε_v) in terms of the Biot coefficient (α) under isotropic compressive stress condition ($\sigma_{11} = \sigma_{22} = \sigma_{33} = \sigma$) (Detournay and Cheng, 1993):

$$\varepsilon_v = 3\varepsilon = \frac{1}{K}(\sigma - \alpha P) \quad (5.2)$$

Note that in Eq.(5.2), an isotropic strain condition ($\varepsilon_{11} = \varepsilon_{22} = \varepsilon_{33} = \varepsilon$) is presumed to occur due to the assumption of an isotropic stress condition with positive sign in compression. Eq.(5.2) shows that when stress and pore pressure (P) are known, volumetric strain can be obtained using the linear isotropic theory of poroelasticity. For the case of non-linear volumetric deformation of porous rocks, Zimmerman et al. (1986) found a fitting correlation equation for stress-strain data gathered from lab experiments on Boise, Bandera, and Berea sandstones as follows:

$$\varepsilon_v = A\sigma - Be^{-\sigma/c} + D \quad (5.3)$$

where the exponential term satisfies the non-linearity of the stress-strain equation. The authors recommended that the fitting constants A, B, C, and D in Eq.(5.3) should be determined using the least squares regression method. We recast Eq.(5.3) for ε_v as a function of effective stress ($\sigma' = \sigma - \alpha P$) in this study. The same shape of fitting correlation equation is derived with the exception of constraining the fitting constants $B' = D'$ to satisfy the initial condition that $\varepsilon_v = 0$ for $\sigma' = 0$.

$$\varepsilon_v = A'\sigma' - B'e^{-\sigma'/c'} + B' \quad (5.4)$$

In a similar way, Liu et al. (2009) developed a macroscopic derivative equation, which treated the porous media as a heterogeneous body of soft (e.g. pores and micro-cracks) and hard (e.g. solid grains) parts, to match the volumetric strain data with the hydrostatic effective stress condition. Their solution used a combination of an exponential function (derived from natural-strain-based Hook's law) and a linear function (derived from engineering-strain-based Hook's law; Jaeger et al., 2007) for soft and hard sections, respectively. Integrating and re-arranging that equation leads to the following solution for the volumetric strain,

$$\varepsilon_v = \frac{(1 - \gamma_S)}{K_H} \sigma' - \gamma_S e^{-\sigma'/K_S} + \gamma_S \quad (5.5)$$

where K_H and K_S are the bulk moduli of hard and soft parts, respectively, and γ_S refers to a ratio of the soft part volume to the bulk volume at the unstressed condition. The similarity between Eq.(5.4) and (5.5) reveals the physical meaning of the fitting constants in Eq.(5.4).

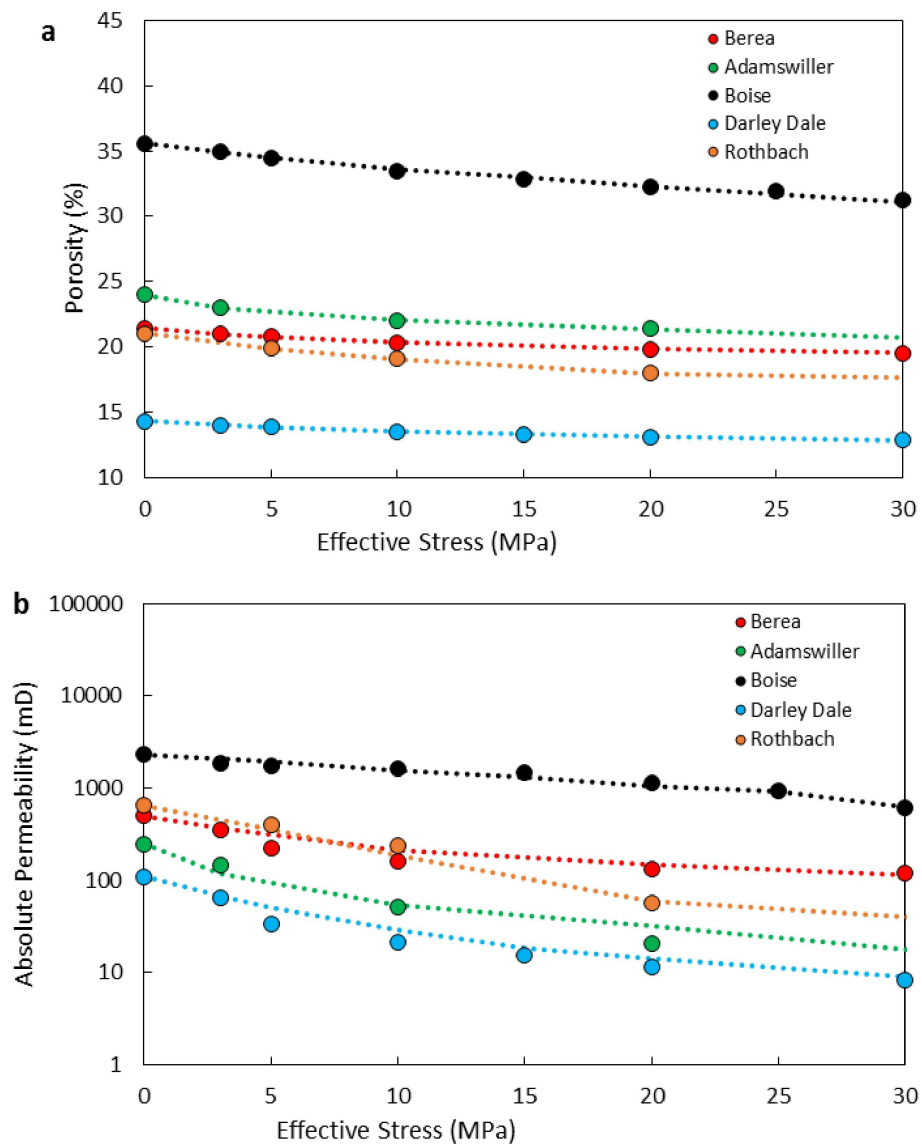
Using Eq.(5.2), Schutjens et al. (2004) derived and successfully applied Eq.(5.6) to calculate compaction-induced porosity reduction for a sandstone reservoir.

$$\Delta\varphi = \frac{\varepsilon_v(\varphi_i - 1)}{1 - \varepsilon_v} \quad (5.6)$$

Here, φ_i is the rock porosity at the initial stress condition. Ignoring the grain compressibility in comparison to pore compressibility, Haghi et al. (2018b) derived Eq.(5.7) for the intact rock stress-dependent porosity (φ_t) calculation.

$$\varphi_t = \frac{\varphi_i - \varepsilon_{vt}}{1 - \varepsilon_{vt}} \quad (5.7)$$

In this paper, the subscript variable “t” indicates that the intrinsic properties of rock (e.g. porosity and absolute permeability) are considered here as time-dependent (or stress-dependent) properties. Stress-dependent porosity data under the isotropic effective confining stress condition for five different sandstones was reported by Zhu and Wong (1997). To evaluate the validity of above-mentioned fitting correlation equations for different sandstones, the experimental data for the effective stress range of 0-30MPa is reproduced in Fig. 5.1a, together with fitting curves based on Eq.(5.4) and (5.7) for volumetric strain and stress-dependent porosity, respectively. The calculated values of the fitting constants are listed in Table 5.1.



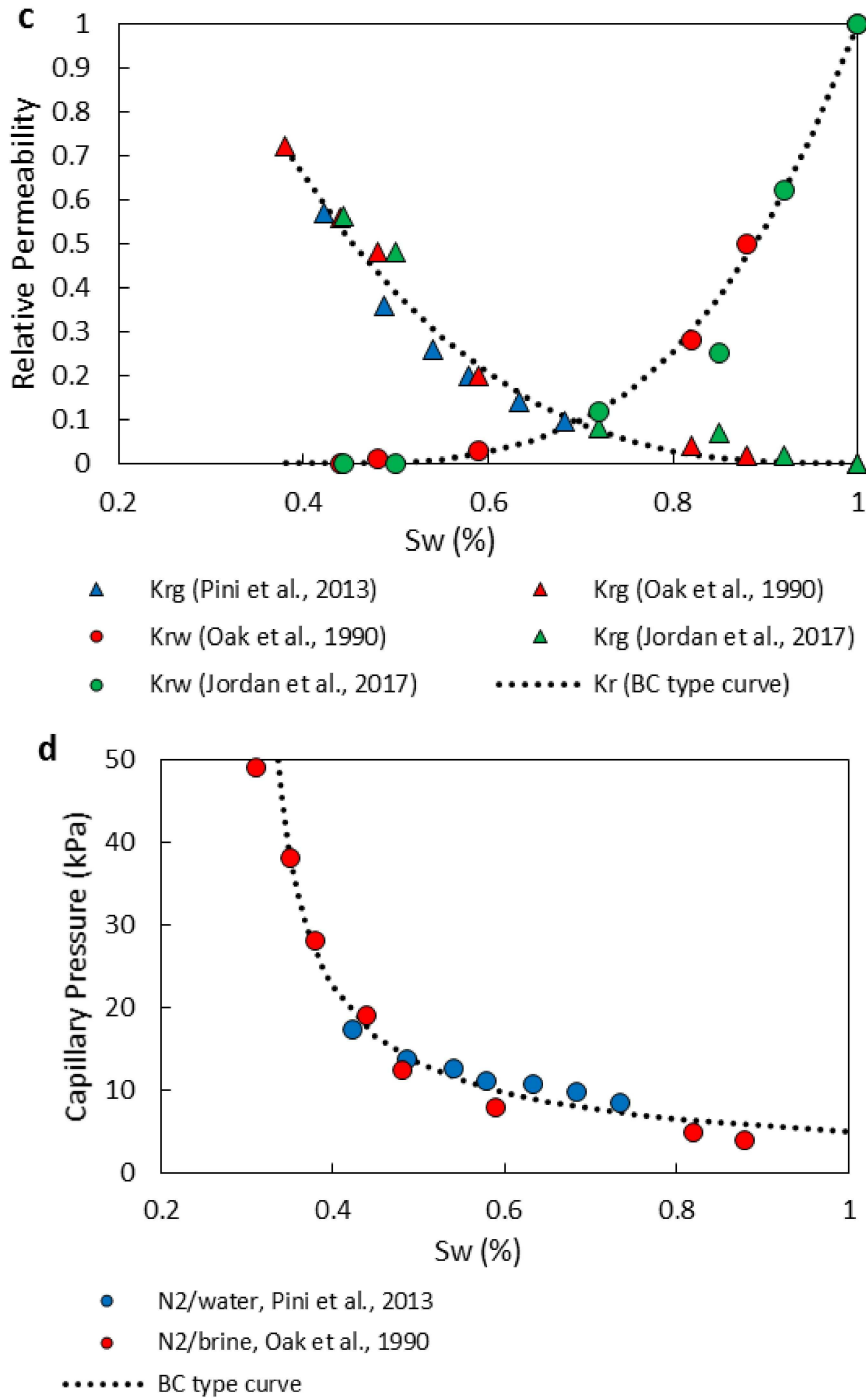


Fig. 5.1 Plots (a) and (b) present stress-dependent porosity and absolute permeability, respectively, for five different sandstone rocks, based on data from Zhu and Wong's (1997) experiment, combined with the fitted curves (dotted lines). Plots (c) and (d) provide relative permeability and capillary pressure curves derived from the literature using an N₂/water (brine) fluid pair on Berea sandstone under less than 10Mpa effective stress condition, combined with the fitted Brooks and Corey correlation.

There is a clear relationship between K_H for each sandstone (Table 5.1) and the corresponding φ_i (Fig. 5.1a); Boise sandstone with the smallest K_H in Table 5.1 (softest specimen) has the greatest φ_i while Darley Dale sandstone with the greatest K_H (stiffest specimen) is the tightest sample.

Table 5.1 Calculated fitting constants in Eq.(5.4)-(5.5) for Zhu and Wong's (1997) experiment

Rock	$A = (1 - \gamma_s)/K_H$ 1/GPa	$B = \gamma_s$ (-)	$C = K_s$ MPa	K_H GPa	Regression R-square
Berea sandstone	0.183	0.01859	9.842	5.37	0.9989
Adamswiller sandstone	0.795	0.01811	3.338	1.24	0.9998
Boise sandstone	1.63	0.01603	5.734	0.60	0.9955
Darley Dale sandstone	0.159	0.01272	10.94	6.21	0.9999
Rothbach sandstone	0.37	0.06699	18.39	2.55	0.9999

5.2.2 Porosity and Permeability Relations

In the absence of measurements, permeability is often estimated using empirical porosity/permeability correlations. Kozeny (1927) and Carman (1939) presented a capillary tube based model ($k = \varphi r^2 / 8 \tau$), where r is the tubes radius, in order to convert rock porosity into absolute permeability (k). For a packing of spherical grains (e.g. sandstones) with diameter d and tortuosity τ , the expression

$$k = \frac{\varphi^3 d^2}{72(1 - \varphi)^2 \tau} \quad (5.8)$$

(Carman, 1956) is commonly used. Dividing Eq.(5.8) at each effective stress condition by the same equation at the initial stress condition, the following equation is developed for stress-dependent absolute permeability (k_t) due to porosity reduction by the application of stress,

$$k_t = k_i \left(\frac{\varphi_t}{\varphi_i} \right)^3 \left(\frac{1 - \varphi_i}{1 - \varphi_t} \right)^2 \left(\frac{\tau_i}{\tau_t} \right) \quad (5.9)$$

where the grain compressibility is assumed to be negligible compared to the pore compressibility ($d_t = d_i$). The hydraulic tortuosity is assumed to vary with the applied effective stress ($\tau_i \leq \tau_t$). A normalized stress-dependent tortuosity term ($\bar{\tau}_t = \tau_t / \tau_i$) in Eq.(5.9) is an unknown stress-dependent variable that is inversely proportional to normalized stress-dependent absolute permeability (k_t / k_i). Several theoretical relations exist in the literature describing

tortuosity as a function of porosity, with porosity as the only variable (Meredith and Tobias, 1962; Berryman, 1981; Koponen et al., 1997; Barrande et al., 2007; Matyka et al., 2008). Using the Archie definition for formation factor (Archie, 1942), Brown (1980) demonstrated tortuosity to be a power law function of porosity with an exponent m related to the rock cementation. In a similar way, we propose the following power law correlation equation of $\bar{\tau}_t$ versus normalized porosity ($\bar{\varphi}_t = \varphi_t/\varphi_i$).

$$\bar{\tau}_t = a\bar{\varphi}_t^{-m} + \epsilon \quad (5.10)$$

where ϵ is a correlation deviation term representing uncertainty in the power law functions, and a is a material constant. To meet the initial condition that $\bar{\tau}_t = 1$ for $\bar{\varphi}_t = 1$, Eq.(5.10) is rearranged, using the constraining condition $a + \epsilon = 1$, as follows:

$$\bar{\tau}_t = a(\bar{\varphi}_t^{-m} - 1) + 1. \quad (5.11)$$

Comparing Eq.(5.11) with the derived equation by Berryman (1981) for tortuosity of a fluid flow path inside the porous media $\tau_t = a(\varphi_t^{-1} - 1) + 1$ (Kimura, 2018), we conclude an analogous physical meaning for a as the grain shape factor in the range of 0-1 (e.g. $a = 0.5$ for spherical grains) and m as a material exponent which relates φ_t and τ_t .

In this study to fit Eq.(5.9) on the experimental results, least squares regression technique is used to calculate the fitting constants a and m in Eq.(5.11) and the results are given in Table 5.2. Fig. 5.1b shows the stress-dependent absolute permeability curves under isotropic effective confining stress in the range of 0-30MPa for the same sandstone samples used in Zhu and Wong's (1997) experiment in a semi-log scale to cover clearly the whole range of data.

Table 5.2 Calculated fitting constants in Eq.(5.11) for Zhu and Wong's (1997) experiment

Rock	a (-)	m (-)	Regression R-square
Berea sandstone	0.9123	13.23	0.8017
Adamswiller sandstone	0.97	14.24	0.9699
Boise sandstone	0.03076	28.51	0.9908
Darley Dale sandstone	0.9848	20.31	0.9247
Rothbach sandstone	0.244	19.82	0.9949

Table 5.2 reveals a systematic decrease in the grain shape factor (a) of the studied specimens from Darley Dale sandstone with the least absolute permeability (less than 100 mD) to Boise sandstone with the greatest absolute permeability (more than 1 Darcy). However, the calculated broad range of 13.23-28.51 for the material constant m is found to be more randomly distributed.

5.2.3 Two-phase Flow

In the presence of two or more immiscible fluids inside the porous media, contrasts in the interfacial properties of different phases introduce further complexity, such as capillary pressure and relative permeability, into the flow equations. As will be demonstrated below, these two-phase flow parameters are dependent on the material strains, and so must be considered as time-dependent properties in systems unless the effective stress is constant.

Numerous models have been proposed to correlate specific saturation-dependent properties, namely relative permeability and capillary pressure curves, with fluid saturation (Purcell, 1949; Burdine, 1953; Corey, 1954; Brooks and Corey; 1966, Van Genuchten, 1980; Kühn, 2004; Romm, 1966; Pan et al., 1996; Pyrak-Nolte et al., 1988; Rossen and Kumar, 1992; Yang et al., 2013). Brooks and Corey's (1966) equations, which define capillary pressure and relative permeability curve as a power law function of wetting-phase saturation, may be the most popular. Similarly, the following power-law drainage capillary pressure, wetting, and non-wetting phase relative permeability equations (Eq.s (5.12), (5.13), (5.14), respectively), which are often called modified Brooks-Corey relations, are commonly used to describe the multiphase flow properties of rock:

$$P_c = P_e(S_w^*)^\beta \quad (5.12)$$

$$k_{rw} = k_{rw-max}(S_w^*)^{n_w} \quad (5.13)$$

$$k_{rnw} = k_{rnw-max}(1 - S_w^*)^{n_{nw}} \quad (5.14)$$

$$S_w^* = \frac{S_w - S_{wir}}{1 - S_{wir} - S_{nwr}} \quad (5.15)$$

In Eq.(5.15) S_{wir} and S_{nwr} refer to the irreducible wetting phase and residual non-wetting phase saturation, respectively. In Eq.s (5.12)-(5.14), P_e , k_{rw-max} , and $k_{rnw-max}$ indicate the entry capillary pressure and relative permeability end-points for the wetting and non-wetting

phases, respectively. The powers β , n_w , and n_{nw} in Eq.s (5.12)-(5.14) should be treated as fitting constants to calibrate the equations with the experimental data. Herein, Eq.s (5.12)-(5.14) are used to fit curves on experimental data from literature and later from this study.

Additionally, many researchers have studied capillary pressure and relative permeability by applying various experimental techniques to different immiscible fluid pairs on a wide range of specimens (Müller, 2011; Krevor et al., 2012; Akbarabadi and Piri, 2013; Dickson et al., 2006; Kim et al., 2012; Plug and Bruining, 2007; Pentland et al., 2011; Pini et al., 2012). The shapes of the capillary pressure curves have been found to be directly related to the rock's pore size distribution, k_r end-point values, and residual saturation (Burdine et al., 1950). These parameters can be used to specify the wettability of different materials (Lefebvre du Prey, 1973; Anderson, 1987).

The multiphase flow properties of Berea sandstone have been under investigation since the early 1990's. Some researchers have carried out the specific case of relative permeability and capillary pressure tests on Berea sandstone using an N₂/water (or brine) fluid pair (Oak et al., 1990; Pini and Benson, 2013). Oak et al. (1990) undertook a large number of comprehensive experimental analyses of relative permeability and capillary pressure on Berea sandstone at room temperature and 5.5 MPa pore pressure. Pini and Benson (2013) introduced a technique to simultaneously determine the capillary pressure and relative permeability curves of Berea sandstone using CO₂/water, CO₂/brine, and N₂/water as fluid pairs at 50⁰C and 3.4 MPa radial effective confining stress (2.4 MPa pore pressure). Jordan et al. (2016) compared the results from Oak et al. (1990) with the findings from their experiments on Berea sandstone at 40⁰C and 8.2 MPa radial effective confining stress (12.4 MPa pore pressure), finding them to be in good agreement. Fig. 5.1c-d illustrate the relative permeability and capillary pressure curves, respectively, from previous experiments on Berea sandstone using nitrogen as the non-wetting phase. Here, we used Brooks and Corey type curves (Eq.s (5.12)-(5.14)) to model the relative permeability and capillary pressure curves using these experimental data at a low effective stress condition (Table 5.3). These curves will be applied later to compare with the stress-dependent curves in this study.

Table 5.3 Calculated fitting constants in Eq.s (5.12)-(5.14) using the least square technique

Parameter	n_w	n_{nw}	β	P_e	Regression R-square
Water (brine) relative Permeability	3.529	-	-	-	0.9994
Gas relative Permeability	-	2.879	-	-	0.9759
Capillary pressure	-	-	-0.7649	5.094	0.9594

5.3 Materials and Equipment

5.3.1 Rock Samples

5.3.1.1 Berea Sandstone

All the test steps were carried out on a single homogeneous Berea sandstone specimen (from Kocurek Industries INC., USA) with a diameter of 3.61 cm and length of 8.87 cm. The sample was dried and stabilized at 100°C for 10 hours. The sample was then evacuated for 24 hours. The cleaned and dried sample was weighed with a high-accuracy scale. Then, a high-speed lab centrifuge (10⁴ rpm) was used to saturate the sample with water for initial porosity determination. The core saturation process with the centrifuge was implemented in steps, with the spinning speed increased incrementally and the sample weighed at the end of each step until the weight of the sample remained constant; its value was determined to be 13.16%. Additionally, an Autosorb Quantachrome 1MP device was employed to evaluate the N₂ gas adsorption data and generate the specific surface area (m²/g) and pore size distribution of the rock using the BET (after Brunauer-Emmett-Teller) and BJH (after Barrett-Joyner-Halenda) techniques, respectively (Fig. 5.2a; Lawrence and Jiang, 2017). The idea behind the BET technique is that at the solid-gas interface the density of gas increases due to the gas adsorption; hence the surface area of solid at liquid nitrogen temperature (77⁰K) could be measured knowing monolayer gas capacity at the interface and cross-sectional area of molecules of gas. Furthermore, dependency of gas capillary condensation pressure with the size of pores provides quantitative information on pore size distribution using BJH technique (Rouquerol et al., 2007). Fig. 5.2a indicated that 94 percent of the pores have a diameter of less than 10 nm within the range of 1-270 nm. The Drop Shape Analyzer (DSA) equipment result, shown in Fig. 5.2b, also elaborated an initial tendency of the rock to the wetting phase (water) with air-water contact angles of 29.9°. The initial permeability of the rock at zero effective stress condition was measured 58 mD at a nominal pore pressure of 1 MPa. The porosity and absolute permeability

decrement were measured stepwise inside the lab setup over the course of the confined cell pressurization. The initial rock density, measured at atmospheric conditions, was 2.055 gr/cm³.

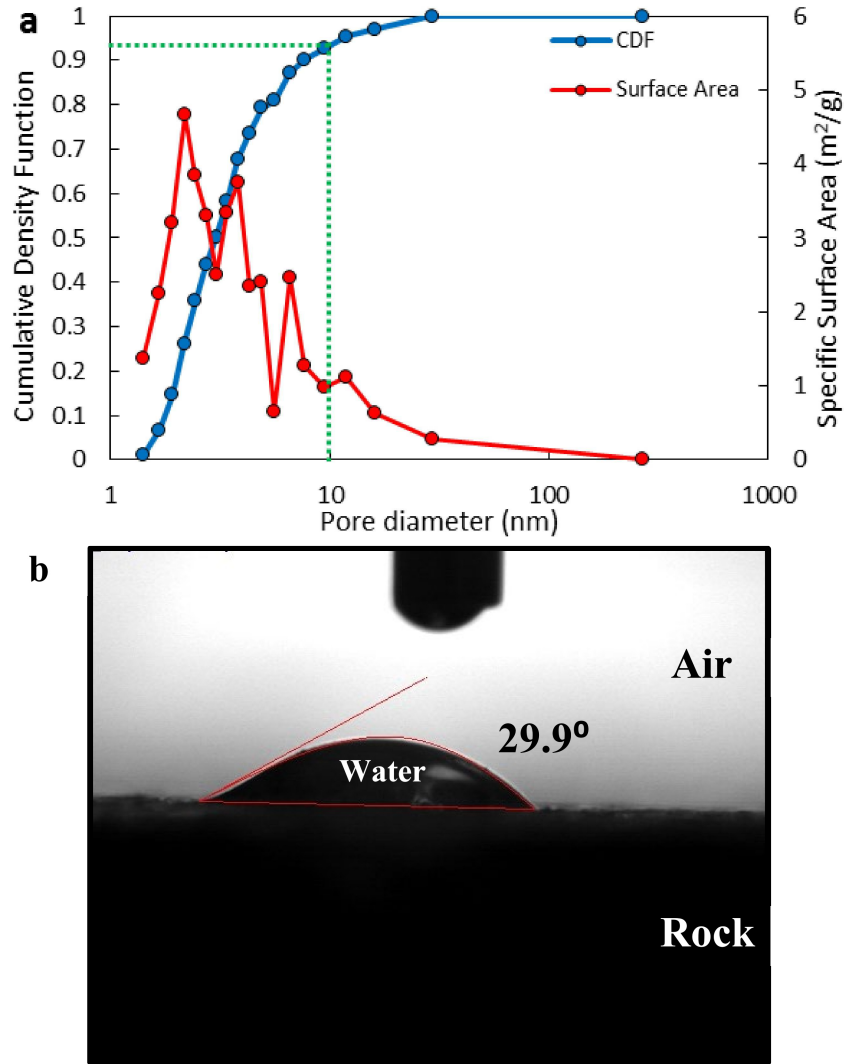


Fig. 5.2 (a) Measured cumulative pore size distribution and specific pore surface area of the Berea sandstone specimen using BJH and BET techniques, respectively, and (b) the contact angle of water droplet at its surface

5.3.1.2 Calumet Carbonate

The same procedures for the re-saturation and properties characterization have been applied to a heterogeneous carbonate core (called Calumet carbonate in this thesis) from the middle Devonian Calumet member of the Waterways formation (McMurray reservoir's downburden formation, Foster Creek North project, Alberta) with a diameter of 3.84 cm and length of 10.3 cm (Fig. 5.3a-b). The initial porosity and absolute permeability of the intact rock

was measured equal to 8.12% and 1.1 μ D, respectively. Measured intact rock absolute permeability in micro-Darcy scale (almost impermeable rock) made the rock a great candidate for induced-fracture fluid flow characterization, without having any concerns about the involvement of matrix flow conductivity effect on the measured properties of fracture. Accordingly, the same core with a single saw-cut fracture (length, width, and aperture of 10.56cm, 3.6cm, and 0.046cm, respectively) has been used for the fracture characterization experiments (Fig. 5.3c-d). The initial porosity and absolute permeability of the fracture was measure equal to 1.51% and 19.79D, respectively.

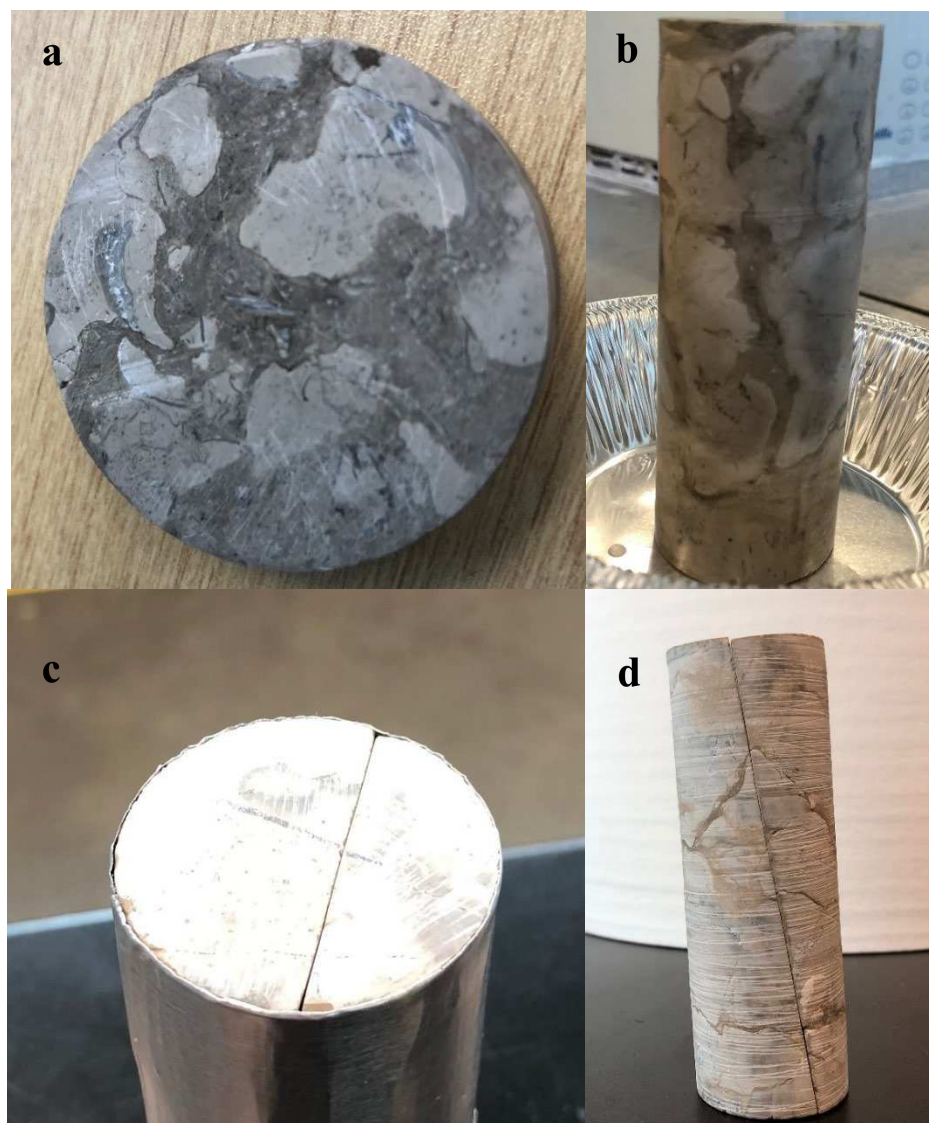


Fig. 5.3 (a)-(b) Intact Calumet carbonate and (c)-(d) artificially fractured specimens

Specific surface area (m^2/g) and pore size distribution of the intact Calumet carbonate using the BET and BJH techniques, respectively are given in Fig. 5.4a, which indicated that 88 percent of the pores have a diameter of less than 10 nm within the range of 1-131 nm. The uniaxial compressive strength and Young's modulus of the intact rock have been measured 36.04MPa and 3GPa, respectively (Fig. 5.4b).

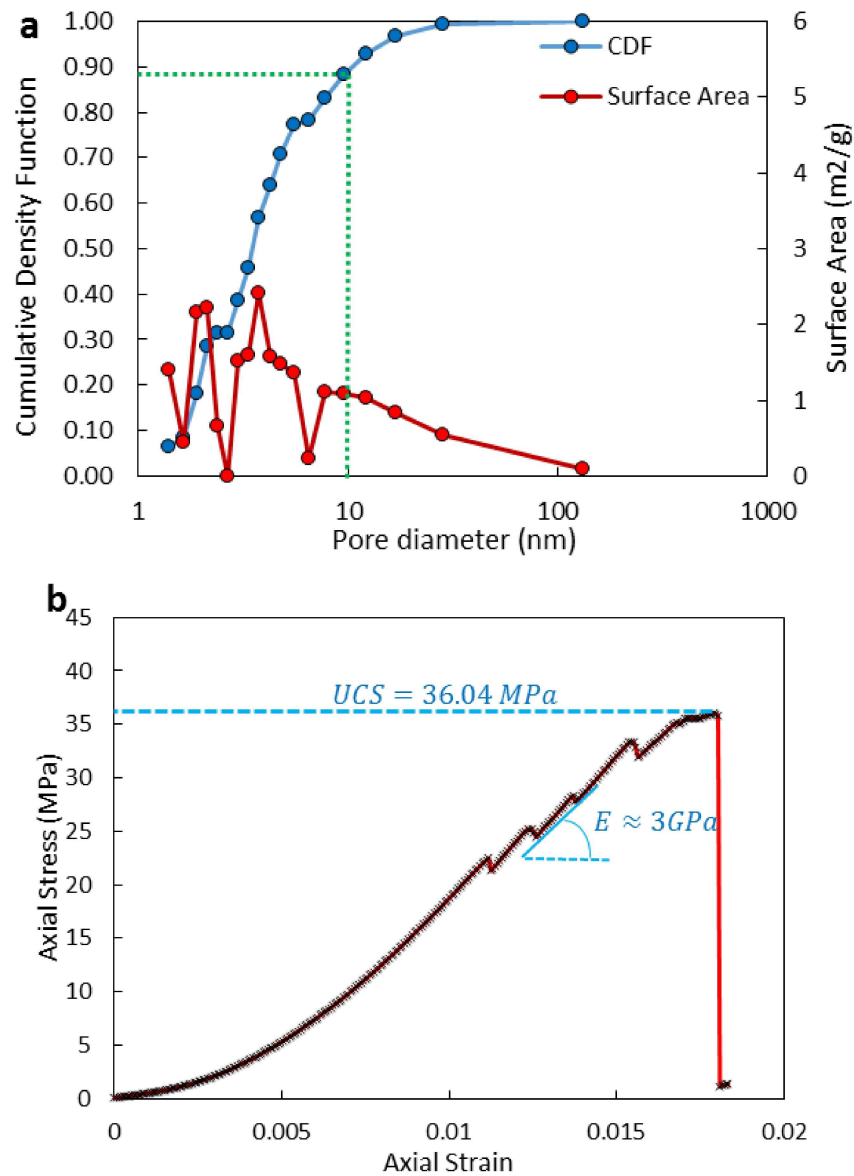


Fig. 5.4 (a) Measured cumulative pore size distribution and specific pore surface area using BJH and BET techniques, respectively and (b) the uniaxial compressive strength test results of the intact Calumet carbonate specimen

The Drop Shape Analyzer (DSA) result proves diverse tendency of different minerals of the rock to the water phase with air-water contact angle ranges of 61.2° to 90.4° for the calcite (dark gray Fig. 5.5b) and ankerite/ferroan-dolomite (light crystal Fig. 5.5a) minerals, respectively. Based on this information, we considered the carbonate specimen to be a mixed-wet rock. The sessile drop test result, Fig. 5.5c, also elaborated an initial tendency of the rock to the oil phase while the rock sample immersed in the silicon oil and allowed to equilibrate. The initial rock density, measured at atmospheric conditions, was 2.564 gr/cm^3 .

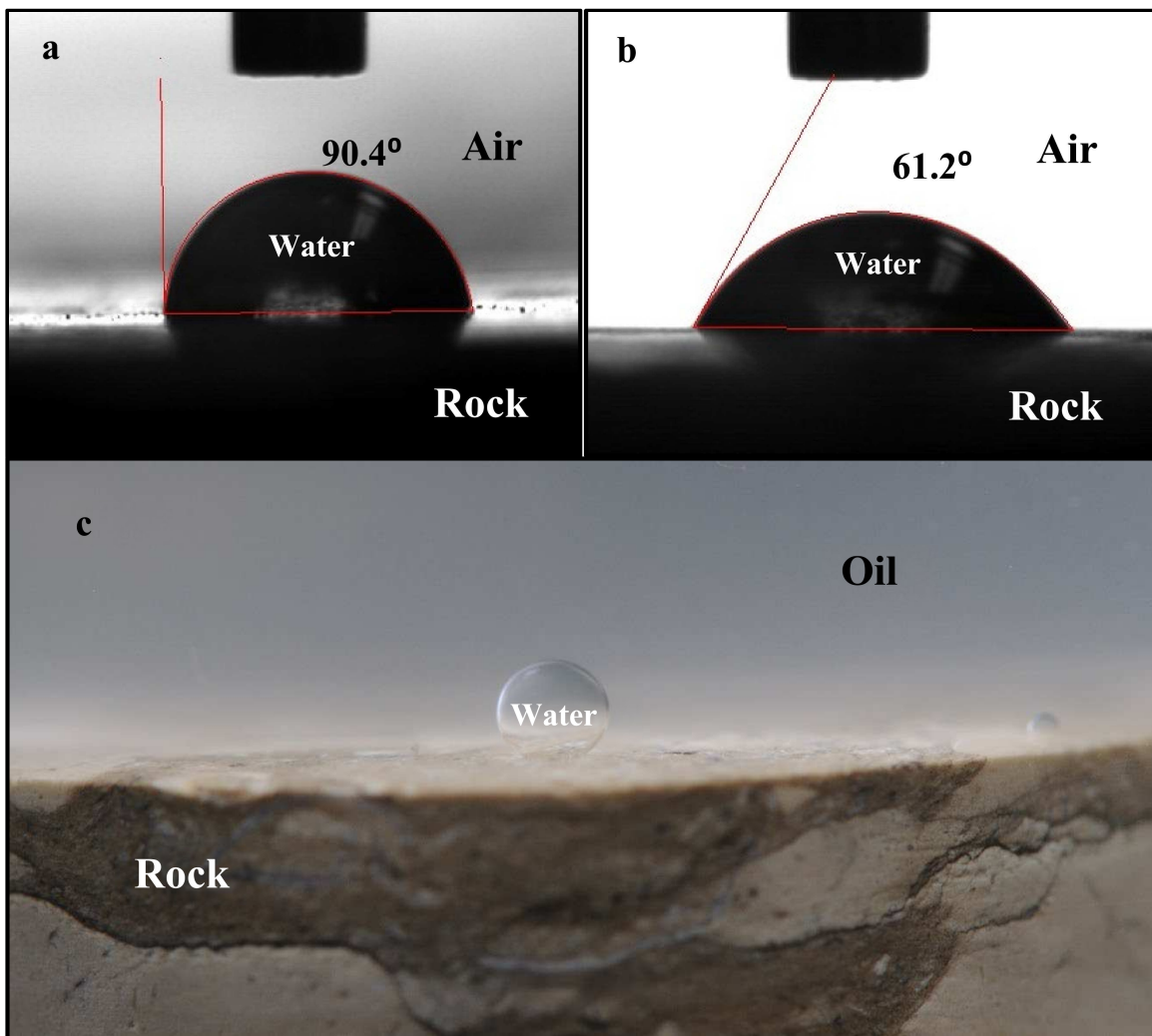


Fig. 5.5 Measured contact angle of water droplet at the dry surface of (a) dark gray and (b) light crystal part of the rock. (c) Sessile drop test result showing an initial wettability of the carbonate rock to the oil phase

5.3.2 Fluids

Nitrogen and fresh water were used for the core flooding experiments. Tap water with a hardness of 181 mg/l, pH of 7.9, and salinity of less than 50 mg/L was used as the wetting phase fluid. The water viscosity was considered to be 0.6527 cp at the test condition (Cooper and Dooley, 2008). Nitrogen gas, which was used as the non-wetting phase to displace water during the drainage process, has a density of ~ 0.1 g/ml and viscosity of ~ 0.184 cp at the test conditions (Lemmon and Jacobsen, 2004).

5.3.3 Core Flooding Set-up

A schematic of the test apparatus is shown in Fig. 5.6. The equipment consists of three main sections: 1) a pore pressure circuit, 2) a confining pressure circuit, and 3) a gas separation unit. The pore pressure circuit contains the sample itself plus two inlet lines for the separate injection of gas and water, one outlet line, three pressure transducers, and a thermocouple.

The specimen was first placed between two porous stones and wrapped inside a flexible lead jacket to prevent the diffusion of gas from the sample into the cell. It was then inserted into a Viton rubber sleeve, and mounted in a triaxial high pressure/temperature cell. Two high-sensitive pressure transducers (Honeywell, FP2000, 344 bar, and 0.25% accuracy) independently measured the inlet pressures at the gas and water lines, and a third read the outlet pressure of the cell. Two syringe pumps were used to inject water (Teledyne ISCO 260 HP) and nitrogen (Teledyne ISCO 260D) into the core through two separate lines. A Teledyne ISCO 260D pump was connected to the outlet of the core through a separation unit that maintained 1MPa pressure at the downstream end of the core. The confining pressure circuit contained the high pressure/temperature cell and two Honeywell FP2000 pressure transducers. A Teledyne ISCO 260 HP pump was used to pressurize and depressurize the confining fluid (water) inside the cell to create the triaxial confining stress. The gas separation unit consisted of 5 high-pressure vertical separation cylinders which were initially water filled (four with 50 ml and one with 500 ml capacity), and which gathered the fluids draining from the core and separated the phases in order to allow for the estimation of the phase saturation inside the core. The whole system was placed into a large Despatch LBB2 oven to maintain a temperature of $40^0(\pm 0.1^0)$ C inside the cell and cylinders, and within all lines.

Data logging from pressure transducers and thermocouples was performed using an Agilent 34972A data acquisition unit. It was combined with LabView-based data logging software, which was designed in-house. The data logging software, which was also connected to the ISCO pump controllers, could read pressures, volumes and flow rates from all pumps.

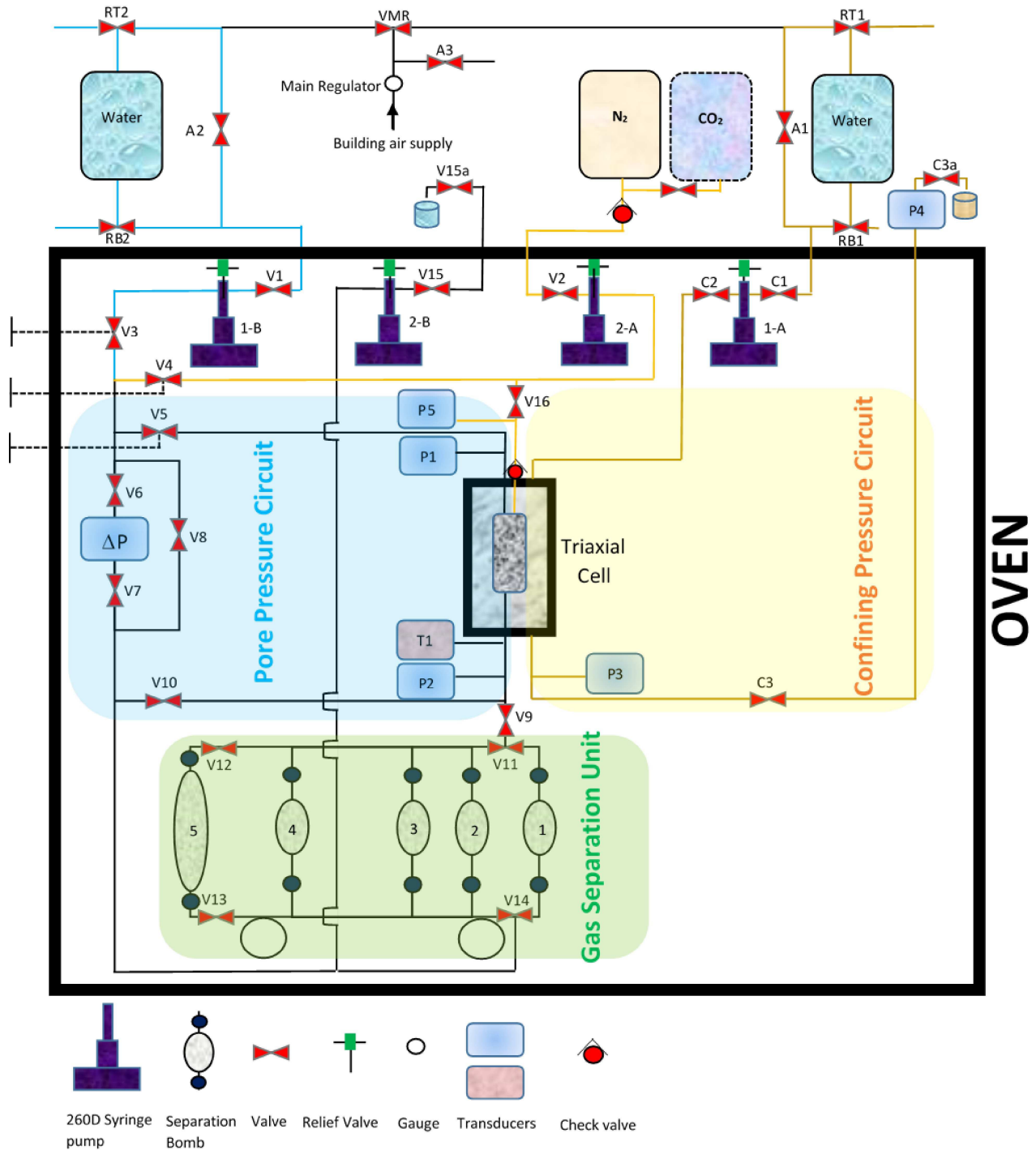


Fig. 5.6 Schematic of the core flooding apparatus

5.4 Methodology

The experiment was conducted at a rising isotropic effective confining stress levels from zero up to 30MPa. In this study, four different parameters: porosity, absolute permeability, drainage relative permeability, and drainage capillary pressure, were measured consecutively at each effective stress level.

Water was initially flushed to the evacuated, dried and cleaned specimen for several hours. Shosa and Cathles (2001) noted that even minor amounts of residual gas in the pore space compromised single-phase permeability measurements. The approach taken here for residual gas minimization was similar to that advocated by Shosa and Cathles (2001) whereby the gases in the pore space were displaced with CO₂ prior to evacuating the sample. The relatively high solubility of CO₂ in the water ensured that any gases remaining in the sample following evacuation will dissolve into the displacing water following re-saturation. Additionally, any evacuation was done over a liquid nitrogen cold trap. While this serves multiple purposes, it is noteworthy as it allows for the quantitative recovery of the water contained within the pore space following specific permeability tests. Once the sample was fully saturated, the confining pressure increased in a stepwise manner, while the back pressure pump maintained the pore pressure at a constant value (1 MPa). After the system temperature (40⁰C) was stabilized, the core was flooded with fresh water at one of several fixed rates (1-5 mL/min). At each rate, the water inlet and outlet pressure data across the core were recorded. After the completion of a single-phase (water) flow test, N₂ was co-injected into the sample through a second inlet line. In a stepwise manner, the flow of nitrogen was increased while the water flow rate was decreased by the same amount. The gas permeability at residual water saturation was determined in the last two steps, during which only the gas phase was injected through the sample at 5 and 10 mL/min. After a steady-state was achieved (typically after 20 pore volumes of injection), the pressure drop and injection pressure at each of the relative flow rates was recorded. The sample was subsequently flushed with CO₂ (50 pore volumes) to fully drive the nitrogen out of the core and decrease the water saturation down to the irreducible water saturation. The system was then purged and dried by a vacuum pump in combination with a condensation chamber that was cooled by liquid nitrogen. The outlet was then shut and water was injected into the core at high pressure (up to 20MPa depending on the confining pressure) using a syringe pump. The pressure was maintained

for several hours to allow the water saturate the sample gradually, displacing and completely dissolving any remaining CO₂. The core re-saturation process was more cumbersome at higher levels of effective confining stress as the times required to bring the core sample back to a defined state increases. The fully re-saturated core was now flooded with pure nitrogen (single-phase) at 6 different rates (1-5 and 8 mL/min); as earlier, the gas inlet and outlet pressure were recorded. The entire procedure was repeated at the higher stress levels without opening the cell.

The Darcy equation was used to calculate permeability (Ahmed and McKinney, 2011). Accordingly, for each permeability test, a steady-state condition was achieved by injecting appropriate volume of phases (10-20 times of core's pore volume). Additionally, the flow was maintained in the laminar regime for all tests ($N_{Re} < 10$ in Eq.(5.16)).

$$N_{Re} = \frac{q\rho d}{A\mu(1 - \phi)} \quad (5.16)$$

In Eq.(5.16) (Seader et al., 2010), the nominal sandstone grain size (d) is 200 μ m (Greenwald, 1981), the core and fracture cross section (A) are 0.16 cm² and 10.24 cm², respectively, and q , ρ , and μ are the flow rate, density, and viscosity of the flushing fluid, respectively.

5.4.1 Stress-Dependent Porosity and Absolute Permeability Measurement

At each stress state, increasing the effective stress induces rock compaction, which will force a certain volume of the pore water (ΔV) back into the pore pressure pump. Rewriting Eq.(5.7), changes in pore volume (V_p) and bulk volume (V_b) can be converted into the changes in the porosity of the sample using the following equation:

$$\phi_t = \frac{(V_p - \Delta V)}{(V_b - \Delta V)} \quad (5.17)$$

Once again, in the case of Eq.(5.17), we assumed zero grain compressibility. In case of fractured specimen, pore volume V_p should be replaced with fracture volume V_f in Eq.(5.17). A second approach was implemented to double-check the measured pore volume changes (ΔV). After applying the additional confining stress on the fully saturated sample with water, all of the water inside the lines and core was drawn out with the vacuum pump; it turned into ice inside the condensation chamber. Because the volume of the lines was known, the pore volume at each

stress state could be easily calculated by that figure from the volume of water in the condensation chamber. The data generated using both techniques were found to be in good agreement.

As noted, we used a HPHT triaxial cell to apply all-around isotropic effective confining stress to the specimen and measured the volumetric strain based on stress-dependent changes in the pore volume of the core instead of using internal LVDT sensors. This way, sleeve compressibility did not impact strain measurements. However, there may still be issues associated with sleeve compliance on the applied stress. Although end-caps and pedestals constructed from stainless steel convey the axial confining stress fully to the core, the thin core sleeve (lead jacket + Viton rubber sleeve) absorbs a small portion of radial confining stress. However, in this study due to the high range of applied confining stress up to 30MPa, we ignored the impact of the sleeve on the radial effective stress, hence in the calculation of stress-dependent porosity.

Absolute permeability is defined as the ability of a porous medium to transmit single-phase non-reactive fluid through a pore network which is 100% saturated with the same fluid (Peters, 2012). For a steady-state linear single-phase incompressible fluid flow in a vertical core (downward flow), the Darcy law can be expressed as follows (Dake, 1983):

$$q = -\frac{kA}{\mu L}(\Delta P - \rho g) \quad (5.18)$$

Based on Eq.(5.18), a graph of ΔP versus q for an experiment of steady-state flow at several rates should be a line with a slope of m . Accordingly, absolute permeability can be calculated using Eq.(5.19).

$$k = \frac{\mu L}{mA} \quad (5.19)$$

In the current study, steady-state permeability test at constant water flow rate was used to measure the absolute permeability of the sample when fully saturated with water. To achieve this, water was initially flushed at 1 mL/min through the sample until the steady-state condition (constant pressure drop across the sample, ΔP_{SS}) was reached. The same process was repeated for several different flow rates (1-5 mL/min).

5.4.2 Stress-dependent Drainage Relative Permeability and Capillary Pressure

Measurement

The approach used in this experiment to measure the relative permeability of confined core inside a triaxial cell was similar to the technique proposed by Hassler (1944), known as the Hassler method (Osaba et al., 1951; Richardson et al., 1952; Peters, 2012). In the current study, we tried to redesign the triaxial compression cell in order to apply Hassler's relative permeability apparatus. At steady-state, given a uniform saturation distribution across the vertical sample with a downward flow direction, the following linear integration of Darcy's law can be used to calculate relative permeability:

$$k_{rw} = -\frac{\mu_w q_w L}{kA(\Delta P_w - \rho_w gL)} \quad (5.20)$$

$$k_{rg} = -\frac{\mu_g q_g L}{kA(\Delta P_g - \rho_g gL)} \quad (5.21)$$

where k_{ri} (i=w or g) defines the relative permeability of phase i. In Eq.(5.21), the gas viscosity at the given experimental condition is assumed to be pressure independent, and the effect of gas expansion along the flow path is considered to have no significant impact on the experimental results (Richardson et al., 1952).

For the drainage test, the experiment started immediately after the water absolute permeability test was fulfilled. Then, wetting and non-wetting (Nitrogen gas) phases were injected simultaneously, at the rates of q_w and q_g , directly into the core through the separate water and gas lines at a flow fraction of $q_w/q_t = 0.8$ or $q_g/q_t = 0.2$ (e.g. 4 ml/min water and 1 mL/min gas), until the steady-state condition was achieved. At the steady-state condition, the recorded pressure drop between the downstream and upstream transducers no longer changed with time. The gas separation cylinders were then weighed and mass-balance was calculated in order to accurately measure the saturation of the sample. As in the method presented by Huo and Benson (2016), the process was repeated for different flow fractions ($q_w/q_t = 0.6, 0.4, 0.2, 0$) at a controlled total volumetric flow rate of 5 mL/min to obtain relative permeability at a wide saturation range. In the final step, to obtain the results for a higher gas flow rate, the gas was flushed at 10 mL/min.

However, as was noted above, the multiphase flow solution from Eqs.(5.20)-(5.21) is not valid in presence of the capillary end-effect (Peters, 2012). To achieve a uniform saturation distribution across the core (or eliminate the capillary end-effect), as recommended by Richardson et al. (1952), thresholds for a high flow rate and sufficient flowing time were assigned for each test. Additionally, a special porous stone with a capillary pressure lower than that of the sandstone rock was placed at the core outlet to ensure that the outlet capillary pressure dropped gradually, from a high value in the porous rock to a negligible value at the pedestal. Additionally, the applied triaxial confining stress ensured that there was good contact between the cores and the porous discs. The use of these techniques resulted in good agreement between the calculated relative permeability curves and previous experimental results in the literature on the same material under similar test conditions.

To measure capillary pressure, a secondary experiment was run using the modified stationary liquid method, first introduced by Leas et al. (1950) (Pini and Benson, 2013). In this method, the capillary end-effect is eliminated by keeping the wetting phase immobile in the core through the application of capillary forces (Osaba et al., 1951). The method can be applied in the calculation of the relative permeability of the non-wetting phase as well. In following the method, the core, initially fully saturated with the wetting phase (water), is flushed with the non-wetting phase (nitrogen) at constant rate of 1 mL/min until a steady-state condition is achieved. Similar to the first technique, the gas separation unit, placed immediately after the cell, collects the whole phases from the core and separates them. The separation bombs weight, known at the initial condition, and the injected gas phase data are applied into the mass-balance equation to calculate the saturation of the wetting phase inside the core at each step. This step is repeated for different rates (1 to 5 and 8 mL/min). Pini and Benson (2013) showed that the difference between the gas inlet pressure and the outlet pressure is equal to capillary pressure at the inlet face of the core ($P_g|_{inlet} - P|_{outlet} = \Delta P_g = P_c|_{inlet}$) when the wetting phase is immobile ($dP_w/dx = 0$) at a steady-state condition. Accordingly, in our study, the drainage capillary pressure curves were measured.

In the absence of capillary end-effect at steady-state condition, previous studies have shown that uniform saturation profile (hence constant k_r and P_c) across the core is a valid assumption while injecting gas and water phases simultaneously; hence Eqs.(5.20)-(5.21) can be

used for drainage relative permeability calculation for our first two-phase technique's experimental data. However, the accuracy of the uniform saturation assumption is in question for the last steps where the core is flushed 100% with gas and water phase becomes immobile (Krevor et al., 2012); although it has been applied broadly in the literature (Peters, 2012; Perrin and Benson, 2010). To confirm the accuracy of the presented k_{rg} end-point at S_{wir} in this study, we re-calculated it using the first derivative of a fitted curve on q_g data as a function of corrected gas pressure drop ($\Delta P_g - P_e$) in Eq.(5.22) instead of their actual values in Eq.(5.21) (Suggested by Krevor et al., 2012 and Pini and Benson, 2013).

$$k_{rg}(S_{wir}) = \left(\frac{\mu_g L}{kA} \right) \frac{dq_g}{d(\Delta P_g - P_e)} \quad (5.22)$$

In this equation, P_e is the entry capillary pressure and the assumption of uniform saturation was no longer applied. Note that we utilized polynomial functions with zero offset to fit curves on the measured data from the second technique (modified stationary liquid method) all at 100% gas flow and then extract its slope at S_{wir} (e.i. $q_g = 8ml/min$) to be inserted in Eq.(5.22).

5.5 Results

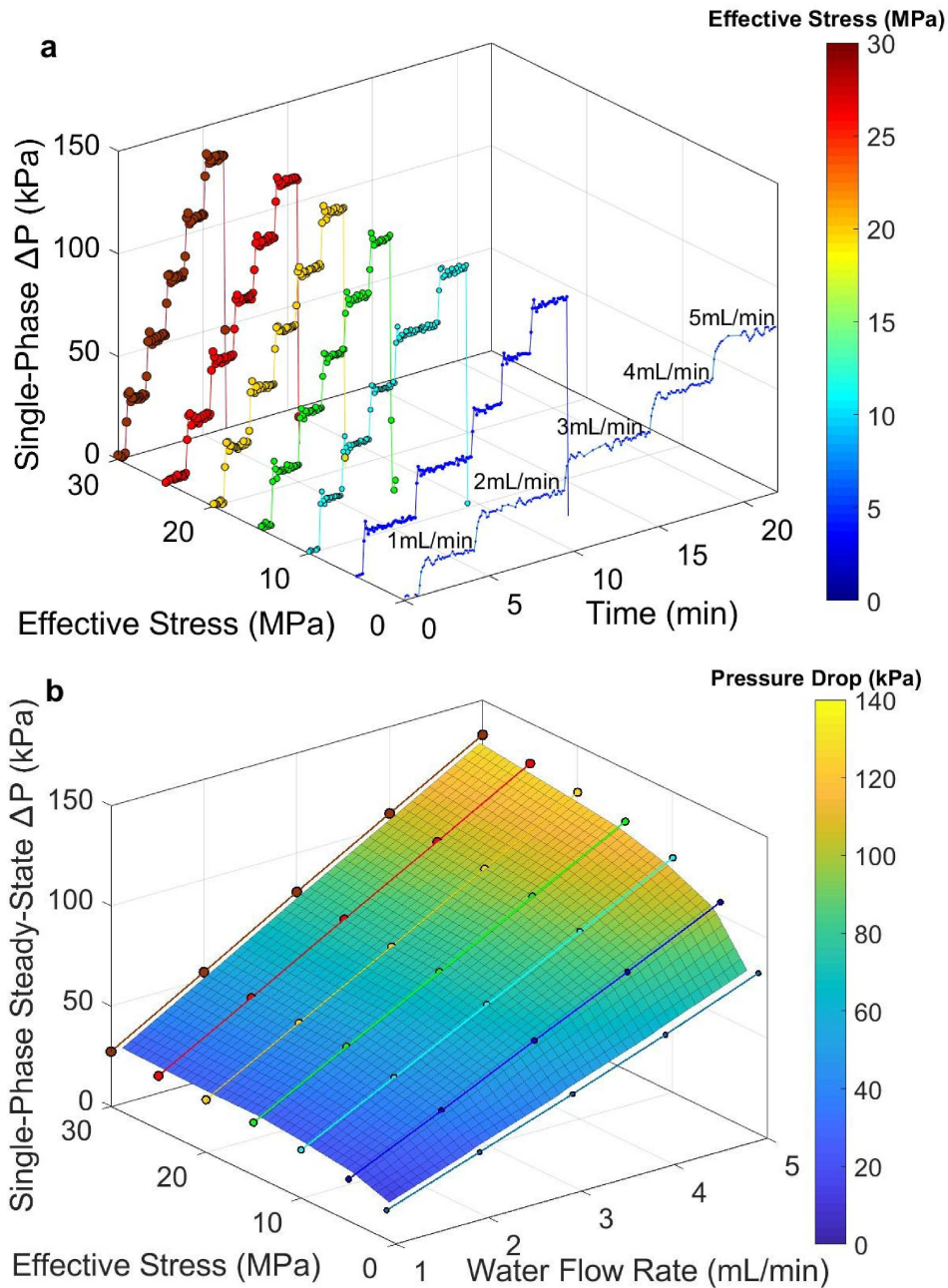
5.5.1 Stress-dependent Porosity and Absolute Permeability

As illustrated in Fig. 5.7a, the pressure drop across the Berea sandstone sample (ΔP) during constant flow permeability tests (1-5 ml/min steps) became greater as effective confining stress increased. The 3D surface of single-phase steady-state pressure drop with effective stress and water flow rate, shown in Fig. 5.7b, demonstrates an upward trend in pressure drop corresponding with increases in both effective stress and flow rate.

Fig. 5.8a shows a decline in measured stress-dependent porosity and absolute permeability values corresponding with increases in effective stress under isotropic effective confining stress conditions; it merges the results of the Berea sandstone experiment carried out in this study with the values calculated using the equations given in section 5.2.

Similarly, Fig. 5.9a presented the measured stress-dependent permeability versus porosity plots of the fractured Calumet carbonate. A plot of normal effective stress versus fracture closure

and loading/unloading hysteresis effect was given in Fig. 5.9b. Using Barton–Bandis fracture model (Eq.(3.42)) to fit a curve on the experimental results, initial stiffness and maximum possible closure of the fracture were calculated equal to 33.71GPa/m and 0.16mm, respectively. Least square regression method was used to calculate these constants in Eq.(3.42).



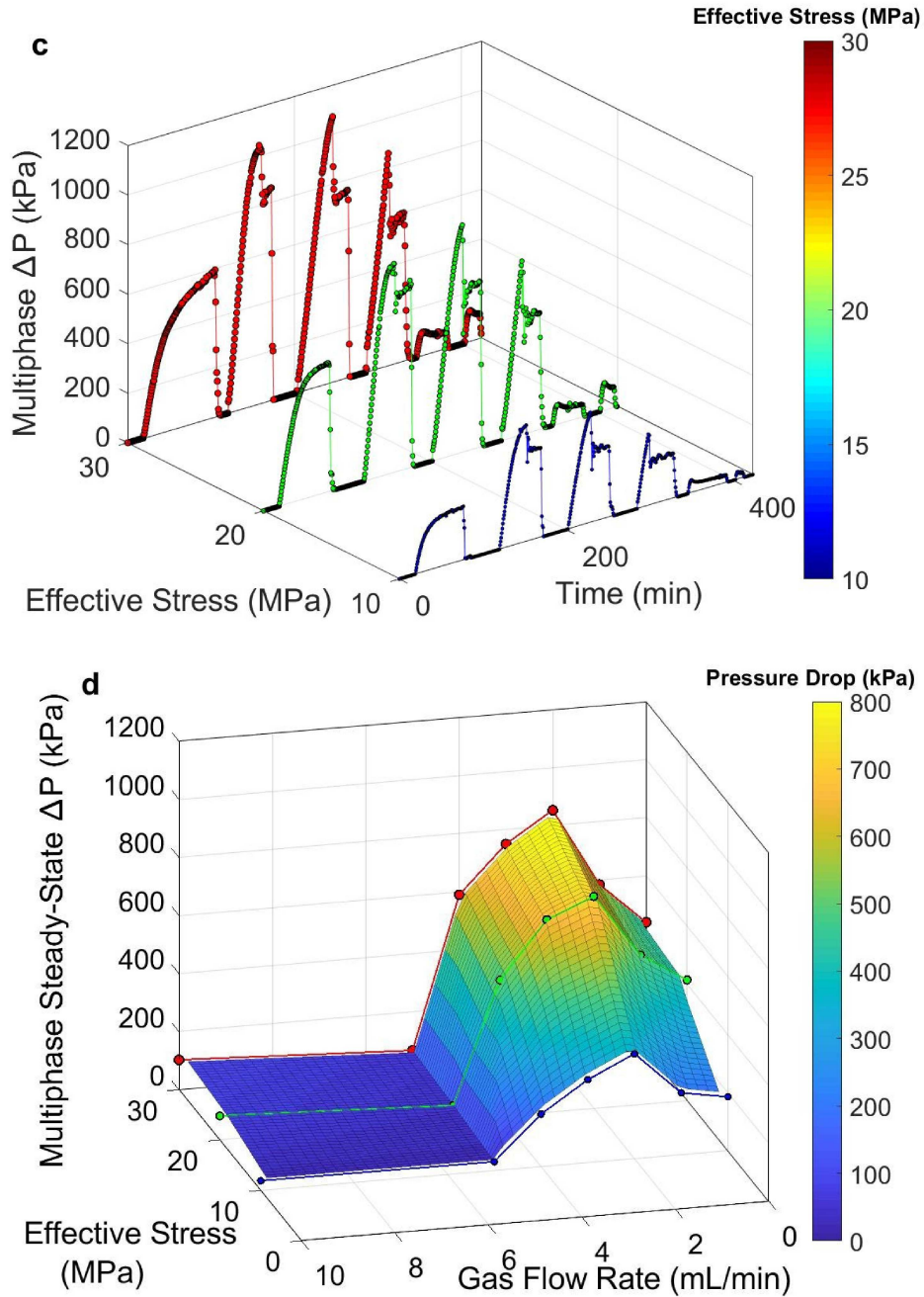


Fig. 5.7 This figure provides 3D plots of stress-dependent single-phase pressure drop versus (a) time (min), and (b) water flow rate (mL/min) and stress-dependent multiphase pressure drop versus (c) time (min), and (d) gas flow rate (mL/min) across the Berea sandstone specimen.

5.5.2 Stress-Dependent Drainage Relative Permeability and Capillary Pressure

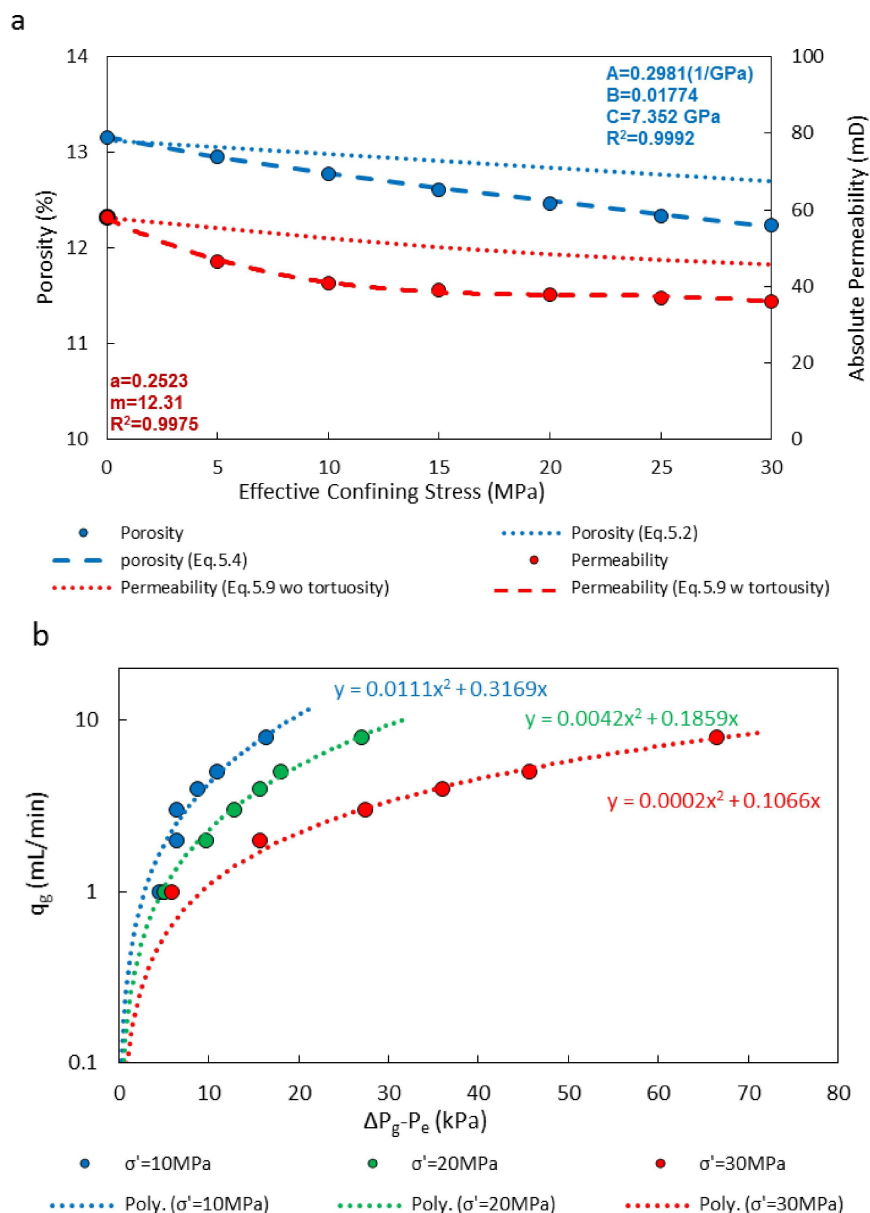
Fig. 5.7c displays pressure drop (ΔP) data from two-phase core flooding experiment across the Berea sandstone sample over time at three different effective confining stresses. Each

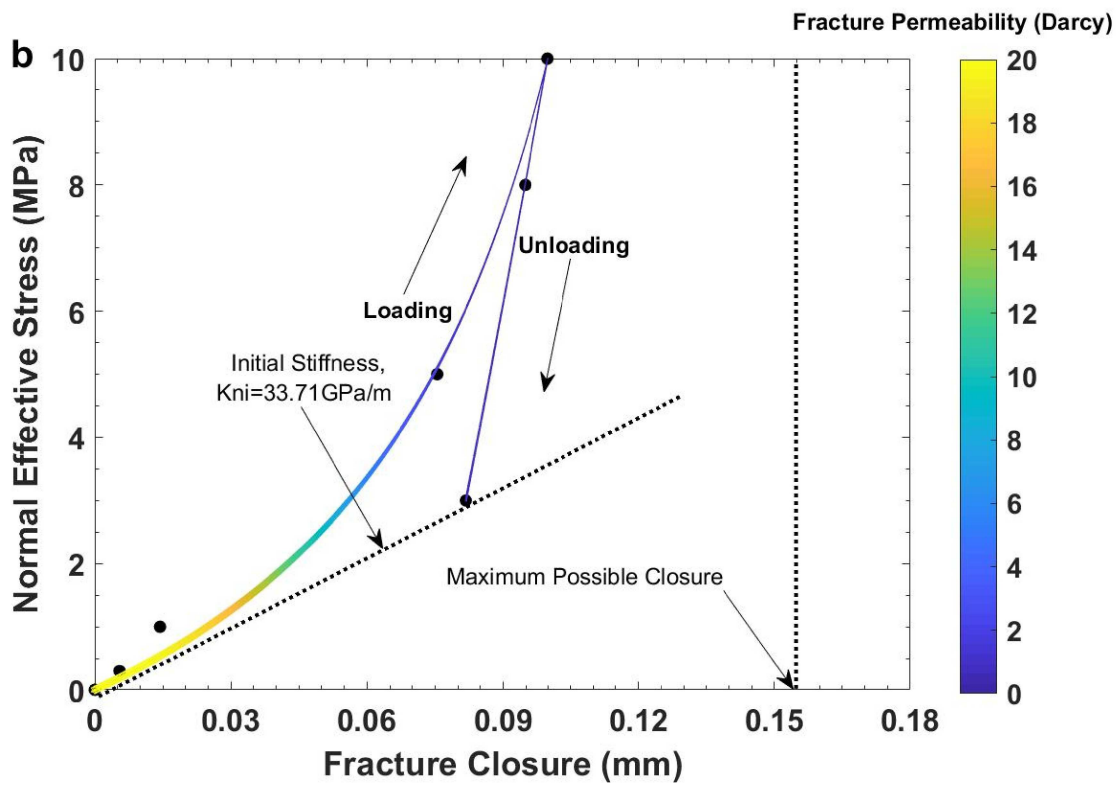
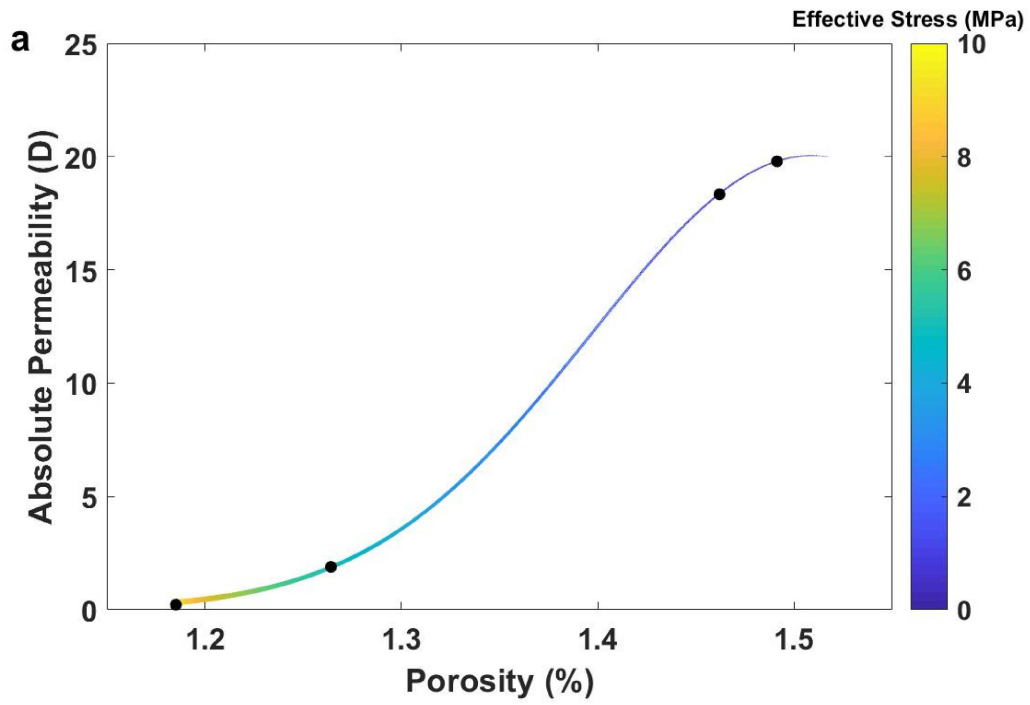
upward ΔP curve corresponds to a single flooding test at a fixed N_2 /water flow fraction. To give a sense on how the pressure drop changes with increases in gas flow rate across the core at a steady-state condition, Fig. 5.7d presents three curves corresponding to three different isotropic effective confining stresses (10, 20, and 30 MPa) applied in this study, fitting a 3D polynomial surface on them. At each two-phase flow ratio, a total of some 10-20 pore volumes of fluids (water + gas) is flushed through the core in order to reach the steady-state condition at which the pressure drop (ΔP) in the core becomes constant. The curves of the measured multiphase steady-state ΔP (Fig. 5.7d), as a function of the gas flow rate at fixed effective confining stress, similarly show an initial rising trend up to the point of $q_g = 2 \text{ mL/min}$ (or $q_g/q_t = 0.4$), and then decline sharply. This can be interpreted by positing that the low effective gas permeability exhibited by the sample from a low initial gas saturation up to a critical gas saturation was followed by a dramatic rise in the gas effective permeability at post-critical gas saturation.

Fig. 5.8b provides the experimental data (Berea sandstone) of gas injection rate (mL/min) versus corrected gas pressure drop ($\Delta P_g - P_e$) at steady-state in semi-log scale combined with the second order polynomial fitted curves. These data are extracted from the second technique (modified stationary liquid method) all at 100% gas flow. Based on Eq.(5.22), k_{rg} at S_{wir} is proportional to the slope of the stress-dependent curves at $q_g = 8 \text{ mL/min}$. The calculated stress-dependent end-points of k_{rg} based on Eq.(5.22) are inserted in Fig. 5.8c (colored stars) to compare with the calculated one based on Eq.(5.21) with uniform saturation assumption. Fig. 5.8c and Fig. 5.9c depict the changes in the experimental relative permeability data under increasing effective stress conditions from intact Berea sandstone and fractured Calumet carbonate experiments, respectively. As it is expected, based on the discussion given in Chapter 3, mixed-wet Calumet carbonate and water-wet Berea sandstone show shifts in relative permeability curves in opposite directions in response to an increase in effective stress. In a same way, Fig. 5.8d and Fig. 5.9d illustrate the evolution in the measured capillary pressure curves at different effective stress conditions for intact Berea sandstone and fractured Calumet carbonate specimens. Results presented in Fig. 5.8d and Fig. 5.9d were obtained mainly by using the second technique, discussed in section 5.4.2. Comparing Fig. 5.8d and Fig. 5.9d, we observe higher stress sensitivity of capillary pressure curves for the Calumet carbonate due to the presence of a well-mated (smooth) artificial fracture. This is also a reason for the non-linear increase of P_c of the fractured Calumet carbonate at 1 MPa effective stress. Additionally, non-

linear k_r curves in Fig. 5.9c contradicts the assumption of the linear classical flow model in a slit. This is due to the impact of effective stress and closure of the well-mated fracture which makes the fracture to act mainly similar to a porous rock.

In Fig. 5.8c-d and Fig. 5.9c-d the modified Brooks-Corey type curves for relative permeability and capillary pressure (Eqs.(5.12)-(5.14)) are given as well. In this research, all of the fitting constants in Eqs.(5.12)-(5.14) have been obtained using least square regression method (Table 5.4). It can be understood from the calculated R^2 in Table 5.4 that the Brooks-Corey type curves describe the capillary pressure and relative permeability data with an acceptable accuracy.





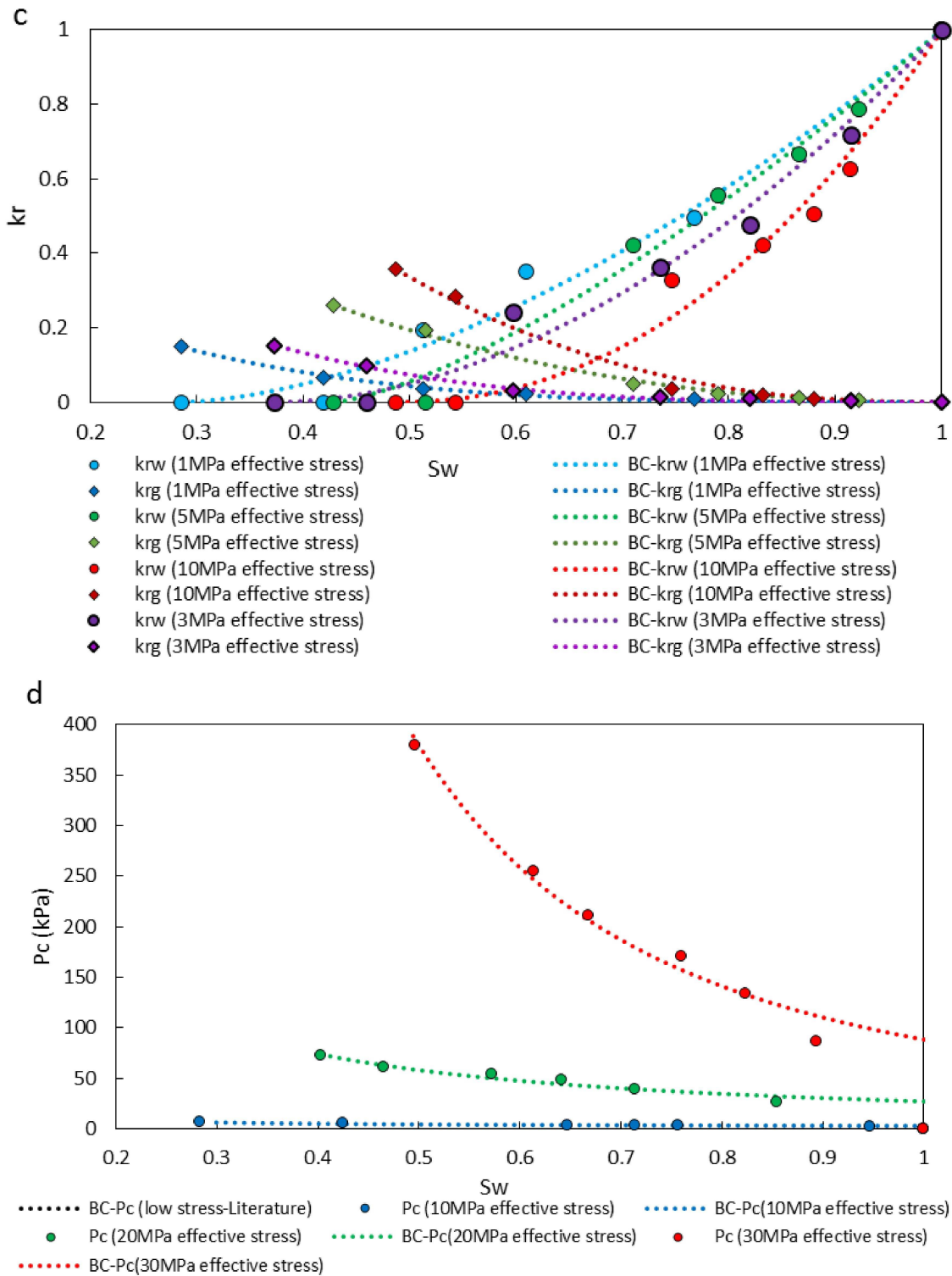


Fig. 5.9 This figure presents our experimental stress-dependent plots of: (a) porosity and absolute permeability, (b) fracture closure, (c) relative permeability curves, and (d) capillary pressure curves of the fractured Calumet carbonate specimen. All data are provided in Appendix B.

Table 5.4 Calculated fitting constants in Eqs.(5.12)-(5.14) for the Berea sandstone experiment

Parameter	σ' (MPa)	S_{wir}	k_r Endpoint	n_w	n_{nw}	β	P_e (MPa)	R-square
k_{rw}	10	0.316	1	2.704	-	-	-	0.964
k_{rg}		-	0.396	-	4.784	-	-	0.9975
P_c		0.309	-	-	-	-0.1659	10.47	0.9742
k_{rw}	20	0.243	1	2.329	-	-	-	0.9837
k_{rg}		-	0.345	-	3.584	-	-	0.9966
P_c		0.236	-	-	-	-0.4716	11.37	0.9682
k_{rw}	30	0.245	1	2.193	-	-	-	0.9941
k_{rg}		-	0.267	-	3.363	-	-	0.9923
P_c		0.265	-	-	-	-0.9687	14.51	0.9770

5.6 Discussion

This study fundamentally investigates stress dependency of multiphase flow properties of porous media. It measures stress-dependent porosity, absolute permeability, relative permeability, and capillary pressure via a continuous procedure implemented on an intact Berea sandstone and fractured Calumet carbonate using nitrogen and water as the flowing phases. The study was novel in that all four petrophysical properties were measured consecutively in a triaxial cell under an isotropic isothermal effective confining stress condition. The equipment enabled us to track the impacts of stress on both single-phase and multiphase flow properties of the samples with high accuracy. Additionally, all parameters were investigated under the exact same stress, pore pressure, and temperature, thus allowing for a more reliable and consistent explication of the results. The experiments were carried out under a wide range of effective stress values (zero up to 30 MPa for Berea sandstone and zero up to 10MPa for Calumet carbonate), which permitted us to position the results reported in the literature for the same liquid pair systems within a framework similar to that of the current study. We were also able to use the results from previous studies as a benchmark to compare with the current experiment at a higher effective stress.

5.6.1 Reproducibility of Sandstone Experimental Data

Reproducibility of the core flooding experimental results is a significant concern especially when we are dealing with water flow through sandstone specimens. A decline in the absolute permeability of Berea sandstone has been reported in the literature in response to water

flushing and several researchers have treated their specimens initially at high temperature ($>500^{\circ}\text{C}$) to constrain their time-dependent property changes due to clay swelling (Oak et al., 1990; Pini and Benson, 2013; Jordan et al., 2016; Reynolds and Krevor, 2015). However, a tremendous impact of heat-treatment at temperatures above 200°C on hydro-mechanical properties (e.g. rock strength, elastic modulus, porosity, and permeability) of sandstone specimens has been proven experimentally (Fang, 2013; Yu et al., 2015; Ranjith et al., 2012). Lintao et al., (2017) revealed a sharp decline in Young's modulus of sandstones from core-scale experiments and shifts in pore size distribution (i.e. increase in porosity) from pore-scale visualization at a temperature higher than 400°C . In this study, we heated the sample initially at a typical average reservoir condition of 100°C for 10 hours to: 1) make the sample dry and stabilized, and 2) avoid dramatic changes in natural hydro-mechanical properties of the sample due to high-temperature heat treatment effect. However, we studied several factors that may affect the reproducibility of the experimental data, and have attempted to minimize their destructive impact on the data, as well as checking the repeatability of results for our study.

The first factor is time and almost all the observed permeability changes of Berea sandstone due to the effect of clay swelling were collected for a long-time intervals (e.g. one year for Oak et al., 1990). The porosity and absolute permeability data illustrated in Fig. 5.8a are measured in a single day to make effective stress the only conditional variable. For multiphase flow tests, the absolute permeability is re-measured at each step to make sure on the validity of the calculated relative permeability and capillary pressure (process is explained in section 5.4).

Secondly, hysteresis effect due to inelastic deformation is a common phenomenon in stress-strain curves of sandstones in which the rock strain do not follow the same path during loading and unloading cycles (Shalev et al., 2014). Applied effective stress on the sample varies by changing either the pore pressure (e.g. during the core flooding) or the confining pressure. It is very important to limit effective stress fluctuation to avoid unintended irreversible deformation due to the hysteresis effect. In our study, we had managed actively to raise effective stress in a stepwise manner and keep the pore pressure fully constant to attenuate the hysteresis effect.

The presence of a second phase inside the porous media is the next significant factor that greatly impacts the measured absolute permeability and lowers it to the effective permeability

(Muskat, 1937). This makes core re-saturation process the biggest challenge that should be tackled when single-phase and multiphase flooding experiments are conducting interchangeably. In this study, a complete process, given early in section 5.4, is used to re-saturate the sample and its success has been confirmed by re-measuring permeability after each re-saturation process.

Keeping the test temperature steady for all the steps is the critical key for test of repeatability of results. Temperature has a major impact not only on fluid and rock independent properties and interactions but even on the mechanical equipment (e.g. transducers and pumps) performance and calibration. Special care has been assigned to this factor in our experiments by locating the whole apparatus inside a fixed temperature oven with temperature oscillation in the range of 0.1°C .

Wettability alteration during flushing the brine saturated specimen with CO_2 is the next concern in CO_2 -sand-water systems. Kim et al., (2012) reported great changes in the brine contact angle (0° - 80°) on the silica surface due to the reaction between dissolved supercritical CO_2 in brine and silica. Mechanistically, brine pH decreases from 6 to 3 as a result of dissolving supercritical CO_2 in it. This acidic environment diminishes the surface negative charge of silica by attaching an H^+ to O^- , which leads to destabilization of water film and increase in the brine contact angle. In the current experiments, CO_2 was only used to displace N_2 from the sandstone specimen at irreducible saturation of water (not brine) at the end of each flooding experiments. Additionally, the flushed CO_2 was evacuated immediately using the vacuum pump and froze in the cold trap at the liquid nitrogen temperature. Using this procedure, we expected minimal changes in contact angle during the core-flooding experiments, which has confirmed experimentally by double-checking the contact angle at the end of each step.

Using the given methodology, we tried to minimize the destructive impact of abovementioned factors on rock properties. As illustrated in Fig. 5.10, we re-measured the stress-dependent porosity and absolute permeability of our Berea specimen after 5 months from its initial measurement (end of the experimental program on Berea sandstone), where we noticed less than 1% and 8% drop in porosity and absolute permeability, respectively. These small declines were interpreted as a consequence of hysteresis effect during loading-unloading cycles and clay swelling.

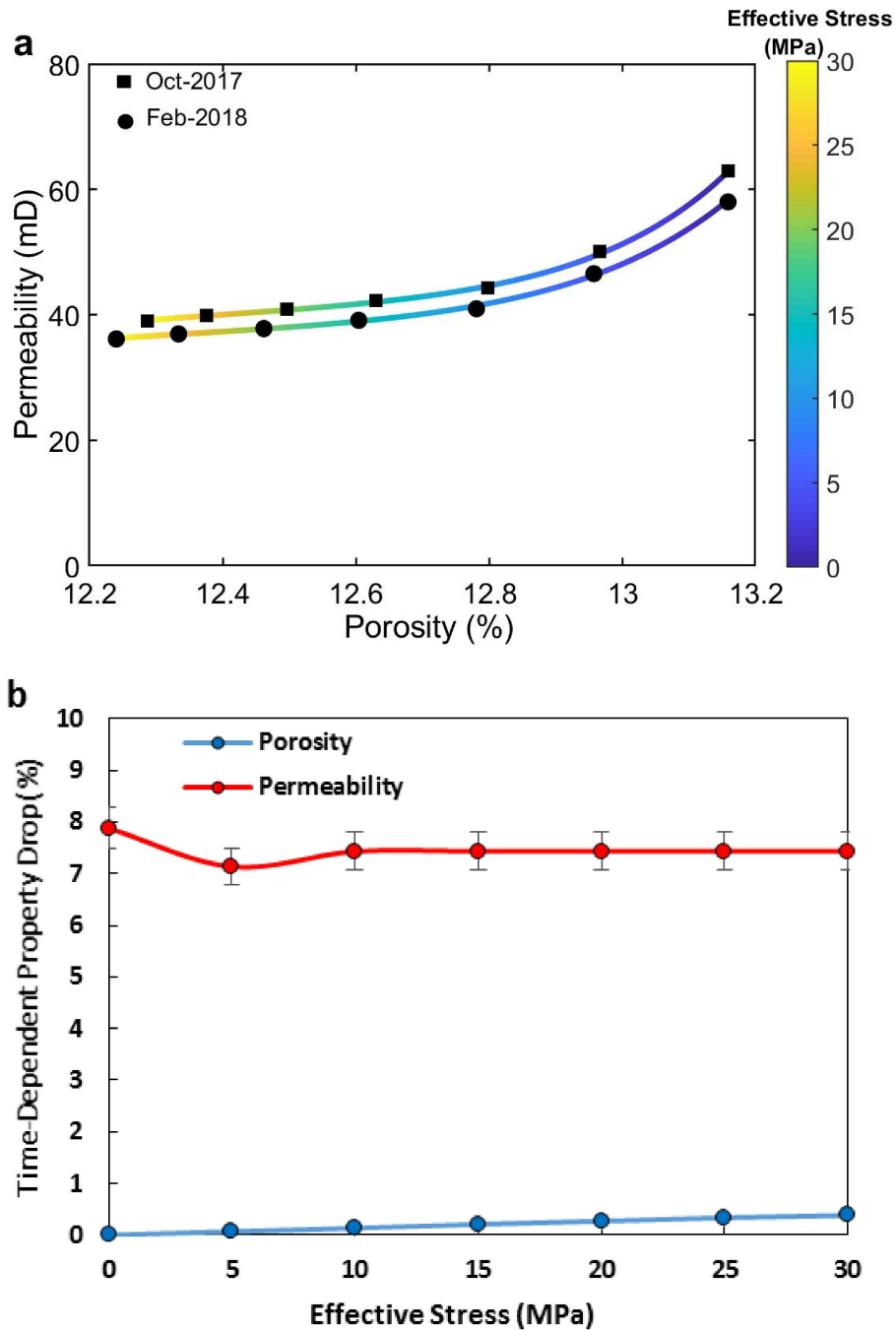


Fig. 5.10 Plot (a) illustrates a small downward shift in stress-dependent porosity-absolute permeability curve of Berea sandstone after 5 months and plot (b) indicates the percentage of decline of each property at different effective stress condition

5.6.2 Stress-Dependent Porosity and Absolute Permeability of Berea Sandstone

In Fig. 5.8a, the blue dotted line is calculated based on linear-poroelastic theory (Eq.(5.2)) with mechanical properties of Berea sandstone taken from the literature. Comparing

the test data (indicated with blue circle symbols) with the dotted line, which is derived from linear-poroelastic theory, reveals the nonlinearity of the stress-dependent porosity of Berea sandstone. It should be considered, however, that a slight change in the elastic parameter of the rock (e.g. Young's modulus) could result in a better match. However, the nonlinear correlation given in Eq.(5.4), when combined with the application of least square regression technique to calculate the constants given in Fig. 5.8a (top right), resulted in a great match with the stress-dependent porosity data (indicated with blue dashed line). Additionally, applying Eq.(5.9) to calculate permeability with the assumption of constant tortuosity (indicated with red dotted line) turns out not to be appropriate in the simulation of the stress-dependent absolute permeability of Berea sandstone (indicated with red circle symbols). The red dashed line is produced by the same equation with the assumption of stress-dependent normalized tortuosity (Eq.(5.11)); least square regression method is used to calculate fitting constants given in Fig. 5.8a (bottom left). This proves the importance of the normalized tortuosity factor in the calculation of the stress-dependent absolute permeability of Berea sandstone. This great change in normalized tortuosity can be a result of stress-induced pore-scale flow-line deformation, pore-shape alteration, flow line blockages, and new tensile micro-cracks creation.

5.6.3 Stress-Dependent Relative Permeability of Berea Sandstone and Two-phase Flow

Modelling

Fig. 5.8c clearly shows a leftward shift in experimental relative permeability data with increasing the effective confining stress. Based on several experiments on Torpedo sandstone samples, Owens and Archer (1971) observed that when the wettability of the rock to the non-wetting phase (which was oil in their experiments) is increased, the intersection of the relative permeability curves of the wetting and non-wetting phases shifts to the left. The current experimental data reveals the same leftward shift of the relative permeability curves which was achieved without changing the wettability of rock to the water, but only with changing the pore size in response to applied effective stress. In the same way, the irreducible water saturation values, which are an indication of the wetting phase resistance against further penetration of the non-wetting phase during the drainage process (Dullien, 2012), decreased significantly with increases in effective stress (Fig. 5.8c). Craig Jr., (1971) indicated that moderately to strongly water-wet rocks tend to have irreducible saturations in the range of 20–40%. Based on this definition, the Berea sandstone rock in this study, apparently, was converted from an initially

strong water-wet rock into a moderate to weak gas-wet rock at effective confining stresses of more than 20 MPa.

A comparison between the calculated end-point of k_{rg} with and without uniform saturation assumption (Eqs.(5.21) and (5.22), respectively) in Fig. 5.8c revealed a fairly uniform distribution of the wetting phase across the homogeneous core at the steady-state condition in this study, as small variations were noticed in the data point. This further showed the conformity of the measured data from two techniques in this study.

Using the relative permeability data measured in this study and the approximate non-wetting phase fractional flow (f_g , Eq.(5.23)), the stress-dependent fractional flow lines versus saturation for the sample at 10, 20, and 30 MPa isotropic isothermal effective confining stress are illustrated in Fig. 5.11a. The drainage end-point mobility ratios ($M_w = (k_{rg-max} \times \mu_w)/(k_{rw-max} \times \mu_g)$) at effective stress equal to 10, 20, and 30 MPa are calculated equal to 14.08, 12.26, and 9.49, respectively.

$$f_g = \frac{1}{1 + \frac{k_{rw}\mu_g}{k_{rg}\mu_w}} \quad (5.23)$$

It is noteworthy that as the core flooding experiment in this study was implemented at a high flow rate, in Eq.(5.23) the impacts of capillary and gravity forces are shown to be negligible compared with the high viscous forces. Fig. 5.11a demonstrates the profound impact of stress on the calculated fractional flow based on the data obtained in this study. Additionally, it provides flooding front gas saturations (S_{gf}) equal to 0.4, 0.532, and 0.573 at the corresponding effective stress conditions of 10, 20, and 30 MPa, respectively.

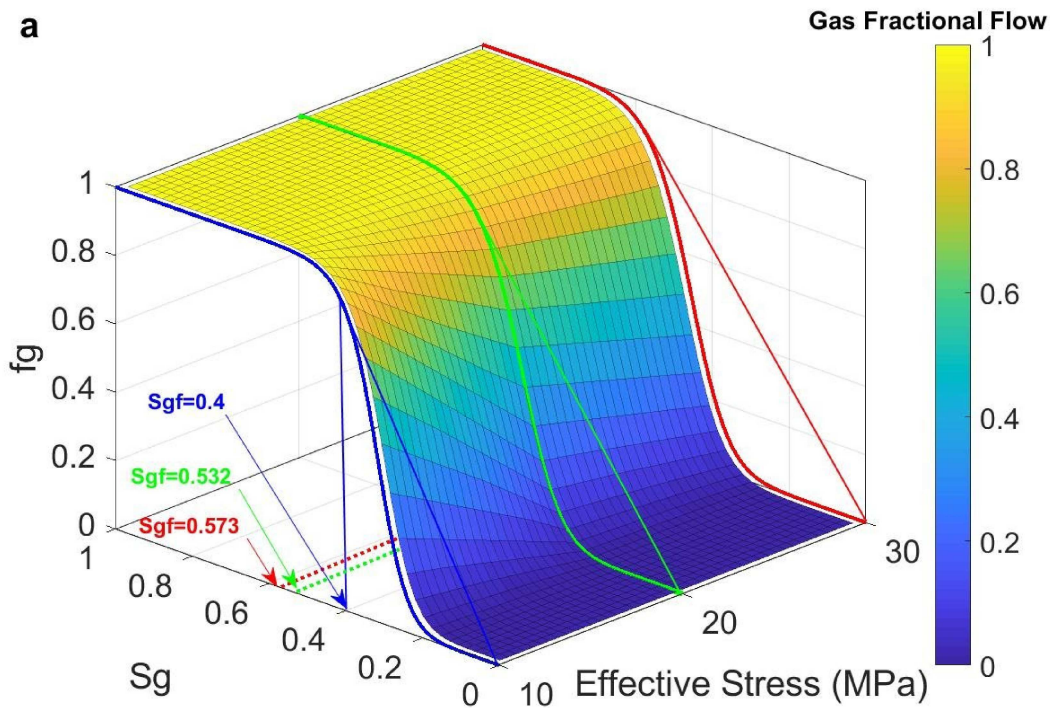
Using the Buckley-Leverett approximate solution and assumptions for immiscible displacement (Buckley and Leverett, 1942), the gas saturation (S_g) versus dimensionless distance from the core inlet (X_D) for the current experimental study was calculated from Eq.(5.24) at constant $T_D = 0.3$ and is depicted in Fig. 5.11b.

$$X_D = T_D \frac{df_g}{dS_g} \quad (5.24)$$

Fig. 5.11b confirms a decreasing trend in the front velocity of the non-wetting phase through the sample as effective confining stress increases, or similarly as the effective permeability of gas decreases. However, the lower front velocity at higher effective stress is accompanied by a higher front gas saturation, which results in a higher sweep efficiency of water with gas.

Fig. 5.12a-b compare the pressure drop (ΔP) versus dimensionless time (T_D) at different effective confining stresses for the simultaneous N_2 and water flow at gas flow fractions of 0.4 (2mL/min nitrogen and 3mL/min of water) and 0.6 (3mL/min nitrogen and 2mL/min of water), respectively.

$$T_D = \frac{qt}{V_p} \quad (5.25)$$



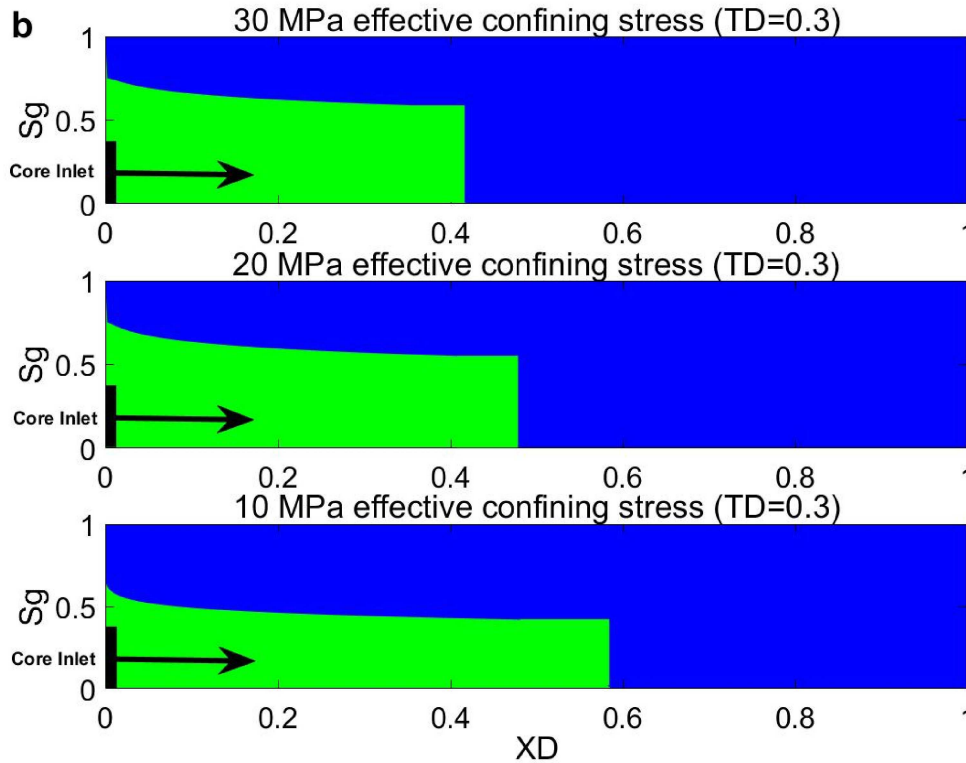


Fig. 5.11 This figure provides: (a) 3D plot of stress-dependent gas fractional flow curves versus gas saturation and (b) stress-dependent gas front location and saturation profile for Berea Sandstone

In Eq.(5.25) (Peters, 2012), used in the calculation of dimensionless time, the pore volume (V_p) is a stress-dependent variable in this study and q is the total mixed phase flow rate. As shown in the plots in Fig. 5.12, all curves present an initial linear increase in ΔP up to a point where their slopes start to decline gradually until they drop off suddenly at a distinct peak value; and finally ΔP becomes steady at a certain level. The initial linear build up in ΔP occurred in response to the accumulating fluid volume inside the tubes before the sample while the flow through the sample was still negligible. Later, as the inlet pressure increased, the flow of water and gas began to increase; and this led to an aberration in the ΔP curve from the initial linear trend. The peak ΔP represents the gas breakthrough time at which the gas arrived at the outlet end of the core; a steady-state condition commenced afterward. Fig. 5.12 also shows that gas breakthrough time increases with increasing effective confining stress at a fixed fluid flow rate and temperature. This is a result of the higher gas effective permeability of the sample under lower effective confining stress. Additionally, it is clear from Fig. 5.12 that excess effective

confining stress results in higher ΔP at a steady-state condition, which corresponds with a lower permeability of the non-wetting phase.

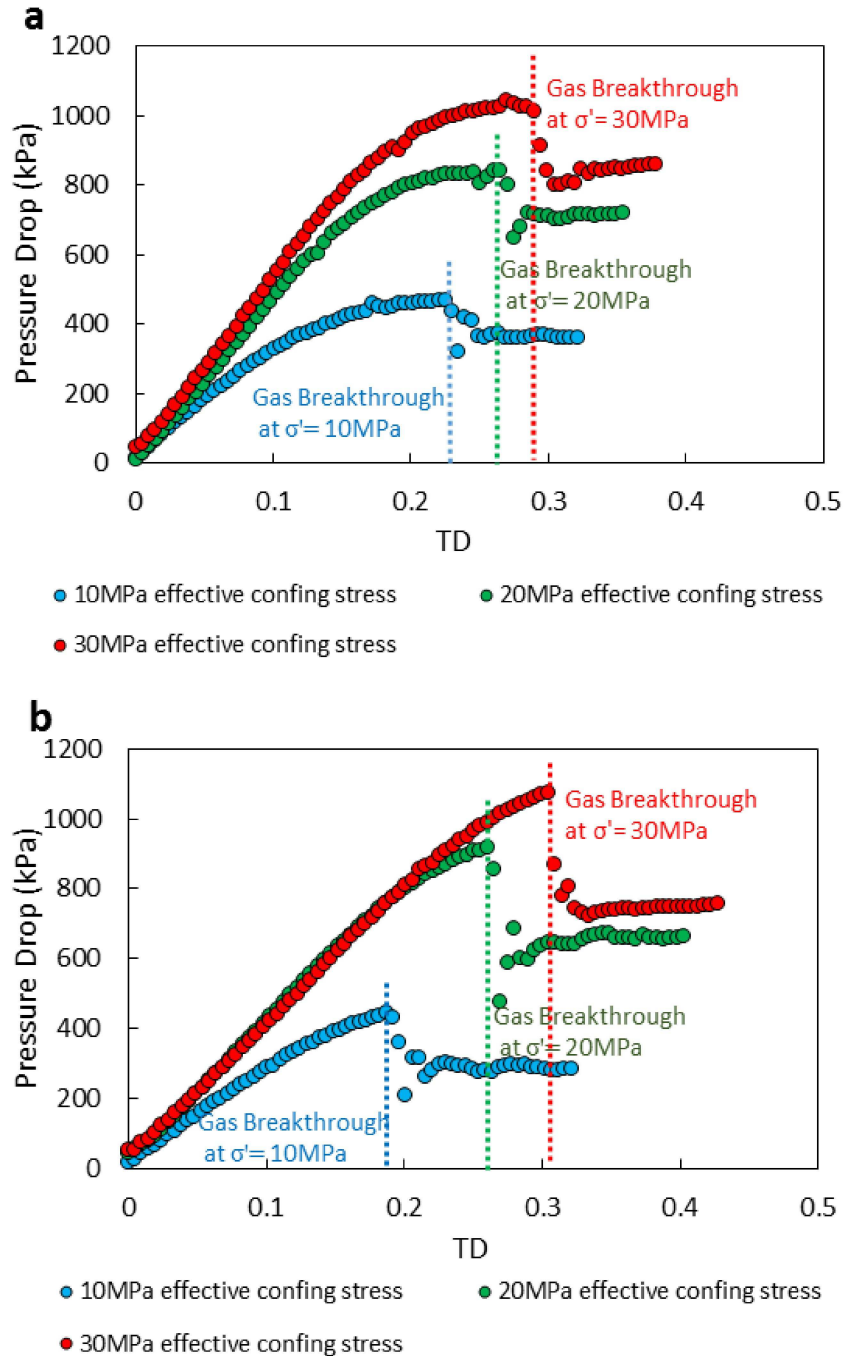


Fig. 5.12 Pressure drop versus dimensionless time at three different effective confining stress conditions during mixed N_2/water core flooding experiment of Berea core at gas fractional flow of: (a) 0.4 and (b) 0.6

5.6.4 Stress-Dependent Capillary Pressures of Berea Sandstone

Fig. 5.8d clearly confirms the hypothesis that increasing confining effective stress leads to an increase in capillary pressure by shrinking the size of pore throats. The increasing trend of the entry capillary pressure values (P_e) in Table 5.4 is an indication of higher capillary threshold pressure which was needed to start the drainage of the non-wetting phase into the pores and the extraction of the wetting phase. Considering the fact that pore compaction is a result of excessive effective confining pressure, based on poroelastic theory, the non-wetting phase required a higher driving force to fill the largest pores within the porous media; this led to a higher threshold pressure. This study revealed only a 7% drop in the porosity of Berea sandstone while a 40% increase in P_e is reported in Table 5.4 by increasing effective stress from 10 MPa to 30 MPa. This could be explained by considering a heterogeneous deformation of the media in the pore-scale (greater deformability of bigger pores).

With this knowledge, the well-known scaling function referred to as the J-Function relationship (Leverett, 1941) must be modified to treat the data presented in this study. The original Leverett J-function (Eq.(5.26)) suggests that the dimensionless capillary pressure function ($J(S_w)$) would be the same for porous media with different porosity and permeability but the same pore structure.

$$J(S_w) = \frac{P_c}{\sigma \cos\theta} \sqrt{\frac{k}{\phi}} \quad (5.26)$$

where θ is the wetting phase contact angle. In applying Eq.(5.26), the dimensionless pore structure function (Γ), which is a function of tortuosity, pore size distribution, and cementation should be constant. In Chapter 3, we assumed Γ to be fixed while applying effective stress in modeling carbonate rock under the assumption that a bundle of capillary tube represents the porous media. However, this study shows that in the case of sandstones, at least, rock tortuosity varies with effective stress (Eq.(5.11)). Hence, in the current study, the original dimensionless Leverett J-function is modified into Eq.(5.27) for the case of stress-dependent experiments.

$$J(S_w, \Gamma) = \Gamma \frac{P_c}{\sigma \cos\theta} \sqrt{\frac{k}{\phi}} \quad (5.27)$$

Using the measured stress-dependent porosity, absolute permeability, and capillary pressure data in this study, the following dimensionless equation for Γ is derived:

$$\Gamma(S_w) = \begin{cases} \frac{(A''S_w^2 + B''S_w - C'')}{(S_w - S_{wir})} & S_w \geq S_{wir} \\ 0 & S_w < S_{wir} \end{cases} \quad (5.28)$$

where S_{wir} is the irreducible wetting phase saturation at the smallest effective confining stress. A'' , B'' , and C'' are the curve-fitting constants and should be calculated using least square regression. Fig. 5.11b shows that the saturation profile in this study is stress-dependent ($S_{wir}(\sigma')$); hence, Eq.(5.28) confirms the dependency of $\Gamma(S_w)$ on effective stress. Using the curve-fitting constants calculated in Table 5.5, it can be seen in Fig. 5.13 that the calculated modified J-function data for the three different effective stress versus saturation converge into a single curve.

Table 5.5 Calculated fitting constants in Eq.(5.28) for the Berea sandstone experiment

Effective Stress (MPa)	A''	B''	C''	Regression R-square
20	0.3863	0.4494	0.1676	0.9955
30	0.678	-0.121	0.02288	0.9998

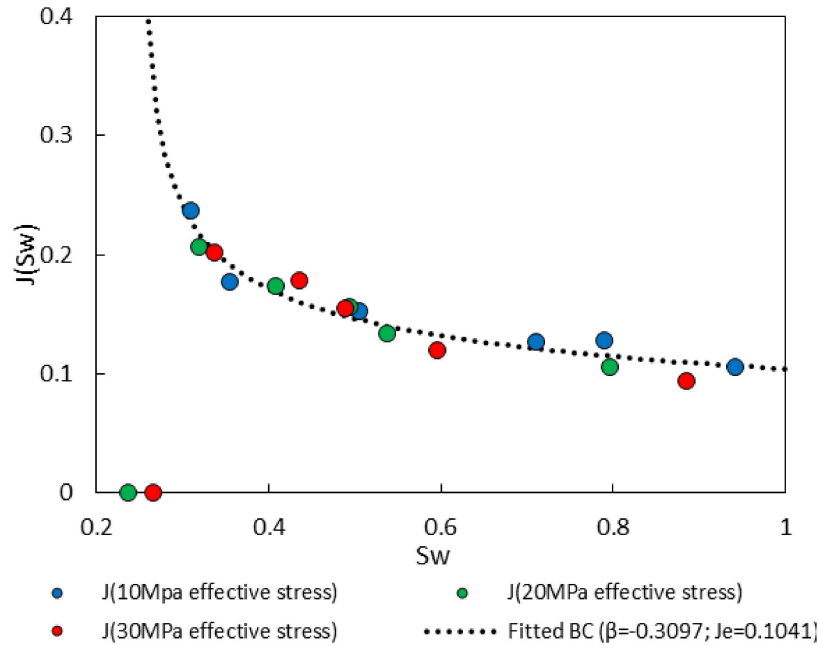


Fig. 5.13 Modified J-function data at three different effective stress conditions for Berea Sandstone

5.7 Conclusions

This study presents an innovative technique to measure porosity, absolute permeability, relative permeability, and capillary pressure under variable isotropic isothermal effective confining stress condition (zero up to 30 MPa, 40°C) using N₂/water as the immiscible fluid pair using consistent and consecutive procedures. The main advantage of the method is that it allows both single-phase and multiphase intact rock and fracture data, independently, for a range of effective stress and saturation to be generated, and can, therefore, be applied to interpret the behavior of rock formations during injection or production. Several significant conclusions are drawn from this study.

This study reports 7% and 38% decreases in the porosity (13.16% to 12.24%) and absolute permeability (58 mD to 36 mD), respectively, of Berea sandstone in response to increasing effective stress from 0 to 30 MPa. In a similar way, fracture porosity and absolute permeability of Calumet carbonate decreases, from 1.5% and 19.79 D to 1.18% and 219 mD, respectively, with an increase in effective confining stress from zero up to 10MPa. Additionally, semi-empirical equations are derived to simulate the behavior of stress-dependent porosity and absolute permeability.

The capillary pressure and relative permeability curves obtained here reflect a high dependency on effective confining stress and show excellent agreement with expected behavior based on the concepts of pore-scale fluid flow theories. This behavior leads to a leftward shift in the intersection of the relative permeability curves of Berea sandstone, together with smaller irreducible wetting phase saturation, which classically can be achieved by switching the initial core with one of less preference to the water (higher two-phase contact angle), or changing the wetting phase (water) with one of less affinity to the surface and higher interfacial tension with gas. In contrary, we have revealed a rightward shift in the intersection of the relative permeability curves of the oil-wet fractured Calumet carbonate, together with the greater irreducible wetting phase saturation. Additionally, the non-wetting phase saturation profile across the core, modeled using a Buckley-Leverett approximate solution, proves the high dependency of saturation distribution on effective confining stress.

Finally, a new definition for the dimensionless Leverett J-function is derived in this study to capture the dependency of dimensionless pore structure function (Γ) with stress. The modified Leverett J-function effectively combines the capillary pressure curves at different effective confining stresses into a single curve.

6. Stress-Dependent Pore Deformation Effects on Multiphase Flow Properties of Porous Media *

Abstract

Relative permeability and capillary pressure are the governing parameters that characterize multiphase fluid flow in porous media for diverse natural and industrial applications, including surface water infiltration into the ground, CO₂ sequestration, and hydrocarbon enhanced recovery. Although the drastic effects of deformation of porous media on single-phase fluid flow have been well established, the stress dependency of flow in multiphase systems is not yet fully explored. Here, stress-dependent relative permeability and capillary pressure are studied in a water-wet carbonate specimen both analytically using fractal and poroelasticity theory and experimentally on the micro-scale and macro-scales by means of X-ray computed microtomography and isothermal isotropic triaxial core flooding cell, respectively. Our core flooding program using water/N₂ phases shows a systematic decrease in the irreducible water saturation and gas relative permeability in response to an increase in effective stress. Intuitively, a leftward shift of the intersection point of water/gas relative permeability curves is interpreted as an increased affinity of the rock to the gas phase. Using a micro-scale proxy model, we identify a leftward shift in pore size distribution and closure of micro-channels to be responsible for the abovementioned observations. Similarly, when the analytical model is fitted to the experimental data, an increase in the tortuosity of the flow path is noted. These findings prove the crucial impact of effective stress-induced pore deformation on multiphase flow properties of rock and explain the physical mechanism controlling those property changes, which are missing from the current characterizations of multiphase flow mechanisms in porous media.

* This chapter was published in Scientific Reports: Haghi, A.H., Chalaturnyk, R., Talman, S. (2019). Stress-Dependent Pore Deformation Effects on Multiphase Flow Properties of Porous Media. Scientific Reports, 9(1), 1-10

6.1 Introduction

An accurate representation of the variation in relative permeability and capillary pressure with phase saturation is a crucial requirement for understanding multiphase fluid flow in hydrocarbon/geothermal reservoirs (Bear, 1972; Adler and Brenner, 1988; Bodvarsson et al., 1980; Gudjonsdottir et al., 2015), vadose zone water transport (Cueto-Felgueroso and Juanes, 2008), and carbon dioxide storage projects (Szulczewski et al., 2012; Bachu, 2015). Many researchers have studied the multiphase flow properties of porous media experimentally at both pore-scale and core-scales with a focus on fluid-fluid and fluid-solid interfacial interactions (Honarpour and Mahmood, 1988; Oak et al., 1990; Rabbani et al., 2017; Akbarabadi and Piri, 2013; Singh et al., 2017; Datta et al., 2014; Pak et al., 2018; Rabbani et al., 2018; Armstrong et al., 2012; Racini et al., 2014). Additionally, several empirical models have been developed to fit curves on the experimental data to reproduce multiphase flow properties (Purcell, 1949; Burdine, 1953; Brooks and Corey, 1966; Van Genuchten, 1980; Pan et al., 1966; Yang et al., 2013). Recent analytical developments on this front have led researchers to suggest a fractal description of pore sizes in porous rocks (Li and Horne, 2004). The investigation of flows in porous media is also an important research field within the numerical community. Complex flows in porous media across scales and in the presence of catalytic or other chemical reactions have been recently numerically performed in (Montessori et al., 2016 and 2015; Falcucci et al., 2016; Montemore et al., 2017) wherein the authors presented novel and efficient numerical approaches to study flows in fractured media. Although diverse in methodology and material type, these experimental, analytical, and numerical studies have routinely treated the porous media as a stress-independent solid with zero solid-solid mechanical interaction. This restriction in the theoretical treatment persists despite the limited, but increasing, body of experimental (McDonald et al., 1991; Khan, 2009; Hamoud et al., 2012; Lian et al., 2012; Huo and Benson, 2016) and analytical (Ofagbohunmi et al., 2012; Lei et al., 2018) evidence of changes to multiphase flow properties with effective stress-induced deformation. Complicated physical behaviors and contradictory findings continue to challenge our understanding of stress-dependent multiphase flow at pore-scale and core-scale (Lei et al., 2018).

Fluid production or injection in subsurface porous media will locally change pore pressures and in-situ stresses (Haghi et al., 2013a and b). These stress changes will, in turn, lead

to pore deformation in response to the pore pressure/stress coupling effect, for which we use the term “geomechanics” to generally describe this process. The earliest theory to account this coupling effect of soils was introduced by Terzaghi (Detournay and Cheng, 1993). However, the linear theory of poroelasticity was first borne from the pioneering work of Biot (Biot, 1941) and is broadly understood from core-scale and pore-scale experimental studies (Jones et al., 2001; Li et al., 2019). Several models have been presented to relate relative permeability and capillary pressure curves to the pore size distribution in porous media (Purcell, 1949; Burdine, 1953; Brooks and Corey, 1966). Typically, few parameters are required to model these curves; these include the irreducible wetting phase (S_{wir}) and/or residual non-wetting phase (S_{nwr}) saturations, end-point relative permeability (k_{r-max}), and one more parameter (λ), which defines any curvature in the dependency of relative permeability on the pore size distribution (Burdine, 1953). A further enhancement of the model was achieved by treating the pore space as a bundle of capillary tubes using fractal (D_f) and tortuosity fractal (D_t) dimensional parameters (Yu et al., 2003; Zheng et al., 2013; Xu et al., 2013; Mo et al., 2015; Gao et al., 2014). The idea of fractal distribution of capillary tubes was then used to solve classic relative permeability and capillary pressure equations (Li and Horne, 2004).

Despite an abundance of experimental studies of relative permeability and capillary pressure from both pore-scale and core-scale studies, the impact of pore deformation induced by effective stress changes on multiphase flow properties remains poorly explored (Huo and Benson, 2016). For conditions of increasing effective stress, existing experimental evidence (McDonald et al., 1991; Lian et al., 2012) reveals contradictory shifts in the relative permeability curves. Recognition of this contradiction has resulted in several authors conducting experiments to tackle the challenges in core-scale experiments (Huo and Benson, 2016) and pore-scale physical models (Li et al., 2019), independently. However, a comprehensive study of multiphase flow properties (e.g. relative permeability and capillary pressure) in both core-scale and pore-scale under a wide range of effective stress conditions has yet to be undertaken.

In this study, we use X-ray computed micro-tomography to quantify the structure and shape of the pores, together with the pore size distribution and two metrics (fractal dimension and degree of anisotropy), of an initially water-wet Indiana limestone specimen at atmospheric pressure. Then, through a series of core-flooding experiments using water/N₂ pair phases, the

stress-dependent porosity, absolute permeability, relative permeability, and capillary pressure of the same specimen are measured under triaxial isotropic effective stress (10MPa to 30MPa) and isothermal (40°C) conditions. Using the measured stress-dependent porosity and pore strain of the core, we reconstruct 3D pore-scale proxy models of the sample at 10, 20, and 30MPa effective stress conditions. This approach provides a simultaneous investigation of the pore and/or throat shape alteration and pore size distribution indices (e.g. fractal dimension) under variable stress conditions. Additionally, an analytical model is developed based on the fractal theory to reproduce and interpolate the stress-dependent relative permeability and capillary pressure curves. We find that increasing the effective stress results in a leftward shift in pore size distribution, closure of micro-channels, and modification to the flow path tortuosity. These changes are responsible for a dramatic upward shift in capillary pressure curve and a decrease in gas relative permeability. Executing experiments under raising effective stress conditions and constant gas flow rates, we show that increasing applied capillary pressure at the pore-scale due to an increase in gas pressure provides additional energy for the gas phase to invade smaller pore channels, leading to a subsequent decrease in the irreducible water saturation. These findings emphasize the complexity of the physical processes responsible for geomechanical controls on multiphase flow properties in porous media. Based on this research, we discuss the significant role of the stress-dependent relative permeability, capillary pressure, and irreducible wetting phase saturation for some interesting applications in engineering and natural process.

6.2 Stress-Dependent Flow Properties from Core-Scale Experiments

A set of single-phase (water) and two-phase (water/N₂) core flooding experiments were conducted on a water-wet Indiana limestone core in a high-pressure triaxial cell under a range of isotropic effective confining stress conditions from 0 to 30MPa and a constant temperature at 40°C. The equipment (Chapter 5) allowed for accurate measurement of porosity, absolute permeability, relative permeability, and capillary pressure at several different effective confining stress conditions.

First, the confined carbonate core inside the cell was fully saturated with deionized water using the procedure given in the *Materials and Methods*. Then, the required confining stress inside the cell was applied and the sample porosity measured. At each stress condition, we performed single-phase water flooding tests at several fixed rates ($q_w = 1 - 5\text{mL}/\text{min}$) to

obtain stress-dependent absolute permeability. Afterward, the Hassler relative permeability method (Osoba et al., 1951; Richardson et al., 1952), in which water and N₂ are simultaneously injected directly into the top of the core through two separate lines, was used to evaluate the steady-state pressure drop across the sample for each phase. These measurements were made at several water fractional flow values ($f_w = 1, 0.8, 0.6, 0.4, 0.2, 0$). For the capillary pressure measurement, we employed the modified stationary liquid method (Leas et al., 1950), keeping the wetting phase (water) immobile in the core while imposing several steady-state gas flow rates ($q_g = 1 - 5$ and $8\text{mL}/\text{min}$). Subtracting the core outlet pressure at steady-state condition from the gas pressure at the inlet provided an estimate of applied dynamic capillary pressure (Pini and Benson, 2013).

6.3 Pore-Scale Observations and Conceptual Proxy Modelling

Before running the core-scale experiments, the carbonate specimen was scanned using a stationary X-ray μCT at atmospheric pressure condition. The resulting 3D pore-scale model was synthetically compacted to achieve a proxy structure for the compacted core that was compatible with the imposed effective confining stress conditions. Fig. 6.1 shows the work flow of the process implemented here. More detailed explanations are provided in the *Materials and Methods*.

6.4 Analytical Modelling of Stress-Dependent Multiphase Flow Properties

As noted in (Yu et al., 2003), some natural porous media are fractals, a fact which has led many researchers to adapt fractal scaling laws to describe the transport and other pore-related properties. Here, the fractal nature of pore sizes was used to develop analytical models for stress-dependent capillary pressure and relative permeability curves, allowing for a better understanding of flow mechanisms on the scale of pores. Based on the fractal scaling laws, the cumulative size-distribution ($N(\bar{r})$) of pores with diameter (\bar{r}) greater than or equal to r was assumed to follow the fractal scaling law given bellow (Yu and Cheng, 2002):

$$N(\bar{r} \geq r) = (r_{max}/r)^{D_f} \quad (6.1)$$

where D_f and r_{max} are the fractal dimension and maximum pore diameter in porous media, respectively. Based on this definition, the equation for stress-dependent capillary pressure ($P_c(\sigma')$) can be shown to be

$$P_c(\sigma') = \left(\frac{P_{ei}}{3-D_T \sqrt{1-\varepsilon_p}} \right) S_w^{-\frac{1}{\lambda}}. \quad (6.2)$$

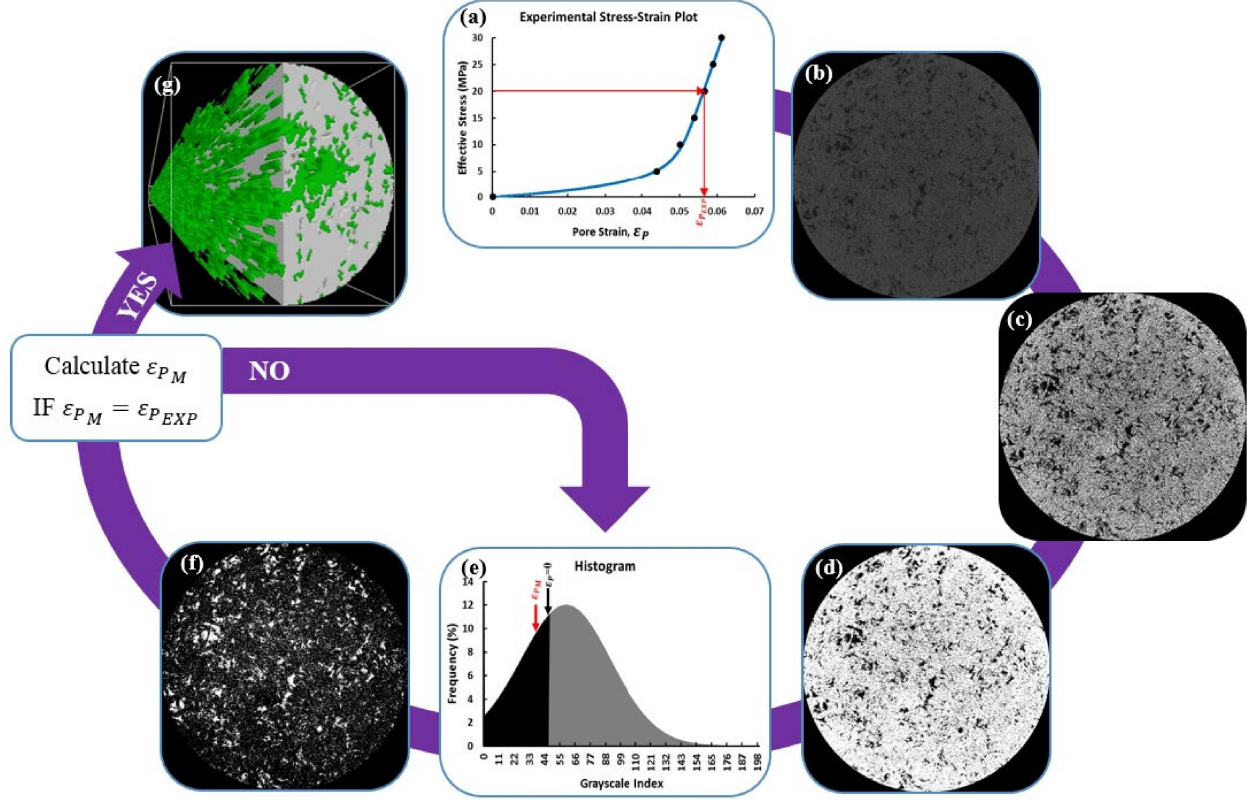


Fig. 6.1 Proxy modelling work flow in 7 steps: (a) Choosing a new effective stress and find experimental pore strain ε_{p_EXP} (b) Uploading original X-ray μ CT Image (c) Filtering (d) Binarization (e) Thresholding (f) Bitwise operation (g) Proxy modelling and analysis based on model pore strain ε_{p_M} .

The terms P_e , ε_p , $\lambda = 3 - D_T - D_f$ and D_T in Eq.(6.2) refer to entry capillary pressure, pore strain, stress-dependent pore size distribution index, and tortuosity fractal dimension, respectively, and the index i indicates the initial stress condition ($\sigma' = 0$) in this study. Based on the non-linear stress-strain equation for the poroelastic materials, ε_p is related to the changes in effective confining stress (σ') using the following equation (Zimmerman et al., 1986), assuming pore strain (ε_p) to be equal to the volumetric strain (ε_v).

$$\varepsilon_p = -\frac{dV_p}{V_{pi}} = A\sigma' - B e^{-\sigma'/C} + B \quad (6.3)$$

where A, B, and C are fitting constants. In chapter 5, we defined the fitting constants in Eq.(6.3) as $A = (1 - \gamma_S)/K_H$, $B = \gamma_S$, and $C = K_S$, where K_H and K_S are the bulk moduli of hard and soft parts of the rock, respectively. γ_S refers to a ratio of the soft part volume to the bulk volume at an unstressed condition. Mixing Eq.(6.2) with Burdine's empirical equation (Burdine, 1953), the following semi-analytical equations are developed for relative permeability curves ($k_r(\sigma')$).

$$k_{rw}(\sigma') = \left(\frac{S_w - S_{wir}}{1 - S_{wir}} \right)^2 \frac{S_w^{\frac{2+\lambda}{\lambda}} - S_{wir}^{\frac{2+\lambda}{\lambda}}}{1 - S_{wir}^{\frac{2+\lambda}{\lambda}}} \quad (6.4)$$

$$k_{rg}(\sigma') = k_{rg-max} \left(\frac{1 - S_w}{1 - S_{wir}} \right)^2 \frac{1 - S_w^{\frac{2+\lambda}{\lambda}}}{1 - S_{wir}^{\frac{2+\lambda}{\lambda}}} \quad (6.5)$$

where S_{wir} and k_{rg-max} are irreducible water saturation and maximum gas relative permeability, respectively. A detailed derivation of the above equations is given in Appendix C.

6.5 Results and Discussions

6.5.1 Core-Scale Approaches

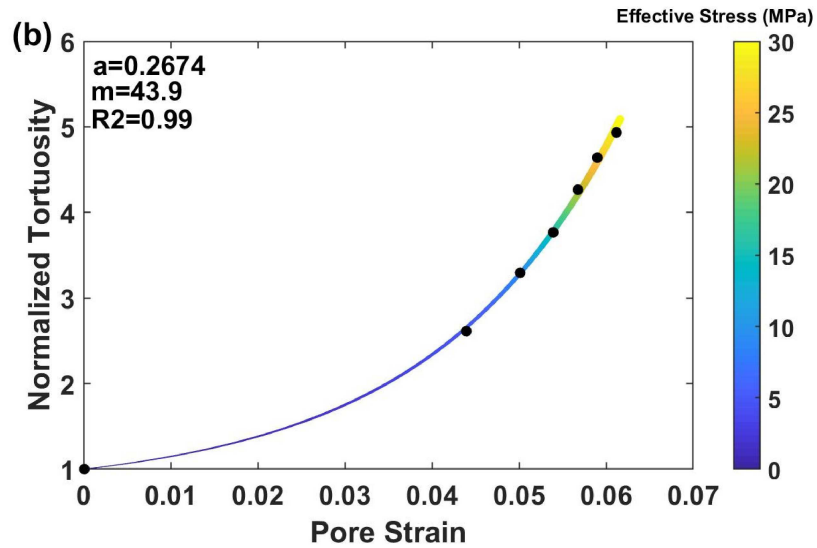
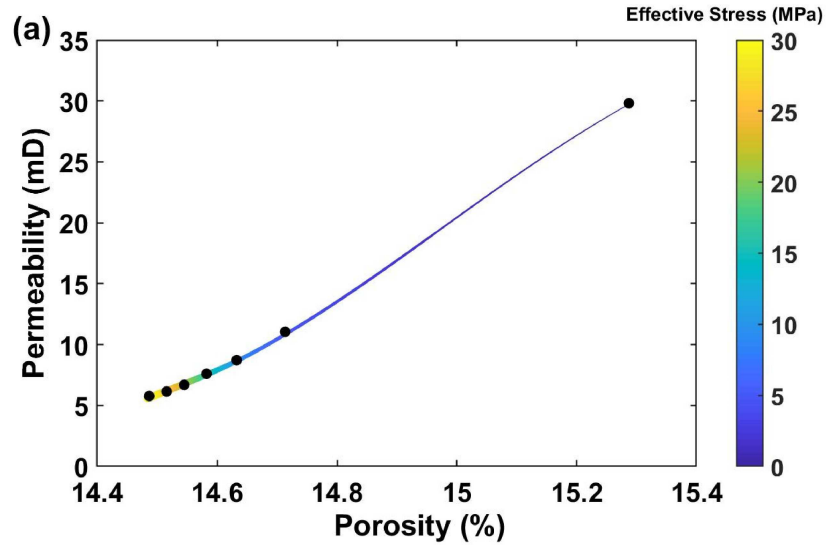
The main contributions of the current research at the core-scale are the experimental results illustrated in Fig. 6.2 of the stress-dependent structural, single-phase flow, and multiphase flow properties of a porous carbonate rock under a wide range of isotropic effective confining stress condition. In Fig. 6.2, circles and squares represent experimental data and colors indicate various effective confining stress conditions. Fig. 6.2a shows the decline in stress-dependent permeability (k) versus stress-dependent porosity (φ) in response to an increasing effective stress condition, where the colored curve is fitted on the experimental data using the following equation based on the Carman and Kozeny correlation (Carman, 1956).

$$k = k_i \left(\frac{\varphi}{\varphi_i} \right)^3 \left(\frac{1 - \varphi_i}{1 - \varphi} \right)^2 \left(\frac{\tau_i}{\tau} \right) \quad (6.6)$$

Here, τ defines the flow path hydraulic tortuosity inside the porous medium. The black circles in Fig. 6.2b represent the calculated normalized tortuosity ($\bar{\tau} = \tau/\tau_i$) from Eq.(6.6) (at known stress-dependent φ and k points) and the experimental pore strain data of the sample. The fitted curve is plotted based on the following equation (Chapter 5),

$$\bar{\tau} = a((1 - \varepsilon_p)^{-m} - 1) + 1 \quad (6.7)$$

where the grain shape factor (a) and material constant (m) are calculated using the least squares regression technique (Fig. 6.2b). This plot clearly reveals an increasing intensity of flow path tortuosity under increasing effective stress conditions. This confirms the simultaneous dual-effect of stress-induced deformation on both pore and connecting-channels sizes, where these are comprehensible through pore strain and hydraulic tortuosity variation, respectively.



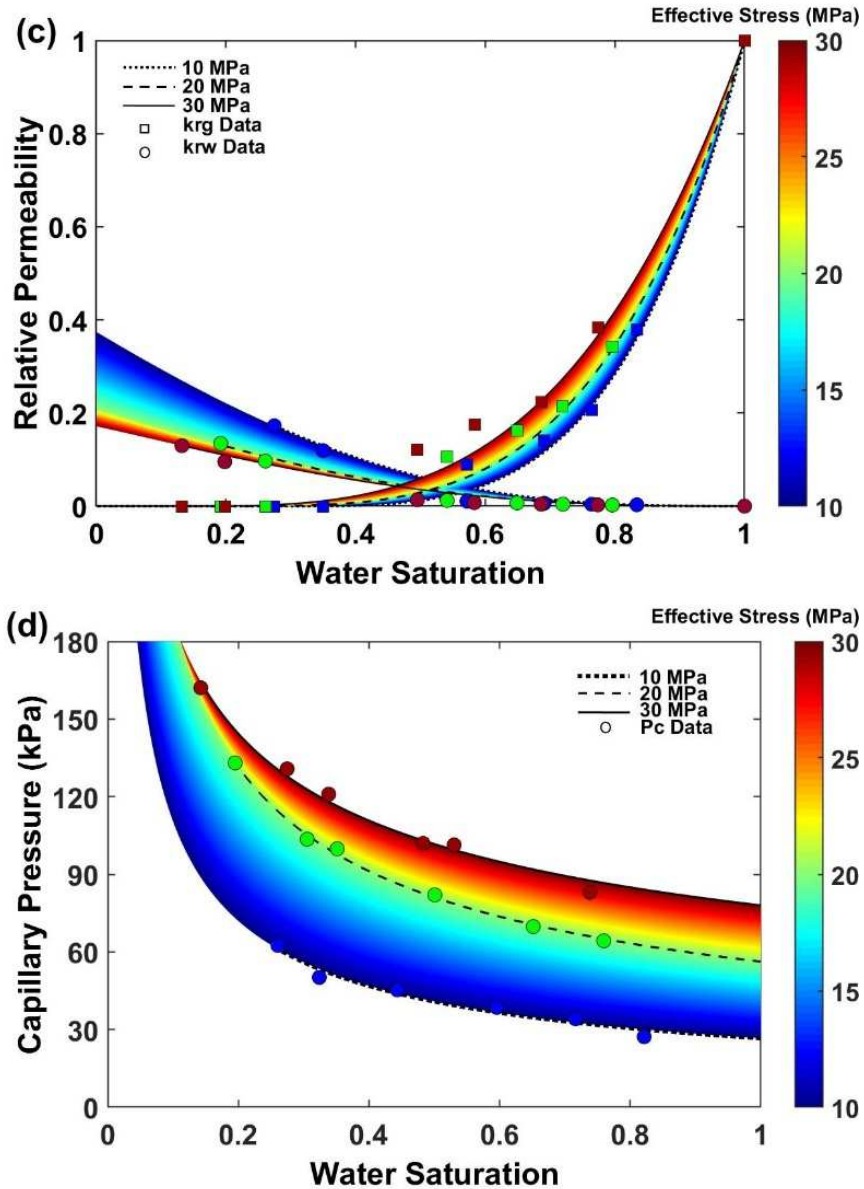


Fig. 6.2 Core-scale experimental results representing the stress dependency of structural, single-phase flow, and multiphase flow properties of the carbonate rock: (a) stress-dependent permeability versus porosity plot, (b) normalized tortuosity versus porosity ratio, (c) stress-dependent relative permeability, and (d) stress-dependent capillary pressure.

Fig. 6.2c-d illustrate the core-scale experimental results of how the stress-dependent multiphase flow properties vary under a range of effective confining stress condition from 10MPa to 30MPa. These two plots are an experimental demonstration of the remarkable controls that geomechanical processes impose on the multiphase flow properties of a porous carbonate rock. Herein, Eq.s (6.2), (6.4-5) are applied as the curve fitting and interpolating equations. More

details are given in Appendix C. The results illustrated in Fig. 6.2c-d show leftward (decreasing S_{wir}) and upward shifts in the relative permeability and capillary pressure curves, respectively. These shifts are conceptually an indication of a decrease in pore sizes, which will be investigated in the next section.

Intuitively, one would expect that a porous medium's increasing affinity to the gas phase should be responsible for the leftward shift of the relative permeability curves and decrease in S_{wir} . However, in our experiments, the interfacial tension and fluid properties were constant. To provide quantitative insight into the increasing affinity of the porous media to the gas phase, we provide important evidence from the experimental data at each stress condition: (1) irreducible water saturation (Fig. 6.3a), (2) water saturation at the intersection point of water and gas relative permeability curves (S_{wm} , Fig. 6.3a), and (3) maximum gas relative permeability (Fig. 6.3b). These observations, together with our knowledge of the non-changing surface and interfacial tension between the phases and solid during the experiments, reveal the remarkable influence of pore and/or channel deformation on our understanding of the wettability of porous media.

Fig. 6.3c illustrates an increase in dynamic capillary pressure end-points as effective stress is increased at constant flow rate conditions. The classical capillary number, defined as the ratio of the viscous forces to the capillary forces (i.e. $Ca = \mu_g Q_{inj} / \gamma A$, (Peters, 2012)), increases slightly as the core cross-sectional area (A) decreases in response to an increase in effective stress. For capillary number calculations, gas viscosity ($\mu_g = 0.184 \text{ mP.s}$), injection rate ($Q_{inj} = 8 \text{ mL/min}$), and interfacial tension ($\gamma = 69.36 \text{ mN/m}$) are taken as stress-independent parameters. Mechanistically, the stress-induced increase of Ca ($3.19 - 3.41 \times 10^{-8}$) under increasing effective stress conditions (0-30MPa) improves the likelihood of capillary desaturation of the water phase in the porous media, based on the capillary desaturation curve (CDC) for drainage process (Peters, 2012); this is consistent with our experimental observations, in which S_{wir} declines as effective stress increases (Fig. 6.3a). However, given the limited range of calculated Ca for our experiments, in the next section further investigations are warranted for a more representative definition of the capillary number at the pore-scale with more reasonable water capillary desaturation values.

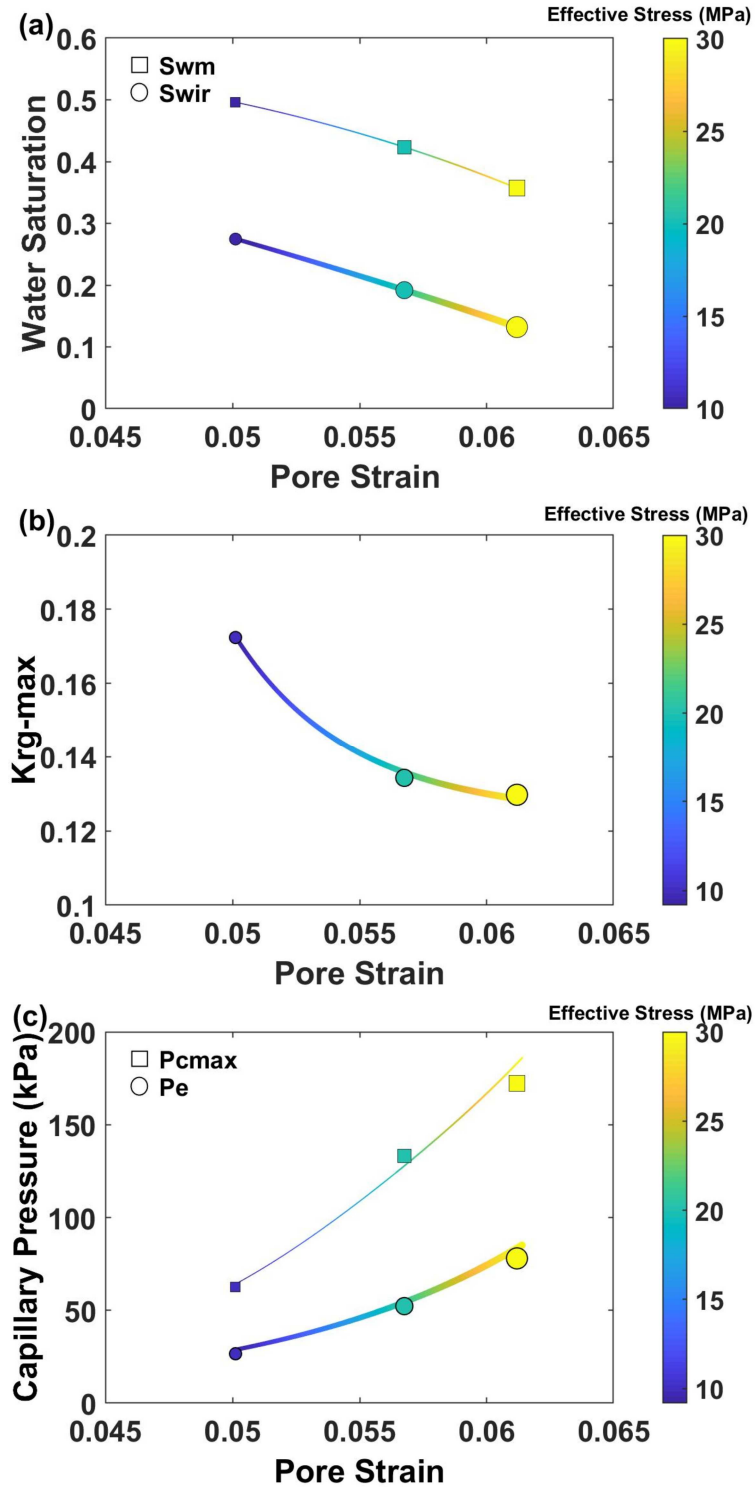


Fig. 6.3 The plots provide stress-dependent (a) irreducible water saturation (S_{wir}) and water saturation at the intersection point of water and gas relative permeability curves (S_{wm}), (b) maximum gas relative permeability (k_{rg-max}), and (c) entry and maximum capillary pressure (P_e and P_{cmax} , respectively).

6.5.2 Pore-Scale Approaches.

In this section, pore-scale manifestations are evaluated to postulate physical mechanisms supporting the significant core-scale stress-dependent multiphase flow properties measured in our experiments. The proxy modeling procedure given in Fig. 6.1 is used to develop conceptual 3D models of deformation at the pore-scale.

A qualitative demonstration of stress-induced capillary desaturation of the water phase in a single pore of our carbonate sample is presented in Fig. 6.4. Here, different colors indicate different effective stress conditions; the color bar corresponding to each is shown on the right side. 3D images of the selected pore at 0MPa (gray) and 30MPa (red) effective stress conditions are compared in the same frame in Fig. 6.4a. The section in the solid black rectangle is magnified in Fig. 6.4b-e to depict the contraction of a channel connecting the main body to a branch pore with effective stress evolution from 0MPa up to 30 MPa.

Increasing effective stress, a simultaneous increase in both maximum applied capillary pressure (Fig. 6.3c) and channel capillary pressure occurs as the capillary radius r decreases (Fig. 6.4b-e) following the Young-Laplace equation $P_c = 2\gamma\cos(\alpha)/r$ (Peters, 2012). When the applied core-scale capillary pressure ($P_c^{Applied} = (P_g - P_w)|_{ss\ cond.}$) becomes equal to the channel capillary pressure at a critical Ca , the gas viscous pressure (ΔP_g) becomes sufficient to expel, counter-currently, the water phase inside the pore through the channel. This leads to capillary desaturation of the water phase inside the pore. Gas viscous pressure is at its highest level at maximum applied capillary pressure ($P_{cmax}^{Applied}$) under each effective stress condition where water saturation decreases to its minimum value at S_{wir} . Scaling down the classical Ca definition for a pore-channel in a porous media, the terms viscous forces and capillary forces can be replaced with viscous pressure and capillary pressure of the channel, respectively (Hilfer and Øren; 1996). At critical state, maximum gas viscous pressure (ΔP_{gmax}) at maximum flow rate and steady-state condition, where water phase is immobile, is assumed to be equal to $P_{cmax}^{Applied}$ (Pini and Benson, 2013).

$$Ca_c = \frac{\Delta P_{gmax}}{P_c} = \frac{P_{cmax}^{Applied} \times r}{2\gamma\cos(\alpha)}. \quad (6.8)$$

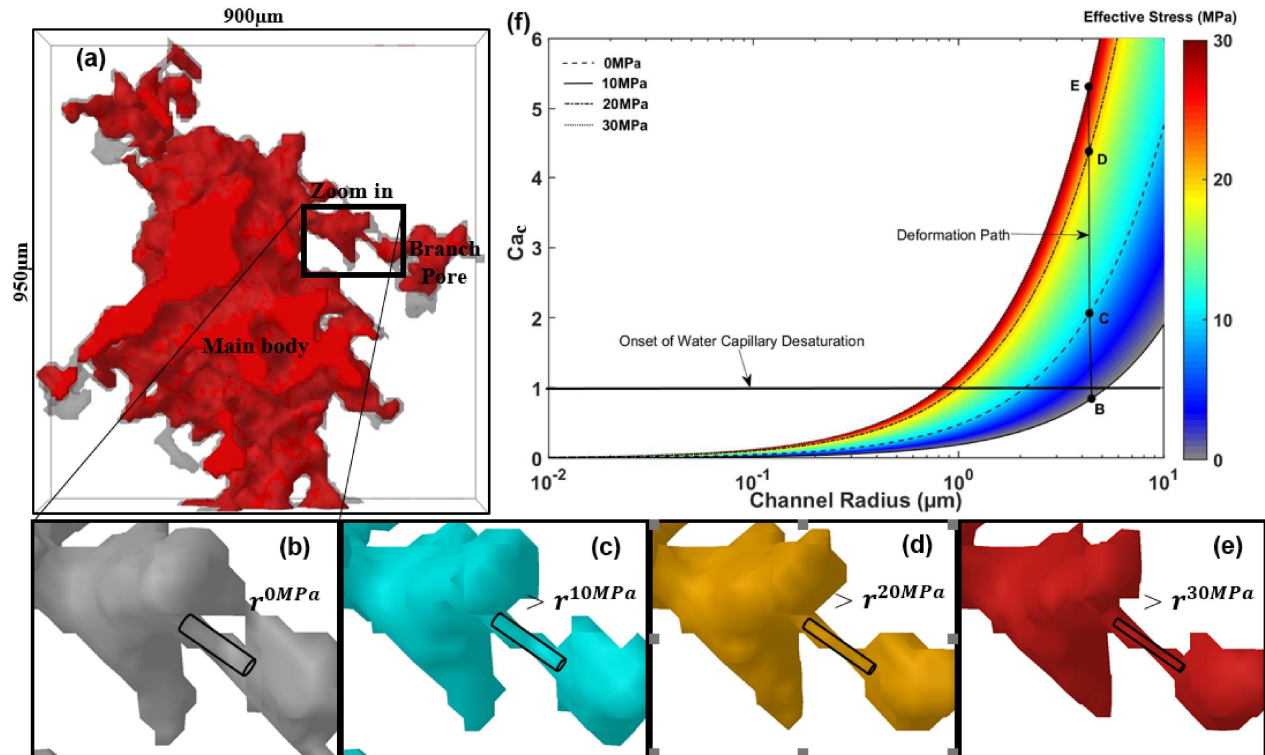
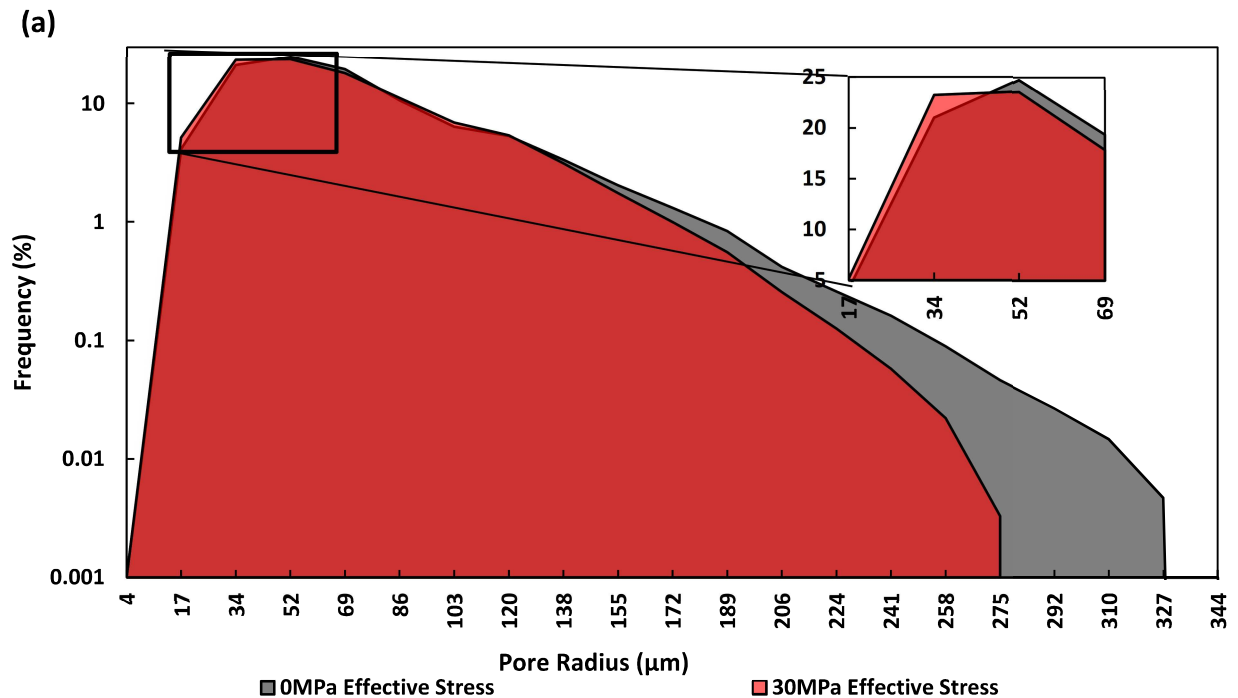


Fig. 6.4 This figure presents: (a) a 3D image of a single pore in the carbonate core (gray) and its proxy model at 30MPa effective stress condition; a single pore channel at (b) 0MPa, (c) 10MPa, (d) 20MPa, and (e) 30MPa effective confining stress condition; and (f) a 3D plot of the channel radius versus the critical capillary number at a range of effective stress conditions from zero to 30MPa.

Eq.(6.8) provides a new definition for the critical capillary number by connecting microscopic and macroscopic terms in a porous media to distinguish the onset of capillary desaturation of water at $Ca_c = 1$ during the constant flow gas drainage process. Using Eq.(6.8), Fig. 6.4f, which provides a multifunctional phase redistribution diagram under variable effective stress conditions, illustrates new insights for stress-dependent critical capillary numbers associated with the pore-channel radius of the carbonate specimen used in this study. At each effective stress condition, the threshold radius of the medium's channels, in which the capillary desaturation of water starts, can be obtained at $Ca_c = 1$. Additionally, the transition of a single channel, through its deformation path, from a gas capillary barrier to a gas flow conduit (or reverse) at different stress conditions can be recognized. With respect to the channel illustrated in Fig. 6.4b-e, increasing effective stress from zero to 10MPa (Fig. 6.4b-c) results in a transition in

the state of the channel from a gas barrier to gas flow conduit; this leads to capillary desaturation of the water phase inside the branch pore. This microscopic transition explains the macroscopic decrease in S_{wm} and S_{wir} in response to an increase in effective stress (Fig. 6.3a). A decrease in S_{wm} and S_{wir} can be translated into an increasing affinity of porous media for the gas phase by increasing effective stress.

To provide further quantitative description of stress-dependent changes in pore-scale structure, pore size distribution, with pore radius (r) being $\geq 4\mu m$ (Fig. 6.5a), and two metrics, namely (1) 3D fractal dimension (D_f) which quantifies how 3D objects fills pore spaces (Fig. 6.5b) and (2) degree of anisotropy (D_A), which is a measure of 3D symmetry of pores in the media (Fig. 6.5c), are calculated at each effective stress condition. Details on these calculations are given in the *Materials and Methods*. As a result of increasing the effective confining stress from 0MPa to 30MPa, a leftward shift in effective pore size distribution (PSD) is observed (Fig. 6.5a), while the mean pore radius decreases from 70 μm to 67 μm , respectively. Additionally, the cumulative frequency of pores with $r \leq 52 \mu m$ increases from 49% at 0MPa effective stress to 52% at 30MPa effective stress; the remaining pores span up to 326.85 μm and 275.25 μm , respectively.



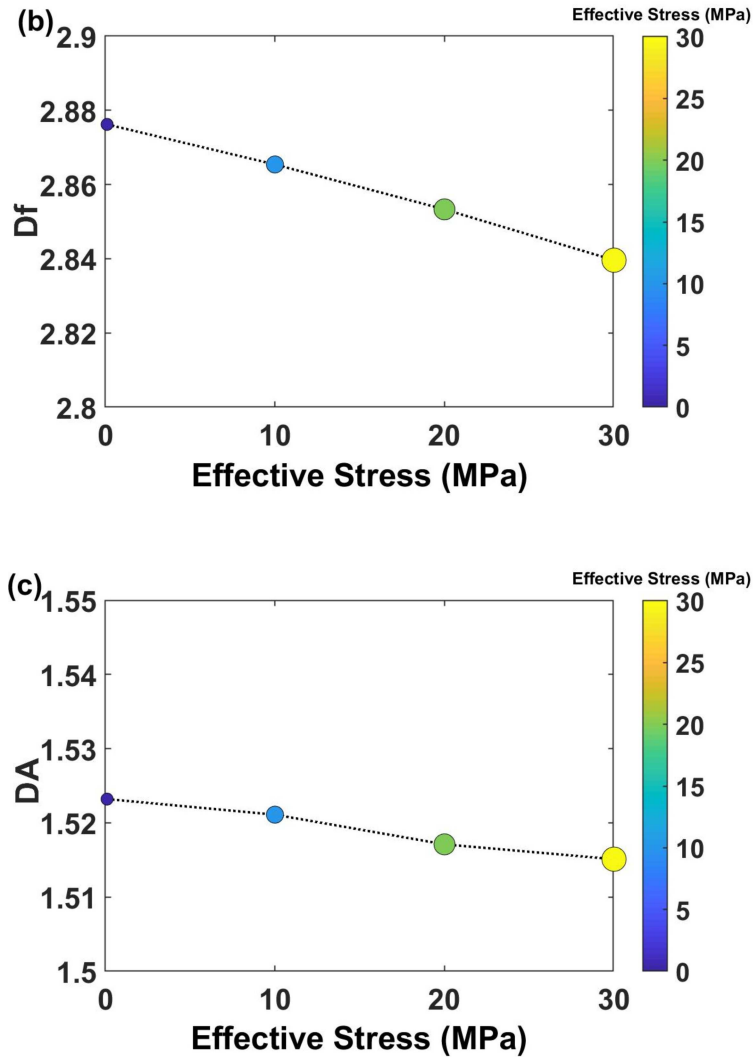


Fig. 6.5 This figure provides insights into stress-dependent (A) 3D pore size distribution in a semi-log plot, (B) 3D fractal dimension (D_f), and (C) 3D degree of anisotropy (D_A) at a range of effective stress conditions from zero to 30MPa for the carbonate sample.

These stress-dependent declines in the mean pore radius and size of the largest effective pore, pore connected to the surface of the core, result in an increasing trend of capillary pressure curves and entry capillary pressure, respectively (Peters, 2012), in response to an increase in effective stress. A similar trend can be realized at the core-scale using the stress-dependent capillary pressure experimental results shown in Fig. 6.2d. Additionally, the leftward shift in PSD justifies the decline in maximum gas relative permeability under increasing effective stress

conditions (Fig. 6.3b). Note that maximum gas relative permeability is calculated at irreducible wetting phase saturation (immobile).

A declining trend was observed in both dimensionless numbers D_f and D_A in response to an increase in effective stress from 0MPa to 30MPa (Fig. 6.5b-c). These two pore structural metrics quantify clearly the rock deformation and its impacts on single-phase and multiphase parameters. The decreasing trend of D_f is an indication of more uniform (i.e. well-sorted) pore sizes (Peters, 2012); its striking impact on decreasing porosity, absolute permeability, and S_{wir} and increasing slope of capillary pressure curves has been shown experimentally and analytically in the literature (Li and Horne, 2004; Yu et al., 2003; Zheng et al., 2013; Xu et al., 2013; Mo et al., 2015; Gao et al., 2014). In a similar way, our calculated D_A represents an increasing state of isotropy of the sample due to pore compaction in response to increasing effective stress.

Previous pore-scale observations (Churcher et al, 1991; Yoo et al., 2019) have shown that a great percent of pores in Indiana limestone are smaller than the resolution limit of the X-ray computed micro-tomography in this study. However, Fig. 6.4f shows that pores in the nano-scale have no chance to pass the onset of water capillary desaturation line through any deformation path line. Hence their deformation does not lead to any changes in the properties for the given effective stress limits (0-30MPa).

6.5.3 Implicational Insights

Simultaneous flow of gases and liquids in natural porous media is an indispensable phenomenon to study when we are dealing with subsurface flow processes. Stress-dependent shifts in the relative permeability and capillary pressure curves have a major impact on our classical methods of understanding, quantifying, and modeling multiphase fluid flow in subsurface formations for a wide range of engineering and natural applications, including enhanced oil recovery, CO₂ subsurface storage, heat energy recovery from geothermal reservoirs, and surface water infiltration in the vadose zone.

Although in this study we have conducted the flooding experiments on a standard carbonate specimen using water (wetting phase) and N₂ (non-wetting phase) phases, the discovered systematic stress-dependent behavior of rock could be extended for a wider range of rocks such as sandstone (Chapter 5) and fluid pairs (e.g. gas + liquid), as gases are typically the

non-wetting phase for most natural porous media. For instance, the stress-dependent upward shift in the entry capillary pressure for the studied carbonate rock, at an increasing effective stress condition from 10MPa to 30MPa (Fig. 6.3c), almost doubles the injection pressure and energy required to push the gas phase into the porous rock. However, the stress-dependent decrease in irreducible wetting phase saturation resulting from increasing the effective stress condition from 10MPa to 30MPa (Fig. 6.3a) leads to an almost 20% increase in the volume of stored gas inside the core and recovery of the wetting phase (i.e. water) from the core. These dramatic changes in gas injection pressure, volume of stored gas, and recovery of the wetting phase are technically and economically significant for similar scenarios such as CO₂ subsurface storage and enhanced recovery of hydrocarbon reservoirs using a miscible/immiscible gas (e.g. CO₂) flooding technique. These stress-dependent processes allow us to predict additional CO₂ storage in subsurface formations. In the same way, stress-dependent leftward shifts in the relative permeability curves facilitate rainwater infiltration into the vadose zone and hot water flow through two-phase geothermal reservoirs. This fundamental study paves the way for a more realistic study of fluid flow mechanisms in any natural and industrial applications which are dealing with multiphase fluid flow properties of rock under variable effective stress conditions.

6.6 Summary and Conclusions

We have shown experimentally the systematic impact of pore deformation as a result of effective stress changes on the single-phase and multiphase fluid flow properties of a carbonate specimen via a series of core-flooding experiments using water/N₂ phases under isothermal and triaxial isotropic effective stress conditions. Our experiments have revealed leftward and upward shifts in the relative permeability and capillary pressure curves, respectively, with increasing effective stress, and have shown a decreasing shift of S_{wir} , S_{wm} , and $k_{rwm\max}$ under increasing effective stress conditions. These experiments have provided us core-scale insights into the linkage between these shifts to decreases in porosity and absolute permeability and increases in pore strain and pore flow tortuosity under an increasing effective stress condition. Fractal and poroelasticity theories were used to drive analytical equations for stress-dependent relative permeability and capillary pressure curves. These equations were used for curve fitting and interpolation in this study.

Using X-ray computed micro-tomography and a proxy modelling technique, we were able to quantify the structure and shape of the pores and channels, pore size distribution, and scaling dimensionless numbers (e.g. fractal dimension and degree of anisotropy) at different effective stress conditions. We have shown that increasing effective stress leads to a leftward shift in PSD and closure of micro-channels. As revealed in the 3D phase redistribution diagram (Fig. 6.4f), we have quantified the stress-dependent threshold radius of the medium's channels at the starting point of capillary desaturation of water in the porous media. Additionally, we have revealed the transition of a single channel, through its deformation path, from a gas capillary barrier into a gas flow conduit in response to an increasing stress conditions, which resulted in the capillary desaturation of the water phase and a macroscopic decrease in S_{wm} and S_{wir} . We have further revealed that leftward shift in PSD is responsible for the increasing trend of capillary pressure curves under an increasing effective stress condition. D_f and D_A metrics proved quantitatively the role of effective stress condition on pore size distribution and pore isotropy, respectively, in porous media.

These findings underscore the significant impact of effective stress on multiphase flow properties of rock, and manifest the physical mechanisms, such as capillary desaturation and capillary gas blockage due to stress-induced mechanical deformation of pores and/or channels, that control those properties.

6.7 Materials and Methods

6.7.1 Core-Scale Experiments

The experiments were conducted on a water-wet Indiana limestone specimen (from Kocurek Industries INC., USA) 3.81cm in diameter and 10.16cm in length. The uniaxial compressive strength and Young's modulus of the rock were 25.78MPa and ≈ 3 GPa, respectively (Fig. 6.6). N_2 and deionized water were used as the flooding phases and CO_2 as the displacing phase. Here, an air-water contact angle (α) of 18.8 degrees were measured using a drop shape analyzer (DSA), which indicated the strong water-wet nature of the specimen (Fig. 6.7). Full re-saturation of the confined sample inside the cell was a key challenge that we tackled using a procedure consisting of 3 steps: (1) flushing the core with 50 pore volume of high pressure CO_2 , (2) vacuuming the sample (at ambient water saturation pressure) from an outlet line over a liquid nitrogen cold trap until a plateau pressure was achieved at the inlet, and (3) injecting high

pressure water into the sample and maintaining the pressure for a few hours before re-flushing it with 50 pore volume of water. The experimental procedure in this study is analogous to the protocol described in Chapter 5 for Berea sandstone, to which readers are referred for additional details.

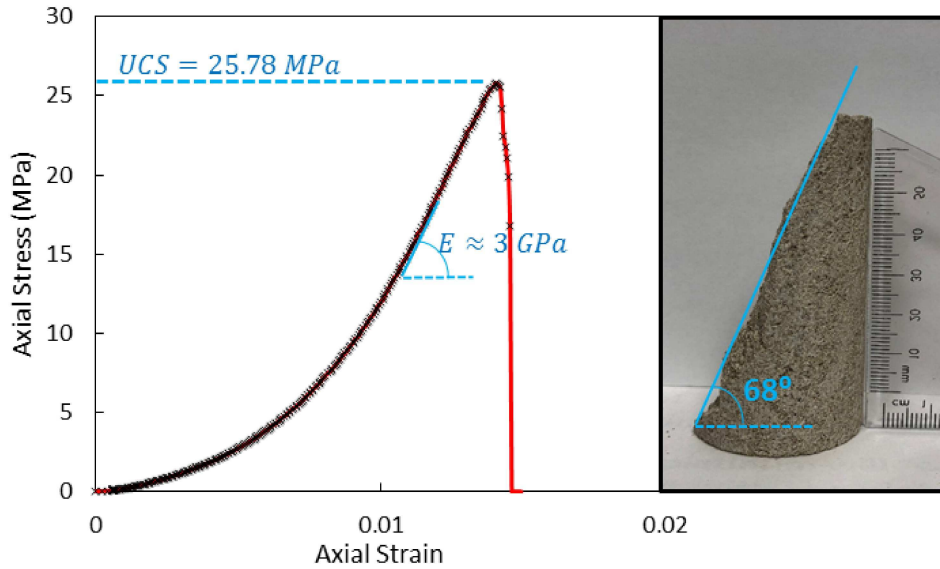


Fig. 6.6 Uniaxial compressive strength test results on an Indiana limestone specimen (3.81cm in diameter and 7.62cm in length) measured based on ISRM suggested standard methods for determining the uniaxial compressive strength and deformability of rock materials (ASTM D7012).

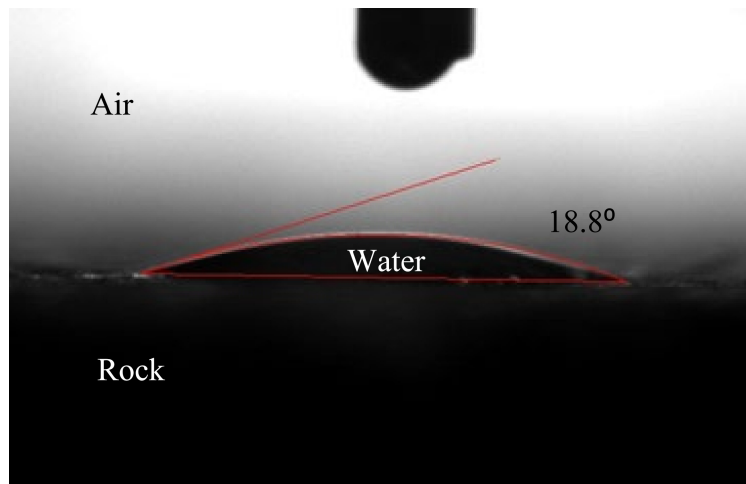


Fig. 6.7 Measured air-water contact angle (α) equal to 18.8 degrees using a drop shape analyzer (DSA) at equilibrium condition. Based on the measured contact angle smaller than 90° , the carbonate is categorized as a strong water-wet rock.

6.7.2 Imaging and Proxy Modelling

The X-ray micro-tomography was performed using the micro-CT imaging suite in the Pharmaceutical Orthopedic Research Lab (PURL) at the University of Alberta. The X-ray source within this equipment is a sealed tube with a voltage of 100kV and a spot size of $<5\mu\text{m}$. The imager scans 360 degrees rotational field-of-view at a time using a 12 bit X-ray detector that is fiber-optically coupled to a scintillator. We scanned an 18 mm length of the full-diameter core 5 mm away from the end face of the core. All tomographic images were at $8.6\ \mu\text{m}$ per voxel resolution. The post-processing and quantifications were performed using the CT Analyser program within Bruker microCT 3D Suite software. The proxy modeling process in this study consisted of 7 steps, and the pore stress-strain plot of the rock from the core-scale experiments was an initial input in this cycle. In the first step, we chose an effective stress condition and identified the corresponding pore strain from our core-scale experiments ($\varepsilon_{p_{EXP}}$). Then the original X-ray μCT images were filtered using median and contrast enhancement techniques. Filtered images were segmented into black and white binary areas representing pores and grains, respectively. Through the thresholding step, a grayscale index smaller than its original value for the rock at zero effective stress was selected manually. Otsu's (1979) thresholding method in 3D space was used initially to define the original grayscale index and match the model's 3D porosity with experimentally measured porosity at zero effective stress. The model's pore system was then assigned as a 3D object through bitwise operation, and its volume and strain ($\varepsilon_{p_M} = (V_{p_{Mi}} - V_{p_M})/V_{p_{Mi}}$) were calculated. $V_{p_{Mi}}$ and V_{p_M} defined as proxy model's initial and stress-dependent pore volume, respectively. This process was repeated iteratively until the pore strain of the proxy model became equal ($\pm 0.1\%$) to its corresponding experimental value and the representative model used for further 3D analysis.

6.7.3 Pore Size Distribution and Pore Metrics

We implemented the 3D calculation of pore size distribution, fractal dimension, and degree of anisotropy using the CT Analyser program within Bruker microCT 3D Suite Software. For the pore network process, firstly, a "skeletonisation" was performed to identify the medial axis of all pores. Secondly, a "sphere-fitting" measurement was made for all of the voxels along this axis. Pore size is defined as the diameter of the largest sphere which meets two conditions: 1) the sphere encloses the point (but the point is not necessarily the center of the sphere), and 2)

the sphere is entirely located within the pore. The Kolmogorov or box-counting method was used to calculate D_f in 3D; following this process, the volume was divided into an array of equal cubes and the number of cubes containing part of the object was counted. The process was repeated over a range of box sizes (3 to 100 voxels). Plotting the box sizes (L) versus the number of occupied boxes ($N(L)$), the slope of log-log linear regression defined D_f . Note that a linear relationship between the number of occupied boxes and box sizes in a log-log plot with the slope of D_f is also a confirmation of fractal nature of the porous sample based on $N(L) \propto L^{-D_f}$, where this was the case in the current study with the slopes given in Fig. 5(b). Finally, mean intercept length (MIL) analysis was used to measure D_A . As part of this process, a grid of lines was sent through the 3D core image containing pores (object) and grains (void) over a large number of 3D angles, and the length of the test line through the analyzed volume was divided by the number of times that the line passed through or intercepted pores. For more details, readers are referred to the software manual (<https://www.bruker.com/products/microtomography.html>).

7. Summary and Conclusions

This thesis presented a new dialogue in the characterization and modeling of geomechanical controls on multiphase fluid flow in NFCR. Although the drastic effect of stress induced-deformation of porous media on single-phase fluid flow is well established in the literature, there are still fundamental gaps associated with the stress dependency of flow in multiphase systems such as NFCR. These gaps lead us to design a comprehensive research plan using analytical, numerical, and experimental approaches to study and further our understanding of the stress dependency on multi-phase flow properties and mechanisms in a number of sedimentary rocks.

7.1 NFCR Case Study in SW of Iran

At the beginning of this research, we have reported interesting field data, the first full stress tensor, and 1D geomechanical model of a giant NFCR case study in SW of Iran. The extensively NE–SW orientation of maximum horizontal stress observed in the study was broadly consistent with both orientations derived from nearby earthquake focal mechanism solutions and the direction of absolute plate motion of the Arabian plate. Hence, the present-day in-situ stress state of the region was likely to be associated with the tectonic forces generated at the Arabian–Eurasian continental collision zone. The study indicated the presence of a normal faulting stress regime in the Bangestan Reservoir located in the deep outer lowland of ZFTB, Iran.

7.2 Semi-Analytical and Numerical Approaches

Introducing novel semi-analytical and sequentially coupled numerical techniques, we have revealed significant shifts in the recovery of NFCR in response to the stress-dependent changes in the intact rock and fracture flow properties. Using the derived semi-analytical solution, we have proved the geomechanical controls on capillary-driven fractional flow and imbibition in NFCR. Employing the equivalent continuum concept, we derived an analytical model to combine geo-dynamic properties of intact rock and fracture; these were calculated independently based on the poroelastic and nonlinear fracture stiffness equations, respectively.

The observed significant geomechanical impacts on ultimate recovery could lead to changes in project economics, hence development strategies.

7.3 Pore-Scale to Core-Scale Experimental Approaches

Finally, our laboratory experimental findings underscored the significant impact of effective stress-induced deformation on single-phase (e.g. absolute permeability) and multiphase (e.g. relative permeability and capillary pressure) flow properties of intact rock and fracture media and manifested the physical mechanisms that control those properties on the microscopic and macroscopic scales. Our experiments on water-wet Berea sandstone and Indiana limestone specimens have shown leftward and upward shifts in the relative permeability and capillary pressure curves, respectively, with increasing effective stress, and have further shown a decreasing shift of S_{wir} , S_{wm} , and k_{rwmax} under increasing effective stress conditions. On the contrary, we have revealed a rightward shift in the intersection of the relative permeability curves of the oil-wet fractured Calumet carbonate, together with the increasing irreducible wetting phase saturation. Using X-ray computed micro-tomography and a proxy modeling technique, we have revealed that increasing effective stress leads to a leftward shift in pore size distribution and closure of micro-channels. These stress-dependent property changes have a major impact on our classical methods of understanding, quantifying, and modeling multiphase fluid flow in subsurface formations for a wide range of engineering and natural applications, including enhanced oil recovery, CO₂ subsurface storage, heat energy recovery from geothermal reservoirs, and surface water infiltration in the vadose zone.

7.4 Future Research

I could recommend the following related challenges for future researches:

- Developing pore network models to investigate the stress-dependent single-phase and multiphase flow properties of a porous media and calibrate the models with experimental and analytical results from the current study.
- The main objective of the current research was to prove the impact of deformation of porous media and fracture closure on single-phase and multiphase flow properties of rock and fluid transport in NFCR. However, due to the complexity and unknown nature of the current problem in terms of phases and rock interactions, deformation under isotropic

effective stress condition was targeted. This research can be continued for the case of deformation under anisotropic effective stress condition of porous media.

- Investigation of the impact of stress-dependent single-phase and multiphase fluid flow properties on the modelling and simulation, projects economics, and development strategies of a real case study (e.g. a depleted NFCR or a geothermal reservoir) with a great number of injection and production wells.

Bibliography

- Abass, H. H., Hedayati, S., & Meadows, D. L. (1996). Nonplanar fracture propagation from a horizontal wellbore: experimental study. *SPE Production & Facilities*, 11(03), 133-137.
- Adler, P. M. & Brenner, H. (1988). Multiphase flow in porous media. *Annual review of fluid mechanics*, 20(1), 35-59.
- Ahmed, T., & McKinney, P. (2011). *Advanced reservoir engineering*. Burlington, MA: Elsevier/Gulf Professional Pub.
- Akbarabadi, M., & Piri, M. (2013). Relative permeability hysteresis and capillary trapping characteristics of supercritical CO₂/brine systems: An experimental study at reservoir conditions. *Advances in Water Resources*, 52, 190-206.
- Alavi, M. (1994). Tectonics of the Zagros orogenic belt of Iran: new data and interpretations. *Tectonophysics*, 229(3-4), 211-238.
- Alavi, M. (2004). Regional stratigraphy of the Zagros fold-thrust belt of Iran and its proforeland evolution. *American journal of Science*, 304(1), 1-20.
- Alavi, M. (2007). Structures of the Zagros fold-thrust belt in Iran. *American Journal of science*, 307(9), 1064-1095.
- Ameen, M. S., Smart, B. G., Somerville, J. M., Hammilton, S., & Naji, N. A. (2009). Predicting rock mechanical properties of carbonates from wireline logs (A case study: Arab-D reservoir, Ghawar field, Saudi Arabia). *Marine and Petroleum Geology*, 26(4), 430-444.
- Anderson, W. G. (1987). Wettability literature survey-part 6: the effects of wettability on water flooding. *Journal of Petroleum Technology*, 39(12), 1-605.
- Asef, M. R., & Farrokhrouz, M. (2010). Governing parameters for approximation of carbonates UCS. *Electron J Geotech Eng*, 15, 1581-1592.
- Archie, G. E. (1952). Classification of carbonate reservoir rocks and petrophysical considerations. *AAPG*, 36(2), 278-298.

- Archie, G. E. (1942). The electrical resistivity log as an aid in determining some reservoir characteristics. *Transactions of the AIME*, 146(01), 54-62.
- Armstrong, R.T., Porter, M.L. & Wildenschild, D. (2012). Linking pore-scale interfacial curvature to column-scale capillary pressure. *Adv Water Resour* 46(0), 55–62.
- ASTM D7012, “Standard Test Methods for Compressive Strength and Elastic Moduli of Intact Rock Core Specimens under Varying States of Stress and Temperatures”
- Bachu, S., (2015). Review of CO₂ storage efficiency in deep saline aquifers. *International Journal of Greenhouse Gas Control*, 40, 188-202.
- Bagheri, M., & Settari, A. (2008). Modeling Fluid Flow in Deformable Fractured Reservoirs using Full Tensor permeability. Paper SPE 113319 presented at the 2009 SPE Europec. In EAGE Annual Conference and Exhibition, Rome, Italy, 9-12.
- Bandis, S. C., Lumsden, A. C., & Barton, N. R. (1983). Fundamentals of rock joint deformation. *International Journal of Rock Mechanics and Mining Sciences & Geomechanics Abstracts*, Vol. 20, No. 6, 249-268.
- Barrande, M., Bouchet, R., & Denoyel, R. (2007). Tortuosity of porous particles. *Analytical chemistry*, 79(23), 9115-9121.
- Berryman, J. G. (1981). Elastic wave propagation in fluid-saturated porous media. *Journal of the Acoustical Society of America*, 69(2), 416-424.
- Barton, N., Bandis, S., & Bakhtar, K. (1985). Strength, deformation and conductivity coupling of rock joints. *International Journal of Rock Mechanics and Mining Sciences & Geomechanics Abstracts*, Vol. 22, No. 3, 121-140.
- Barton, C. A., Zoback, M. D., & Moos, D. (1995). Fluid flow along potentially active faults in crystalline rock. *Geology*, 23(8), 683-686.
- Bear, J. (2013). *Dynamics of fluids in porous media*. Courier Corporation.
- Behbahani, H., & Blunt, M. J. (2005). Analysis of Imbibition in Mixed-Wet Rocks Using Pore-Scale Modeling. *SPE Journal* 10 (4): 466–474. SPE-90132-PA.
- Bell, J. (1996). Petro Geoscience 1. In situ stresses in sedimentary rocks (part 1): measurement techniques. *Geoscience Canada*, 23(2).

- Bell, J. (1996). Petro geoscience 2. In situ stresses in sedimentary rocks (part 2): applications of stress measurements. *Geoscience Canada*, 23(3).
- Berberian, F., Muir, I. D., Pankhurst, R. J., & Berberian, M. (1982). Late Cretaceous and early Miocene Andean-type plutonic activity in northern Makran and Central Iran. *Journal of the Geological Society*, 139(5), 605-614.
- Berberian, M., & King, G. C. P. (1981). Towards a paleogeography and tectonic evolution of Iran. *Canadian journal of earth sciences*, 18(2), 210-265.
- Biot, M. A. (1941). General theory of three-dimensional consolidation. *Journal of applied physics*, 12(2), 155-164.
- Blanton, T. L., & Olson, J. E. (1997). Stress magnitudes from logs: effects of tectonic strains and temperature. In *SPE Annual Technical Conference and Exhibition*. Society of Petroleum Engineers.
- Bodvarsson, G. S., O'Sullivan, M. J. & Tsang, C. F. (1980). The sensitivity of geothermal reservoir behavior to relative permeability parameters (No. SGP-TR-50-31). Earth Sciences Division, LBNL (Lawrence Berkeley National Laboratory (LBNL), Berkeley, CA)
- Bourbiaux, B. J., & Kalaydjian, F. J. (1990). Experimental study of cocurrent and countercurrent flows in natural porous media. *SPE Reservoir Engineering*, 5(03), 361-368.
- Boynton, R. S. (1980). *Chemistry and Technology of Lime and Limestone*. John Wylie & Sons. Inc., New York.
- Breckels, I. M., & Van Eekelen, H. A. M. (1982). Relationship between horizontal stress and depth in sedimentary basins. *Journal of Petroleum Technology*, 34(09), 2-191.
- Bredehoeft, J. D., Wolff, R. G., Keys, W. S., & Shuter, E. (1976). Hydraulic fracturing to determine the regional in situ stress field, Piceance Basin, Colorado. *Geological Society of America Bulletin*, 87(2), 250-258.
- Brooks, R. H., & Corey, A. T. (1966). Properties of porous media affecting fluid flow. *Journal of the Irrigation and Drainage Division*, 92(2), 61-90.

- Brown, R. J. (1980). Connection between formation factor for electrical resistivity and fluid-solid coupling factor in Biot's equations for acoustic waves in fluid-filled porous media. *Geophysics*, 45(8), 1269-1275.
- Brown, E. T., & Hoek, E. (1978). Trends in relationships between measured in-situ stresses and depth. In *International Journal of Rock Mechanics and Mining Sciences & Geomechanics Abstracts*, Vol. 15, No. 4, 211-215.
- Brotons, V., Tomás, R., Ivorra, S., Grediaga, A., Martínez-Martínez, J., Benavente, D., & Gómez-Heras, M. (2016). Improved correlation between the static and dynamic elastic modulus of different types of rocks. *Materials and structures*, 49(8), 3021-3037.
- Buckley, S. E., & Leverett, M. (1942). Mechanism of fluid displacement in sands. *Transactions of the AIME*, 146(01), 107-116.
- Burchette, T. P. (2012). Carbonate rocks and petroleum reservoirs: a geological perspective from the industry. *Geological Society, London, Special Publications*, 370(1), 17-37.
- Burdine, N. T., Gournay, L. S., & Reichertz, P. P. (1950). Pore size distribution of petroleum reservoir rocks. *Journal of Petroleum Technology*, 2(07), 195-204.
- Burdine, N. (1953). Relative permeability calculations from pore size distribution data. *Journal of Petroleum Technology*, 5(03), 71-78.
- Cardwell, W. T., & Parsons, R. L. (1949). Gravity drainage theory. *Trans. AIME*, 179(1), 199-215.
- Carman, P.C. (1956). *Flow of gases through porous media*. London, England: Butterworths Scientific Publications
- Carman, P. C. (1939). Permeability of saturated sands, soils and clays. *The Journal of Agricultural Science*, 29(2), 262-273.
- Choquette, P. W., & Pray, L. C. (1970). Geologic nomenclature and classification of porosity in sedimentary carbonates. *AAPG*, 54(2), 207-250.
- Churcher, P. L., French, P. R., Shaw, J. C., & Schramm, L. L. (1991). Rock properties of Berea sandstone, Baker dolomite, and Indiana limestone. In *SPE International Symposium on Oilfield Chemistry* (Vol. 20, p. 22). Anaheim, CA: Society of Petroleum Engineers.

- Cinco-Ley, H. (1981). Transient pressure analysis for fractured wells. *Journal of petroleum technology*, 33(09), 1-749.
- Cooper, J. R., & Dooley, R. B. (2008). Release of the IAPWS formulation 2008 for the viscosity of ordinary water substance. The International Association for the Properties of Water and Steam. Available at <http://www.iapws.org>
- Corey, A. T. (1954). The interrelation between gas and oil relative permeabilities. *Producers monthly*, 19(1), 38-41.
- Craig, F. F. (1971). The reservoir engineering aspects of water flooding. New York: HL Doherty Memorial Fund of AIME, Vol. 3, 45-47.
- Cueto-Felgueroso, L., & Juanes, R. (2008). Nonlocal interface dynamics and pattern formation in gravity-driven unsaturated flow through porous media. *Physical Review Letters*, 101(24), 244504.
- Cundall, P. A., & Lemos, J. V. (1990). Numerical simulation of fault instabilities with a continuously-yielding joint model. *Rockbursts and Seismicity in Mines*, Balkema, S, 147-152.
- Daemen, J. J., & Schultz, R. A. (Eds.). (1995). *Rock Mechanics: Proceedings of the 35th US Symposium on Rock Mechanics*. CRC Press.
- Dake, L. P. (1983). *Fundamentals of reservoir engineering* (Vol. 8). Amsterdam: Elsevier Scientific Pub. Co.
- Datta, S.S., Dupin, J.B. & Weitz, D.A. (2014). Fluid breakup during simultaneous two-phase flow through a three-dimensional porous medium. *Phys Fluids* 26(6), 062004.
- DeMets, C., Gordon, R. G., Argus, D. F., & Stein, S. (1994). Effect of recent revisions to the geomagnetic reversal time scale on estimates of current plate motions. *Geophysical research letters*, 21(20), 2191-2194.
- DeMets, C., Gordon, R. G., & Argus, D. F. (2010). Geologically current plate motions. *Geophysical Journal International*, 181(1), 1-80.

- Desroches, J. (1995). Stress testing with the micro-hydraulic fracturing technique—focus on fracture reopening. In Proceedings of the 35th US symposium on rock mechanics. Rotterdam: Balkema, 217-223.
- Detournay, E., & Cheng, A. H. D. (1993). Fundamentals of poroelasticity. In C. Fairhurst, (Eds.) Comprehensive rock engineering: principles, practice and projects. Volume 2: Analysis and design methods (Chapter 5, 113–171). New York: Pergamon Press Inc.
- Dickson, J. L., Gupta, G., Horozov, T. S., Binks, B. P., & Johnston, K. P. (2006). Wetting phenomena at the CO₂/water/glass interface. *Langmuir*, 22(5), 2161-2170.
- Dullien, F. A., (2012). Porous media: fluid transport and pore structure. Burlington, MA: Elsevier Science
- Ehrenberg, S. N., & Nadeau, P. H. (2005). Sandstone vs. carbonate petroleum reservoirs: A global perspective on porosity-depth and porosity-permeability relationships. *AAPG*, 89(4), 435-445.
- Elfeel, M. A., Al-Dhahli, A., Geiger, S., & van Dijke, M. I. (2016). Fracture-matrix interactions during immiscible three-phase flow. *Journal of Petroleum Science and Engineering*, 143, 171-186.
- El Rabaa, W. (1989). Experimental study of hydraulic fracture geometry initiated from horizontal wells. In SPE Annual Technical Conference and Exhibition. Society of Petroleum Engineers.
- Elyasi, A., Goshtasbi, K., Saeidi, O., & Torabi, S. R. (2014). Stress determination and geomechanical stability analysis of an oil well of Iran. *Sadhana*, 39(1), 207-220.
- Engelder, T. (2014). Stress regimes in the lithosphere (Vol. 151). Princeton University Press.
- Falcon, N. L. (1961). Major earth-flexuring in the Zagros Mountains of south-west Iran. *Quarterly Journal of the Geological Society*, 117(1-4), 367-376.
- Falcucci, G., Succi, S., Montessori, A., Melchionna, S., Prestininzi, P., Barroo, C., & Kaxiras, E. (2016). Mapping reactive flow patterns in monolithic nanoporous catalysts. *Microfluidics and Nanofluidics*, 20(7), 105
- Fang, H., (2013). Foundation engineering handbook. Boston, MA: Springer US

- Fernø, M. A. (2012). Enhanced oil recovery in fractured reservoirs. *Introduction to Enhanced Oil Recovery (EOR) Processes and Bioremediation of Oil-Contaminated Sites*, 89(110), 89-110.
- Fjar, E., Holt, R. M., Raaen, A. M., Risnes, R., & Horsrud, P. (2008). *Petroleum related rock mechanics (Vol. 53)*. Elsevier.
- Gao, H., Yu, B., Duan, Y. & Fang, Q. (2014). Fractal analysis of dimensionless capillary pressure function. *International Journal of Heat and Mass Transfer*, 69, 26-33
- Gardner, G. H. F., Gardner, L. W., & Gregory, A. R. (1974). Formation velocity and density diagnostic basics for stratigraphic traps. *Geophysics*, 39(6), 770-780.
- Geertsma, J. (1957). A remark on the analogy between thermoelasticity and the elasticity of saturated porous media. *Journal of the Mechanics and Physics of Solids*, 6(1), 13-16.
- Gluyas, J., & Swarbrick, R. (2013). *Petroleum geoscience*. John Wiley & Sons.
- Goodman, R. E. (1989). *Introduction to rock mechanics (Vol. 2)*. New York: Wiley.
- Greenwald, R. F. (1981). *Volumetric response of porous media to pressure variations*. Ph.D. thesis, Univ. of Calif., Berkeley, 1980
- Gudjonsdottir, M., Palsson, Eliasson, H. J. & Saevarsdottir, G. (2015). Calculation of relative permeabilities from field data and comparison to laboratory measurements. *Geothermics*, 54, 1-9.
- Haghi, A. H., Kharrat, R., Asef, M. R., & Rezazadegan, H. (2013). Present-day stress of the central Persian Gulf: implications for drilling and well performance. *Tectonophysics*, 608, 1429-1441.
- Haghi, A. H., Kharrat, R., & Asef, M. R. (2013). A case study for HCL-based fracturing and stress determination: A Deformation/Diffusion/Thermal approach. *Journal of Petroleum Science and Engineering*, 112, 105-116.
- Hagoort, J. (1980). Oil recovery by gravity drainage. *Society of Petroleum Engineers Journal*, 20(03), 139-150.
- Hamoud, M., R.J. Chalaturnyk and J. Leung. 2012. Influence of Geomechanical Processes on Relative Permeability. *Canadian Rock Mechanics Symposium*, Edmonton, Alberta, 9.

- Hartmann, A., Goldscheider, N., Wagener, T., Lange, J., & Weiler, M. (2014). Karst water resources in a changing world: Review of hydrological modeling approaches. *Reviews of Geophysics*, 52(3), 218-242.
- Hassanizadeh, S. M., & Gray, W. G. (1993). Thermodynamic basis of capillary pressure in porous media. *Water resources research*, 29(10), 3389-3405.
- Hassler, G. L., (1944). U.S. Patent No. 2,345,935. Washington, DC: U.S. Patent and Trademark Office.
- Haugen, A., Ferno, M. A., & Graue, A. (2008). Numerical Simulation and Sensitivity Analysis of In Situ Fluid Flow in MRI Laboratory Waterfloods of Fractured Carbonate Rocks at Different Wettabilities. In *SPE Annual Technical Conference and Exhibition*. Society of Petroleum Engineers, Denver, Colorado, SPE-116145.
- Hayavi MT, Abdideh M. (2016). Estimation of in-situ horizontal stresses using the linear poroelastic model and minifrac test results in tectonically active area. *Russian Journal of Earth Sciences*, 16(4).
- Heidbach, O., Tingay, M., Barth, A., Reinecker, J., Kurfeß, D., & Müller, B. (2010). Global crustal stress pattern based on the World Stress Map database release 2008. *Tectonophysics*, 482(1-4), 3-15.
- Heidbach, O., M. Rajabi, X. Cui, K. Fuchs, B. Müller, J. Reinecker, K. Reiter, M. Tingay, F. Wenzel, F. Xie, M. O. Ziegler, M.-L. Zoback, and M. D. Zoback (2018). The World Stress Map database release 2016: Crustal stress pattern across scales. *Tectonophysics*, 744, 484-498.
- Heidbach, O., Rajabi, M., Ziegler, M., & Reiter, K. (2016). The World Stress Map database release 2016-global crustal stress pattern vs. absolute plate motion. In *EGU General Assembly Conference Abstracts (Vol. 18)*.
- Hilfer, R. & Øren, P.E. (1996). Dimensional analysis of pore scale and field scale immiscible displacement. *Transport in Porous Media*, 22(1), 53-72.
- Honarpour, M. & Mahmood, S. M. (1988). Relative-permeability measurements: An overview. *Journal of petroleum technology*, 40(08), 963-966.

- Hossain, M. M., Rahman, M. K., & Rahman, S. S. (2000). Hydraulic fracture initiation and propagation: roles of wellbore trajectory, perforation and stress regimes. *Journal of Petroleum Science and Engineering*, 27(3-4), 129-149.
- Hubbert, M. K., & Willis, D. G. (1972). Mechanics of hydraulic fracturing. *AAPG*, 239-257.
- Hudson, J. A., & Harrison, J. P. (2000). *Engineering rock mechanics: an introduction to the principles*. Elsevier.
- Huo, D., & Benson, S. M. (2016). Experimental Investigation of Stress-Dependency of Relative Permeability in Rock Fractures. *Transport in Porous Media*, 1-24.
- Elfeel, M. A., Al-Dhahli, A., Geiger, S., & van Dijke, M. I. (2016). Fracture-matrix interactions during immiscible three-phase flow. *Journal of Petroleum Science and Engineering*, 143, 171-186.
- Iglauer, S., Salamah, A., Sarmadivaleh, M., Liu, K., & Phan, C. (2014). Contamination of silica surfaces: Impact on water-CO₂-quartz and glass contact angle measurements. *International Journal of Greenhouse Gas Control*, 22, 325-328.
- Jaeger, J. C., Cook, N. G. W., & Zimmerman, R. W. (2007). *Fundamentals of rock mechanics*, 4th edn Blackwell. Maiden, MA.
- Jordan, P. B. (2016). Two-phase relative permeability measurements in Berea sandstone at reservoir conditions (Doctoral dissertation).
- Jones, C., Al-Quraishi, A., Somerville¹, J., & Hamilton, S. (2001). Stress Sensitivity of Saturation and End-Point Relative Permeability. Society of Core Analysts, Edinburgh, Scotland.
- Karimaie, H., & Torsæter, O. (2007). Effect of injection rate, initial water saturation and gravity on water injection in slightly water-wet fractured porous media. *Journal of Petroleum Science and Engineering*, 58(1-2), 293-308.
- Karimnezhad, M., Jalalifar, H., & Kamari, M. (2014). Investigation of caprock integrity for CO₂ sequestration in an oil reservoir using a numerical method. *Journal of Natural Gas Science and Engineering*, 21, 1127-1137.

- Khan, A. H. (2009). Shear Induced Relative Permeability Changes in Uncemented Sands. Masters of Science in Engineering Thesis, University of Texas at Austin, USA.
- Kim, Y., Wan, J., Kneafsey, T. J., & Tokunaga, T. K. (2012). Dewetting of silica surfaces upon reactions with supercritical CO₂ and brine: pore-scale studies in micromodels. *Environmental science & technology*, 46(7),
- Kimura, M. (2018). Prediction of tortuosity, permeability, and pore radius of water-saturated unconsolidated glass beads and sands. *Journal of the Acoustical Society of America*, 143(5), 3154-3168.
- Kirsch, C. (1898). Die theorie der elastizitat und die bedurfnisse der festigkeitslehre. *Zeitschrift des Vereines Deutscher Ingenieure*, 42, 797-807.
- Koponen, A., Kataja, M., & Timonen, J. (1997). Permeability and effective porosity of porous media. *Physical Review E*, 56(3), 3319.
- Kozeny, J. (1927). Uber kapillare leitung der wasser in boden. *Royal Academy of Science, Vienna, Proc. Class I*, 136, 271-306.
- Krevor, S., Pini, R., Zuo, L., & Benson, S. M. (2012). Relative permeability and trapping of CO₂ and water in sandstone rocks at reservoir conditions. *Water resources research*, 48(2).
- Kühn, M. (2004): *Reactive Flow Modeling of Hydrothermal Systems*. Springer, Berlin
- Lawrence, M., & Jiang, Y. (2017). Porosity, pore size distribution, micro-structure. In *Bio-aggregates Based Building Materials* (39-71). Springer, Dordrecht.
- Leas, W. J., Jenks, J. H., & Russell, C. D. (1950). Relative permeability to gas. *Journal of Petroleum Technology*, 2(03), 65-72.
- Lee, M. Y., & Haimson, B. C. (1989). Statistical evaluation of hydraulic fracturing stress measurement parameters. In *International Journal of Rock Mechanics and Mining Sciences & Geomechanics Abstracts*, Vol. 26, No. 6, 447-456.
- Lei, G., Mo, S., Dong, Z., Wang, C. & Li, W. (2018). Theoretical and experimental study on stress-dependency of oil–water relative permeability in fractal porous media. *Fractals*, 26(02), 1840010.

- Lefebvre du Prey, E. J. (1973). Factors affecting liquid-liquid relative permeabilities of a consolidated porous medium. *Society of Petroleum Engineers Journal*, 13(01), 39-47.
- Lemmon, E. W., & Jacobsen, R. T. (2004). Viscosity and thermal conductivity equations for nitrogen, oxygen, argon, and air. *International journal of thermophysics*, 25(1), 21-69.
- Leverett, M. (1941). Capillary behavior in porous solids. *Transactions of the AIME*, 142(01), 152-169.
- Li, J. J., Liu, Y., Gao, Y. J., Cheng, B. Y., & Jiang, H. Q. (2019). Pore-scale study of the pressure-sensitive effect of sandstone and its influence on multiphase flows. *Petroleum Science*, 16(2), 382-395.
- Li, P., Chalaturnyk, R. J., & Polikar, M. (2004). Issues with reservoir geomechanical simulations of the SAGD process. *Journal of Canadian Petroleum Technology*, 43(05).
- Li, P., Chalaturnyk, R. J., & Tan, T. B. (2006). Coupled reservoir geomechanical simulations for the SAGD process. *Journal of Canadian Petroleum Technology*, 45(01).
- Li, K., & Horne, R. N. (2006). Comparison of methods to calculate relative permeability from capillary pressure in consolidated water-wet porous media. *Water resources research*, 42(6).
- Li, K. & Horne, R.N. (2004). Universal capillary pressure and relative permeability model from fractal characterization of rock. *Stanford Geothermal Workshop on Geothermal Reservoir Engineering*, Stanford University, Stanford, California
- Li, J.J., Liu, Y., Gao, Y.J., Cheng, B.Y. & Jiang, H.Q. (2019). Pore-scale study of the pressure-sensitive effect of sandstone and its influence on multiphase flows. *Petroleum Science*, 16, 382-395.
- Lian, P., Cheng, L., & Ma, C. Y., (2012). The characteristics of relative permeability curves in naturally fractured carbonate reservoirs. *Journal of Canadian Petroleum Technology*, 51(02), 137-142.
- Lintao, Y., Marshall, A. M., Wanatowski, D., Stace, R., & Ekneligoda, T. (2017). Effect of high temperatures on sandstone—a computed tomography scan study. *International Journal of Physical Modelling in Geotechnics*, 17(2), 75-90.

- Liu, H. H., Rutqvist, J., & Berryman, J. G. (2009). On the relationship between stress and elastic strain for porous and fractured rock. *International Journal of Rock Mechanics and Mining Sciences*, 46(2), 289-296.
- Lucia, F. J. (1995). Rock-fabric/ petrophysical classification of carbonate pore space for reservoir characterization. *AAPG bulletin*, 79(9), 1275-1300.
- Martin, C. D., & Chandler, N. A. (1993). Stress heterogeneity and geological structures. In *International journal of rock mechanics and mining sciences & geomechanics abstracts*, Vol. 30, No. 7, 993-999.
- Matyka, M., Khalili, A., & Koza, Z. (2008). Tortuosity-porosity relation in porous media flow. *Physical Review E*, 78(2), 026306.
- Mattax, C. C., & KYTE, J. R. (1962). Imbibition oil recovery from fractured, water-drive reservoir. *Society of Petroleum Engineers Journal*, 2(02), 177-184.
- McClusky, S., Reilinger, R., Mahmoud, S., Ben Sari, D., & Tealeb, A. (2003). GPS constraints on Africa (Nubia) and Arabia plate motions. *Geophysical Journal International*, 155(1), 126-138.
- McDonald, A.E., Beckner, B.L., Chan, H.M., Jones, T.A., Wooten, S.O. (1991). Some important considerations in the simulation of naturally fractured reservoirs. SPE 21814, presented at SPE meeting, Denver, Colorado.
- McQuarrie, N. (2004). Crustal scale geometry of the Zagros fold-thrust belt, Iran. *Journal of Structural Geology*, 26(3), 519-535.
- McWhorter, D. B., & Sunada, D. K. (1990). Exact integral solutions for two-phase flow. *Water Resources Research*, 26(3), 399-413.
- Meredith, R.E. & Tobias, C.W. (1962): Conduction in heterogeneous systems. In: Tobias, C.W. (ed.) *Advances in Electrochemistry and Electrochemical Engineering 2.*, Interscience Publishers, New York.
- Mo, S.Y., He, S.L., Lei, G., Gai, S.H. & Liu, Z.K. (2015). Effect of the drawdown pressure on the relative permeability in tight gas: A theoretical and experimental study. *Journal of Natural Gas Science and Engineering*, 24, 264-271.

- Molaghab, A., Taherynia, M. H., Aghda, S. M. F., & Fahimifar, A. (2017). Determination of minimum and maximum stress profiles using wellbore failure evidences: a case study in deep oil well in the southwest of Iran. *Journal of Petroleum Exploration and Production Technology*, 7(3), 707-715.
- Montemore, M. M., Montessori, A., Succi, S., Barroo, C., Falcucci, G., Bell, D. C., & Kaxiras, E. (2017). Effect of nanoscale flows on the surface structure of nanoporous catalysts. *The Journal of chemical physics*, 146(21), 214703.
- Moore, C. H., & Wade, W. J. (2013). The nature and classification of carbonate porosity. In *Carbonate Reservoirs* (Chapter 4, Vol. 67, 51-65). Amsterdam: Elsevier.
- Montessori, A., Prestininzi, P., La Rocca, M., & Succi, S. (2015). Lattice Boltzmann approach for complex nonequilibrium flows. *Physical Review E*, 92(4), 043308.
- Montessori, A., Prestininzi, P., La Rocca, M., Falcucci, G., Succi, S., & Kaxiras, E. (2016). Effects of Knudsen diffusivity on the effective reactivity of nanoporous catalyst media. *Journal of Computational Science*, 17, 377-383.
- Morris, J. P., Lomov, I. N., & Glenn, L. A. (2003). A constitutive model for stress-induced permeability and porosity evolution of Berea sandstone. *Journal of Geophysical Research: Solid Earth*, 108(B10), 2252.
- Muskat, M. (1937), The flow of fluids through porous media, *Journal of Applied Physics*, 8(4), 274–282.
- Müller, N. (2011). Supercritical CO₂-brine relative permeability experiments in reservoir rocks—literature review and recommendations. *Transport in porous media*, 87(2), 367-383.
- Najibi, A. R., Ghafoori, M., Lashkaripour, G. R., & Asef, M. R. (2015). Empirical relations between strength and static and dynamic elastic properties of Asmari and Sarvak limestones, two main oil reservoirs in Iran. *Journal of Petroleum Science and Engineering*, 126, 78-82.
- Nelson, R. (2001). *Geologic analysis of naturally fractured reservoirs*. Elsevier.

- Nolte, K. G., & Economides, M. J. (1989). Fracturing diagnosis using pressure analysis. *Reservoir Stimulation*, 7-28.
- Oak, M. J., Baker, L. E., & Thomas, D. C. (1990). Three-phase relative permeability of Berea sandstone. *Journal of Petroleum Technology*, 42(08), 1-054.
- Ojagbohunmi, S., Chalaturnyk, R. J., & Leung, J. Y. W. (2012). Coupling of Stress-Dependent Relative Permeability and Reservoir Simulation. In *SPE Improved Oil Recovery Symposium*. Society of Petroleum Engineers, Oklahoma, USA, SPE-154083-MS.
- Osoba, J. S., Richardson, J. G., Kerver, J. K., Hafford, J. A., & Blair, P. M. (1951). Laboratory measurements of relative permeability. *Journal of Petroleum Technology*, 3(02), 47-56.
- Otsu, N. (1979). A threshold selection method from gray-level histograms. *IEEE transactions on systems, man, and cybernetics*, 9(1), 62-66.
- Owens, W. W., & Archer, D. (1971). The effect of rock wettability on oil-water relative permeability relationships. *Journal of Petroleum Technology*, 23(07), 873-878.
- Pak, T., Archilha, N. L., Mantovani, I. F., Moreira, A. C., & Butler, I. B. (2018). The dynamics of nanoparticle-enhanced fluid displacement in porous media-a pore-scale study. *Scientific reports*, 8(1), 11148.
- Pak, T., Butler, I. B., Geiger, S., van Dijke, M. I., & Sorbie, K. S. (2015). Droplet fragmentation: 3D imaging of a previously unidentified pore-scale process during multiphase flow in porous media. *Proceedings of the National Academy of Sciences*, 112(7), 1947-1952.
- Pan, X., Wong, R.C., Maini, B.B. (1996): Steady-state two-phase in a smooth parallel fracture, paper 96-39. The Petroleum Society in Calgary, Alberta.
- Pariseau, W. G. (2011) *Design Analysis in Rock Mechanics* 2nd Edition, CRC Press, Appendix B
- Pentland, C. H., El-Maghraby, R., Iglauer, S., & Blunt, M. J. (2011). Measurements of the capillary trapping of super-critical carbon dioxide in Berea sandstone. *Geophysical Research Letters*, 38(6).

- Perrin, J. C., & Benson, S. (2010). An experimental study on the influence of sub-core scale heterogeneities on CO₂ distribution in reservoir rocks. *Transport in porous media*, 82(1), 93-109.
- Peters, E. J. (2012). *Advanced Petrophysics: Dispersion, interfacial phenomena (Vol. 2)*. Austin, TX: Live Oak Book Company
- Pierdominici, S., Mariucci, M. T., & Montone, P. (2011). A study to constrain the geometry of an active fault in southern Italy through borehole breakouts and downhole logs. *Journal of Geodynamics*, 52(3-4), 279-289.
- Pini, R., & Benson, S. M. (2013). Simultaneous determination of capillary pressure and relative permeability curves from core-flooding experiments with various fluid pairs. *Water Resources Research*, 49(6), 3516-3530.
- Pini, R., Krevor, S. C., & Benson, S. M. (2012). Capillary pressure and heterogeneity for the CO₂/water system in sandstone rocks at reservoir conditions. *Advances in Water Resources*, 38, 48-59.
- Plug, W. J., & Bruining, J. (2007). Capillary pressure for the sand–CO₂–water system under various pressure conditions. Application to CO₂ sequestration. *Advances in Water Resources*, 30(11), 2339-2353.
- Plumb, R. A., & Hickman, S. H. (1985). Stress-induced borehole elongation: A comparison between the four-arm dipmeter and the borehole televiewer in the Auburn geothermal well. *Journal of Geophysical Research: Solid Earth*, 90(B7), 5513-5521.
- Plumb, R. A. (1989). Fracture patterns associated with incipient wellbore breakouts. In *ISRM International Symposium. International Society for Rock Mechanics and Rock Engineering*, Pau, France, ISRM-IS-1989-098.
- Pooladi-Darvish, M., & Firoozabadi, A. (2000). Cocurrent and countercurrent imbibition in a water-wet matrix block. *SPE Journal*, 5(01), 3-11.
- Purcell, W. R. (1949). Capillary pressures-their measurement using mercury and the calculation of permeability therefrom. *Journal of Petroleum Technology*, 1(02), 39-48.

- Pyrak-Nolte, L. J., Cook, N. G., & Nolte, D. D. (1988). Fluid percolation through single fractures. *Geophysical Research Letters*, 15(11), 1247-1250.
- Rabbani, H. S., Joekar-Niasar, V., Pak, T., & Shokri, N. (2017). New insights on the complex dynamics of two-phase flow in porous media under intermediate-wet conditions. *Scientific reports*, 7(1), 4584.
- Rabbani, H. S., Zhao, B., Juanes, R., & Shokri, N. (2018). Pore geometry control of apparent wetting in porous media. *Scientific reports*, 8(1), 15729
- Raeini, A.Q., Blunt, M.J. & Bijeljic, B. (2014). Direct simulations of two-phase flow on micro-CT images of porous media and upscaling of pore-scale forces. *Adv. Water Resources Research*, 74(0), 116–126.
- Rajabi, M., Sherkati, S., Bohlooli, B., & Tingay, M. (2010). Subsurface fracture analysis and determination of in-situ stress direction using FMI logs: An example from the Santonian carbonates (Ilam Formation) in the Abadan Plain, Iran. *Tectonophysics*, 492(1-4), 192-200.
- Ranjith, P. G., Viete, D. R., Chen, B. J., & Perera, M. S. A. (2012). Transformation plasticity and the effect of temperature on the mechanical behaviour of Hawkesbury sandstone at atmospheric pressure. *Engineering Geology*, 151, 120-127.
- Reynolds, C., & Krevor, S. (2015). Characterizing flow behaviour for gas injection: Relative permeability of CO₂-brine and N₂-water in heterogeneous rocks. *Water Resources Research*, 51, 9464– 9489.
- Richardson, J. G., Kerver, J. K., Hafford, J. A., & Osoba, J. S. (1952). Laboratory determination of relative permeability. *Journal of Petroleum Technology*, 4(08), 187-196.
- Ricou, L. E. (1974). L'évolution géologique de la région de Neyriz (Zagros iranien) et l'évolution structurale des zagrides. These, Université d'Orsay, France.
- Romm, E. S. (1966). Flow characteristics of fractured rocks. Nedra, Moscow, 283.
- Rossen, W. R., & Kumar, A. T. (1992). Single-and two-phase flow in natural fractures. SPE Annual Technical Conference and Exhibition. Society of Petroleum Engineers, Washington, D.C., SPE-24915-MS.

- Rouquerol, J., Llewellyn, P., & Rouquerol, F. (2007). Is the BET equation applicable to microporous adsorbents. *Stud. Surf. Sci. Catal*, 160(07), 49-56.
- Saeidi, O., & Ahmadi, M. (2012). Determination of Stress Orientation and Magnitude in a Directional Well Bore, Case Study: Mansouri-54 Wellbore of Southwest Iranian Oilfield. *ISRM (India) Journal*, 1(1), 25-30.
- Schmid, K. S., Alyafei, N., Geiger, S., & Blunt, M. J. (2016). Analytical solutions for spontaneous imbibition: fractional-flow theory and experimental analysis. *SPE Journal*, 21(06), 2-308.
- Schmid, K. S., & Geiger, S. (2012). Universal scaling of spontaneous imbibition for water-wet systems. *Water resources research*, 48(3).
- Schroeder, J. W. (1944). *Essai sur la structure de l'Iran*. *Eclogae geologicae helvetiae*.
- Schutjens, P. M. T. M., Hanssen, T. H., Hettema, M. H. H., Merour, J., De Bree, P., Coremans, J. W. A., & Helliesen, G. (2004). Compaction-induced porosity/permeability reduction in sandstone reservoirs: Data and model for elasticity-dominated deformation. *SPE Reservoir Evaluation & Engineering*, 7(03), 202-216.
- Seader, J. D., E. J. Henley, & D. K. Roper (2010), *Separation Process Principles*, 3rd ed. Wiley, New York.
- Segall, P. (1989). Earthquakes triggered by fluid extraction. *Geology*, 17(10), 942-946.
- SellaGF, D., & REVEL, M. (2002). A Model for Recent Plate Velocities from Space Geodesy. *Journal of Geophysical Research*, 107(B4), 1.
- Settari, A., Walters, D. A., & Behie, G. A. (1999). Reservoir geomechanics: New approach to reservoir engineering analysis. In *Technical Meeting/Petroleum Conference of the South Saskatchewan Section*. Petroleum Society of Canada, 99-116.
- Singh, K., Menke, H., Andrew, M., Lin, Q., Rau, C., Blunt, M. J., & Bijeljic, B. (2017). Dynamics of snap-off and pore-filling events during two-phase fluid flow in permeable media. *Scientific reports*, 7(1), 5192.

- Shadizadeh, S. R., Habibnia, B. A., & Syllabee, R. (2009). Investigation and selection of suitable layers in bangestan reservoir for hydraulic fracturing operation. *Scientia Iranica. Transaction C, Chemistry, Chemical Engineering*, 16(2), 149.
- Shalev, E., Lyakhovsky, V., Ougier-Simonin, A., Hamiel, Y., & Zhu, W. (2014). Inelastic compaction, dilation and hysteresis of sandstones under hydrostatic conditions. *Geophysical Journal International*, 197(2), 920-925.
- Shosa, J. D., & Cathles, L. M. (2001). Experimental investigation of capillary blockage of two phase flow in layered porous media. In *Petroleum Systems of Deep-Water Basins: Global and Gulf of Mexico Experience: Proceedings of the GCSSEPM Foundation, 21st Annual Bob F. Perkins Research Conference*, 725-739.
- Song, L., & Hareland, G. (2012). Minimum horizontal stress profile from logging data for Montney Formation of North East British Columbia. In *SPE Canadian Unconventional Resources Conference*. Society of Petroleum Engineers, Calgary, Canada, SPE-162233-MS.
- Sone, H., & Zoback, M. D. (2014). Viscous relaxation model for predicting least principal stress magnitudes in sedimentary rocks. *Journal of Petroleum Science and Engineering*, 124, 416-431.
- Stocklin, J. (1968). Structural history and tectonics of Iran: a review. *AAPG bulletin*, 52(7), 1229-1258.
- Stöcklin, J. (1974). Possible ancient continental margins in Iran. In *The geology of continental margins (873-887)*. Springer, Berlin, Heidelberg.
- Szulczewski, M. L., MacMinn, C. W., Herzog, H. J., & Juanes, R. (2012). Lifetime of carbon capture and storage as a climate-change mitigation technology. *Proceedings of the National Academy of Sciences*, 109(14), 5185-5189.
- Tingay, M. R., Hillis, R. R., Swarbrick, R. E., Morley, C. K., & Damit, A. R. (2009). Origin of overpressure and pore-pressure prediction in the Baram province, Brunei. *AAPG Bulletin*, 93(1), 51-74.

- Tingay, M. R., Hillis, R. R., Morley, C. K., King, R. C., Swarbrick, R. E., & Damit, A. R. (2009). Present-day stress and neotectonics of Brunei: Implications for petroleum exploration and production. *AAPG Bulletin*, 93(1), 75-100.
- Thiercelin, M. J., & Plumb, R. A. (1994). A core-based prediction of lithologic stress contrasts in east Texas formations. *SPE Formation Evaluation*, 9(04), 251-258.
- Torsæter, O., & Silseth, J. K. (1985). The effects of sample shape and boundary conditions on capillary imbibition. In *North Sea Chalk Symp.*, Stavanger.
- Tortike, W. S., & Ali, S. M. (1993). Reservoir simulation integrated with geomechanics. *Journal of Canadian Petroleum Technology*, 32(05).
- Van Genuchten, M. T. (1980). A closed-form equation for predicting the hydraulic conductivity of unsaturated soils 1. *Soil science society of America journal*, 44(5), 892-898.
- Vernant, P., Nilforoushan, F., Hatzfeld, D., Abbassi, M. R., Vigny, C., Masson, F., & Tavakoli, F. (2004). Present-day crustal deformation and plate kinematics in the Middle East constrained by GPS measurements in Iran and northern Oman. *Geophysical Journal International*, 157(1), 381-398.
- Viksund, B. G., Morrow, N. R., Ma, S., Wang, W., & Graue, A. (1998). Initial water saturation and oil recovery from chalk and sandstone by spontaneous imbibition. In *Proceedings, 1998 International Symposium of Society of Core Analysts*, The Hague, SCA-9814.
- Wang, H. F. (2017). *Theory of linear poroelasticity with applications to geomechanics and hydrogeology*. Princeton University Press.
- Wang, H. (2000). *Theory of linear poroelasticity with applications to geomechanics and hydrogeology*. Princeton University Press.
- Warren, J. E., & Root, P. J. (1963). The behavior of naturally fractured reservoirs. *SPE Journal*, 3(03), 245-255.
- Washburn, E. (1921), The dynamics of capillary flow, *Phys. Rev.* 17, 273–283.
- Xu, P., Qiu, S., Yu, B. & Jiang, Z., (2013). Prediction of relative permeability in unsaturated porous media with a fractal approach. *International Journal of Heat and Mass Transfer*, 64, 829-837.

- Yaghoubi, A. A., & Zeinali, M. (2009). Determination of magnitude and orientation of the in-situ stress from borehole breakout and effect of pore pressure on borehole stability—Case study in Cheshmeh Khush oil field of Iran. *Journal of Petroleum Science and Engineering*, 67(3-4), 116-126.
- Yang, Z., Niemi, A., Fagerlund, F., & Illangasekare, T. (2013). Two-phase flow in rough-walled fractures: comparison of continuum and invasion-percolation models. *Water Resources Research*, 49, 993–1002.
- Yoo, H., Park, J., Lee, Y., & Lee, J. (2019). An experimental investigation into the effect of pore size distribution on the acid-rock reaction in carbonate acidizing. *Journal of Petroleum Science and Engineering*, 180, 504-517.
- Yu, B. & Cheng, P., (2002). A fractal permeability model for bi-dispersed porous media. *International Journal of Heat and Mass Transfer*, 45(14), 2983-2993.
- Yu, B., Li, J., Li, Z. & Zou, M. (2003). Permeabilities of unsaturated fractal porous media. *International journal of multiphase flow*, 29(10), 1625-1642.
- Yu, J., Chen, S. J., Chen, X., Zhang, Y. Z., & Cai, Y. Y. (2015). Experimental investigation on mechanical properties and permeability evolution of red sandstone after heat treatments. *Journal of Zhejiang University-SCIENCE A*, 16(9), 749-759.
- Zare, M. R., Shadizadeh, S. R., & Habibnia, B. (2010). Mechanical stability analysis of directional wells: a case study in Ahwaz oilfield. In *Nigeria Annual International Conference and Exhibition*. Society of Petroleum Engineers, Tinapa - Calabar, Nigeria, SPE-136989-MS.
- Zhang, X., Morrow, N. R., & Ma, S. (1996). Experimental verification of a modified scaling group for spontaneous imbibition. *SPE Reservoir Engineering*, 11(04), 280-285.
- Zhou, X., Morrow, N. R., & Ma, S. (2000). Interrelationship of wettability, initial water saturation, aging time, and oil recovery by spontaneous imbibition and waterflooding. *SPE Journal*, 5(02), 199-207.
- Zhu, W., & Wong, T. F. (1997). The transition from brittle faulting to cataclastic flow: Permeability evolution. *Journal of Geophysical Research: Solid Earth*, 102(B2), 3027-3041.

- Zimmerman, R.W., Somerton, W.H., & King, M.S., (1986). Compressibility of porous rocks. *Journal of Geophysical Research*, 91(B12), pp.12765-12777.
- Zheng, X., Zhigang, C. & Weichuan, L. (2013). Gas/water flowing ability influence experimental study of permeability stress sensibility in tight gas reservoir. *Well Logging Technology*, 4, 360-363.
- Zhu, W., & Wong, T. F. (1997). The transition from brittle faulting to cataclastic flow: Permeability evolution. *Journal of Geophysical Research: Solid Earth*, 102(B2), 3027-3041.
- Zoback, M. D., Barton, C. A., Brudy, M., Castillo, D. A., Finkbeiner, T., Grollmund, B. R., & Wiprut, D. J. (2003). Determination of stress orientation and magnitude in deep wells. *International Journal of Rock Mechanics and Mining Sciences*, 40(7-8), 1049-1076.
- Zoback, M. D. (2010). *Reservoir geomechanics*. Cambridge University Press.
- Zoback, M. D., & Haimson, B. C. (1983). *Hydraulic fracturing stress measurements*. US National Academy of Sciences.

Appendix A* : Derivation of Similarity Variable

As noted in section 3.3.1, one boundary condition for the unidirectional displacement of the non-wetting phase by entry of the wetting phase during spontaneous imbibition (ignoring the gravity) is:

$$q_w(x = 0, t) = \frac{C}{\sqrt{t}} \quad (\text{A1})$$

Now, recalling the continuity equation (Eq.(3.10)), at $x=0$ we have:

$$\frac{\partial}{\partial t}(S_w \varphi) = -\frac{\partial}{\partial x} \left(F \frac{C}{\sqrt{t}} \right) \quad (\text{A2})$$

where the capillary-driven fractional flow function F is defined as (McWhorter and Sunada, 1990):

$$F = \frac{q_w}{q_w(x = 0, t)} \quad (\text{A3})$$

As the term $\frac{C}{\sqrt{t}}$ in Eq.(A2) is independent from x , Eq.(A2) can be rewritten as follows:

$$-\frac{\partial}{\partial t}(S_w \varphi) = \frac{C}{\sqrt{t}} \frac{\partial F}{\partial x} \quad (\text{A4})$$

Similarly, it may be written as

$$\frac{C}{\sqrt{t}} \frac{\partial F}{\partial S_w} \frac{\partial S_w}{\partial x} + \frac{\partial(S_w \varphi)}{\partial t} = 0 \quad (\text{A5})$$

Eq.(A5) is a hyperbolic PDE. Based on calculus, the total differential of $S_w \varphi$ is given by

$$\frac{\partial(S_w \varphi)}{\partial x} \frac{dx}{dt} + \frac{\partial(S_w \varphi)}{\partial t} = \frac{d(S_w \varphi)}{dt} \quad (\text{A6})$$

Subtracting Eq.(A5) from Eq.(A6), we obtain

* This appendix was published in: Haghi, A. H., Chalaturnyk, R., & Geiger, S. (2018). New Semi-Analytical Insights into Stress-Dependent Spontaneous Imbibition and Oil Recovery in Naturally Fractured Carbonate Reservoirs. *Water Resources Research*, 54(11), 9605-9622.

$$\left(\varphi \frac{dx}{dt} - \frac{C}{\sqrt{t}} \frac{\partial F}{\partial S_w}\right) \frac{\partial S_w}{\partial x} = \frac{d(S_w \varphi)}{dt}. \quad (\text{A7})$$

In Eq.(A7), the porosity (φ) is considered to be independent from x . One can decompose Eq.(A7) into the following simultaneous equations:

$$\left(\varphi \frac{dx}{dt} - \frac{C}{\sqrt{t}} \frac{\partial F}{\partial S_w}\right) = 0 \quad (\text{A8})$$

$$\frac{d(S_w \varphi)}{dt} = 0. \quad (\text{A9})$$

Eq.(A9) indicates a fixed $S_w \varphi$ along the characteristic path given in Eq.(A8). Integrating Eq.(A8) to measure the distance x traveled by constant $S_w \varphi$ at a time t , we arrived to the following relation for the similarity variable:

$$\frac{2C}{\varphi} \frac{\partial F}{\partial S_w} = \frac{x}{\sqrt{t}} = \omega \quad (\text{A10})$$

Appendix B*: Berea Sandstone Experimental Database

This supporting information provides the experimental stress-dependent porosity, absolute permeability, relative permeability, and capillary pressure database corresponds to the plots given in Fig. 5.8-d in the main article.

Table 5.1. Stress-dependent porosity and absolute permeability database

Effective Confining Stress	Porosity	Absolute Permeability
MPa	%	mD
0	13.16	58
5	12.96	46.55
10	12.78	40.95
15	12.60	39.10
20	12.46	37.79
25	12.33	36.94
30	12.24	36.14

* This appendix was published in: Haghi, A.H., Talman, S., Chalaturnyk, R. (2020). Consecutive Experimental Determination of Stress-dependent Fluid Flow Properties of Berea Sandstone and Implications for Two-phase Flow Modelling. *Water Resources Research*, 56(1), <https://doi.org/10.1029/2018WR024245>

Table 5.2. Stress-dependent relative permeability database

σ' (MPa)	k_{rw}	k_{rg}	S_w
10	1	0	1
	0.697	0.006	0.93
	0.309	0.007	0.80
	0.260	0.013	0.68
	0.206	0.027	0.60
	0	0.313	0.33
	0	0.396	0.32
20	1	0	1
	0.645	0.006	0.90
	0.341	0.008	0.76
	0.250	0.014	0.69
	0.177	0.025	0.59
	0	0.288	0.29
	0	0.345	0.24
30	1	0	1
	0.603	0.005	0.84
	0.309	0.006	0.78
	0.234	0.011	0.67
	0.149	0.019	0.57
	0	0.223	0.3
	0	0.267	0.24

Table 5.3. Stress-dependent capillary pressure database

σ' (MPa)	P_c (kPa)	S_w
10	0	1
	9.48	0.94
	11.48	0.79
	11.4	0.71
	13.77	0.50
	15.99	0.35
	21.33	0.31
20	0	1
	11.11	0.79
	15.77	0.54
	18.80	0.49
	21.68	0.41
	23.99	0.32
	33.03	0.24
30	0	1
	12.9	0.88
	22.75	0.6
	34.36	0.49
	42.98	0.43
	52.72	0.34
	73.55	0.26

Appendix C*: Analytical Model Derivation

Here, we describe the mathematical process to develop Eq.(6.2) and Eqs.(6.4)-(6.5) based on the fractal scaling law (N) given in Eq.(6.1) and its first derivative ($dN = -D_f r_{max}^{D_f} r^{-D_f-1} dr$). To model the classical capillary pressure plots (e.g. Fig. 6.2d) at each certain water saturation (S_w) with the application of fractal capillary tubes, we employ a typical simplifying assumption dividing the tubes into two groups: (1) tubes with a radius smaller than r , which are fully filled with water and (2) the remaining tubes which are fully filled with gas; we ignore the volume of the thin film of water with a thickness on the order of nanometers. On the basis of this assumption, S_w in the porous media is calculated using the following equation (Gao et al., 2014):

$$S_w = \frac{V_{water}}{V_p} = \frac{\int_{r_{min}}^r \pi r^2 L_r dN}{\int_{r_{min}}^{r_{max}} \pi r^2 L_r dN}, \quad (6.1)$$

where the actual length of the convoluted capillary tubes (L_r) is assumed to follow the fractal scaling law $L_r = r^{1-D_T} L^{D_T}$ (Yu and Cheng, 2002). Here, D_T and L are the tortuosity fractal dimension and representative length of straight capillary tubes, respectively, where at D_T equal to 1 (straight tubes), $L_r = L$. Integrating Eq.(6.9), we derive the following relationship for S_w ,

$$S_w = \left(\frac{2\gamma \cos(\alpha)}{r_{max} P_c} \right)^{3-D_T-D_f}. \quad (6.2)$$

* This appendix was published in: Haghi, A.H., Chalaturnyk, R., Talman, S. (2019). Stress-Dependent Pore Deformation Effects on Multiphase Flow Properties of Porous Media. Scientific Reports, 9(1), 1-10

In Eq.(6.10), we replace the tube radius r with P_c using the Young-Laplace equation (Hilfer and Øren, 1996) and assume the fraction of minimum to maximum tube radius (r_{min}/r_{max}) in the medium is negligible, which is a reasonable assumption for most natural porous rocks (Yu and Cheng, 2002). Under a homogeneous pore strain condition, the strain of the tube with maximum radius (r_{max}) is derived as follows:

$$\varepsilon_p = 1 - \frac{V_p}{V_{pi}} = 1 - \left(\frac{r_{max}}{r_{maxi}} \right)^{3-D_T}. \quad (6.3)$$

For simplification, D_T and L for the tube with maximum radius are assumed here to be stress-independent, although the actual length (L_r) remains stress-dependent. Mixing Eq.(6.10) with Eq.(6.11) and rearranging it, by applying the Young-Laplace equation (Hilfer and Øren, 1996) to the tube with maximum radius ($P_e = 2\gamma\cos(\alpha)/r_{max}$), leads to Eq.(6.2) for stress-dependent capillary pressure curve as a function of water saturation, which is analogous to the well-known Brooks and Corey empirical equation (Brooks and Corey, 1966). The first term on the right-hand side of Eq.(6.2) defines the stress-dependent entry capillary pressure,

$$P_e(\sigma') = \frac{P_{ei}}{\sqrt[3-D_T]{1-\varepsilon_p}}. \quad (6.4)$$

For the final step, we replace the P_c term in the Burdine empirical equations (Burdine, 1953) for wetting (water) and non-wetting phase (gas) drainage relative permeability curves (Eq.(6.13) and (6.14), respectively) with the derived definition of P_c in Eq.(6.2) and integrate Eqs.(6.13)-(6.14) to develop Eqs.(6.4)-(6.5) for $k_{rw}(\sigma')$ and $k_{rg}(\sigma')$, respectively.

$$k_{rw} = \left(\frac{S_w - S_{wir}}{1 - S_{wir}} \right)^2 \frac{\int_{S_{wir}}^{S_w} dS_w / (P_c)^2}{\int_{S_{wir}}^1 dS_w / (P_c)^2} \quad (6.5)$$

$$k_{rw} = k_{rg-max} \left(\frac{1 - S_w}{1 - S_{wir}} \right)^2 \frac{\int_{S_w}^1 dS_w / (P_c)^2}{\int_{S_{wir}}^1 dS_w / (P_c)^2} \quad (6.6)$$

Analytical Model Results

We use power-law fitting correlation ($ax^b + c$) to interpolate the stress-dependent S_{wm} , S_{wir} , and k_{rg-max} data as a function of pore strain in Figs.3a-b. Fitting the non-linear stress-strain correlation equation (Eq.(6.3)) to the experimental data (Fig. 6.1a), we measure the constants γ_S , K_H , and K_S as being equal to 0.046, 1.91 GPa, and 2.328 MPa, respectively. Knowing the stress-strain relationship, we quantify $P_e(\sigma')$ using Eq.(6.12) with the fitting constants $D_T = 2.99$ and $P_{e_i} = 0.3kPa$; the curve is illustrated in Fig. 6.3c. Then, fitting the derived formula for stress-dependent capillary pressure (Eq.(6.2)) on the experimental data with the application of least squares regression technique, we estimate stress-dependent λ to be equal to 1.62, 1.9, and 2.612 at 10, 20, and 30 MPa effective confining stress conditions, respectively. In the same way, we use power-law fitting correlation ($\lambda = a(\sigma')^b + c$) to interpolate λ as a function of effective stress using the least square regression method. All of the fitting constants are summarized in Table 6.1. These interpolated stress-dependent properties are applied to Eq.(6.2) to model the stress-dependent capillary pressure data (Fig. 6.2d) and in the same method to Eqs.(6.4)-(6.5) to model the stress-dependent relative permeability data (Fig. 6.2c).

Table 6.1 Calculated fitting constants for the power-law correlation functions using least square regression technique.

Parameter	Fitting Constant		
	<i>a</i>	<i>b</i>	<i>c</i>
S_{wm}	-3.322×10^4	4.231	0.6011
S_{wir}	-73.81	1.81	0.6023
k_{rg-max}	3.56×10^{-16}	-10.88	0.123
λ	5.384×10^{-5}	2.901	1.575